Fermilab

FERMILAB-THESIS-2003-18

Measurement of the Diffractive Structure Function of the Antiproton in Proton-Antiproton Collisions at $\sqrt{s} = 1800$ and 630 GeV

A thesis presented to the faculty of

The Rockefeller University

in partial fulfillment of the requirements for

the degree of Doctor of Philosophy

by

Kenichi Hatakeyama

2003

Acknowledgments

I would like to thank the entire Rockefeller University experimental high energy physics group. I am most grateful to my research advisor, Professor Konstantin Goulianos, for sharing with me his enthusiasm for high energy physics and diffractive physics. I enjoyed a lot working on experimental data analyses and hardware projects under his guidance. I benefited very much from constant discussions with him.

I consider myself fortunate for having an opportunity to meet such colleagues as Professor Anwar Ahmad Bhatti, Professor Luc Demortier, Professor Stefano Lami, Dr. Kerstin Borras, Dr. Mary Convery, Dr. Michele Gallinaro, Dr. Koji Terashi and Dr. Christina Mesropian. I have learned a great deal of experimental physics and professionalism by working with them. My special thanks go to Professor Luc Demortier, Professor Konstantin Goulianos, Professor Anwar Ahmad Bhatti and Dr. Mary Convery for their extremely careful reading of the manuscript and numerous important corrections, which will hopefully make this dissertation less painful to the reader. Of course, I alone am responsible for the errors and inadequacies that remain.

I would like to thank Professor Emeritus Shunichi Hasegawa, who gave me the opportunity to join the CDF experiment when I was at Waseda University. Also, I would like to thank Professor Emeritus Yoichi Fujimoto and Professor Kunitaka Kondo for their guidance and support. I am grateful to Professor Junsuke Iwai who helped me so much not only in physics studies but also in life during my stay at Fermilab.

I am thankful to the entire QCD group of the CDF experiment for numerous discussions and suggestions. Especially, I would like to thank Dr. Mike Albrow for his constant interest in this research. I also thank Dr. Hosai Nakada and Dr. Hirofumi

Ikeda from University of Tsukuba for their help especially in the technical aspects of the experimental data analysis.

I thank my fellow graduate students, Dr. Alexander Akopian, Dr. Andrei Solodsky and Mr. Andrea Bocci for sharing with me the unforgettable experience of being a graduate student at The Rockefeller University. I am grateful to The Rockefeller University for its hospitality and for providing me with an exceptional research opportunity.

I am grateful to Dr. Tetsuo Arisawa, Dr. Hidemi Akimoto, Mr. Shin Uesaka, Mr. Yasuhiro Yoda, Mr. Junji Yamamuro, Mr. Kimihiko Ono, Mr. Norihisa Usui and other members of the Waseda University experimental high energy physics group for their help.

This thesis would not have been possible without the dedicated effort of the entire CDF collaboration. All CDF members have my sincerest thanks.

Finally, my most important acknowledgment is for the love, support and encouragement of my parents.

Contents

Acknowledgments **iii**

List of Figures **ix**

List of Tables **xxi**

Abstract **1**

1 Introduction **3**

2 Diffraction Phenomenology **8**

2.1 High Energy Hadronic Diffraction 8

2.1.1 Elastic Scattering 9

2.1.2 Single Diffractive Dissociation 10

2.1.3 Regge Approach 11

2.2 Rapidity and Rapidity Gaps 15

2.3 Hard Diffraction 18

2.3.1 Hard Diffraction at Hadron Colliders 18

2.3.2 Hard Diffraction at HERA 20

2.3.3 Single Diffractive Dijet Production in $p\bar{p}$ Collisions 23

2.4 Phenomenological Models for Hard Diffraction 26

3 Accelerator and Detector **28**

3.1 The Fermilab Tevatron Collider in 1995−1996 28

3.2 The Collider Detector at Fermilab 32

3.2.1 Calorimetry 34

3.2.2 Vertex Detector 44

3.2.3 Beam-Beam Counters 45

3.2.4 Roman Pot Spectrometer . . . 47
3.3 Trigger System . . . 54
3.4 Data Acquisition System . . . 56

4 Data and Event Selection **59**
4.1 Data Samples . . . 60
4.1.1 Diffractive Triggers and Data Samples . . . 60
4.1.2 Non-Diffractive Data Samples . . . 62
4.2 Event Selection . . . 63
4.2.1 Diffractive Inclusive Samples . . . 63
4.2.2 Non-Diffractive Inclusive Samples . . . 77
4.2.3 Jet Clustering Algorithm . . . 77
4.2.4 Jet Energy Correction . . . 80
4.2.5 Dijet Event Samples . . . 83
4.3 Background Fractions and Event Selection Efficiencies . . . 84
4.3.1 Beam-Gas Interaction Background . . . 88
4.3.2 Non-Diffractive Overlap Background . . . 89
4.3.3 Single Vertex Cut Efficiency . . . 100
4.4 Cross Sections . . . 111
4.4.1 Diffractive Inclusive Samples . . . 111
4.4.2 Diffractive Dijet Samples . . . 115
4.4.3 Non-Diffractive Dijet Samples . . . 119
4.4.4 Ratio of Diffractive Dijet to Non-Diffractive Dijet Cross Sections 120
4.5 Comparison of Diffractive Inclusive and Diffractive Dijet Event Kinematics . . . 123
4.6 Comparison of Diffractive Dijet and Non-Diffractive Dijet Kinematics 127

5 Measurement of the Diffractive Structure Function **133**
5.1 Ratio of Diffractive Dijet to Non-Diffractive Dijet Rates : $R_{\frac{SD}{ND}}$ . . . 134
5.2 Measurement of the Diffractive Structure Function : F_{jj}^{D} . . . 144
5.2.1 Definition of F_{jj}^{D} . . . 144
5.2.2 Extraction of F_{jj}^{D} . . . 148
5.2.3 F_{jj}^{D} as a Function of β . . . 150
5.2.4 F_{jj}^{D} as a Function of β and ξ . . . 154
5.3 Comparison with HERA Results . . . 160
5.3.1 Results from the H1 1994 Data . . . 160
5.3.2 Results from the H1 1997 Data . . . 166

5.4 Comparison between $\sqrt{s} = 630$ and 1800 GeV 168
5.4.1 Comparison in Terms of $R_{\frac{SD}{ND}}$ 169
5.4.2 Comparison in Terms of F_{jj}^{D} 172
5.5 Comparison with Results from Double Pomeron Exchange Dijet Events 178
5.6 Comparison with Results from Hard Single Diffraction with Rapidity Gaps 182
5.7 Comparison with UA8 Results 186
5.7.1 Summary of UA8 Results 186
5.7.2 Comparing Data 187

6 Summary and Conclusions **195**
6.1 Measurement of F_{jj}^{D} 195
6.2 Comparison with HERA Results 196
6.3 Comparison between $\sqrt{s} = 630$ and 1800 GeV 197
6.4 Comparison with Results from Double Pomeron Exchange Dijet Events 198
6.5 Comparison with Results from Single Diffractive J/ψ Events 198
6.6 Comparison with UA8 Results 199
6.7 Suggestions for the Future 199
6.7.1 Q^2-Dependence of F_{jj}^{D} 200
6.7.2 F_{jj}^{D} at Low ξ 200
6.7.3 Dijet Production by Double Pomeron Exchange 201

The CDF Collaboration **202**

A Reconstruction of ξ and t from a Roman Pot Track **209**

B Roman Pot Acceptance **213**
B.1 Antiproton Beam Characteristics 214
B.2 Comparison between Data and Monte Carlo Simulation 216
B.3 Roman Pot Acceptance Evaluation 227
B.4 Resolutions in ξ and t 227

C Events with Two Roman Pot Tracks **232**

D Calorimeter Hot Towers **235**
D.1 The 1800 GeV Data 235
D.2 The 630 GeV Data 237

Bibliography **242**

List of Figures

2.1 Illustrations for (a) elastic scattering, (b) single diffractive dissociation, (c) double diffractive dissociation, and (d) double pomeron exchange. . 9
2.2 Regge diagrams for (a) total, (b) elastic scattering, and (c) single diffractive dissociation cross sections. 12
2.3 The total pp and $p\bar{p}$ single diffractive cross sections measured for $\xi < 0.05$ along with predictions based on Eq. (2.12) and the pomeron flux renormalization model [31]. 14
2.4 Rapidity distribution in the final state of (a) a non-diffractive event and (b) a single diffractive event. 17
2.5 Schematic diagrams describing particle production in (a) deep inelastic ep scattering and (b) diffractive dissociation in a deep inelastic ep interaction. 21
2.6 Schematic diagrams for (a) non-diffractive dijet production and (b) single diffractive dijet production. 23

3.1 A schematic view of the Fermilab accelerator complex for $p\bar{p}$ collisions. 29
3.2 An isometric cut-away view of the CDF detector. 33
3.3 A longitudinal view of one quadrant of the CDF detector. 33
3.4 Segmentation of the CDF calorimeters in η-ϕ space. 36
3.5 A cut-away view of one wedge of the Central Electromagnetic calorimeter (CEM). 38
3.6 An exploded view of the layer of the Plug Electromagnetic calorimeter (PEM) proportional tube array. 40
3.7 A cross section view of a chamber of the Forward Electromagnetic calorimeter (FEM). 43
3.8 A schematic view of one of the beam-beam counter planes. 46
3.9 A top view of the outgoing antiproton beam line. 47

3.10 A top view of the Roman Pot spectrometer. The Roman Pot spectrometer consists of three Roman Pot detector stations which are spaced 98.5 cm apart from one another along the beam line. The structure of the scintillation fiber tracking detector is shown in the inset. 48
3.11 Arrangement of the Roman Pot detector. The Roman Pot detector, consisting of a scintillation trigger counter and an X-Y scintillation fiber tracking detector, is mounted in a vessel attached to the vacuum beam pipe and vacuum chamber by bellows. 49
3.12 One ribbon consisting of four scintillation fibers used for the Roman Pot tracking detector. 50
3.13 Arrangement of the Roman Pot scintillation fiber tracking detector for the X direction. Two layers of 20 scintillation fiber ribbons are mounted in parallel, forming a superlayer. Each superlayer is divided into 79 channels of 0.267 mm width. 52
3.14 Two typical hit patterns in the Roman Pot scintillation fiber tracking detector. (a) Both layers have a hit. (b) Only one layer has a hit. . . . 52
3.15 A track reconstructed from hits in the Roman Pot scintillation fiber tracking detectors in the X (Y) direction. 53
3.16 The Roman Pot acceptance as a function of ξ and $|t|$ for the (a) 1800 GeV and (b) 630 GeV runs. 54
3.17 A schematic drawing of data flow through the CDF data acquisition system. 57

4.1 Instantaneous luminosity distributions for the (a) 630 GeV Roman Pot triggered data, (b) 1800 GeV Roman Pot triggered data, (c) 630 GeV minimum bias data, and (d) 1800 GeV minimum bias data. 62
4.2 Missing E_T distributions for the (a) 1800 GeV and (b) 630 GeV data samples. 64
4.3 (a) Vertex multiplicity distributions for runs 75644−75678 (left) and 75713−75738 (right) of the 1800 GeV data sample. (b) Vertex multiplicity distributions for runs 74849−74978 (left) and 75000−75110 (right) of the 630 GeV data sample. 66
4.4 Distributions of z_{vtx} for the (a) 1800 GeV and (b) 630 GeV data samples. 67
4.5 ADC count distributions of the three Roman Pot trigger counters and total ADC count distributions of the three trigger counters for the (a) 1800 GeV and (b) 630 GeV data samples. 67

4.6 Reconstructed Roman Pot track multiplicity distributions for the (a) 1800 GeV and (b) 630 GeV data samples. 68
4.7 The hit pattern of Roman Pot tracks for the 630 GeV data sample. . . 69
4.8 Distributions of *two-hit* Roman Pot tracks in the fiber detectors in which the reconstructed Roman Pot track does not have hits. 71
4.9 The distribution of the angle θ_X^{RP} of the reconstructed tracks with respect to the beam line in the horizontal direction. 72
4.10 West BBC multiplicity (left) and FCAL tower multiplicity (right) distributions for events in the 630 GeV data sample with $\theta_X^{RP} \geq 0$ (top) and $\theta_X^{RP} < 0$ (bottom). 72
4.11 Reconstructed ξ (left) and $|t|$ (right) distributions for the (a) 1800 GeV and (b) 630 GeV data samples. 73
4.12 Distributions of inclusive single diffractive events as a function of ξ and $|t|$ in the (a) 1800 GeV and (b) 630 GeV data samples. 74
4.13 Distributions of ξ (left) and $|t|$ (right) for the (a) 1800 GeV and (b) 630 GeV diffractive inclusive samples. These distributions are corrected for the Roman Pot acceptance. 75
4.14 West BBC multiplicity distributions for the (a) 1800 GeV and (b) 630 GeV data samples. 76
4.15 Distributions of $\not\!\!E_T$ for the (a) 1800 GeV and (b) 630 GeV minimum bias data samples. 78
4.16 Distributions of z_{vtx} for the (a) 1800 GeV and (b) 630 GeV minimum bias data samples. 78
4.17 A diffractive dijet candidate event in the 1800 GeV data sample. . . . 85
4.18 A diffractive dijet candidate event in the 630 GeV data sample. 86
4.19 East BBC multiplicity (left) and FCAL tower multiplicity (right) distributions for the (a) 1800 GeV and (b) 630 GeV SD inclusive samples. The enhancement at the zero bin is possibly due to beam-gas diffractive interactions. 90
4.20 West BBC multiplicity (top) and FCAL tower multiplicity (bottom) distributions for the 1800 GeV SD inclusive sample (open histograms). Left (right) plots are for runs with a maximum west BBC hit = 14 (11). Distributions for the ND inclusive sample are normalized at the maximum BBC hit bin of 14 or 11, and in the region $N_{FCAL} \geq 20$ (cross-hatched histograms). 93

4.21 West BBC multiplicity (top) and FCAL tower multiplicity (bottom) distributions for the 1800 GeV SD dijet sample of $E_T^{jet1,2} \geq 7$ GeV (open histograms). Left (right) plots are for runs with a maximum BBC hit = 14 (11). Distributions for the ND dijet sample are normalized at the maximum BBC hit bin of 14 or 11, and in the region $N_{FCAL} \geq 20$ (cross-hatched histograms). 95
4.22 West BBC multiplicity (a,b) and FCAL tower multiplicity (c,d) distributions for the 630 GeV SD inclusive sample (open histograms). In order to estimate the ND overlap background contribution, ND distributions are normalized to the SD distributions at $N_{BBC} = 14$ and in the region $N_{FCAL} \geq 10$ (cross-hatched histograms). (e,f) West FCAL tower multiplicity distributions for the SD sample (open histograms) and ND overlap background (cross-hatched histograms) after the requirement of west BBC multiplicity ≤ 4. 97
4.23 West BBC multiplicity (a,b) and FCAL tower multiplicity (c,d) distributions for the 630 GeV SD dijet sample of $E_T^{jet1,2} \geq 7$ GeV (open histograms). In order to estimate the ND overlap background contribution, ND distributions are normalized to the SD distributions in the regions $9 \leq N_{BBC} \leq 14$ and $N_{FCAL} \geq 10$ where the ND overlap background is dominant (cross-hatched histograms). (e,f) West FCAL tower multiplicity distributions for the SD sample (open histograms) and ND overlap background (cross-hatched histograms) after the requirement of west BBC multiplicity ≤ 4. 99
4.24 (a) Vertex multiplicity distribution for the 1800 GeV SD inclusive subsample without vertex cuts in the trigger. (b) East BBC and FCAL tower multiplicity distributions for zero vertex events in the 1800 GeV SD inclusive subsample (solid lines), and the single interaction event contributions estimated from the distributions for the single vertex events (dotted lines). (c) West BBC and FCAL tower multiplicity distributions for multiple vertex events in the 1800 GeV SD inclusive subsample (solid lines), and those for the single vertex events normalized in the regions $0 \leq N_{BBC} \leq 2$ and $0 \leq N_{FCAL} \leq 3$ (dotted lines). . 104

4.25 West BBC multiplicity (top) and FCAL tower multiplicity (bottom) distributions for multiple vertex events in the 1800 GeV SD dijet sample of $E_T^{jet1,2} \geq 7$ GeV (solid lines), and those for the single vertex events normalized in the regions $0 \leq N_{BBC} \leq 2$, and $0 \leq N_{FCAL} \leq 3$ (dotted lines). 106
4.26 (a) Vertex multiplicity distribution for the 630 GeV SD inclusive sample. (b) East BBC and FCAL tower multiplicity distributions for zero vertex events in the 630 GeV data (solid lines), and the single interaction event contributions estimated from the distributions for the single vertex events (dotted lines). (c) West BBC and FCAL tower multiplicity distributions for multiple vertex events in the 630 GeV data (solid lines), and the estimated single interaction event contributions (cross-hatched areas). 107
4.27 West BBC and FCAL tower multiplicity distributions for multiple vertex events in the 630 GeV SD dijet sample of $E_T^{jet1,2} \geq 7$ GeV (solid lines), the estimated multiple interaction event contributions (dotted lines), and the estimated single interaction event contributions (cross-hatched histograms). 110
4.28 Distributions of (1) ξ and (2) $|t|$ for the diffractive inclusive (histograms) and diffractive dijet (points) data samples, and the ratio of diffractive dijet events to diffractive inclusive events as a function of (3) ξ and (4) $|t|$ for the (a) 1800 GeV and (b) 630 GeV data samples. The dijet data samples are selected by requiring at least two jets with $E_T \geq 7$ GeV in an event. 126
4.29 Distributions of (1) the leading jet E_T (E_T^{jet1}), (2) the next-to-leading jet E_T (E_T^{jet2}), and (3) the mean E_T of the leading two jets, $E_T^* = (E_T^{jet1} + E_T^{jet2})/2$, for the $E_T^{jet1,2} \geq 7$ GeV diffractive dijet (points) and non-diffractive dijet (histograms) samples collected at (a) $\sqrt{s} = 1800$ GeV and (b) $\sqrt{s} = 630$ GeV. 128
4.30 Distributions of (1) the leading jet E_T (E_T^{jet1}), (2) the next-to-leading jet E_T (E_T^{jet2}), and (3) the mean E_T of the leading two jets, $E_T^* = (E_T^{jet1} + E_T^{jet2})/2$, for the $E_T^{jet1,2} \geq 7$ GeV diffractive dijet (points) and non-diffractive dijet (histograms) samples collected at (a) $\sqrt{s} = 1800$ GeV and (b) $\sqrt{s} = 630$ GeV. The non-diffractive distributions are normalized to the diffractive distributions at high E_T ($E_T \geq 15$ GeV). 129

4.31 Distributions of (1) the leading jet η (η^{jet1}), (2) the next-to-leading jet η (η^{jet2}), and (3) the mean η of the leading two jets, $\eta^* = (\eta^{jet1} + \eta^{jet2})/2$, for the $E_T^{jet1,2} \geq 7$ GeV diffractive dijet (points) and non-diffractive dijet (histograms) samples collected at (a) $\sqrt{s} = 1800$ GeV and (b) $\sqrt{s} = 630$ GeV. 130

4.32 Distributions of the azimuthal angle difference $\Delta\phi_{jj}$ between the leading two jets for the $E_T^{jet1,2} \geq 7$ GeV diffractive dijet (points) and non-diffractive dijet (histograms) samples collected at (a) $\sqrt{s} = 1800$ GeV and (b) $\sqrt{s} = 630$ GeV. 131

4.33 Distributions of the azimuthal angle difference $\Delta\phi_{jj}$ between the leading two jets for diffractive dijet (points) and non-diffractive dijet (histograms) events with $E_T^{jet1,2} \geq 7$ GeV and $E_T^* = (E_T^{jet1} + E_T^{jet2})/2 \geq 10$ GeV collected at (a) $\sqrt{s} = 1800$ GeV and (b) $\sqrt{s} = 630$ GeV, and with (c) $E_T^{jet1,2} \geq 10$ GeV and (d) $E_T^{jet1,2} \geq 15$ GeV collected at $\sqrt{s} = 1800$ GeV. 132

5.1 (a) Distributions of $x_{\bar{p}}$ for the $E_T^{jet1,2} \geq 7$ GeV SD dijet sample and the estimated ND overlap background contribution. (b) The $x_{\bar{p}}$ distribution for the $E_T^{jet1,2} \geq 7$ GeV ND dijet sample. (c) Shape comparison of $x_{\bar{p}}$ distributions for the SD dijet and ND dijet samples. (d) The ratio of SD to ND event rates for dijet events with $E_T^{jet1,2} \geq 7$ GeV as a function of $x_{\bar{p}}$. 136

5.2 The ratio of SD to ND event rates for dijet events with $E_T^{jet1,2} \geq 7$ GeV as a function of $x_{\bar{p}}$ for SD events in the region $0.035 \leq \xi \leq 0.095$ and $|t| \leq 1.0$ GeV^2. The distribution is fitted to the power law form $R_{\frac{SD}{ND}}(x_{\bar{p}}) = R_0(x_{\bar{p}}/0.0065)^{-r}$ in the indicated region. 137

5.3 Ratios of SD to ND event rates for dijet events with $E_T^{jet1,2} \geq 7$ GeV as a function of $x_{\bar{p}}$, in which up to three jets with $E_T \geq 5$ GeV are used in evaluating $x_{\bar{p}}$ (filled circles), only the leading two jets are used (upward triangles), up to four jets with $E_T \geq 5$ GeV are used (downward triangles), and only the leading two jets are used for dijet exclusive events with $E_T^{jet3} < 5$ GeV (open circles). 139

5.4 Distributions of $x_{\bar{p}}$ for the SD dijet sample, ND overlap background events, and ND dijet sample (top two plots in the left side sets), shape comparison of $x_{\bar{p}}$ distributions for the SD dijet and ND dijet samples (bottom left plot in the left side sets), and the ratio of SD dijet to ND dijet event rates as a function of $x_{\bar{p}}$ (bottom right plot in the left side sets and enlarged versions in the right side plots) for the dijet samples of (a) $E_T^{jet1,2} \geq 10$ GeV and (b) $E_T^{jet1,2} \geq 15$ GeV. 141
5.5 The ratio of SD to ND event rates as a function of $x_{\bar{p}}$ for the dijet samples of three jet E_T thresholds, $E_T^{jet1,2} \geq 7$ (circles), 10 (squares) and 15 (triangles) GeV (a) without a requirement on the third jet and (b) with a $E_T^{jet3} < 5$ GeV requirement. 142
5.6 The ratio of SD to ND event rates for dijet events with $E_T^{jet1,2} \geq 7$ GeV as a function of $x_{\bar{p}}$ in the region $x_{\bar{p}} \geq 0.001$ for six ξ intervals of width $\Delta\xi = 0.01$ centered at 0.04 to 0.09. 143
5.7 The distribution of $F_{jj}(x)$ evaluated using GRV98LO at $Q^2 = 75$ GeV^2. 145
5.8 Distributions of $F_{jj}^D(\beta)$ extracted from dijet events with $E_T^{jet1,2} \geq 7$ GeV using the GRV98LO [40] (circles), CTEQ5L [41] (squares) and MRST98LO [42] (triangles) PDF sets. 146
5.9 Distributions of the leading two jet mean E_T squared, $(E_T^*)^2 = \left((E_T^{jet1} + E_T^{jet2})/2\right)^2$, for (a) SD dijet and (b) ND dijet events with $E_T^{jet1,2} \geq 7$ GeV. 147
5.10 Distributions of $F_{jj}^D(\beta)$ extracted from dijet events with $E_T^{jet1,2} \geq 7$ GeV using the non-diffractive structure function F_{jj} evaluated at $Q^2 =$ 49 (filled circles), 75 (squares), 100 (triangles), and 150 GeV^2 (open circles). 147
5.11 The distribution of $F_{jj}^D(\beta)$ on a logarithmic scale extracted from dijet events with $E_T^{jet1,2} \geq 7$ GeV for the region $0.035 \leq \xi \leq 0.095$ and $|t| \leq 1.0$ GeV^2. 151
5.12 The distribution of $F_{jj}^D(\beta)$ on a linear scale extracted from dijet events with $E_T^{jet1,2} \geq 7$ GeV for the region $0.035 \leq \xi \leq 0.095$ and $|t| \leq 1.0$ GeV^2. 152
5.13 Distributions of $F_{jj}^D(\beta)$ extracted from dijet events with $E_T^{jet1,2} \geq 7$ GeV, in which up to three jets with $E_T \geq 5$ GeV are used in evaluating β (filled circles), only the leading two jets are used (upward triangles), up to four jets with $E_T \geq 5$ GeV are used (downward triangles), and only the leading two jets are used for dijet exclusive events with $E_T^{jet3} <$ 5 GeV (open circles). 153

5.14 Distributions of $F_{jj}^D(\beta)$ extracted from dijet events with $E_T^{jet1,2} \geq 7$ GeV for six ξ intervals of width $\Delta\xi = 0.1$. 155
5.15 (a) Values of the exponent n from fits with $F_{jj}^D(\beta) = B_0(\beta/0.1)^{-n}$ to the $F_{jj}^D(\beta)$ distributions extracted from dijet events with $E_T^{jet2} \geq 7$ GeV for six ξ intervals. (b) Values of the parameter B_0 from fits with $F_{jj}^D(\beta) = B_0(\beta/0.1)^{-n}$ to the $F_{jj}^D(\beta)$ distributions extracted from dijet events with $E_T^{jet1,2} \geq 7$ GeV for six ξ intervals (circles), and $1/N_{incl}\, dN/d\xi$ for SD inclusive events (triangles). 157
5.16 Distributions of $F_{jj}^D(\beta)$ extracted from dijet events with $E_T^{jet1,2} \geq 7$ GeV for six ξ intervals. This figure is similar to Figure 5.14, but shows a wider β region. 159
5.17 Distributions of $F_{jj}^D(\beta, \xi)$ versus ξ obtained using dijet events with $E_T^{jet1,2} \geq 7$ GeV for eight $\log\beta$ intervals of width $\Delta(\log\beta) = 0.2$ centered at -1.5 to -0.1. 161
5.18 The exponent m from fits with $C\xi^{-m}$ to $F_{jj}^D(\beta, \xi)$ extracted from dijet events with $E_T^{jet1,2} \geq 7$ GeV for the region $0.035 \leq \xi \leq 0.095$ and $|t| \leq 1.0$ GeV^2, as a function of β 162
5.19 The distribution of $F_{jj}^D(\beta)$ (points) extracted from dijet events with $E_T^{jet1,2} \geq 7$ GeV for the region $0.035 \leq \xi \leq 0.095$ and $|t| \leq 1.0$ GeV^2, compared with expectations from the diffractive parton distributions in the proton extracted from diffractive deep inelastic scattering by the H1 collaboration [9]. 164
5.20 The distribution of $F_{jj}^D(\beta)$ extracted from dijet events with $E_T^{jet1,2} \geq 7$ GeV in this analysis for the region $0.035 \leq \xi \leq 0.095$ and $|t| \leq 1.0$ GeV^2 compared with predictions from the recent (2002) [12] and previous [9] leading order QCD fits by the H1 collaboration. 167
5.21 (a) Distributions of $x_{\bar{p}}$ for the 630 GeV SD dijet sample of $E_T^{jet1,2} \geq 7$ GeV and $E_T^* = (E_T^{jet1} + E_T^{jet2})/2 \geq 10$ GeV, and the estimated ND overlap background contribution. (b) The $x_{\bar{p}}$ distribution for the ND dijet sample. (c) Shape comparison of $x_{\bar{p}}$ distributions for the SD dijet and ND dijet samples. (d) The ratio of the SD dijet to ND dijet event rates as a function of $x_{\bar{p}}$. 169

5.22 The ratio of SD dijet to ND dijet event rates as a function of $x_{\bar{p}}$ measured at $\sqrt{s} = 630$ (filled circles) and 1800 GeV (open circles), in the region $0.035 \leq \xi \leq 0.095$ and $|t| \leq 0.2$ GeV^2 for the SD data sample. Dijet events are selected by requiring $E_T^{jet1,2} \geq 7$ GeV and $E_T^* = (E_T^{jet1} + E_T^{jet2})/2 \geq 10$ GeV. Up to three jets with $E_T \geq 5$ GeV are used in evaluating $x_{\bar{p}}$. 171
5.23 The ratio of SD dijet to ND dijet event rates as a function $x_{\bar{p}}$ measured at (a) $\sqrt{s} = 630$ GeV and (b) $\sqrt{s} = 1800$ GeV; in evaluating $x_{\bar{p}}$, up to three jets with $E_T \geq 5$ GeV are used (circles), only the leading two jets are used (upward triangles), and up to four jets with $E_T \geq 5$ GeV are included (downward triangles). 172
5.24 The ratio of SD dijet to ND dijet event rates as a function of $x_{\bar{p}}$ measured at $\sqrt{s} = 630$ (filled circles) and 1800 GeV (open circles), in the region $0.035 \leq \xi \leq 0.095$ and $|t| \leq 0.2$ GeV^2 for the SD data samples. (a) Only the leading two jets are used in evaluating $x_{\bar{p}}$. (b) Up to four jets with $E_T \geq 5$ GeV are used in evaluating $x_{\bar{p}}$. 173
5.25 Distributions of $F_{jj}^D(\beta)$ extracted from dijet events with $E_T^{jet1,2} \geq 7$ GeV and $E_T^* = (E_T^{jet1} + E_T^{jet2})/2 \geq 10$ GeV for the region $0.035 \leq \xi \leq 0.095$ and $|t| \leq 0.2$ GeV^2 at $\sqrt{s} = 630$ (filled circles) and 1800 GeV (open circles). Up to three jets with $E_T \geq 5$ GeV are used in evaluating β. 174
5.26 Distributions of $F_{jj}^D(\beta)$ extracted from dijet events with $E_T^{jet1,2} \geq 7$ GeV and $E_T^* = (E_T^{jet1} + E_T^{jet2})/2 \geq 10$ GeV for the region $0.035 \leq \xi \leq 0.095$ and $|t| \leq 0.2$ GeV^2 at $\sqrt{s} = 630$ (filled circles) and 1800 GeV (open circles). (a) Only the leading two jets are used in evaluating β. (b) Up to four jets with $E_T^{jet} \geq 5$ GeV are used in evaluating β. 175
5.27 Illustrations of (a) event topology in pseudorapidity η and (b) diagram for dijet production in double pomeron exchange. 178
5.28 Ratios of DPE to SD (SD to ND) dijet event rates per unit ξ, shown as open (filled) circles, as a function of x-Bjorken of the struck parton in the proton (antiproton). The inset shows $\tilde{R}(x)$ per unit ξ versus ξ, where the tilde over the R indicates the weighted average of the $R(x)$ points in the region of x within the vertical dashed lines. 181
5.29 Ratios of SD to ND J/ψ (circles) and dijet (triangles) event rates per unit ξ as a function of x-Bjorken of the struck parton in the proton (antiproton) associated with the rapidity gap. 184

5.30 (a) Observed x(2-jet) distribution for the UA8 data in the region $0.04 < \xi < 0.10$, and expected distributions for the hard and soft structure functions with arbitrary normalizations. (b) Results of x(2-jet) calculation in PYTHIA for $\xi = 0.07$, assuming the entire momentum of the pomeron participates in the hard scattering. 188
5.31 The azimuthal angle difference $\Delta\phi_{jj}$ between the leading two jets for the UA8 (points) and CDF (histogram) data samples. 189
5.32 Distributions of x(2-jet) for SD dijet events with $\Delta\phi_{jj} \geq 135^\circ$ (solid line) and $\Delta\phi_{jj} < 135^\circ$ (dashed line) in the CDF data. 190
5.33 Distributions of x(2-jet) for SD dijet events in the UA8 (points) and CDF (histogram) data samples. 191
5.34 (a) Distributions of x(2-jet) for SD dijet events with $0.04 \leq \xi < 0.06$ (solid line), $0.06 \leq \xi < 0.08$ (dashed line), and $0.08 \leq \xi \leq 0.10$ (dotted line). (b) Distributions of x(2-jet) for SD dijet events in the UA8 (points) and CDF (histogram) data samples. In the CDF distribution, events are weighted so that the ξ distribution becomes similar to that of the UA8 data. 192
5.35 Distributions of x(2-jet) for the CDF SD dijet events with (solid line) and without (dashed line) the $|\eta^{jet1,2}| \leq 2$ cut. 194

B.1 The upper two plots show two-dimensional distributions of reconstructed vertices on the X-Y plane for run 75020. The lower two plots show the projection in the X and Y directions, respectively. . . . 215
B.2 The standard deviation σ of the vertex distribution as a function of run number in X (top) and Y (bottom) directions for the (a) diffractive and (b) non-diffractive data samples. 215
B.3 Distributions of the position X^{RP} of reconstructed Roman Pot tracks in the horizontal direction relative to the center of the beam pipe for the data (points) and the MC simulation (histogram) for each run. . . 218
B.4 Distributions of the angle θ_X^{RP} of reconstructed Roman Pot tracks in the horizontal direction with respect to the beam line for the data (points) and the MC simulation (histogram) for each run. 219
B.5 Distributions of the position Y^{RP} of reconstructed Roman Pot tracks in the vertical direction relative to the center of the beam pipe for the data (points) and the MC simulation (histogram) for each run. 220

B.6 Distributions of the angle θ_Y^{RP} of reconstructed Roman Pot tracks in the vertical direction with respect to the beam line for the data (points) and the MC simulation (histogram) for each run. 221
B.7 Reconstructed ξ distributions for the data (points) and the MC simulation (histogram) for each run. 222
B.8 Reconstructed $|t|$ distributions for the data (points) and the MC simulation (histogram) for each run. 223
B.9 Distributions of the azimuthal angle $\phi_{\bar{p}}$ of quasielastically-scattered recoil antiprotons for the data (points) and the MC simulation (histogram) for each run. 224
B.10 Distributions of the Roman Pot track hit pattern for the data (points) and the MC simulation (histogram) for each run. The MC distributions are normalized to the data distributions at the zero bin. 225
B.11 Ratios of the data to the MC simulation in the class=1 and 2 bins in Figure B.10 as a function of run number. 226
B.12 The Roman Pot acceptance as a function of ξ and $|t|$ for the three sets of Monte Carlo event samples; (a) for runs 74849−74978, (b) for runs 75000−75049, and (c) for runs 75109−75110. 228
B.13 Distributions of the difference between the reconstructed ξ and the generated ξ for the three sets of Monte Carlo event samples; (a) for runs 74849−74978, (b) for runs 75000−75049, and (c) for runs 75109−75110. 230
B.14 Distributions of the difference between the reconstructed t and the generated t for the three sets of Monte Carlo event samples; (a) for runs 74849−74978, (b) for runs 75000−75049, and (c) for runs 75109−75110. 231

C.1 The hit channel differences between two reconstructed Roman Pot tracks on the (a,b) Roman Pot 1 X and Y detectors, (c,d) Roman Pot 2 X and Y detectors, and (e,f) Roman Pot 3 X and Y detectors for the 630 GeV diffractive data. 233
C.2 The Roman Pot hit patterns when the hit channel difference is 2, 4 and 5. 234

D.1 Distributions of leading jets on the plane of detector-η versus ϕ for 1800 GeV diffractive dijet events with at least two jets with $E_T \geq 7$ GeV in runs 75644−75713 (left) and 75714−75738 (right). 236

D.2 Distributions of leading (left) and next-to-leading (right) jets on the plane of detector-η versus ϕ for 1800 GeV non-diffractive dijet events with at least two jets with $E_T \geq 7$ GeV. 237
D.3 Distributions of EM fraction of jets in the five categories of hot spots and outside the hot spots for the 1800 GeV diffractive dijet sample. . 238
D.4 Distributions of leading (left) and next-to-leading (right) jets on the plane of detector-η versus ϕ for 1800 GeV diffractive dijet (top) and non-diffractive dijet (bottom) events with at least two jets with $E_T \geq 7$ GeV which survive the hot tower filter requirements. 239
D.5 Distributions of the leading two jets on the plane of detector-η versus ϕ for 630 GeV diffractive dijet events with at least two jets with $E_T \geq 7$ GeV (a) in runs 74919−74959 and (b) in the other runs before the hot tower filter is applied, and (c) in runs 74919−74959 after the hot tower filter is applied. 240
D.6 Distributions of the leading two jets on the plane of detector-η versus ϕ for 630 GeV non-diffractive dijet events with at least two jets with $E_T \geq 7$ GeV (a) in runs 74919−74959 and (b) in the other runs before the hot tower filter is applied, and (c) in runs 74919−74959 after the hot tower filter is applied. 240
D.7 Distributions of EM fraction of the leading two jets in 630 GeV non-diffractive dijet events with at least two jets with $E_T \geq 7$ GeV (a) in runs 74919−74959 in the hot spot and (b) in the other runs for the entire η-ϕ plane, and (c) in runs 74919−74959 for the entire η-ϕ plane after the hot tower filter is applied. 241

List of Tables

3.1 Characteristics of the CDF calorimeter subsystems. 35

4.1 Dead channels of the Roman Pot fiber tracking detectors. 69
4.2 Underlying event E_T subtracted from jet E_T in this analysis. 83
4.3 Number of Roman Pot triggered events after each selection cut. 87
4.4 Number of non-diffractive events after each selection cut. 88
4.5 Number of events, efficiencies and background fractions for the 1800 GeV diffractive dijet and diffractive inclusive samples. 116
4.6 Number of events, efficiencies and background fractions for the 630 GeV diffractive dijet and diffractive inclusive samples. 118
4.7 Systematic uncertainties in the normalization of the single diffractive (SD) dijet to non-diffractive (ND) dijet cross section ratio at $\sqrt{s} = 1800$ GeV. 124
4.8 Systematic uncertainties in the normalization of the single diffractive (SD) dijet to non-diffractive (ND) dijet cross section ratio at $\sqrt{s} = 630$ GeV. 125

5.1 Fit parameters R_0 and r, and $\chi^2/d.o.f.$ for different event samples and different numbers of jets included in the $x_{\bar{p}}$ determination. 138
5.2 Fit parameters R_0 and r and $\chi^2/d.o.f.$ for the dijet samples of $E_T^{jet1,2} \geq$ 7, 10 and 15 GeV in the region $0.035 \leq \xi \leq 0.095$. 140
5.3 Fit parameters R_0 and r and $\chi^2/d.o.f.$ for six ξ intervals. 143
5.4 Fit parameters B_0 and n, and $\chi^2/d.o.f.$ for different event samples and different numbers of jets included in the β determination. 154
5.5 Fit parameters B_0 and n, and $\chi^2/d.o.f.$ for six ξ intervals. 154
5.6 Fit parameters n and m for different event samples and different numbers of jets included in the β determination. 158

5.7 Number of events, efficiencies and background fractions for the 1800 GeV SD dijet and inclusive samples in the region $0.035 \leq \xi \leq 0.095$ and $|t| \leq 0.2$ GeV^2. 168
5.8 Number of events in the UA8 and CDF data samples in three ξ intervals. 190

A.1 Tevatron configuration from the CDF nominal collision point (BØ) to the position of the Roman Pot detector stations. 212

D.1 Summary of hot towers in the 1800 GeV data samples. 238

Abstract

A measurement of the effective diffractive structure function F_{jj}^D of the antiproton obtained from a study of single diffractive dijet events produced in association with a leading antiproton in $p\bar{p}$ collisions at the center-of-mass energy $\sqrt{s} = 1800$ and 630 GeV is presented. Inclusive samples of single diffractive events were collected during the Tevatron collider run of 1995−1996 using the Collider Detector at Fermilab (CDF) by triggering on a leading antiproton detected in a forward Roman Pot spectrometer. From these samples, single diffractive dijet subsamples were selected by requiring two or more jets with transverse energy $E_T \geq 7$ GeV in an event.

From the dijet data samples, an effective leading order diffractive structure function F_{jj}^D of the antiproton is extracted. In the kinematic region of antiproton fractional momentum loss $0.035 \leq \xi \leq 0.095$, four-momentum transfer squared $|t| \leq 1.0$ GeV^2 and $\beta = x_{\bar{p}}/\xi < 0.5$, where $x_{\bar{p}}$ is the Bjorken scaling variable of the struck parton in the antiproton, $F_{jj}^D(\beta, \xi)$ is found to have the form $F_{jj}^D(\beta, \xi) \propto \beta^{-1.0\pm0.1}\xi^{-0.9\pm0.1}$ at $\sqrt{s} = 1800$ GeV.

To address the question of QCD factorization in diffraction processes, i.e. universality of the diffractive structure function, several comparisons are made on the measured F_{jj}^D. In comparisons with expectations based on results obtained in diffractive deep inelastic scattering experiments at HERA, F_{jj}^D measured in this analysis is

found to be smaller by approximately an order of magnitude, indicating a breakdown of QCD factorization in diffraction processes. In comparisons with results obtained in $p\bar{p}$ collisions at $\sqrt{s} = 630$ GeV, the ratio in normalization of the measured F_{jj}^D at the two energies is found to be $R_{\frac{630}{1800}} = 1.3 \pm 0.2(\text{stat})^{+0.4}_{-0.3}(\text{syst})$. This is compatible with the factorization expectation of unity, but is also in agreement within errors with predictions in the range $1.6-1.8$ from phenomenological models that explain the suppression of the diffractive structure function in $p\bar{p}$ collisions relative to that in $\gamma^* p$ collisions.

Comparisons with results from a study of dijet events by double pomeron exchange and single diffractive events containing a J/ψ meson by the CDF collaboration, and with results from a study of single diffractive dijet events obtained by the UA8 collaboration in $p\bar{p}$ collisions at $\sqrt{s} = 630$ GeV are also presented.

Chapter 1

Introduction

The fundamental theory of strong interactions, Quantum Chromodynamics (QCD), has been very successful in describing hadronic interactions at high momentum transfers; predictions based on perturbative QCD have shown good agreement with experimental measurements of high transverse momentum (hard) processes, such as high-p_T jet production and high-Q^2 deep inelastic scattering (DIS). However, interactions at low momentum transfers, which make up the bulk of the hadronic cross section, cannot be fully described in terms of QCD since they do not contain the hard energy scale that is needed for the perturbative QCD calculation to converge. Low transverse momentum (soft) processes in hadronic interactions include diffractive phenomena, such as elastic scattering and diffractive dissociation.

Approximately 15 % of the high energy inelastic $p\bar{p}$ collisions are due to single diffractive dissociation, $p+\bar{p} \to p+X$ or $p+\bar{p} \to X+\bar{p}$, in which either the incoming proton or antiproton escapes intact retaining a large fraction of its initial longitudinal momentum x_F, and X denotes "anything". The value of x_F is typically $x_F > 0.85$. The quasielastically-scattered leading particle is separated from the diffractive final

state X in rapidity[1] space. The region in rapidity space devoid of final state particles is called a *rapidity gap*. The rapidity gap is generally thought to be associated with the exchange of a strongly-interacting color-singlet object carrying the quantum numbers of the vacuum. This color-singlet object is generally referred to as the *pomeron* in honor of the Russian physicist I. Y. Pomeranchuk (1913−1966), who studied the asymptotic behavior of high energy elastic scattering, the "mother" of hadronic diffractive physics. The single diffractive dissociation process was predicted early in 1960 by M. L. Good and W. D. Walker [1] and has been studied since then; however, the underlying mechanism of this process and the nature of the pomeron are not yet well understood.

With high energy accelerators becoming available worldwide, it was suggested that it would be valuable to study diffraction processes which have soft and hard properties at the same time [2]. Such processes are called hard diffraction processes. Studying hard diffraction processes could give us some understanding of the underlying dynamics of diffractive dissociation in the framework of perturbative QCD. It might also allow us to probe the parton distributions in the hadron contributing to diffractive dissociation, called diffractive parton distributions, which may lead to the parton distributions in the pomeron. This would be an important step toward a better understanding of soft interactions and of color confinement.

A typical example of hard diffraction processes is jet production in $p\bar{p}$ collisions with a leading proton or antiproton associated with a large rapidity gap. This process was first observed by the UA8 experiment at the CERN $Sp\bar{p}S$ collider at $\sqrt{s} = 630$ GeV [3, 4]. Later, hard diffraction processes in ep collisions, such as diffractive DIS [5, 6] and hard diffractive photoproduction [7, 8], were observed by the ZEUS [5, 8]

[1] See Section 2.2 for the definition of rapidity.

and H1 [6, 7] collaborations at the DESY ep collider HERA. These collaborations investigated the quark and gluon contents of the diffractive exchange by measuring the diffractive DIS cross section and the diffractive F_2 structure function of the proton [9, 10, 11, 12], as well as the hadronic final state in diffractive DIS [13, 14] and diffractive photoproduction [15, 16, 17].

More recently, two experiments at the Fermilab Tevatron $p\bar{p}$ collider, CDF and DØ, reported results on hard single diffraction processes in $p\bar{p}$ collisions at $\sqrt{s} = 1800$ and 630 GeV, including W [18], dijet [19, 20], b-quark [21], and J/ψ production [22]. In these analyses, single diffractive events are identified not by the leading particle but by using the rapidity gap signature. W production is sensitive to the quark content of the diffractive exchange; on the other hand, dijet production and b-quark production are more sensitive to the gluon content. By combining results on single diffractive W, dijet and b-quark production, the CDF collaboration obtained the gluon fraction in the diffractive exchange (pomeron), $F_g^D = 0.54^{+0.16}_{-0.14}$ [21]. This result is in agreement with the gluon fraction obtained by the ZEUS collaboration from measurements of the jet cross section in diffractive photoproduction [15] and of the diffractive F_2 structure function of the proton [5]. However, the production rates for hard single diffraction processes measured at the Tevatron were found to be about $5-10$ times lower than predictions [23, 24] based on the diffractive parton distribution functions of the proton extracted from the HERA data on diffractive DIS [5, 6, 9, 10] and on diffractive photoproduction of jets [15]. This discrepancy in the production rates indicates a severe breakdown of QCD factorization in diffraction processes, i.e. the diffractive parton distribution functions of the proton extracted from the HERA data are not directly applicable to the Tevatron data.

In the analysis described in this dissertation, an effective leading order diffractive

structure function of the antiproton is measured using single diffractive dijet events produced in $p\bar{p}$ collisions at $\sqrt{s} = 1800$ and 630 GeV collected with the Collider Detector at Fermilab (CDF). The single diffractive data used in this analysis were collected by triggering on a leading antiproton detected in a Roman Pot spectrometer installed downstream of the antiproton beam line. The diffractive structure function measured at $\sqrt{s} = 1800$ GeV is compared with that at $\sqrt{s} = 630$ GeV, and with expectations based on results obtained in diffractive DIS experiments at HERA [9, 12], as well as with results from a study of dijet production in double pomeron exchange events at the Fermilab Tevatron [25] in order to further characterize how QCD factorization breaks down in diffraction processes.

This dissertation is structured as follows. Chapter 2 presents an introduction to high energy hadronic diffraction, including an overview of phenomenological models of hard diffraction. It also addresses the physics motivations for the analysis described in this dissertation. In Chapter 3, the Fermilab accelerator complex and the CDF detector are described, placing a special emphasis on the detector components relevant to the analysis. The data collection, trigger requirements, and the single diffractive/non-diffractive dijet candidate selection are described in Chapter 4. This chapter also presents comparisons between single diffractive inclusive and single diffractive dijet events, and between single diffractive dijet and non-diffractive dijet events. In Chapter 5, results on the ratio of single diffractive dijet to non-diffractive dijet event rates as a function of the momentum fraction x of the antiproton carried by the struck parton and the measurement of the effective diffractive structure function of the antiproton are presented. The results are compared between $\sqrt{s} = 1800$ and 630 GeV. They are also compared with results from the DESY ep collider HERA [9], results from a study of dijet production in double pomeron exchange events at the Fer-

milab Tevatron [25], results from a study of single diffractive J/ψ production [22], and results from a study of single diffractive dijet events at the CERN $Sp\bar{p}S$ collider [4]. Finally, Chapter 6 presents a summary of all results from the analysis described in this dissertation and conclusions.

Chapter 2

Diffraction Phenomenology

2.1 High Energy Hadronic Diffraction

Hadronic diffraction is generally defined as a reaction in which no quantum numbers are exchanged between particles colliding at high energies [26]. The exchanged object between the colliding particles which carries the quantum numbers of the vacuum is generally referred to as the pomeron and will be denoted by $I\!P$. There are two classes of diffractive phenomena in high energy hadron-hadron collisions: elastic scattering and diffractive dissociation. Diffractive dissociation can be subdivided into several categories. Typical examples are single diffractive dissociation, double diffractive dissociation and double pomeron exchange. These processes are summarized below and in Figure 2.1.

Elastic scattering: both incoming particles escape intact from the collision,

$$a + b \to a + b. \tag{2.1}$$

Single diffractive dissociation: one of the incoming particles is scattered quasielas-

tically while the other dissociates into a cluster of final state particles,

$$a + b \to a + X_b, \tag{2.2}$$

where X_b [1] has the quantum numbers of b.

Double diffractive dissociation: each incoming particle dissociates into a cluster of final state particles with the same quantum numbers as the incoming particle,

$$a + b \to X_a + X_b. \tag{2.3}$$

Double pomeron exchange: both incoming particles are scattered quasielastically and a cluster of particles X with the quantum numbers of the vacuum is produced,

$$a + b \to a + X + b. \tag{2.4}$$

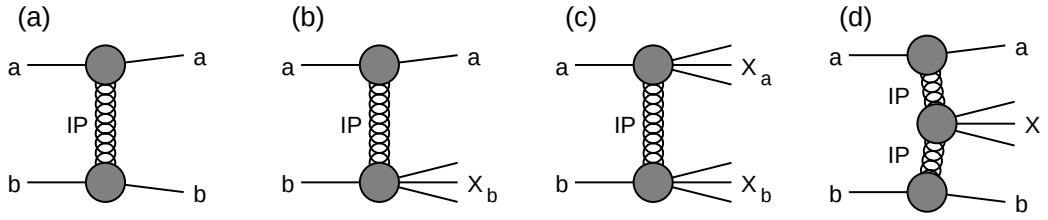

Figure 2.1: Illustrations for (a) elastic scattering, (b) single diffractive dissociation, (c) double diffractive dissociation, and (d) double pomeron exchange.

2.1.1 Elastic Scattering

Hadronic elastic scattering is analogous to the classical diffraction of light. In optics, the intensity of the light diffracted off by an absorbing disk is given by

$$I(\theta) = I(0) \left(\frac{2J_1(x)}{x} \right)^2 \approx I(0) \left(1 - \frac{r^2}{4}(k\theta)^2 \right), \tag{2.5}$$

[1] The subscript is omitted in the other sections.

where $J_1(x)$ is the first order Bessel function, r is the radius of the absorbing disk, θ is the scattering angle of the light, k is the wave number of the photons, and $x = kr\sin\theta \approx kr\theta$ at small angles.

The differential cross section for hadron-hadron elastic scattering at small angles behaves as

$$\frac{d\sigma_{EL}}{dt} \approx \left.\frac{d\sigma_{EL}}{dt}\right|_{t=0} e^{-b_{EL}|t|} \approx \left.\frac{d\sigma_{EL}}{dt}\right|_{t=0} (1 - b_{EL}(p\theta)^2), \tag{2.6}$$

where t is the four-momentum transfer squared and p is the momentum of the incident hadron scattered at the angle θ. The slope parameter b_{EL} is related to the radius of the absorbing disk by $b_{EL} = r^2/4$. For a target proton of radius $\approx 1/m_\pi$, where m_π is the pion mass, $b_{EL} \approx 13$ GeV^{-2}. This agrees approximately with the measured values of the slope parameter for $pp/p\bar{p}$ elastic scattering at high energies [27].

2.1.2 Single Diffractive Dissociation

Single diffractive dissociation can be thought of as the quasielastic scattering between two hadrons, in which one of the hadrons escapes intact while the other is excited into a high mass state without changing its quantum numbers. To keep one of the colliding particles intact, not only the transverse momentum transfer but also the longitudinal momentum transfer between the two colliding particles is required to be small. In single diffractive dissociation in which a proton is scattered quasielastically, the longitudinal momentum transfer Δp_L to the proton is required to be smaller than the inverse of the longitudinal proton radius r_L [28],

$$\Delta p_L \lesssim \frac{1}{r_L} \approx m_\pi \cdot \frac{p_0}{m_p}, \tag{2.7}$$

where p_0 is the momentum of the proton and m_p is the proton mass. In terms of the fractional momentum loss of the quasielastically-scattered proton ξ, Eq. (2.7) can be

written as

$$\xi \approx \frac{\Delta p_L}{p_0} \lesssim \frac{m_\pi}{m_p} \approx 0.15. \tag{2.8}$$

The kinematics of single diffractive dissociation can be described with two variables, ξ and t. The variable ξ is related to the mass M_X of the dissociation products X by $\xi \approx M_X^2/s$. In the pomeron picture of single diffractive dissociation, ξ is the momentum fraction of the incident hadron transferred to the pomeron, and t is the square of the pomeron mass and is always negative, indicating that the pomeron is a virtual object. Experimentally, before the Tevatron data were available, it was known that the cross section for $pp/p\bar{p}$ single diffractive dissociation at low ξ and low $|t|$ is well described by

$$\frac{d\sigma_{SD}}{d\xi dt} \overset{\propto}{\sim}^{2} \frac{1}{\xi}\, e^{b_{SD}t}, \tag{2.9}$$

where b_{SD} is approximately one half of b_{EL} [28]. This can be understood in terms of the form factor of the $I\!Ppp$ vertex, $F(t)$. The amplitude of elastic scattering has two $I\!Ppp$ vertices, and that of single diffractive dissociation contains only one $I\!Ppp$ vertex. Therefore, the t-dependence of the elastic scattering cross section is given by $F^4(t) \approx e^{b_{EL}t}$, while that of the single diffractive cross section is expected to be $F^2(t) \approx e^{b_{SD}t}$, so that $b_{SD} = b_{EL}/2$.

2.1.3 Regge Approach

Traditionally, Regge theory is used to describe diffraction processes [26]. In Regge theory, hadronic interactions are described in terms of t-channel exchanges of Regge trajectories, $\alpha(t)$, and scattering amplitudes have a $s^{\alpha(t)}$ dependence. Among all Regge trajectories, the pomeron trajectory $\alpha_{I\!P}(t)$ has the largest value at $t = 0$,

[2]The symbol " $\overset{\propto}{\sim}$ " means "approximately proportional to", and is used throughout this dissertation.

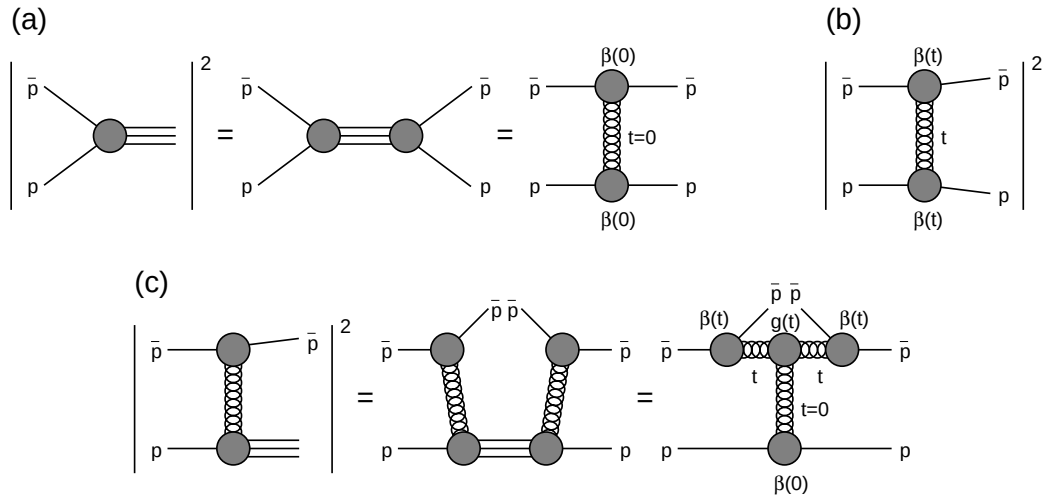

Figure 2.2: Regge diagrams for (a) total, (b) elastic scattering, and (c) single diffractive dissociation cross sections [28].

resulting in a dominant contribution to hadronic cross sections at high energies.

The pomeron exchange diagrams for $p\bar{p}$ interactions are shown in Figure 2.2. Through the optical theorem, the total cross section is proportional to the elastic scattering amplitude at $t = 0$. The total, elastic and single diffractive cross sections due to pomeron exchange are given by

$$\sigma_T = \beta^2_{I\!Ppp}(0) \left(\frac{s}{s_0}\right)^{\alpha_{I\!P}(0)-1}, \tag{2.10}$$

$$\frac{d\sigma_{EL}}{dt} = \frac{\beta^4_{I\!Ppp}(t)}{16\pi} \left(\frac{s}{s_0}\right)^{2(\alpha_{I\!P}(t)-1)}, \tag{2.11}$$

$$\frac{d^2\sigma_{SD}}{d\xi dt} = \frac{\beta^2_{I\!Ppp}(t)}{16\pi} \xi^{1-2\alpha_{I\!P}(t)} \left[\beta_{I\!Ppp}(0) g(t) \left(\frac{s'}{s_0}\right)^{\alpha_{I\!P}(0)-1}\right], \tag{2.12}$$

where $\alpha_{I\!P}(t) = 1 + \epsilon + \alpha' t$ is the pomeron trajectory, $\beta_{I\!Ppp}(t)$ is the coupling of the pomeron to the proton, $g(t)$ is the triple-pomeron coupling, $s' = M_X^2 \approx s\xi$ is the square of the center-of-mass energy of the $I\!P$-p system, and s_0 is an energy scale parameter traditionally set to the hadron mass scale of 1 GeV^2. The most recently determined value of ϵ, obtained from a fit to the pp, $p\bar{p}$, $\pi^{\pm}p$ and $K^{\pm}p$ total cross sections, is $\epsilon = 0.104 \pm 0.002$ [27]. The value of α' obtained from elastic scattering

data is $\alpha' \approx 0.25$ GeV^{-2}. In analogy with Eq. (2.10), the term in the bracket in Eq. (2.12) may be interpreted as the $I\!Pp$ total cross section,

$$\sigma_T^{I\!Pp}(s') = \beta_{I\!Ppp}(0)g(0)\left(\frac{s'}{s_0}\right)^{\alpha_{I\!P}(0)-1} = \sigma_0^{I\!Pp}\left(\frac{s'}{s_0}\right)^{\alpha_{I\!P}(0)-1}, \tag{2.13}$$

where $g(t) = g(0)$ is used, since it was found experimentally that $g(t)$ does not depend on t [28]. The remaining factor in Eq. (2.12),

$$f_{I\!P/p}(\xi, t) = \frac{\beta_{I\!Ppp}^2(t)}{16\pi}\xi^{1-2\alpha_{I\!P}(t)} = K\xi^{1-2\alpha_{I\!P}(t)}F^2(t), \tag{2.14}$$

where $K = \beta_{I\!Ppp}^2(0)/16\pi$, is generally called the pomeron flux factor, which may be interpreted as the probability that the proton emits a pomeron. The function $F(t)$ represents the form factor of the $I\!Ppp$ vertex. A. Donnachie and P. Landshoff proposed [29] that the appropriate form factor for $pp/p\bar{p}$ elastic scattering and single diffractive dissociation is the isoscalar electromagnetic form factor measured in electron-nucleon scattering,

$$F_1(t) = \frac{4m_p^2 - 2.8t}{4m_p^2 - t}\left(\frac{1}{1 - t/(0.7\text{ GeV}^2)}\right)^2. \tag{2.15}$$

These formulae were found to provide a good description of experimental data in the Fermilab fixed target and CERN ISR collider energy range ($\sqrt{s} \lesssim 60$ GeV) [28]. However, as the energy increases, they suffer from unitarity problems, which are especially severe in the case of single diffractive dissociation. At a given s value, the total single diffractive cross section, which behaves as $\sigma_{SD} \lesssim s^{2\epsilon}$, exceeds the total cross section, which behaves as $\sigma_T \lesssim s^{\epsilon}$. The CDF experiment reported [30] that the s-dependence of the single diffractive cross section is approximately flat at Tevatron energies, in contrast to the Regge expectation of $s^{2\epsilon}$ dependence.

Several solutions have been proposed to account for the discrepancy between Regge theory expectations and experimental measurements. One solution was proposed

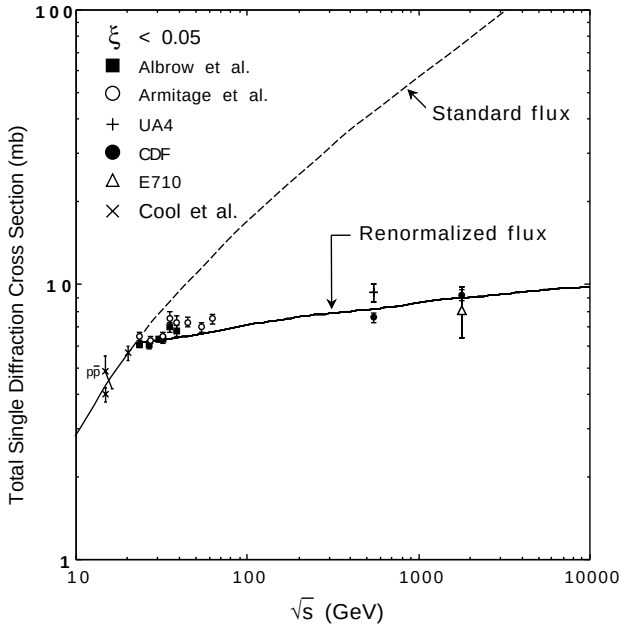

Figure 2.3: The total pp and $p\bar{p}$ single diffractive cross sections measured for $\xi < 0.05$ along with predictions based on Eq. (2.12) and the pomeron flux renormalization model [31]. This figure is adapted from Figure 1 in Ref. [31].

by K. Goulianos, and is generally referred to as the pomeron flux renormalization model [31]. In this model, the pomeron flux factor $f_{I\!P/p}(\xi, t)$ has to be normalized to unity when its integral over available phase space exceeds unity. This procedure practically cancels out the $s^{2\epsilon}$ dependence of the single diffractive cross section and gives good agreement with the experimental data as shown in Figure 2.3.

S. Erhan and P. E. Schlein originally attributed this discrepancy to a damping of the hadron-hadron diffraction cross section at low ξ and low $|t|$ values [32], and more recently to a decrease of the pomeron intercept at higher $\sqrt{s}$ energies [33], as expected in unitarization (multi-pomeron exchange) calculations. C.-I Tan explains this discrepancy by implementing a final state screening correction to the factorization formula with "flavoring" for the pomeron as the primary dynamical mechanism for setting the relevant energy scale [34]. This solution shares some features with that

proposed by S. Erhan and P. E. Schlein [32].

2.2 Rapidity and Rapidity Gaps

In hadron collision experiments, the longitudinal distribution of final state particles is often discussed in terms of the rapidity y (longitudinal rapidity) defined as

$$y \equiv \tanh^{-1}\beta_z = \frac{1}{2}\ln\left(\frac{E+p_z}{E-p_z}\right) = \ln\left(\frac{E+p_z}{m_T}\right), \tag{2.16}$$

where β_z $(= v_z/c = p_z/E)$ is the relativistic longitudinal velocity, p_z is the longitudinal momentum, and m_T is the transverse mass $({m_T}^2 = m^2 + {p_T}^2)$; p_T denotes the transverse momentum. If a Lorentz transformation is made to another frame moving at velocity β_z' along the longitudinal direction, then

$$\begin{aligned} y' &= \ln\left(\frac{E'+p_z'}{m_T}\right) = \ln\left(\frac{\gamma'(E-\beta_z' p_z)+\gamma'(p_z-\beta_z' E)}{m_T}\right) \\ &= y + \frac{1}{2}\ln\left(\frac{1-\beta_z'}{1+\beta_z'}\right) = y - \tanh^{-1}\beta_z', \end{aligned} \tag{2.17}$$

so that the rapidity y is additive under longitudinal Lorentz boosts. In hadron-hadron collisions, the center-of-mass system of the interesting parton-parton scattering is generally boosted along the longitudinal direction with respect to that of the two incoming hadrons. Therefore, it is convenient to discuss the longitudinal distribution of final state particles in terms of rapidity, which transforms simply under longitudinal boosts.

In the non-relativistic limit, i.e. $v \ll 1$, $E \approx m$ and $p_z \approx m v_z$, the rapidity y reduces to the longitudinal velocity of the particle v_z. In the case of small m, i.e. $m \ll p$, the rapidity y can be approximated as

$$y \approx \frac{1}{2}\ln\left(\frac{p+p_z}{p-p_z}\right) = \frac{1}{2}\ln\left(\frac{1+\cos\theta}{1-\cos\theta}\right) = -\ln\tan\frac{\theta}{2} = \eta, \tag{2.18}$$

where θ is the polar angle of the particle with respect to the colliding beam direction. The variable η is termed pseudorapidity. The variables rapidity and pseudorapidity are used interchangeably throughout this dissertation.

In the case of no interaction taking place between two incoming particles, i.e. no four-momentum being exchanged between them, both incoming particles retain their original four-momenta, which is equivalent to setting $p_T = 0$. Therefore, the rapidities y_+ and y_- of the particles in their center-of-mass system are

$$y_+ = -y_- \approx \ln \frac{\sqrt{s}}{m}, \tag{2.19}$$

where y_+ (y_-) is for the particle running in the positive (negative) z direction and the approximation $E = \sqrt{s}/2 \approx |p_z|$ is made. For simplicity, all particle masses are assumed to be equal to m in this paragraph. For non-diffractive events in which both incoming particles dissociate into a system X, the maximum and minimum rapidities of the system X are given by

$$y_{X,max} \approx \ln \frac{\sqrt{s}}{m}, \quad y_{X,min} \approx -\ln \frac{\sqrt{s}}{m}. \tag{2.20}$$

For single diffractive events in which the particle running in the negative z direction is scattered quasielastically, the minimum rapidity of the quasielastically-scattered recoil (leading) particle $y_{recoil,min}$ is attained when $p_T = 0$, that is,

$$y_{recoil,min} \approx -\ln \frac{\sqrt{s}(1-\xi)}{m} \approx -\ln \frac{\sqrt{s}}{m}. \tag{2.21}$$

The maximum rapidity of the system X is the same as that in non-diffractive events,

$$y_{X,max} \approx \ln \frac{\sqrt{s}}{m}. \tag{2.22}$$

The minimum rapidity of the system X pertains to a particle with longitudinal momentum $p_z \approx \xi \cdot \sqrt{s}/2$,

$$y_{X,min} \approx -\ln \frac{\sqrt{s}\,\xi}{m}. \tag{2.23}$$

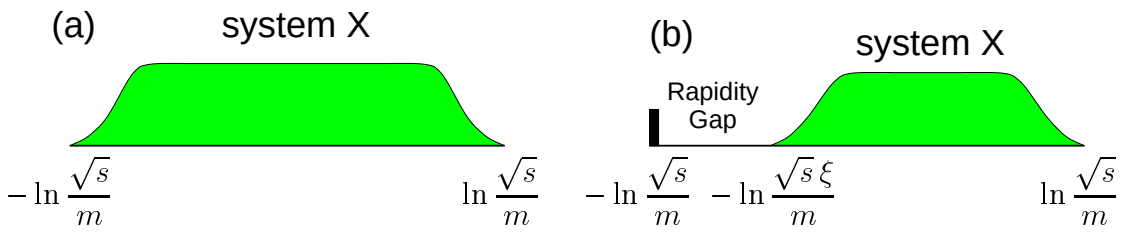

Figure 2.4: Rapidity distribution in the final state of (a) a non-diffractive event and (b) a single diffractive event.

Therefore, the rapidity region devoid of particles, called a rapidity gap, between the quasielastically-scattered recoil particle and the system X is expected to span the region

$$\Delta y_{gap} = y_{X,min} - y_{recoil,min} \approx -\ln \xi. \tag{2.24}$$

According to the scaling law proposed by R. P. Feynman [35], the longitudinal distribution of final state particles is

$$\frac{dN}{dy} \sim \rho, \tag{2.25}$$

where the particle density ρ is approximately constant over the phase space available for the dissociation products. In terms of rapidity intervals Δy between final state particles, the distribution obtained from Poisson fluctuations is given by

$$\frac{dN}{d\Delta y} \underset{\sim}{\propto} e^{-\rho \Delta y}. \tag{2.26}$$

Thus, in non-diffractive events, rapidity gaps are exponentially suppressed. In diffractive events, the distribution of rapidity intervals between the leading particle and the system X behaves as

$$\frac{dN}{d\Delta y} \sim \text{constant}. \tag{2.27}$$

Therefore, diffractive dissociation is often defined as events containing large rapidity gaps in the final state which are not exponentially suppressed [26].

2.3 Hard Diffraction

Diffractive physics drew considerable attention when it was suggested [2] that it would be valuable to study diffraction processes containing a hard scattering, which are generally called hard diffraction processes. By studying hard diffraction processes, one would be able to probe the probability distribution for partons in the hadron which is scattered quasielastically, which may lead to the partonic structure function of the pomeron. The important point of this idea is that it gives a possibility of understanding the mechanism of diffractive dissociation in the framework of perturbative QCD.

2.3.1 Hard Diffraction at Hadron Colliders

The cross section for a hard scattering in a non-diffractive $p\bar{p}$ interaction can be expressed, due to the QCD factorization property, as a convolution of parton-level cross sections with the parton distribution functions in the proton and antiproton:

$$\frac{d^2\sigma_{ND}}{dx_p dx_{\bar{p}} d\hat{t}} = \sum_{a,b} f_{a/p}(x_p, Q^2) f_{b/\bar{p}}(x_{\bar{p}}, Q^2) \frac{d\hat{\sigma}_{ab}}{d\hat{t}}, \tag{2.28}$$

where x_p and $x_{\bar{p}}$ are the momentum fractions of the interacting partons in the proton and antiproton, and $f_{a/p}(x_p, Q^2)$ and $f_{b/\bar{p}}(x_{\bar{p}}, Q^2)$ are the parton distribution functions of the proton and antiproton, respectively. The cross section for the scattering of partons of types a and b is denoted by $\hat{\sigma}_{ab}$, and $\hat{t}$ is the square of the four-momentum transfer between the interacting partons. In Eq. (2.28), the renormalization and factorization scales are assumed to be equal to the characteristic scale of the hard scattering denoted by Q. For hard scattering processes such as dijet production and W/Z production, the parton-parton scattering cross section is calculable. One of the remarkable features of QCD is that, at least for non-diffractive interactions, the parton

distribution functions of the proton and antiproton are universal. In other words, the parton distribution functions can be extracted from any process and applied to other processes. The parton distribution functions are derived from a global fit to experimental measurements of a variety of scattering processes.

The cross section for a hard scattering in a single diffractive $p\bar{p}$ interaction may be expressed in a similar manner to Eq. (2.28) as

$$\frac{d^2\sigma_{SD}}{dx_p dx_{\bar{p}} d\xi dt d\hat{t}} = \sum_{a,b} f_{a/p}(x_p, Q^2) f^D_{b/\bar{p}}(x_{\bar{p}}, Q^2, \xi, t) \frac{d\hat{\sigma}_{ab}}{d\hat{t}}, \tag{2.29}$$

where the antiproton is assumed to be scattered quasielastically. The function $f^D_{b/\bar{p}}(x_{\bar{p}}, Q^2, \xi, t)$ represents the probability distribution for partons in the antiproton which is scattered quasielastically with particular values of ξ and t. This function is generally called the diffractive parton distribution function. One of the most important issues in diffractive physics is whether hard diffraction processes obey QCD factorization. In other words, the question is whether the diffractive parton distribution functions are universal. This question can be addressed by comparing the diffractive parton distribution functions extracted from different processes or at different energies.

Another important question in hard diffraction is the validity of so-called Regge factorization. Assuming Regge factorization, the diffractive parton distribution functions of the proton can be expressed as products of a function which depends only on ξ and t, and a function which depends on $\beta = x/\xi$ and Q^2,

$$f^D_{a/p}(x, Q^2, \xi, t) = f_{I\!P/p}(\xi, t)\, f_{a/I\!P}(\beta, Q^2). \tag{2.30}$$

The variable β can be interpreted as the momentum fraction of the interacting parton in the pomeron emitted from the proton. Under Regge factorization, which is assumed in the Ingelman-Schlein model [2], diffractive dissociation can be thought to be due to

the exchange of a pomeron with the parton distributions $f_{a/I\!P}(\beta, Q^2)$. The function $f_{I\!P/p}(\xi, t)$ is then the pomeron flux factor, which in this model is the same as that in soft diffraction.

As mentioned in Chapter 1, single diffractive dijet production in $p\bar{p}$ collisions was first observed by the UA8 collaboration [3, 4] at the CERN $Sp\bar{p}S$ collider at $\sqrt{s} = 630$ GeV, and later by the CDF [19] and DØ [20] collaborations at the Fermilab Tevatron collider at $\sqrt{s} = 1800$ and 630 GeV. The CDF collaboration has also observed single diffractive W [18], b-quark [21], and J/ψ production [22].

W production is sensitive to the quark content of the diffractive exchange; on the other hand, dijet and b-quark production are more sensitive to the gluon content. By combining results on single diffractive W, dijet, and b-quark production, the CDF collaboration measured the gluon fraction in the diffractive exchange (pomeron) to be $F_g^D = 0.54^{+0.16}_{-0.14}$ [21]. This result is in agreement with the gluon fraction obtained by the ZEUS collaboration from measurements of the jet cross section in diffractive photoproduction [15] and of the diffractive F_2 structure function of the proton in diffractive deep inelastic scattering [5], which is described in Section 2.3.2. However, the production rates for hard diffraction processes measured at the Tevatron were found to be about 5−10 times lower than predictions [23, 24] based on the diffractive parton distributions obtained from fits to the HERA data on diffractive deep inelastic scattering [5, 6, 10] and on diffractive photoproduction of jets [15], indicating a severe breakdown of QCD factorization in diffraction processes.

2.3.2 Hard Diffraction at HERA

Experiments at the DESY ep collider HERA, the ZEUS and H1 collaborations, have made extensive studies of diffractive events in deep inelastic scattering (DIS)

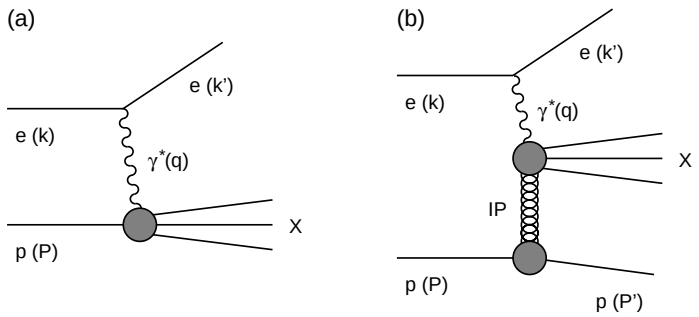

Figure 2.5: Schematic diagrams describing particle production in (a) deep inelastic ep scattering and (b) diffractive dissociation in a deep inelastic ep interaction.

and photoproduction. The non-diffractive and diffractive DIS processes are shown schematically in Figure 2.5.

The cross section for non-diffractive DIS can be written as

$$\frac{d^2\sigma_{ep\to eX}}{dxdQ^2} = \frac{2\pi\alpha_{em}^2}{xQ^4}\left(1+(1-y)^2\right)F_2(x,Q^2), \tag{2.31}$$

where α_{em} is the electromagnetic coupling constant, and the longitudinal structure function and Z^0 exchange are neglected. Deep inelastic scattering events can be described with the variables,

$$Q^2 = -q^2, \quad x = \frac{Q^2}{2P\cdot q}, \quad y = \frac{P\cdot q}{P\cdot k}, \tag{2.32}$$

where Q^2 is the negative of the squared four-momentum transfer carried by the virtual photon, x is the Bjorken scaling variable, y is the inelasticity variable, i.e. the fractional energy transferred to the proton in its rest frame, and P, k and q are the four-momenta of the incoming proton, incoming electron, and virtual photon, respectively. The center-of-mass energy of the virtual photon-proton system is $W = \sqrt{(P+q)^2} \approx \sqrt{Q^2(1/x-1)}$.

With diffractive variables $\xi = q\cdot(P-P')/q\cdot P$ and $t = (P-P')^2$, where P' is the four-momentum of the quasielastically-scattered proton, the diffractive DIS cross section can be expressed in terms of the diffractive F_2 structure function $F_2^D(x,Q^2,\xi,t)$

as

$$\frac{d^4\sigma_{ep\to eXp}}{dxdQ^2d\xi dt} = \frac{2\pi\alpha_{em}^2}{xQ^4}\left(1+(1-y)^2\right)F_2^D(x,Q^2,\xi,t). \tag{2.33}$$

Changing variables from x to $\beta = Q^2/(2(P-P')\cdot q) = x/\xi$, the above equation can be written as

$$\frac{d^4\sigma_{ep\to eXp}}{d\beta dQ^2d\xi dt} = \frac{2\pi\alpha_{em}^2}{\beta Q^4}\left(1+(1-y)^2\right)F_2^D(\beta,Q^2,\xi,t). \tag{2.34}$$

Based on Eq. (2.34), the diffractive structure function $F_2^D(\beta,Q^2,\xi,t)$ can be extracted from the diffractive DIS cross section. When diffractive dissociation is identified not by the presence of the leading proton but by the presence of the rapidity gap, t cannot be measured and the $F_2^D(\beta,Q^2,\xi,t)$ is integrated over t, giving $F_2^D(\beta,Q^2,\xi)$.

In leading order QCD, the non-diffractive F_2 structure function can be written in terms of the quark and antiquark distribution functions $f_{q_i}(x,Q^2)$ and $f_{\bar{q}_i}(x,Q^2)$ as

$$F_2(x,Q^2) = \sum_i e_{q_i}^2 x\left(f_{q_i}(x,Q^2)+f_{\bar{q}_i}(x,Q^2)\right), \tag{2.35}$$

where e_{q_i} is the electric charge of the quark q_i, and the sum is carried out over all the quark flavors. Note that the F_2 structure function does not depend on the gluon distribution at leading order, since the photon does not couple directly to gluons. However, at next-to-leading order, the F_2 structure function depends also on the gluon distribution through the $g\to q\bar{q}$ process. In analogy with Eq. (2.35), the diffractive F_2 structure function can be expressed in terms of the diffractive quark and antiquark distribution functions $f_{q_i}^D(x,Q^2,\xi,t)$ and $f_{\bar{q}_i}^D(x,Q^2,\xi,t)$ as

$$F_2^D(x,Q^2,\xi,t) = \sum_i e_{q_i}^2 x\left(f_{q_i}^D(x,Q^2,\xi,t)+f_{\bar{q}_i}^D(x,Q^2,\xi,t)\right). \tag{2.36}$$

Under the Regge factorization assumption, F_2^D can be factorized as

$$F_2^D(\beta,Q^2,\xi,t) = f_{I\!P/p}(\xi,t)F_2^{I\!P}(\beta,Q^2). \tag{2.37}$$

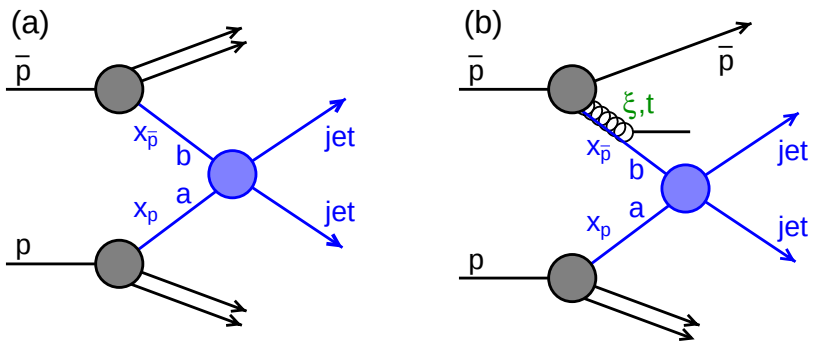

Figure 2.6: Schematic diagrams for (a) non-diffractive dijet production and (b) single diffractive dijet production.

The function $F_2^{I\!P}(\beta, Q^2)$ may be interpreted as the F_2 structure function of the pomeron. The $F_2^{I\!P}$ was found to have a Q^2-dependence consistent with logarithmic behavior as in normal QCD evolution. Therefore, the β- and Q^2-dependence of $F_2^{I\!P}$ has been analyzed in terms of the QCD evolution of the structure function of the pomeron, as suggested by J. C. Collins *et al.* [36]. Assuming the evolution of $F_2^{I\!P}$, the diffractive parton distributions, including the gluon distribution, were extracted using the DGLAP equations [37].

Diffractive photoproduction of high-p_T jets is sensitive to both the diffractive quark and diffractive gluon distributions through the $\gamma q \to qg$ and $\gamma g \to q\bar{q}$ processes, and thus has been used to check the diffractive parton distribution functions derived from diffractive DIS.

2.3.3 Single Diffractive Dijet Production in $p\bar{p}$ Collisions

A typical hard scattering process in $p\bar{p}$ collisions is dijet production. Schematic diagrams for non-diffractive dijet and single diffractive dijet production in $p\bar{p}$ collisions are shown in Figure 2.6. The cross sections for non-diffractive dijet production and

single diffractive dijet production can be expressed as

$$\frac{d^3\sigma^{jj}_{ND}}{dx_p dx_{\bar{p}} d\hat{t}} = \sum_{a,b} f_{a/p}(x_p, Q^2) f_{b/\bar{p}}(x_{\bar{p}}, Q^2) \frac{d\hat{\sigma}_{ab\to jj}}{d\hat{t}}, \tag{2.38}$$

$$\frac{d^5\sigma^{jj}_{SD}}{dx_p dx_{\bar{p}} d\xi dt d\hat{t}} = \sum_{a,b} f_{a/p}(x_p, Q^2) f^D_{b/\bar{p}}(x_{\bar{p}}, Q^2, \xi, t) \frac{d\hat{\sigma}_{ab\to jj}}{d\hat{t}}. \tag{2.39}$$

In Eq. (2.39), the antiproton is assumed to be scattered quasielastically. The parton-parton scattering subprocesses $gg \to gg$, $qg \to qg$ and $qq \to qq$ give the dominant contribution to the dijet production cross section in hadron-hadron collisions. In leading order matrix elements, these dominant subprocesses have very similar angular dependence. Furthermore, their magnitudes are approximately

$$gg \to gg : qg \to qg : qq \to qq \approx 1 : \frac{C_F}{C_A} : \left(\frac{C_F}{C_A}\right)^2, \tag{2.40}$$

where $C_F = 4/3$ and $C_A = 3$ are color factors. Therefore, in terms of the single effective non-diffractive structure function of the proton defined as

$$F_{jj}(x, Q^2) = x\Big[f_g(x, Q^2) + \frac{C_F}{C_A} \sum_i \big(f_{q_i}(x, Q^2) + f_{\bar{q}_i}(x, Q^2)\big)\Big], \tag{2.41}$$

the non-diffractive dijet cross section is given by

$$\frac{d^3\sigma^{jj}_{ND}}{dx_p dx_{\bar{p}} d\hat{t}} \approx \frac{F_{jj}(x_p, Q^2)}{x_p} \frac{F_{jj}(x_{\bar{p}}, Q^2)}{x_{\bar{p}}} \frac{d\hat{\sigma}_{gg\to jj}}{d\hat{t}}. \tag{2.42}$$

This approximation [38], generally called the single effective subprocess approximation, holds within ≈ 10 % over all dijet production phase space [39]. If the single effective proton structure function for diffractive interactions is defined as

$$F^D_{jj}(x, Q^2, \xi, t) = x\Big[f^D_g(x, Q^2, \xi, t) + \frac{C_F}{C_A} \sum_i \big(f^D_{q_i}(x, Q^2, \xi, t) + f^D_{\bar{q}_i}(x, Q^2, \xi, t)\big)\Big], \tag{2.43}$$

the single diffractive dijet cross section can be expressed as

$$\frac{d^5\sigma^{jj}_{SD}}{dx_p dx_{\bar{p}} d\xi dt d\hat{t}} = \frac{F_{jj}(x_p, Q^2)}{x_p} \frac{F^D_{jj}(x_{\bar{p}}, Q^2, \xi, t)}{x_{\bar{p}}} \frac{d\hat{\sigma}_{gg\to jj}}{d\hat{t}}. \tag{2.44}$$

The function $F_{jj}^D(x, Q^2, \xi, t)$ is referred to as the (effective) diffractive structure function throughout this dissertation.

In this dissertation, the measurement of the effective diffractive structure function F_{jj}^D of the antiproton is presented. To extract F_{jj}^D, first we measure the ratio of the single diffractive dijet event rate in a certain ξ and t region to the non-diffractive dijet event rate as a function of $x_{\bar{p}}$, which is, in leading order QCD, approximately equal to the ratio of the effective diffractive structure function F_{jj}^D to the effective non-diffractive structure function F_{jj}, as shown in Eq. (2.45),

$$\begin{aligned} R_{\frac{SD}{ND}}(x_{\bar{p}}, \xi, t) &\approx \frac{\int dx_p \int d\hat{t} \frac{F_{jj}(x_p, Q^2)}{x_p} \frac{F_{jj}^D(x_{\bar{p}}, Q^2, \xi, t)}{x_{\bar{p}}} \frac{d\hat{\sigma}_{gg\to jj}}{d\hat{t}}}{\int dx_p \int d\hat{t} \frac{F_{jj}(x_p, Q^2)}{x_p} \frac{F_{jj}(x_{\bar{p}}, Q^2)}{x_{\bar{p}}} \frac{d\hat{\sigma}_{gg\to jj}}{d\hat{t}}} \\ &\approx \frac{F_{jj}^D(x_{\bar{p}}, \langle Q^2 \rangle, \xi, t)}{F_{jj}(x_{\bar{p}}, \langle Q^2 \rangle)}, \end{aligned} \tag{2.45}$$

where $\langle Q^2 \rangle$ should be set to the typical value of the square of the hard scale for the dijet data samples used, e.g. the mean transverse energy squared of the leading two jets. The usual non-diffractive parton distribution functions have been derived from a global fit to experimental results from a variety of scattering processes [40, 41, 42], and are presently well known. The effective non-diffractive structure function can be reconstructed from the well-known usual non-diffractive parton distribution functions. By multiplying the measured ratio $R_{\frac{SD}{ND}}$ by the effective non-diffractive structure function, the effective diffractive structure function F_{jj}^D is obtained.

The F_{jj}^D measured at $\sqrt{s} = 1800$ GeV is compared with that at $\sqrt{s} = 630$ GeV and with expectations based on the diffractive parton distribution functions obtained from diffractive DIS [9, 12]. To further characterize how QCD factorization breaks down in diffraction processes, the F_{jj}^D is also compared with that extracted from a study of dijet production in double pomeron exchange events [25].

2.4 Phenomenological Models for Hard Diffraction

Several phenomenological models have been proposed to account for the observed breakdown of factorization in diffractive events. Some models attribute the breakdown of factorization to a suppression of the hadron-hadron diffraction cross section resulting from additional exchanges of soft partons carrying colors and thus spoiling the diffractive signature of rapidity gaps [43, 44]. In these models, predictions based on the factorization formula have to be multiplied by the so-called rapidity gap survival probability [45], which represents the probability that no additional soft parton is exchanged between the colliding hadrons.

The pomeron flux renormalization model, which was originally proposed by K. Goulianos [31] to account for the observed s-dependence of soft (inclusive) single diffractive dissociation, also explains the breakdown of factorization observed in hard diffraction. In QCD language, this model basically attributes the suppression of the hadron-hadron diffraction cross section to the high densities of low-x partons in high energy hadron-hadron collisions which lead to saturation effects [46]. Recently, A. Bialas suggested [47] that the breakdown of factorization could naturally be explained in terms of the Good-Walker [1] picture of diffractive dissociation, in which diffractive dissociation is treated as a consequence of absorption of the particle wave. In this picture, the correction to the factorization formula is obtained in terms of the elastic $p\bar{p}$ amplitude at low momentum transfers, and is similar to what is expected in the pomeron flux renormalization model. The models by S. Erhan and P. E. Schlein [32, 33] or by C.-I Tan [34], which were originally proposed to reproduce the observed s-dependence of soft single diffractive dissociation, may be used to address the breakdown of factorization observed in hard diffraction processes through

the Ingelman-Schlein model [2], i.e. by inserting the pomeron flux factor from these models into Eq. (2.30) and then inserting Eq. (2.30) into Eq. (2.29).

The soft color interaction (SCI) model and the generalized area law (GAL) model, which have been developed to better understand soft non-perturbative QCD and to provide a unified description of all types of final states with and without rapidity gaps, were found to give a reasonable description of diffractive DIS processes observed at HERA and single diffractive hard processes observed at the Tevatron [48]. In the Monte Carlo program incorporating the SCI model or the GAL model, a new stage of soft color interactions is introduced after the perturbative processes described by matrix elements and parton showers, but before the hadronization process. The SCI model is formulated on a parton basis, with soft color exchange between quarks and gluons, whereas the GAL model is formulated on a string basis. In both cases, the basic assumption is that the soft color exchange changes the topology of the confining color force fields given by the perturbative QCD interaction.

The measurements presented in this dissertation will hopefully help us establish adequate phenomenological models for diffractive dissociation, which will be an important step toward a more fundamental understanding of diffractive dissociation and of the nature of the pomeron.

Chapter 3

Accelerator and Detector

The Fermi National Accelerator Laboratory (Fermilab) is one of the premier institutions for elementary particle physics. It is the home of a powerful accelerator called the Tevatron, which collides protons and antiprotons at the highest center-of-mass energy in the world. The Collider Detector at Fermilab (CDF) is one of two multipurpose detectors built at collision points of the Tevatron. The data samples used in this analysis were collected by CDF during the 1995−1996 Tevatron run.

We begin this chapter by describing the process of producing protons and antiprotons, accelerating them to energies of 900 or 315 GeV, and colliding them. We then describe the various components of the CDF detector associated with this analysis, and finally discuss the CDF data acquisition system.

3.1 The Fermilab Tevatron Collider in 1995−1996

The Fermilab accelerator complex consists of several stages of acceleration as shown in Figure 3.1. The first stage of acceleration is provided by a direct voltage accelerator, the Cockcroft-Walton. In this device, electrons are injected into hydrogen

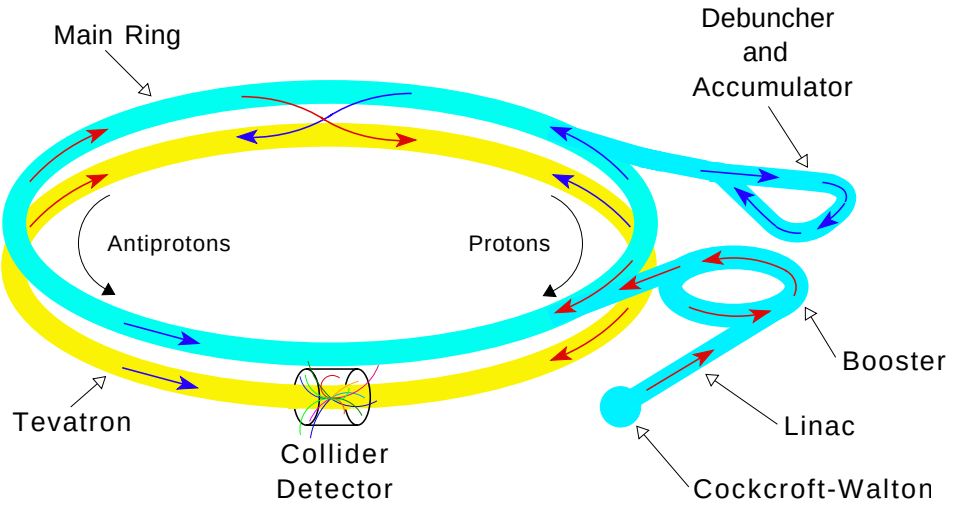

Figure 3.1: A schematic view of the Fermilab accelerator complex for $p\bar{p}$ collisions.

atoms, and the resultant negatively charged ions consisting of two electrons and one proton are accelerated by a positive voltage to about 750 keV. The ions are directed to the second stage of the acceleration process provided by the Linac.

The Linac is a 145 m long, two-stage linear accelerator that accelerates the ions to the energy of 401.5 MeV. The first stage of the Linac consists of five radio frequency (RF) cavities that resonate at 201.25 MHz. The second stage of the Linac is a side-coupled accelerator that consists of nine RF cavities operating at 805 MHz. Each of the cavities contains alternating drift tubes and accelerating gaps. An alternating electric field is applied to the drift tubes. When the electric field is in the direction that slows down the injected negative ions, the ions are hiding in the drift tubes; when the electric field is in the opposite direction, the ions appear in the gap regions and are accelerated. Before the ions go to the next stage, they pass through a carbon foil and lose electrons.

Protons leaving the Linac enter the Booster accelerator. The Booster accelerator is

a proton synchrotron accelerator about 150 m in diameter. It consists of 96 combined function dipole/quadrupole magnets with 17 RF cavities interspersed. The magnets are used to provide a stable and circular orbit for protons. With an RF of 53 MHz, the booster provides 84 regions of stable acceleration, called buckets. The collection of protons residing in each bucket is referred to as a bunch. The protons circulate in the Booster accelerator about 20,000 times in 33 ms, and are accelerated to the energy of about 8 GeV.

The Main Ring is also a synchrotron machine with a 1 km radius and 18 RF cavities resonating at 53 MHz. A total of 774 dipole magnets and 240 focusing quadrupole magnets are used to maintain protons in a stable and circular orbit. During colliding beam operation, it fulfills two functions. First, it provides a source of 120 GeV protons that are used to produce antiprotons. Second, after antiprotons are injected into the Main Ring, it accelerates protons and antiprotons to the energy of 150 GeV.

In order to produce antiprotons, protons accelerated to 120 GeV in the Main Ring are transported to a tungsten target. The collisions produce secondary particles that include antiprotons. Those antiprotons are collected and transported to the Debuncher ring which debunches the antiprotons by the stochastic cooling technique [49]. The antiprotons are then transported to the Antiproton Accumulator ring. When roughly 10^{11} antiprotons are accumulated, they are injected into the Main Ring and are accelerated to 150 GeV simultaneously with the protons, but in the opposite direction.

The protons and antiprotons accelerated to the energy of 150 GeV are injected into the Tevatron. The Tevatron, located 65 cm below the Main Ring in the same tunnel, is a proton-antiproton colliding synchrotron that uses superconducting magnets cooled down to 4.6 K by liquid helium. A total of 774 dipole magnets and 216 quadrupole

focusing magnets are used to steer protons and antiprotons around their 6.28 km orbit. A total of eight RF cavities are used to accelerate protons and antiprotons in the Tevatron. The RF systems of both the Tevatron and the Main Ring resonate at 53 MHz. During Run 1 (1992−1996), the Tevatron counter-circulated six bunches of protons and six bunches of antiprotons with a time between bunch crossings of 3.5 μs.

In the Tevatron, protons and antiprotons are accelerated simultaneously to 900 or 315 GeV. The two beams are kept isolated by electrostatic separators. When the beams reach the designated energy, high power (low-β) quadrupole magnets installed in the CDF experimental hall are activated to direct protons and antiprotons to a head-on collision at the center of the detector, and then the beams are scraped using collimators to remove peripheral beam halo particles.

The instantaneous luminosity of the Tevatron is given by

$$\mathcal{L}_{inst} = \frac{N_p N_{\bar{p}} f}{\mathcal{A}}, \tag{3.1}$$

where N_p and $N_{\bar{p}}$ are the numbers of protons and antiprotons per bunch, f is the frequency of bunch crossings and $\mathcal{A}$ is the effective area of the crossing beams. The numbers of protons and antiprotons in the bunches continuously decreases with time due to beam losses and beam-gas interactions, so that after some time the bunches are dumped and new bunches are injected. The period of time when the same proton and antiproton bunches are kept cycling is referred to as a store. During a typical store of about 8−18 hours, the luminosity decreases by approximately an order of magnitude.

3.2 The Collider Detector at Fermilab

The Collider Detector at Fermilab (CDF) is a multipurpose detector located at one of six nominal interaction regions of the Tevatron. The CDF detector is approximately forward-backward and azimuthally symmetric, with the geometric center located at the nominal interaction point. Figures 3.2 and 3.3 present an isometric cut-away view and a quarter view of the CDF detector, respectively. It is approximately 10 m high, extends about 27 m from end to end, and weighs over 5000 tons.

Components of the CDF detector include the tracking, calorimetry and muon subsystems. The tracking systems reside inside a solenoidal magnetic field of about 1.4 T, generated by a superconducting solenoid magnet 3 m in diameter and 4.8 m long. The solenoidal magnetic field is maintained by circulating a 4650 A current through 1164 turns of a solenoidal coil made of superconducting Nd-Ti/Cu material. The solenoidal magnetic field bends the trajectory of a charged particle, and the curvature of its trajectory allows us to measure its momentum and charge. The tracking systems also provide a measurement of vertices from which charged particles emanate in a given event.

The tracking volume is surrounded by calorimeters which are used to measure the electromagnetic and hadronic energy of both charged and neutral particles. The charged and neutral particles make showers in a large mass volume of the calorimeters and deposit their energies. A *jet*, a cluster of particles traveling approximately in the same direction, is measured using calorimeters by making an energy cluster from energies deposited in calorimeter cells. Muon detectors are mounted outside of the calorimeters. The calorimeters and other materials between the beam axis and the muon detectors absorb a large fraction of hadrons. Therefore, most of the particles

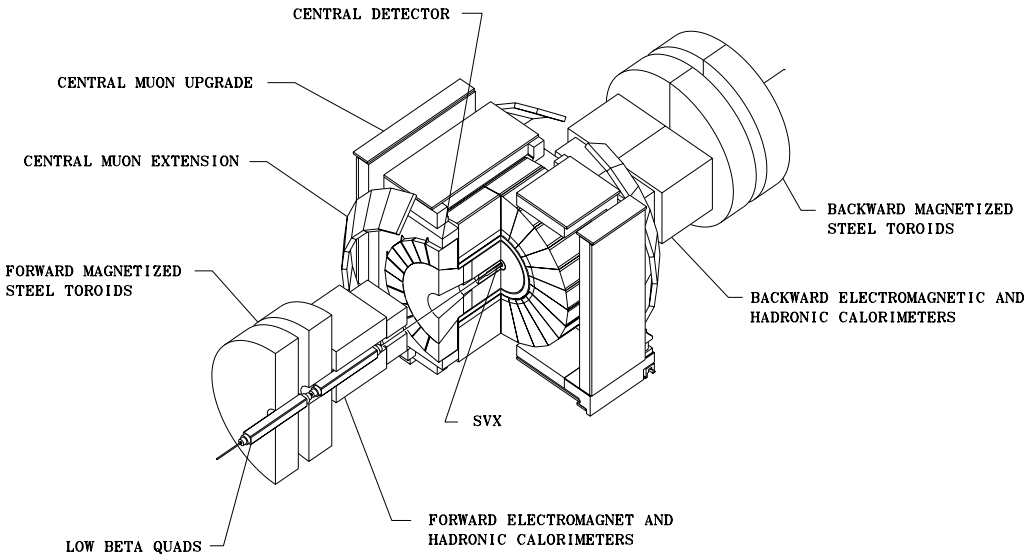

Figure 3.2: An isometric cut-away view of the CDF detector.

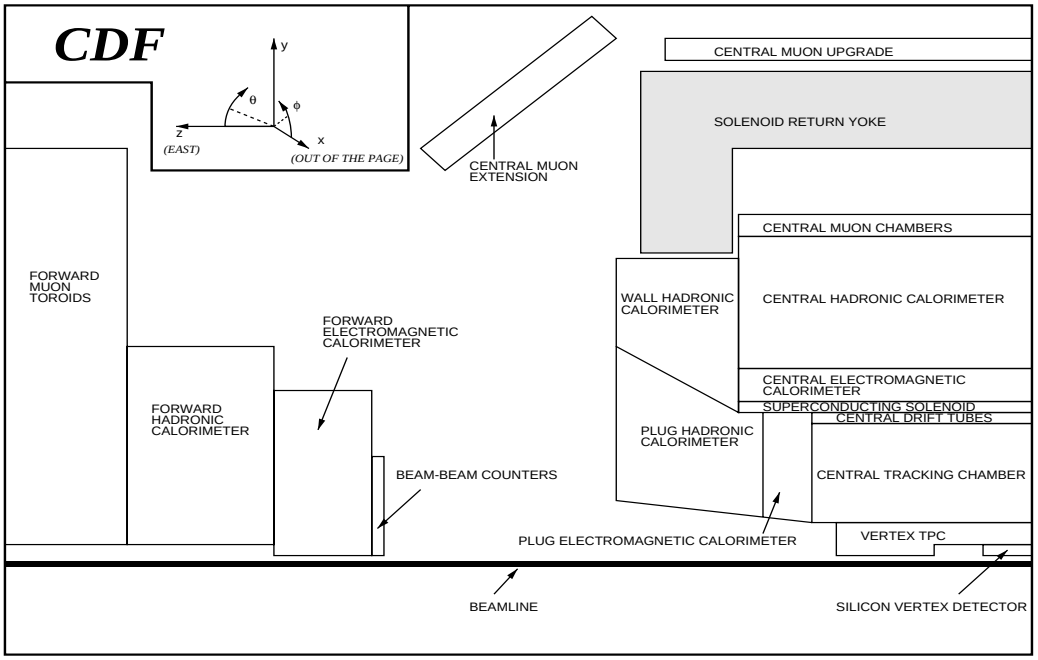

Figure 3.3: A longitudinal view of one quadrant of the CDF detector.

reaching the muon detectors are indeed muons.

CDF uses a right-handed Cartesian coordinate system (x, y, z) with its origin at the nominal interaction point. The positive z-axis lies along the beam line in the proton running direction (from west to east), the positive y-axis points vertically upward, and the positive x-axis points radially outward in the horizontal plane of the Tevatron ring. In addition to this coordinate system, a cylindrical coordinate system (r, θ, ϕ) is also used to describe the detector and characteristics of particles. The distance r is measured from the z-axis. The azimuthal angle ϕ is measured from the positive x-axis. The polar angle θ is defined as the angle measured from the positive z-axis. It is usually given in terms of the pseudorapidity η. The coordinate system employed by CDF is shown in the inset of Figure 3.3. Two forms of pseudorapidity are used in this dissertation. The *detector-η* measures the pseudorapidity with respect to the nominal interaction point at the center of the detector. It is generally used to specify the physical segmentation of the detector. The *event-η* measures the pseudorapidity with respect to the event vertex.

The following sections present a brief description of the CDF detector components that are important to this analysis. A more detailed description of the detector can be found in Ref. [50].

3.2.1 Calorimetry

The CDF calorimeter system consists of electromagnetic (EM) and hadronic (HA) components, and is partitioned into three main detector regions according to their pseudorapidity coverage. The central region ($|\eta| \lesssim 1.3$) contains the Central Electromagnetic calorimeter (CEM), the Central Hadron calorimeter (CHA), and the EndWall Hadron calorimeter (WHA). The endplug regions ($1.1 \lesssim |\eta| < 2.4$) con-

Table 3.1: Characteristics of the CDF calorimeter subsystems. The quoted energy resolutions for the electromagnetic calorimeters are for incident electrons and photons, and for the hadron calorimeters are for incident isolated pions. E_T is given in GeV. The position resolutions are averages for the calorimeter subsystems. X_0 refers to radiation lengths and λ_0 refers to interaction lengths, respectively.

Calorimeter subsystem	$\|\eta\|$ coverage	Energy resol. $\sigma(E)/E$	Position resol. (cm^2)	Depth
CEM	$\|\eta\| < 1.1$	$13.5\,\%/\sqrt{E_T} \oplus 1.7\,\%$	0.2×0.2	$18\ X_0$
CHA	$\|\eta\| < 0.9$	$50\,\%/\sqrt{E_T} \oplus 3\,\%$	10×5	$4.5\ \lambda_0$
WHA	$0.7 < \|\eta\| < 1.3$	$75\,\%/\sqrt{E_T} \oplus 4\,\%$	10×5	$4.5\ \lambda_0$
PEM	$1.1 < \|\eta\| < 2.4$	$28\,\%/\sqrt{E_T} \oplus 2\,\%$	0.2×0.2	$18 - 21\ X_0$
PHA	$1.3 < \|\eta\| < 2.4$	$130\,\%/\sqrt{E_T} \oplus 4\,\%$	2×2	$5.7\ \lambda_0$
FEM	$2.2 < \|\eta\| < 4.2$	$25\,\%/\sqrt{E_T} \oplus 2\,\%$	0.2×0.2	$25\ X_0$
FHA	$2.3 < \|\eta\| < 4.2$	$130\,\%/\sqrt{E_T} \oplus 4\,\%$	3×3	$7.7\ \lambda_0$

tain the Plug Electromagnetic calorimeter (PEM) and the Plug Hadron calorimeter (PHA). The forward regions ($2.2 \lesssim |\eta| < 4.2$) contain the Forward Electromagnetic calorimeter (FEM) and the Forward Hadron calorimeter (FHA). The CEM contains the Central Electromagnetic Strip chamber (CES) which measures the shower position and transverse shower profile at the depth corresponding to the maximum average transverse development of an electromagnetic shower. The pseudorapidity coverage, energy and position resolutions, and depth of these calorimeter components except for the CES are summarized in Table 3.1.

All of the CDF calorimeter subsystems use *shower sampling* to measure particle energies. They consist of many layers of absorber material (lead for the electromagnetic calorimeters[1] and steel for the hadron calorimeters) interleaved with layers of active media. Each calorimeter subsystem is segmented in pseudorapidity and azimuth, forming a projective tower geometry that points back to the nominal interaction point.

[1]Precisely speaking, the absorber of the FEM is comprised of 96 % lead and 6 % antimony as described later.

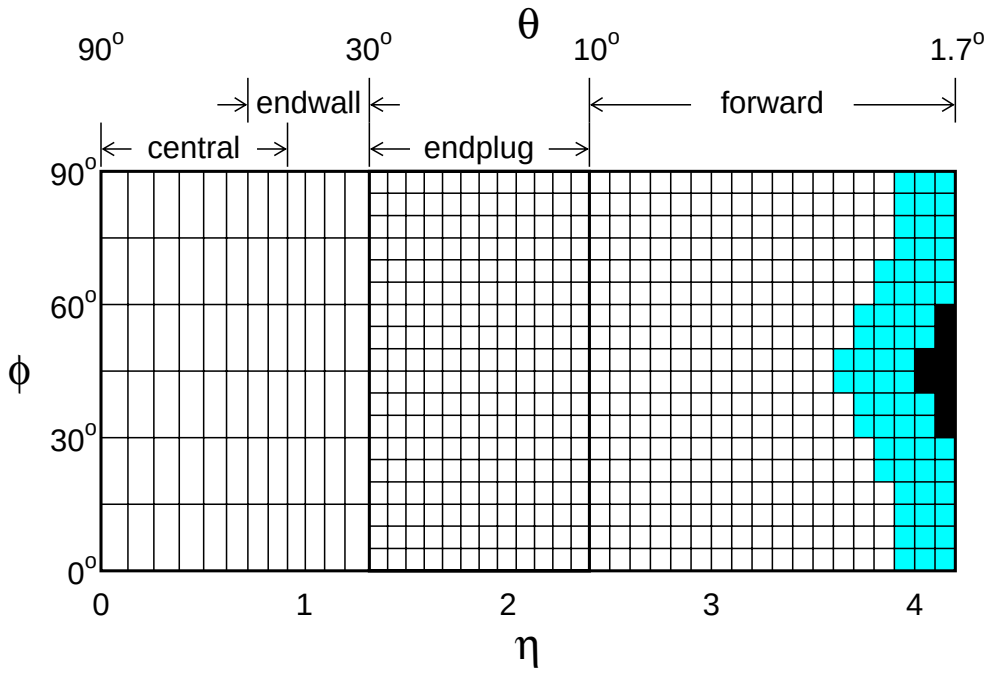

Figure 3.4: Segmentation of the CDF calorimeters in η-ϕ space. The EM calorimeters have full ϕ coverage out to $|\eta| = 4.2$. In the shaded region, the hadron calorimeter is short in depth due to the cutoff for low-β quadrupole magnets. The black region is not covered by the hadron calorimeters due to the hole for the Tevatron beam pipe.

The tower segmentation and nominal coverage of the various calorimeter subsystems is shown in Figure 3.4. The size of each tower is approximately $0.1(\eta) \times 15^{\circ}(\phi)$ in the central and endwall calorimeters, and $0.1(\eta) \times 5^{\circ}(\phi)$ in the plug and forward calorimeters.

Central Calorimeters

The central calorimeters consist of 48 modules (24 on each side of $z = 0$): each module covers 15° in ϕ and extends about 2.5 m along the beam axis on either side of $z = 0$. These modules are stacked into four free standing C-shaped arches which can be rolled into and out of the detector.

The Central Electromagnetic calorimeter (CEM) [51] is located immediately out-

side of the solenoidal magnet. It covers 360° in ϕ and $-1.1 < \eta < 1.1$ in η, and has a depth of 35 cm which corresponds to 18 radiation lengths. The CEM consists of 31 layers of 3.175 mm thick lead absorber interleaved with 5 mm thick layers of SCSN-38 polystyrene scintillator. Each wedge module of the CEM is divided into ten towers with a projective geometry. Every tower covers approximately 0.1 units in η and 15° in ϕ. The general layout of a CEM module is shown in Figure 3.5. The light from each tower is collected by two wavelength shifters mounted on opposite sides of the tower in azimuth and transmitted to phototubes (Hamamatsu R850) by lightguides. The energy resolution of the CEM for electrons between 10 and 100 GeV is

$$\frac{\sigma(E)}{E} = \frac{13.5\,\%}{\sqrt{E_T}} \oplus 1.7\,\%,$$

where E_T is the transverse energy of the electrons in GeV and the symbol $\oplus$ indicates that the two independent terms are added in quadrature.

The CEM is immediately followed by the Central Hadron calorimeter (CHA) and EndWall Hadron calorimeter (WHA) [52] which cover the pseudorapidity regions of $|\eta| < 0.9$ and $0.7 < |\eta| < 1.3$, respectively. Both CHA and WHA consist of 48 modules. Each module is segmented into projective towers, each of which covers an area of about $0.1(\eta) \times 15°(\phi)$. Each tower in the CHA and WHA is matched by a tower in the CEM. The CHA is made up of 32 layers of 2.5 cm thick steel absorber interleaved with 1.0 cm thick layers of polymethyl methacrylate (PMMA) scintillator. The WHA is composed of 15 layers of 5.0 cm thick steel absorber alternating with 1.0 cm thick PMMA scintillator. The absorber of the WHA is twice as thick as that of the CHA since, for a given E_T, the total energy in the WHA is on average a factor $\sqrt{2}$ larger than that in the CHA. Both calorimeters have a total depth of 4.5 interaction lengths. The light from a plastic scintillator is collected by wavelength shifter strips,

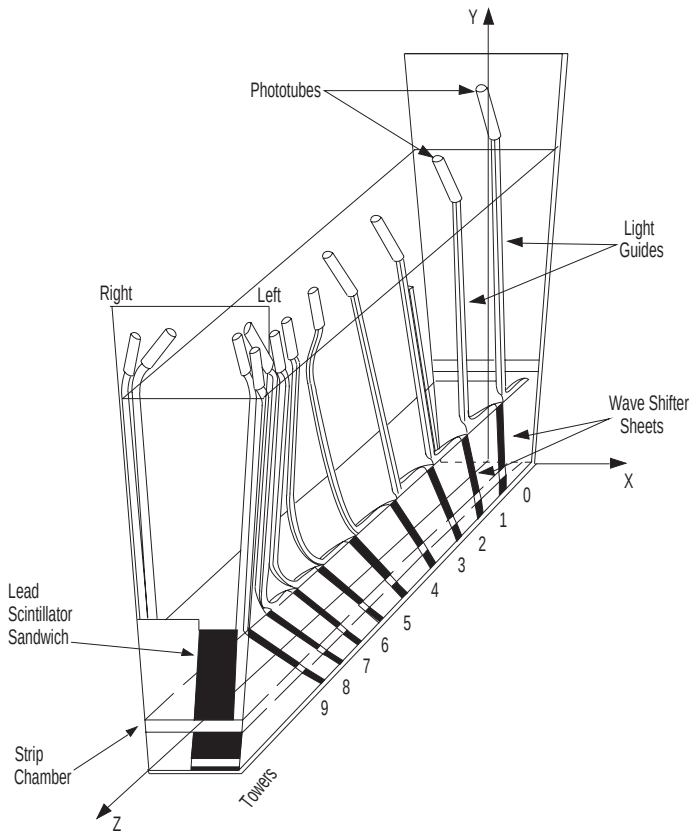

Figure 3.5: A cut-away view of one wedge of the Central Electromagnetic calorimeter (CEM).

which lie along the long sides of the scintillator sheets. The light from each tower is collected by two phototubes positioned on opposite sides in azimuth. The 12-stage Thorn-EMI 9954 phototube is used for the CHA and the 10-stage Thorn-EMI 9902 phototube is used for the WHA. The energy resolution of the CHA and WHA for charged pions between 10 and 150 GeV was found to be

$$\frac{\sigma(E)}{E} = \frac{50\,\%}{\sqrt{E_T}} \oplus 3\,\% \quad \text{(CHA)},$$

$$\frac{\sigma(E)}{E} = \frac{75\,\%}{\sqrt{E_T}} \oplus 4\,\% \quad \text{(WHA)},$$

respectively.

The initial calibration of the central calorimeters was performed with 50 GeV

electrons and pions in a test beam [53]. A cosmic-ray test was also performed on all modules of the central calorimeters [54]. To maintain the initial calibration, three calibration systems [55] are employed in the CEM.

- A 3 mCi ^{137}Cs gamma source was used to monitor long term variations. The source was moved into the calorimeter module by a motor driver.

- A Xenon flasher system was employed to test the response of the wavelength shifters. The trigger signal passed through a pulse shaping circuit and caused a Xenon bulb to flash. A specially designed optical fiber passed the light into a scintillator rod. The scintillator rod absorbed the light and re-emitted it into the wavelength shifters.

- A green LED signal was used to check short term variations of the CEM phototubes. (A nitrogen laser system was used to check short term variations of the CHA/WHA phototubes.)

The ^{137}Cs source calibration was performed during the accelerator shutdown periods, while the calibrations with the flasher systems were carried out about every 20 hours (before the beginning of a new Tevatron store).

Endplug Calorimeters

The endplug calorimeters cover the holes at $\theta \approx 30^\circ$ and 150° outlined by the CEM and WHA like "endcaps". Each endplug calorimeter consists of four fan-shaped 90° quadrants. There is a concentric conical hole with an opening angle of 10° with respect to the beam axis to accommodate the Tevatron beam pipe.

The Plug Electromagnetic calorimeter (PEM) [56] covers $1.1 < |\eta| < 2.4$ in η. The PEM is about 53 cm long in the z direction, which corresponds to $18-21$ radiation

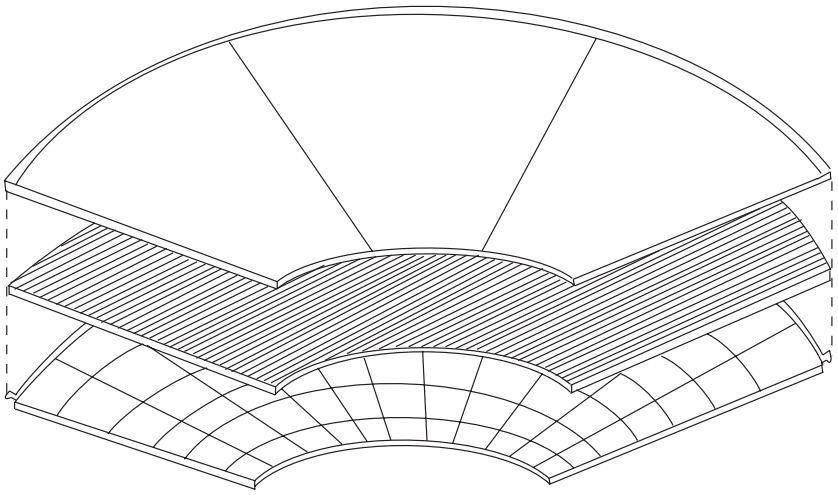

Figure 3.6: An exploded view of the layer of the Plug Electromagnetic calorimeter (PEM) proportional tube array. The lower layer shows the cathode pad segmentation that provides a projective tower geometry.

lengths depending on the polar angle. The PEM consists of four fan-shaped quadrants with an outer radius of 140 cm; each quadrant consists of 34 layers of gas proportional tube arrays interleaved with 2.7 mm thick lead absorber panels. An exploded view of one quadrant of the PEM is shown in Figure 3.6. The proportional tubes are made up of conductive plastic tubes of a square inner cross section of 7 mm $\times$ 7 mm with 0.8 mm thick walls. Each tube contains a 50 μm gold-plated tungsten anode wire at the center. Each plane of the tube arrays in a quadrant consists of 156 tubes which are arranged side by side in a plane perpendicular to the beam axis. A 50 %-50 % admixture of argon-ethane with a small addition of ethyl alcohol is used for the tubes. The tube layers are sandwiched by a pair of 1.6 mm thick copper-clad G-10 cathode panels. On one side of the panel, the copper is segmented into pads to provide a projective tower geometry. In the polar angle, the segmentation is $\Delta\eta \approx 0.09$ between 1.41 and 2.4 in η, and smaller ($\Delta\eta = 0.05$) for larger angles. The

segmentation is 5° in azimuthal angle. The area of the pads ranges from about 3 cm $\times$ 3 cm to 10 cm $\times$ 19 cm in the first layer, depending on η, and increases up to 30 % with increasing z. On the other side of the G-10 panel, the cathode signals from the pads are transmitted radially to the outer edge of the quadrant by etched strip lines. Summing up pad signals longitudinally gives a single tower signal. Each tower has three longitudinal segmentations. The first longitudinal segment contains the first 5 layers, the second the next 24 layers, and the third the last 5 layers, respectively. All PEM towers were calibrated by a 100 GeV electron beam. The energy resolution of the PEM was found to be

$$\frac{\sigma(E)}{E} = \frac{28\,\%}{\sqrt{E_T}} \oplus 2\,\%$$

with 20$-$200 GeV electron beams.

The Plug Hadron calorimeter (PHA), located directly behind the PEM, covers $1.3 < |\eta| < 2.4$ in η and is arranged in twelve 30° sections. The PHA consists of 21 layers of 5.1 cm (6.4 cm after the fourth layer) thick steel absorber layers interleaved with gas proportional tube layers. The PHA has a total depth of 5.7 interaction lengths. The PHA gas proportional tubes are resistive plastic tubes with a cross section of 8 mm $\times$ 14 mm containing a 50 μm diameter gold-plated tungsten anode wire at the center. The tubes are aligned side by side in a plane perpendicular to the beam axis, and sandwiched by a pair of cathode planes. The cathode plane of one 30° PHA section consists of 72 (12 in η $\times$ 6 in ϕ) electrically distinct pads on the inner side, which are connected to the outer side through a hole. Copper traces on the outer side of the cathode plane lead the cathode signals radially to the outer edge of the chamber. The signals from each layer are ganged together longitudinally to form 72 towers in one 30° sector. The PHA tower segmentation is $\Delta\eta \approx 0.09$ in η and 5° in ϕ. The calibration of the PHA calorimeter was achieved with charged

pion beams. The energy resolution of the PHA for 20−230 GeV charged pions was measured to be

$$\frac{\sigma(E)}{E} = \frac{130\,\%}{\sqrt{E_T}} \oplus 4\,\% \; .$$

Forward Calorimeters

The forward calorimeters are located in the small angle regions in both the proton and antiproton beam directions. They are completely separated from the central and endplug calorimeters as shown in Figure 3.3.

The Forward Electromagnetic calorimeter (FEM) [57] is located about 6.5 m from the nominal interaction point and accommodates the Tevatron beam pipe at either end of the CDF detector. The FEM has a pseudorapidity coverage of $2.2 < |\eta| < 4.2$ ($12^\circ > \theta > 2^\circ$ on the positive η side) and full azimuthal coverage. The FEM is approximately 3 m on a side and 1 m deep. It consists of 30 sampling layers of proportional tube chambers with cathode and readout, interleaved with 0.48 cm thick layers of absorber composed of 94 % lead and 6 % antimony. The total depth corresponds to 25 radiation lengths. Figure 3.7 shows a cross section view of the FEM chamber. Each proportional tube has an inner cross section of 7 mm in the beam direction and 10 mm perpendicular to the beam. A 50 μm diameter gold-plated tungsten anode wire runs through the center of each tube. The proportional tube layers are partitioned into four 90° sections. The copper cathode plane of one 90° chamber is segmented into 360 pads to provide a tower geometry. Each pad subtends 0.1 units of η and 5° of ϕ. The cathode pads are scaled in size every other layer so that the resultant towers project back to the nominal interaction point. Cathode signals are carried to the outer edge of the chamber by ribbon cables. The pads are ganged together longitudinally with two segmentations, each of which consists of 15

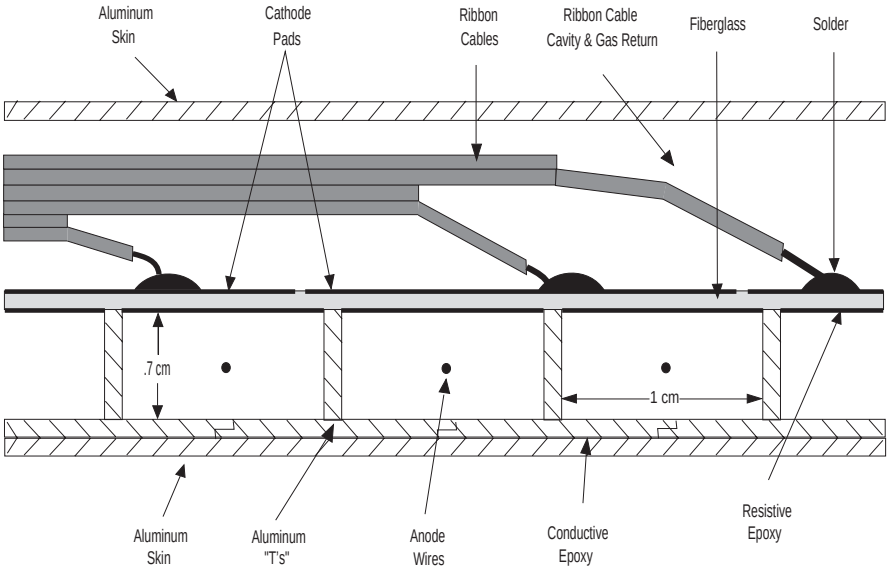

Figure 3.7: A cross section view of a chamber of the Forward Electromagnetic calorimeter (FEM).

sampling layers. The FEM was calibrated with electron beams. By changing the electron energy from 20 to 200 GeV, the energy resolution was measured to be

$$\frac{\sigma(E)}{E} = \frac{25\,\%}{\sqrt{E_T}} \oplus 2\,\% \; .$$

The Forward Hadron calorimeter (FHA) [58] is positioned right behind the FEM. The FHA covers $2.3 < |\eta| < 4.2$ in η ($12^\circ > \theta > 2^\circ$ in θ on the positive η side). The FHA calorimeter is partitioned into four 90° sections in the same way as the FEM calorimeter. Each of these sections consists of 27 sampling layers (204 cm $\times$ 196 cm $\times$ 2.5 cm) of gas proportional tube chambers alternating with 5.1 cm thick layers (213 cm $\times$ 213 cm $\times$ 5.1 cm) of steel absorber. The FHA has a depth of 7.7 interaction lengths. The chamber structure of the FHA is similar to that of the FEM. The cathode surface of each 90° section is segmented into 19 bins in pseudorapidity ($\Delta\eta = 0.1$) and 18 bins in azimuth ($\Delta\phi = 5^\circ$). The signals from each cathode pad at fixed η and ϕ are ganged to form a projective tower. The FHA was calibrated with

20−200 GeV charged pion beams. The energy resolution of the FHA for pions in the range of 20−200 GeV is

$$\frac{\sigma(E)}{E} = \frac{130\,\%}{\sqrt{E_T}} \oplus 4\,\% \; .$$

The FHA output was found to be consistent with a linear response up to 200 GeV with no evidence of saturation.

3.2.2 Vertex Detector

The Vertex detector (VTX) is a gas drift chamber that surrounds and provides mechanical support for the Silicon Vertex detector (SVX). Its main functions are to provide precise two-dimensional tracking information for charged particles in the r-z plane and to measure the position of primary $p\bar{p}$ interaction vertices along the z-axis.

The VTX is 2.8 m long in the z direction and covers the pseudorapidity region of $|\eta| < 3.5$. It consists of 28 time projection chamber modules, each of which is divided into two drift regions by a central high voltage grid. The modules are placed end to end along the beam direction. Each module is 9.4 cm long in z, and is segmented into eight wedges, which cover 45° in ϕ. The 10 outer modules have an inner radius of 6.5 cm, while the 18 inner modules have an inner radius of 11.5 cm to accommodate the SVX detector. The outer radius is 28 cm for all the modules. In each module, sense wires are strung tangent to the azimuthal direction on either side of the high voltage grid in planes transverse to the beam. There are 24 and 16 sense wires mounted in each drift region of 10 outer and 18 inner modules, respectively.

The drift regions are filled with a 50 %-50 % mixture of argon-ethane gas. Charged particles traversing the gas ionize it. The freed electrons drift along the beam axis to the sense wires, resulting in a voltage drop in the sense wires. The drift time

and radial positions of the sense wires are used to reconstruct the r-z profile of the track. Each module is canted 15° in ϕ with respect to the neighboring modules so that some limited ϕ information can be obtained for tracks crossing through more than one module.

The measurement of the z position of the $p\bar{p}$ interactions was achieved by locating the convergences of the reconstructed charged particle tracks in the event. The uncertainty in the measurement of the z vertex position z_{vtx} was in the range of $1-2$ mm, depending on the multiplicity of charged tracks associated with the reconstructed vertex. The multiplicity of reconstructed vertices in the event gives a good estimate of the number of $p\bar{p}$ interactions in the bunch crossing.

3.2.3 Beam-Beam Counters

The Beam-Beam Counters (BBCs) are two planes of 16 scintillation counters mounted in front of the forward calorimeters on both positive η (east) and negative η (west) sides (one plane on each side). The counters provide a *minimum bias* trigger for the CDF detector, and also serve as the primary luminosity monitor.

In each BBC, scintillation counters are arranged in a rectangle around the beam pipe, forming four concentric squares, as shown in Figure 3.8. The counters cover the pseudorapidity regions of $3.24 < |\eta| < 5.90$ ($4.47° > \theta > 0.32°$ on the positive η side) at a distance of 5.8 m from the center of the detector. The dimensions of the counters are determined such that each counter covers an approximately equal pseudorapidity interval of $\Delta\eta = 0.7$.

Each scintillation counter is read out by two phototubes mounted on both ends of the counter. A hit of a counter requires that both phototubes have signals above a certain threshold. The counters have excellent timing resolution ($\sigma < 200$ ps), and

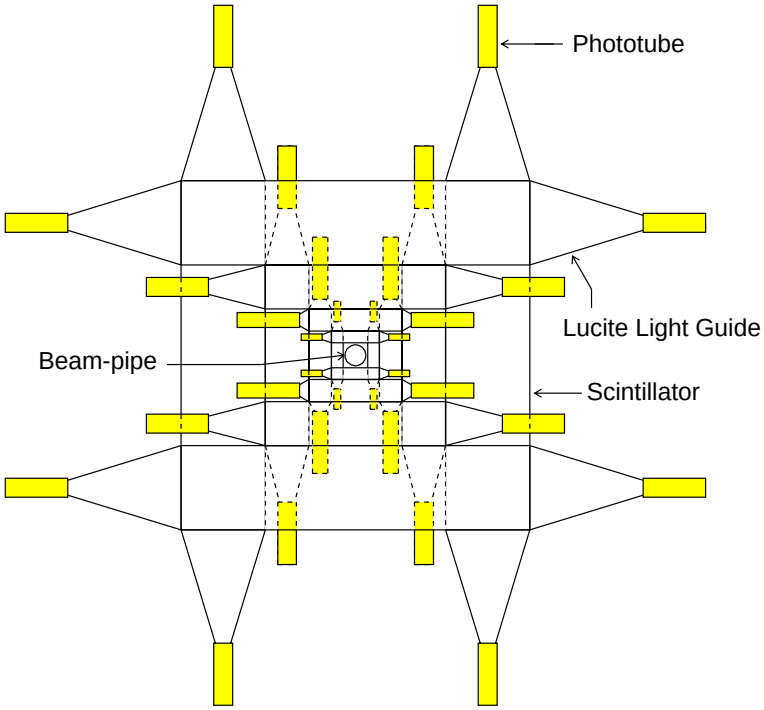

Figure 3.8: A schematic view of one of the beam-beam counter planes. The shaded parts show the photomultiplier tubes for read out.

so provide a good measurement of the time of interactions. Coincident hits of the east and west counters within a 15 ns time window centered at 20 ns after the bunch crossing act as a minimum bias trigger.

The instantaneous (integrated) luminosity is obtained by measuring the rate (number) of coincidences of the east and west counters divided by the effective BBC cross section. The effective BBC cross section σ_{BBC} is $\sigma_{BBC} = 51.15 \pm 1.60$ mb at $\sqrt{s} = 1800$ GeV [59] and $\sigma_{BBC} = 39.9 \pm 1.2$ mb at $\sqrt{s} = 630$ GeV [60].

In this analysis, BBC information is also used to look for a rapidity gap signature in single diffractive events.

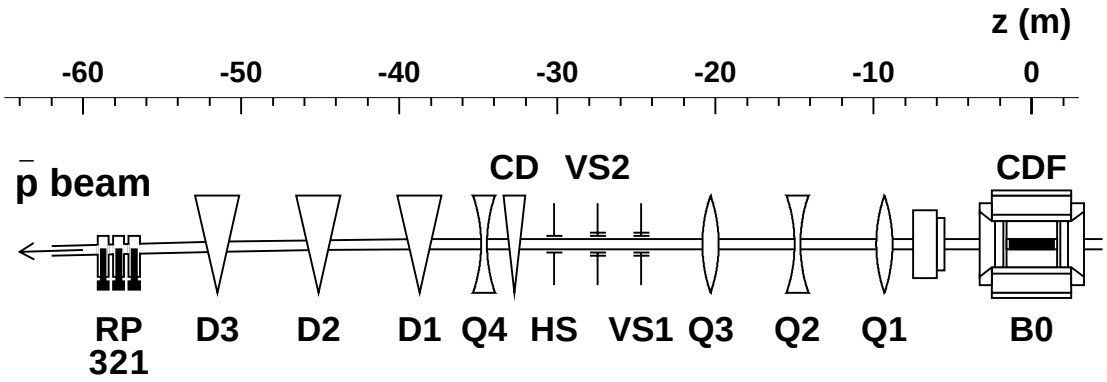

Figure 3.9: A top view of the outgoing antiproton beam line. The elements D1, D2 and D3 are dipole magnets which bend antiprotons toward the inside of the Tevatron ring, and CD is a correction dipole magnet which bends antiprotons downward and toward the inside of the Tevatron ring. Q1 and Q3 (Q2 and Q4) are quadrupole magnets which focus antiprotons in the horizontal (vertical) direction. The elements VS1 and VS2 are electrostatic beam separators which bend antiprotons upward, and the separator HS bends antiprotons toward the outside of the Tevatron ring. RP1, 2 and 3 are three Roman Pot detector stations.

3.2.4 Roman Pot Spectrometer

Before the Tevatron collider run of 1995−1996, a Roman Pot spectrometer was added to CDF to detect leading antiprotons carrying a substantial longitudinal beam momentum fraction x_F. The value of x_F is typically 0.90−0.97. The Roman Pot spectrometer was used to collect inclusive single diffractive events by triggering the CDF detector on leading antiprotons. It also provided information about the deviation and angle of a leading antiproton relative to the antiproton beam line, which give the fractional momentum loss ξ and four-momentum transfer squared t of the leading antiproton in conjunction with the $p\bar{p}$ interaction point of the event and the beam transport matrix between the Roman Pot spectrometer and the interaction point.

Figure 3.9 shows a top view of the outgoing antiproton beam line between the CDF nominal collision point (BØ) and the Roman Pot spectrometer. The quadrupole mag-

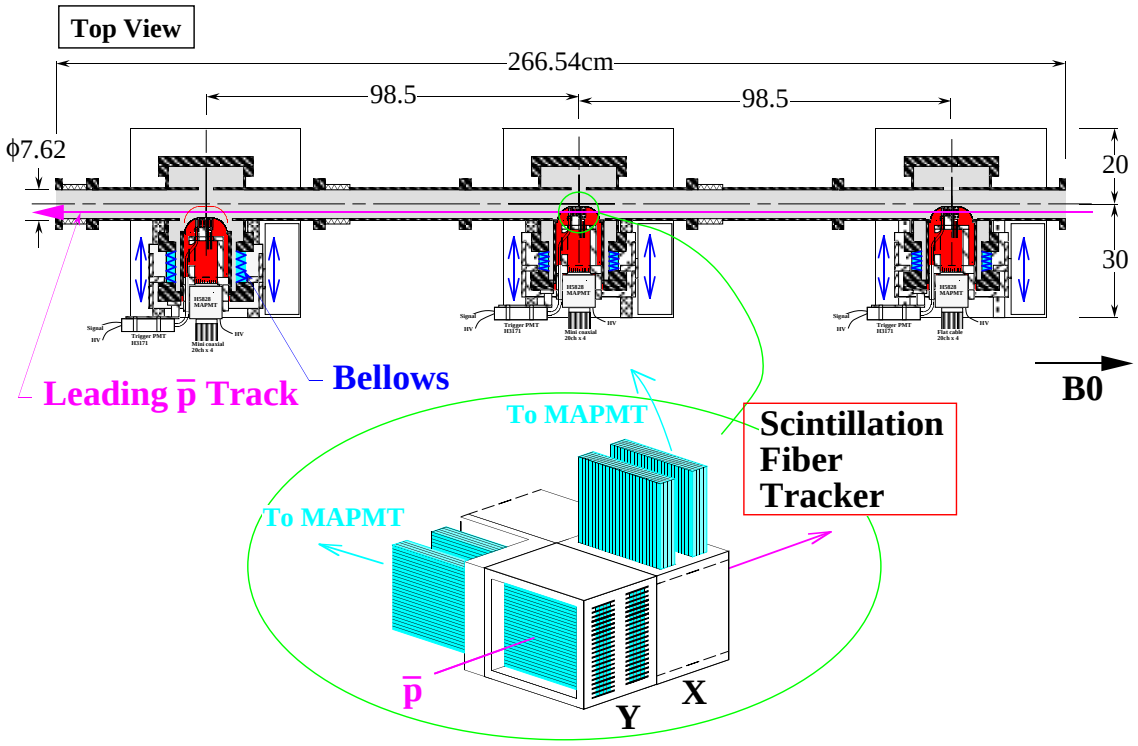

Figure 3.10: A top view of the Roman Pot spectrometer. The Roman Pot spectrometer consists of three Roman Pot detector stations which are spaced 98.5 cm apart from one another along the beam line. The structure of the scintillation fiber tracking detector is shown in the inset.

nets Q1 and Q3 focus antiprotons in the horizontal direction, and Q2 and Q4 in the vertical direction. The electrostatic beam separators VS1 and VS2 bend antiprotons upward, and separator HS toward the outside of the Tevatron ring. The dipole magnets D1, D2 and D3 bend antiprotons toward the inside of the Tevatron ring, and the correction dipole magnet CD bends antiprotons downward and toward the inside of the Tevatron ring. In a single diffractive interaction, the incoming antiproton loses a small fraction (typically less than 10−15 %) of its momentum, and thus gets bent by the dipole magnets D1, D2 and D3 at a slightly larger angle than the antiproton beam, but stays in the beam pipe. Therefore, the leading antiproton can be detected by the Roman Pot spectrometer mounted close ($\approx$ 1 cm) to the beam line.

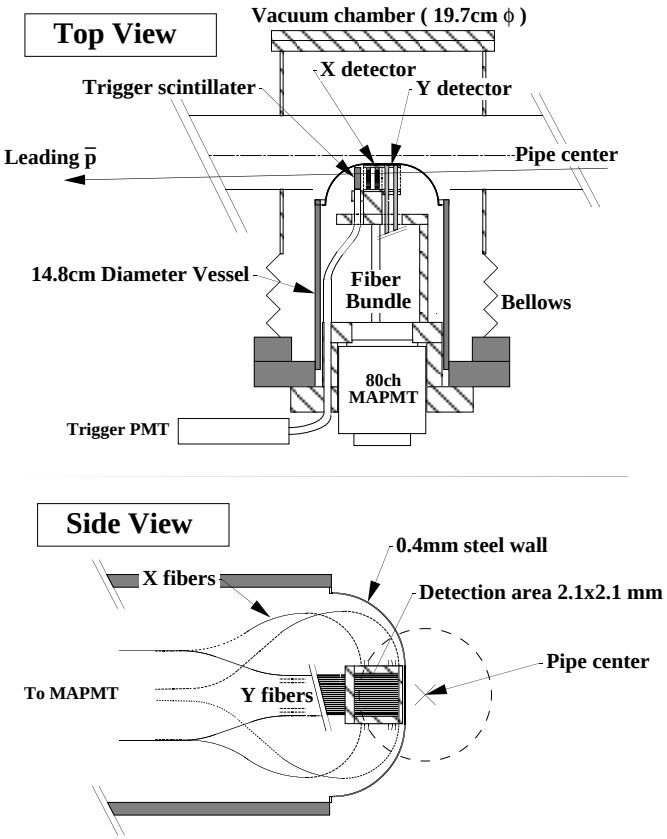

Figure 3.11: Arrangement of the Roman Pot detector. The Roman Pot detector, consisting of a scintillation trigger counter and an X-Y scintillation fiber tracking detector, is mounted in a vessel attached to the vacuum beam pipe and vacuum chamber by bellows.

The Roman Pot spectrometer consists of three Roman Pot detector stations which are placed inside the Tevatron ring downstream of the antiproton beam about 57 m away from the CDF nominal collision point. The stations are spaced 98.5 cm apart from one another along the beam axis and the total length of the spectrometer including the beam pipe is 266.54 cm, as shown in Figure 3.10.

Figure 3.11 shows the arrangement of a Roman Pot detector station. Each station is equipped with a scintillation trigger counter and an X-Y scintillation fiber tracking detector mounted in a vessel attached to the vacuum beam pipe and vacuum chamber

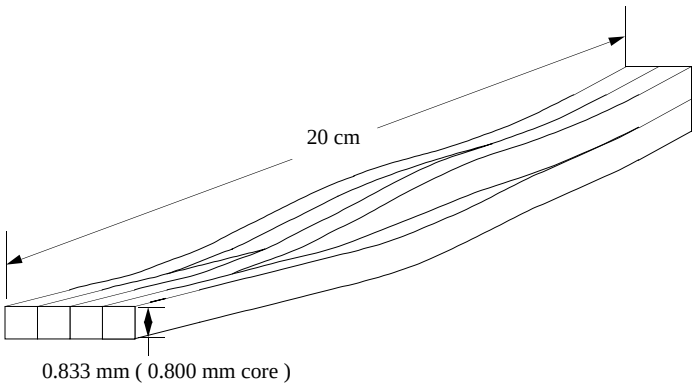

Figure 3.12: One ribbon consisting of four scintillation fibers used for the Roman Pot tracking detector.

by bellows. The Roman Pot detectors were brought close to the circulating beams by remotely controlled motors after beam conditions became stable.

Trigger Counter

The scintillation trigger counter (Bicron BC404) is 8 mm thick, and has a fiducial area of 21 mm $\times$ 21 mm. The scintillation light from the trigger counter is transmitted through a lightguide to a phototube, HAMAMATSU H3171-03, placed at the back side of the Roman Pot detector station.

Tracking Detector

The scintillation fiber tracking detector of each station contains four layers of scintillation fiber ribbons mounted in planes perpendicular to the beam line, two for the X direction and two for the Y direction. The fibers used are KURARAY SCSF81 with a single acrylic cladding. Each fiber is 20 cm long and 0.833 mm $\times$ 0.833 mm square and contains a scintillation core of 0.800 mm $\times$ 0.800 mm square. One ribbon is made of four scintillation fibers which are arranged inline along the beam direction at the detection side to increase the path length of the particle, and into a square at

the PMT side to fit the anode of the multianode photomultiplier tube (MAPMT), as shown in Figure 3.12. Scintillation light from the hit fibers is transmitted to the MAPMT, 80-channel HAMAMATSU H5828, mounted at the back side of the Roman Pot detector station.

One layer consists of 20 scintillation fiber ribbons. Two layers are mounted in parallel, forming a superlayer as shown in Figure 3.13. In each layer, 20 ribbons are placed in parallel and spaced one third of the scintillation core width from each other. The gaps between the ribbons are filled with aluminized mylar. The two layers are displaced from each other by two thirds of the scintillation core width; therefore each ribbon can be divided into three channels. Consequently, each superlayer has a total of 79 channels of 0.267 mm width. The distance between the centers of the layers along the beam axis is 8.5 mm. With this arrangement of the scintillation fiber tracking detector, we expect two typical patterns of fiber hits: (a) a leading antiproton hits fibers in both layers, (b) a leading antiproton hits a fiber in one layer and passes through a gap between ribbons in the other layer. These two hit patters are depicted in Figure 3.14.

Acceptance and Resolution

A Roman Pot track is reconstructed from a fit to the X-Y Roman Pot tracking detector hit positions as shown in Figure 3.15. The Roman Pot track position resolution is approximately 100 μm. The diffractive variables ξ and t are determined from (a) the position and angle of the reconstructed Roman Pot track relative to the beam line, (b) the position of the event vertex, and (c) the beam transport matrix between the interaction point and the Roman Pot spectrometer, as described in detail in Appendix A.

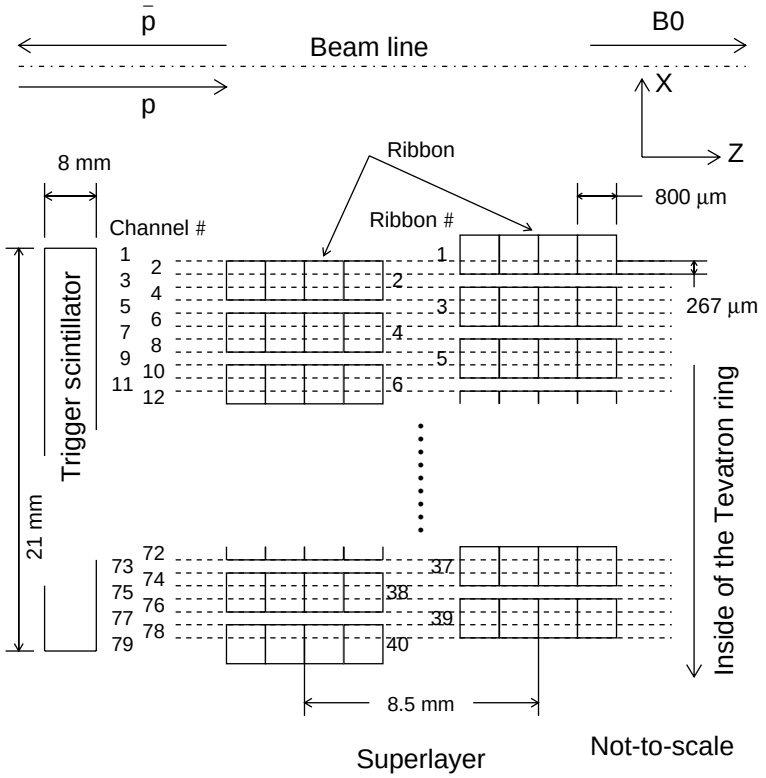

Figure 3.13: Arrangement of the Roman Pot scintillation fiber tracking detector for the X direction. Two layers of 20 scintillation fiber ribbons are mounted in parallel, forming a superlayer. Each superlayer is divided into 79 channels of 0.267 mm width.

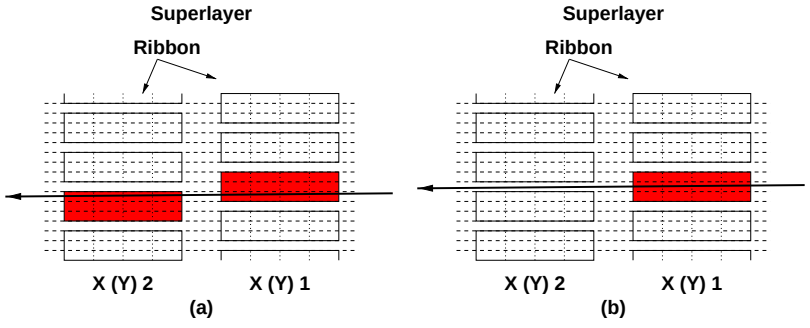

Figure 3.14: Two typical hit patterns in the Roman Pot scintillation fiber tracking detector. The filled regions are ribbons which have a hit. (a) Both layers have a hit. (b) Only one layer has a hit.

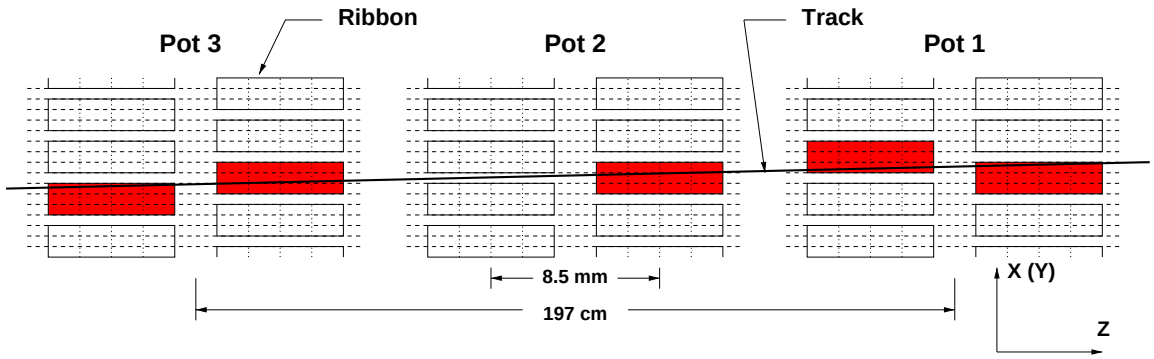

Figure 3.15: A track reconstructed from hits in the Roman Pot scintillation fiber tracking detectors in the X (Y) direction. The filled regions are ribbons which have a hit.

The acceptance of the Roman Pot spectrometer and resolutions in ξ and t determinations are evaluated using a Monte Carlo simulation as described in Appendix B. The simulation takes into account the beam profile and angular spread at the interaction point, the Tevatron magnetic lattice between the interaction point and the position of the Roman Pot spectrometer, and the geometry and resolution of the Roman Pot spectrometer. The Roman Pot acceptance at $\sqrt{s} = 1800$ and 630 GeV is shown as a function of ξ and t in Figure 3.16. The acceptance at $\sqrt{s} = 630$ GeV is similar to that at 1800 GeV at the same ξ and for t scaled down by a factor of $(1800/630)^2$. The average Roman Pot acceptance is 72 % in the region $0.035 < \xi < 0.095$ and $|t| < 1.0$ GeV^2 at $\sqrt{s} = 1800$ GeV, and 59 % in the region $0.035 < \xi < 0.095$ and $|t| < 0.2$ GeV^2 at $\sqrt{s} = 630$ GeV. The estimated resolutions in ξ and t are $\sigma(\xi) = 0.001$ and $\sigma(t) = 0.07$ GeV^2 in the region $0.035 < \xi < 0.095$ and $|t| < 1.0$ GeV^2 at $\sqrt{s} = 1800$ GeV, and $\sigma(\xi) = 0.0015$ and $\sigma(t) = 0.02$ GeV^2 in the region $0.035 < \xi < 0.095$ and $|t| < 0.2$ GeV^2 at $\sqrt{s} = 630$ GeV.

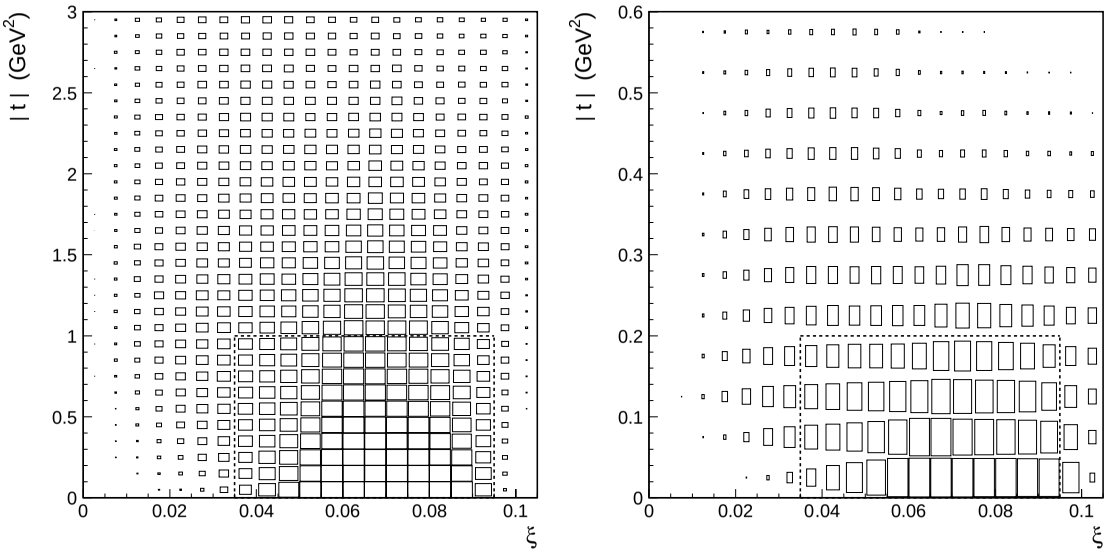

(a) 1800 GeV (b) 630 GeV

Figure 3.16: The Roman Pot acceptance as a function of ξ and $|t|$ for the (a) 1800 GeV and (b) 630 GeV runs. The area of the rectangle in each bin is proportional to the Roman Pot acceptance; a full box corresponds to an acceptance of 100 %. The dashed lines represent the ξ-t regions used in this analysis.

3.3 Trigger System

In standard Tevatron operation mode with six proton bunches and six antiproton bunches, bunch crossings occur every 3.5 μs around the center of the CDF detector, corresponding to a rate of 286 kHz. The maximum rate of the permanent data storage media used by CDF is a few events per second. Therefore, the data acquisition (DAQ) system needs to select interesting events at a rate of a few Hz out of events occurring at a rate of several hundred kHz.

Another concern for the the DAQ system is to minimize the dead-time that occurs when event information is being read out of the detector electronics and processed. During dead-time, the DAQ system cannot access the information from a new bunch crossing. Because every bunch crossing has an equal chance to produce an interesting

event, it is important to examine as many bunch crossings as possible.

To fulfill these requirements, CDF developed a sophisticated online three-level trigger system [61]. Each level examines fewer events in greater detail than the preceding level. The Level 1 and Level 2 triggers are implemented in specially designed hardware, while the Level 3 trigger is implemented in software running on commercial computers. Individual trigger paths can be prescaled, which means that only a fraction of events that meet the requirements of that trigger level are accepted. This is done to keep the trigger accept rate manageable without making the trigger requirements too stringent.

Level 1 Trigger

The Level 1 trigger system examines every bunch crossing and makes a trigger decision within the time between bunch crossings of 3.5 μs, and thus has no dead-time. The Level 1 trigger, implemented in custom-designed hardware, uses fast analog outputs from the front-end electronics of the various detector components. The Level 1 trigger accepts about 1$-$2 % of events, reducing the rate from 286.278 kHz to a few kHz. The events accepted by the Level 1 trigger are passed on to the Level 2 trigger.

Level 2 Trigger

The Level 2 trigger system requires about 25$-$35 μs to process an event delivered from Level 1. The Level 2 trigger is also implemented in specially designed hardware and uses fast analog outputs from the detector front-end electronics. During the processing time, the next 7$-$10 bunch crossings are ignored by the DAQ system, causing about 10$-$20 % of dead-time. The Level 2 trigger accept rate is limited to a peak of about 40$-$45 Hz. If an event is accepted by Level 2, the data of the event are digitized by the front-end electronics mounted on the detector, and then scanners

read out the full event. The digitization and scanning processes take about 3 ms, causing another few percent dead-time. The scanners can buffer events (store events in a queue before processing); therefore once the event is read out, the DAQ system is alive again and can trigger on a new event.

Level 3 Trigger

The Level 3 trigger is the last stage of the online trigger system. After Level 2, fully digitized event information is sent to a farm of 64 Silicon Graphics processors, on which a FORTRAN reconstruction code including various filtering algorithms is executed. The Level 3 reconstruction software is a subset of the offline reconstruction code. Simpler and faster algorithms are used in the Level 3 trigger due to the time constraints. The Level 3 trigger uses about one CPU second to process an event. The Level 3 output rate is about 10 Hz. The Level 3 trigger buffers events and processes them in parallel, incurring no dead-time. All the events passing the Level 3 trigger are logged to staging disks, and then copied to 8 mm tapes.

3.4 Data Acquisition System

The CDF detector has a total of about 150,000 electronic channels. To read out these channels, CDF used two types of crate-based front-end electronic systems: the RABBIT system [62] and the FASTBUS system [63]. The Redundant Analog Bus-Based Information Transfer (RABBIT) system was developed at Fermilab by the Particle Instrumentation Group to deal with the wide dynamic range ($1 : 100,000$) required by the calorimeter readout. The RABBIT system is used mainly for the read-out of the calorimeters and muon detectors. The digitized RABBIT signals are read out by MX scanners. Most of the tracking detectors are read out by the FASTBUS

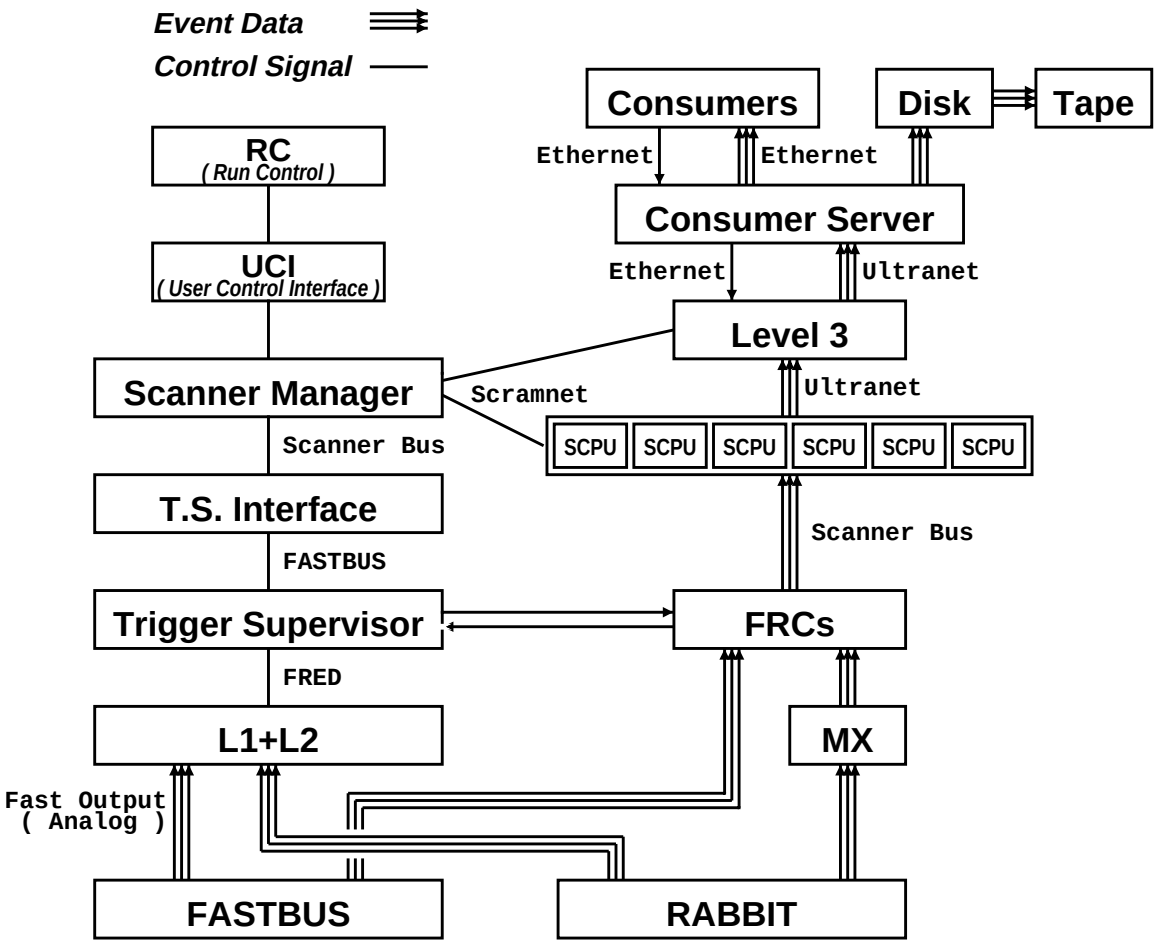

Figure 3.17: A schematic drawing of data flow through the CDF data acquisition system.

system. FASTBUS readout controllers (FRCs) read out data from the FASTBUS front-end electronics, and also provide the interface to the MX scanners.

A schematic drawing of data flow through the CDF data acquisition system is given is Figure 3.17. The Level 1 and Level 2 triggers receive fast analog outputs from the detectors through dedicated cables. Once the Level 2 trigger accepts an event, the decision is sent via the Front-end Readout and Decision (FRED) boards to the Trigger Supervisor (TS) FASTBUS module which instructs the FRCs to read out the event data. Six single-board VME-based processors, called Scanner CPUs

(SCPUs), read out a subset of the FRCs over a custom-built Scanner Bus. The SCPUs, running the VxWorks operating system, arrange the information received from the FRCs into data banks which are organized by the detector components. The SCPUs are controlled by another VME-based processor, called the Scanner Manager (SM), through a dedicated reflective memory network, scramnet (shared common RAM network). When all the FRCs finish loading an event, the TS notifies the SM via the Trigger Supervisor Interface (TSI), and when all the SCPUs finish loading the event, the SM tells the TS via the TSI to release the front-end buffers so that another event can be loaded. The SM also controls the data flow through a ultranet distributor to the Level 3 system and notifies the Level 3 system when the data transfer of the event is complete.

The data of events accepted by the Level 3 trigger are transfered to a dedicated Silicon Graphics machine, the Consumer Server (CS), via ultranet. The CS then passes event information to Consumers through ethernet for monitoring luminosity conditions, trigger rates, detector performance, rates of well known physics processes (e.g. J/ψ production) and so on. The CS also runs data logger programs which write accepted events on staging disks and subsequently to 8 mm tapes.

Chapter 4

Data and Event Selection

Before the Tevatron collider run of 1995−1996, the Roman Pot (RP) spectrometer was installed downstream of the antiproton beam as described in Section 3.2.4, and a trigger system based on antiprotons detected in the Roman Pot spectrometer was prepared to collect inclusive single diffractive (SD) events, $p + \bar{p} \rightarrow X + \bar{p}$. In this chapter, details of the diffractive[1] trigger system and the diffractive event selection are described.

In addition to the diffractive data samples, non-diffractive (ND) data samples are used in this analysis to compare diffractive events with non-diffractive events. The non-diffractive data samples and event selection are also described in this chapter.

[1] Hereafter, "diffractive" and "single diffractive" are used interchangeably.

4.1 Data Samples

4.1.1 Diffractive Triggers and Data Samples

The diffractive trigger system is designed to collect events with a high momentum leading antiproton in the Roman Pot spectrometer. The selection requirements at each of the three trigger levels are described in the following paragraphs.

Level 1: Level 1 requires a three-fold coincidence of the Roman Pot scintillation trigger counters. The timing of the coincidence was adjusted to the outgoing antiproton bunch to veto background due to the incoming proton bunch which passes the position of the Roman Pot spectrometer about 370 ns earlier than the outgoing antiproton bunch. In addition, during the latter part of the Tevatron run at $\sqrt{s} = 630$ GeV (run ≥ 75000), some minimal energy deposition was required on the east microplug calorimeter at Level 1, since a significant fraction (approximately 46 %) of triggers up to that time were found to be due to beam halo particles. The triggered events were prescaled to $50-200$ Hz and sent to Level 2.

Level 2: At level 2, the diffractive trigger is split into two paths, one is the *diffractive inclusive trigger* and the other is the *diffractive dijet trigger*. Since events collected with the diffractive dijet trigger are not used in this analysis, only the diffractive inclusive trigger is explained below. The diffractive inclusive trigger performed prescaling of events to the rate of about 1 Hz. The prescale factor was dynamically varied depending on the instantaneous luminosity.

Level 3: During the 630 GeV Tevatron running, there was no requirement at Level 3 for the diffractive inclusive trigger. During the 1800 GeV Tevatron running, if

the number of the Roman Pot X or Y layers with ≥ 6 hits was larger than 4, the event was rejected. Events rejected by this requirement are presumably due to hadron showers produced by beam halo particles interacting at the beam pipe or the Roman Pot detector wall. Furthermore, during the former part of the 1800 GeV Tevatron run (run $\leq$ 75678), additional requirements were imposed on the number of reconstructed vertices. For each event, vertex reconstruction is performed using primarily the information provided by the Vertex detector (VTX). The reconstructed vertices are ranked from class 5 to 12 on the basis of tracks associated with each vertex. In general, the larger the value of the class, the larger the number of tracks associated with the vertex. Events were required to have at least one vertex of class ≥ 5 in order to remove empty events associated with a beam halo particle detected in the Roman Pot spectrometer. In the meantime, events with more than one vertex of class 12 were rejected to remove multiple interaction events.

A total of about 1.3 million events were collected with the diffractive trigger at $\sqrt{s} = 630$ GeV in runs 74849−75110 (December 13−21, 1995) at an average instantaneous luminosity of $\langle \mathcal{L}_{inst} \rangle \approx 1.3 \times 10^{30}$ cm^{-2}s^{-1}. The 1800 GeV data sample used in this analysis was collected during the special low luminosity Tevatron running in runs 75644−75738 (January 18−23, 1996). About 3.1 million events were collected at an average instantaneous luminosity of $\langle \mathcal{L}_{inst} \rangle \approx 0.16 \times 10^{30}$ cm^{-2}s^{-1}. The data collected at low luminosities are good for diffraction studies because the rate of non-diffractive overlap background in which non-diffractive $p\bar{p}$ interactions are superimposed on a diffractive $p\bar{p}$ interaction occurring in the same bunch crossing is low. Since particles produced in the overlapping non-diffractive interactions fill the rapidity gap associated with diffractive interactions, non-diffractive overlap background events are

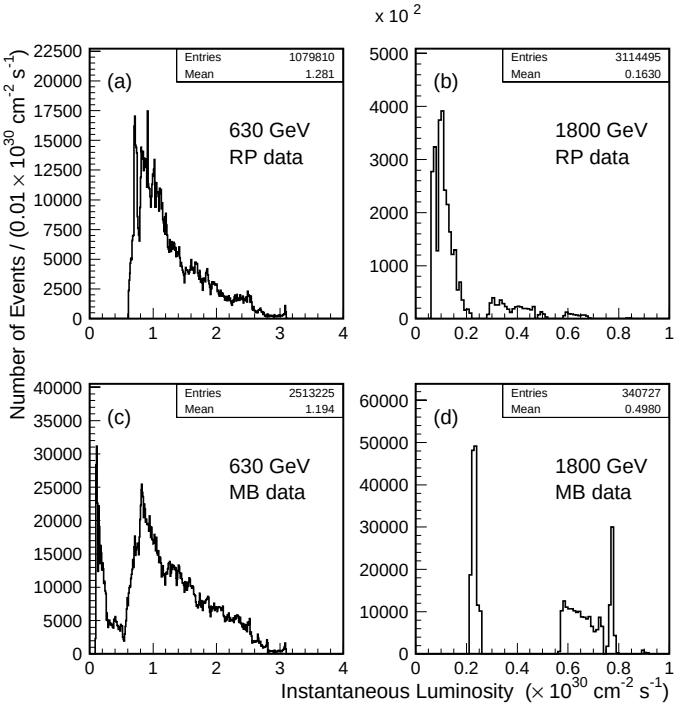

Figure 4.1: Instantaneous luminosity distributions for the (a) 630 GeV Roman Pot triggered data, (b) 1800 GeV Roman Pot triggered data, (c) 630 GeV minimum bias data, and (d) 1800 GeV minimum bias data.

inappropriate for diffraction studies. The instantaneous luminosity distributions for the 1800 and 630 GeV data samples are shown in Figure 4.1.

4.1.2 Non-Diffractive Data Samples

In order to compare diffractive events with non-diffractive events, non-diffractive data samples are also used in this analysis. Non-diffractive inclusive events were collected with a minimum bias trigger requiring a coincidence between two forward beam-beam counter (BBC) scintillation tile arrays. Approximately 2.5 million minimum bias events were collected with the Tevatron running at $\sqrt{s} = 630$ GeV in runs 74606−75110 (December 6−21, 1995) at typical luminosities $\langle \mathcal{L}_{inst} \rangle \approx 1.2 \times 10^{30}$ cm^{-2}s^{-1}. The 1800 GeV data sample used in this analysis was collected

during the special low luminosity Tevatron running in runs 75671−75712 (January 19−21, 1996) at an average instantaneous luminosity of $\langle \mathcal{L}_{inst} \rangle \approx 0.50 \times 10^{30}$ cm^{-2}s^{-1}. There are approximately 341,000 events in this sample. The instantaneous luminosity distributions for the 1800 and 630 GeV minimum bias data samples are shown in Figure 4.1.

4.2 Event Selection

4.2.1 Diffractive Inclusive Samples

The diffractive data samples collected with the diffractive trigger contain a fraction of events which are not appropriate for this analysis, such as events containing a cosmic-ray particle signal and events triggered by a beam halo particle in lieu of a quasielastically-scattered leading antiproton. These events are rejected by additional requirements described below.

Cosmic-Ray Background and Missing E_T

First, the COSFLT filter is applied to the data samples to reject background events mainly due to cosmic-ray particles, main ring splashes and calorimeter phototube discharges. This filter rejects events containing *out-of-time* energy in the Central Hadron calorimeter (CHA) and the EndWall Hadron calorimeter (WHA) above 6 GeV. The out-of-time energy is defined to be the energy outside of the time window of −20 to 35 ns for the CHA and −20 to 55 ns for the WHA with respect to the nominal proton-antiproton bunch crossing time. The background sources, such as cosmic-ray particles, main ring splashes and calorimeter phototube discharges, give signals to the CDF detector randomly in time; on the other hand, signals from proton-

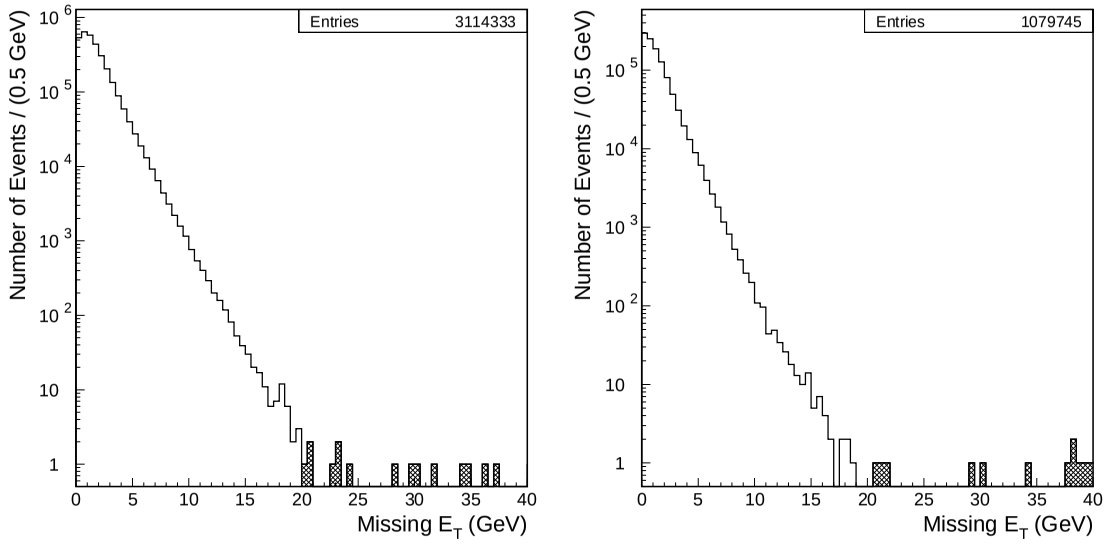

(a) 1800 GeV (b) 630 GeV

Figure 4.2: Missing E_T distributions for the (a) 1800 GeV and (b) 630 GeV data samples. The events in the cross-hatched regions are rejected by the selection cut $\not\!\!E_T \leq 20$ GeV.

antiproton interactions appear in the CDF detector right after the proton-antiproton bunch crossing time. Therefore, removing events containing a significant amount of energy deposited out of time with respect to the nominal proton-antiproton bunch crossing time reduces background events efficiently.

In-time cosmic-ray background events and background events with only electromagnetic energy will survive the COSFLT filter. To further reduce background events, a selection cut is imposed on missing E_T, $\not\!\!E_T$, which is defined as the magnitude of the vector sum of the transverse energy in the calorimeters. Figure 4.2 shows $\not\!\!E_T$ distributions for events which survive the COSFLT filter. The figure shows a fraction of events with large $\not\!\!E_T$ which are presumably background due to, e.g. cosmic-ray particles and phototube discharges. Only events with $\not\!\!E_T \leq 20$ GeV are retained for further analysis.

Event Vertex

Figure 4.3 shows distributions of the number of vertices of class ≥ 5 for the 1800 and 630 GeV data samples. There are no events in the zero bin of the left plot of Figure 4.3(a) because, in runs ≤ 75678 of data taking at $\sqrt{s} = 1800$ GeV, events were required to have at least one vertex of class ≥ 5 at the Level 3 trigger in order to remove empty events associated with beam halo particles.

In Figure 4.3(b), the fraction of events with zero vertices of class ≥ 5 is substantially reduced in the right plot since a certain amount of energy deposition on the east microplug calorimeter, covering $4.5 < \eta < 5.5$, was required at the Level 1 trigger in runs ≥ 75000 of data taking at $\sqrt{s} = 630$ GeV in order to reject empty events associated with beam halo particles. We select events with a single vertex of class ≥ 5 in order to remove events overlapped by non-diffractive events occurring in the same proton-antiproton bunch crossing and also empty events associated with beam halo particles.

Figure 4.4 shows z_{vtx} distributions. The z_{vtx} cut, $|z_{vtx}| \leq 60$ cm, is applied to ensure that the event is well contained within the CDF detector.

Roman Pot Track

ADC count distributions of the Roman Pot trigger counters are shown in Figure 4.5. Clear peaks are found around 400 ADC counts in the distributions of the individual trigger counters and around 1200 ADC counts in the total ADC count distributions of the three trigger counters, which correspond to the signal of a single minimum ionizing particle (MIP). To select events containing a single MIP detected in the Roman Pot trigger counters, each of the three Roman Pot trigger counters is required to have ADC counts greater than or equal to 250, and the total ADC counts of the

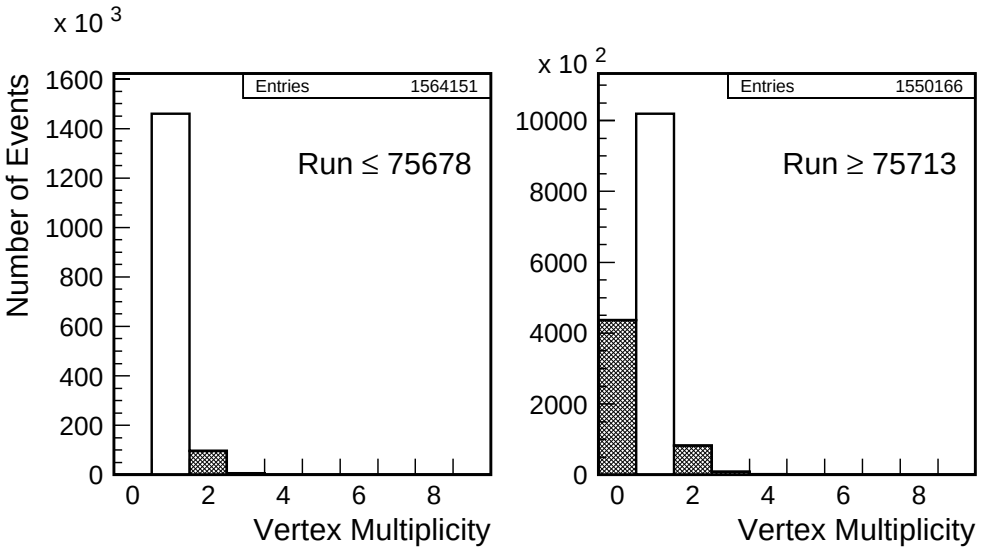

(a) 1800 GeV

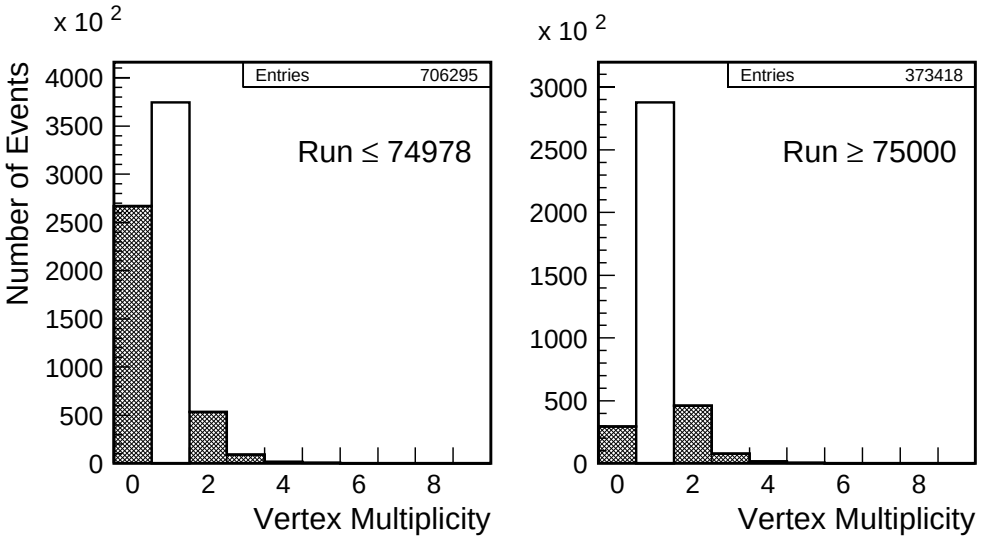

(b) 630 GeV

Figure 4.3: (a) Vertex multiplicity distributions for runs 75644−75678 (left) and 75713−75738 (right) of the 1800 GeV data sample. (b) Vertex multiplicity distributions for runs 74849−74978 (left) and 75000−75110 (right) of the 630 GeV data sample. The events in the cross-hatched regions are rejected by the single vertex cut.

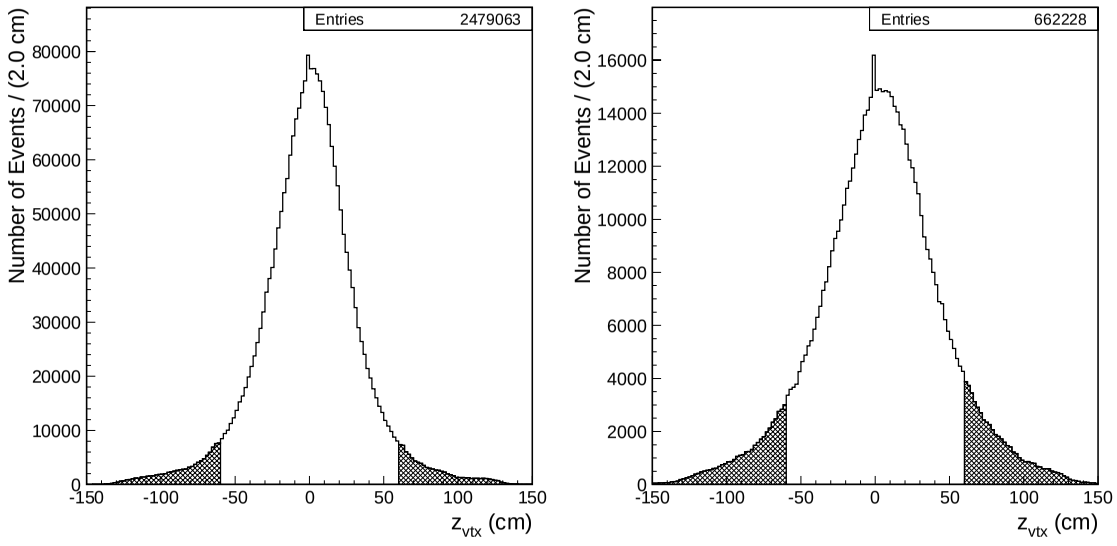

(a) 1800 GeV (b) 630 GeV

Figure 4.4: Distributions of z_{vtx} for the (a) 1800 GeV and (b) 630 GeV data samples. The events in the cross-hatched regions are removed by the z_{vtx} cut $|z_{vtx}| \leq 60$ cm.

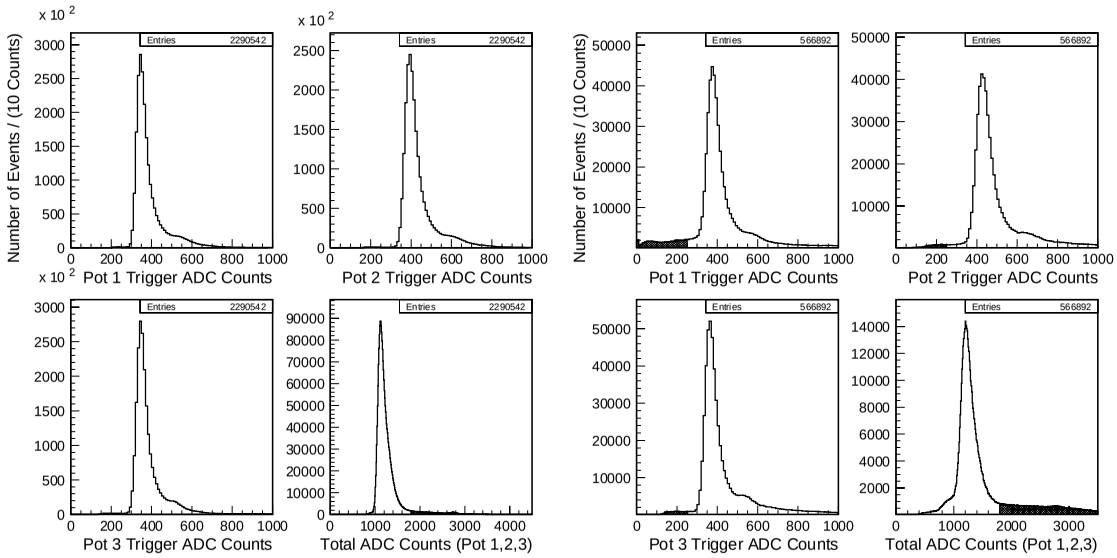

(a) 1800 GeV (b) 630 GeV

Figure 4.5: ADC count distributions of the three Roman Pot trigger counters and total ADC count distributions of the three trigger counters for the (a) 1800 GeV and (b) 630 GeV data samples. The events in the cross-hatched regions are removed by the 1 MIP cut, i.e. $\mathrm{ADC}_i \geq 250$ ($i = 1, 2$ and 3) and $\Sigma_{i=1}^{3}\mathrm{ADC}_i \leq 1800$.

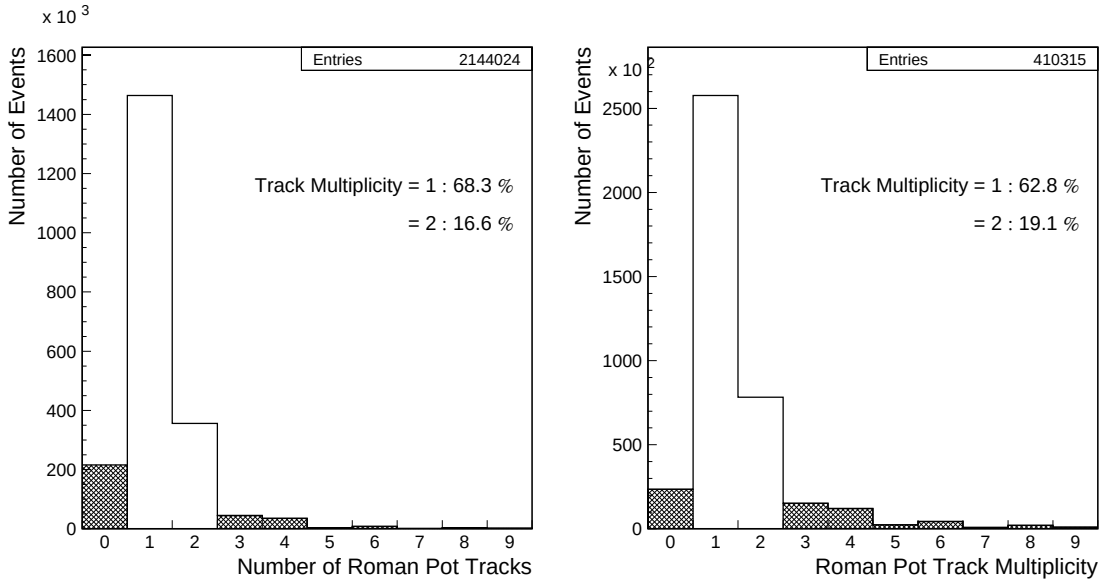

(a) 1800 GeV (b) 630 GeV

Figure 4.6: Reconstructed Roman Pot track multiplicity distributions for the (a) 1800 GeV and (b) 630 GeV data samples. Only the events with one or two Roman Pot tracks are used in this analysis. For events with two tracks, the track with the smaller χ^2 is used to reconstruct ξ and t values.

three Roman Pot trigger counters is required to be smaller than or equal to 1800.

Figure 4.6 shows reconstructed Roman Pot track multiplicity distributions; 68.3 (62.8) % of events have only one reconstructed Roman Pot track, but 16.6 (19.1) % of events contain two Roman Pot tracks in the 1800 (630) GeV data sample. As explained in Appendix C, when two reconstructed tracks are present, one of them is usually due to optical cross talk in the Roman Pot fiber tracking detector. We select events with one or two Roman Pot tracks. In the case of events with two Roman Pot tracks, the track with the smaller χ^2 is used to reconstruct ξ and t values. For events with two Roman Pot tracks in the 630 GeV data sample, the two tracks are required to be adjacent. More details are provided in Appendix C.

The hit patterns of Roman Pot tracks for the 630 GeV data sample are shown in

Table 4.1: Dead channels of the Roman Pot fiber tracking detectors. All the dead channels on the Pot 1 X detector were fixed before the 1800 GeV run started.

Run # ($\sqrt{s}$ energy)	Dead channels		
	Pot 1 X	Pot 1 Y	Pot 2 Y
74849−74978 (630 GeV)	10−12,16−22,24−28,32−38,40−44 48−54,56−64,68−74,76−78	20−22,76−78	10−12
75000−75049 (630 GeV)	10−12,16−18,24−28 40−44,60−64		
75109−75110 (630 GeV)	10−12,24−28 40−44,60−64		
75644−75738 (1800 GeV)			

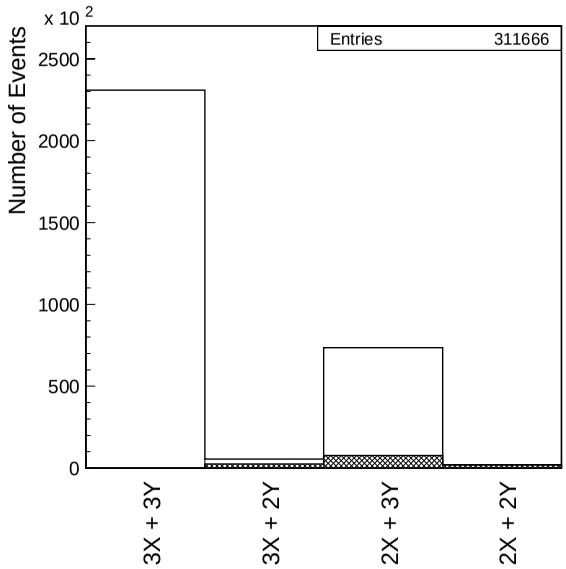

Figure 4.7: The hit pattern of Roman Pot tracks for the 630 GeV data sample. "$3X + 3Y$" is for tracks which have hits on three Roman Pots both in X and Y directions. "$3X + 2Y$" ("$2X + 3Y$") is for tracks which have hits on three Roman Pots in X (Y) and on two Roman Pots in Y (X). "$2X + 2Y$" is for tracks which have hits only on two Roman Pots both in X and Y directions. In the 630 GeV data sample, in addition to events with a $3X + 3Y$ track, events with a $3X + 2Y$ ($2X + 3Y$) track are also retained for further analysis if the track points to one of the dead channel positions of the Roman Pot fiber detector on which the track does not have a hit. The events in the cross-hatched areas are rejected by these requirements.

Figure 4.7. In the 630 GeV data sample, approximately 26 % of Roman Pot tracks have hits only on two Roman Pot detectors in the X and/or Y directions. This is because the Roman Pot fiber tracking detectors had sizable numbers of dead channels during the 630 GeV run, as shown in Table 4.1 (especially the X detector of Roman Pot 1). In the 1800 GeV data sample, only events with Roman Pot tracks having hits on both the X and Y tracking detectors of each of the three Roman Pot stations are accepted for further analysis. In the 630 GeV data sample, we accept events with Roman Pot tracks having

(a) hits on three Roman Pot detectors both in X and Y directions, or

(b) hits on three Roman Pot detectors in X (Y) direction and on two detectors in Y (X) direction.

It is found that a large fraction of tracks with two hits are concentrated in the vicinity of the dead channel positions as shown in Figure 4.8; such tracks are most likely due to real leading antiprotons. On the other hand, tracks not close to dead channels are probably due to detector noise and are thus removed from the data sample.

Figure 4.9 shows the θ_X^{RP} distribution for the 630 GeV data sample, where θ_X^{RP} is the angle of a reconstructed Roman Pot track with respect to the beam line in the horizontal direction. When an antiproton is bent toward the inside of the Tevatron ring, θ_X^{RP} is positive. Since quasielastically-scattered leading antiprotons carry slightly less momentum than beam antiprotons, they get bent toward the inside of the Tevatron ring by the dipole magnets, and are thus expected to have positive θ_X^{RP}. Nevertheless, a small peak is found in the negative θ_X^{RP} region. The west BBC and forward calorimeter (FCAL) tower multiplicities for events with $\theta_X^{RP} \geq 0$ and $\theta_X^{RP} < 0$ are shown in Figure 4.10. Events with $\theta_X^{RP} < 0$ have much higher multiplicities in the

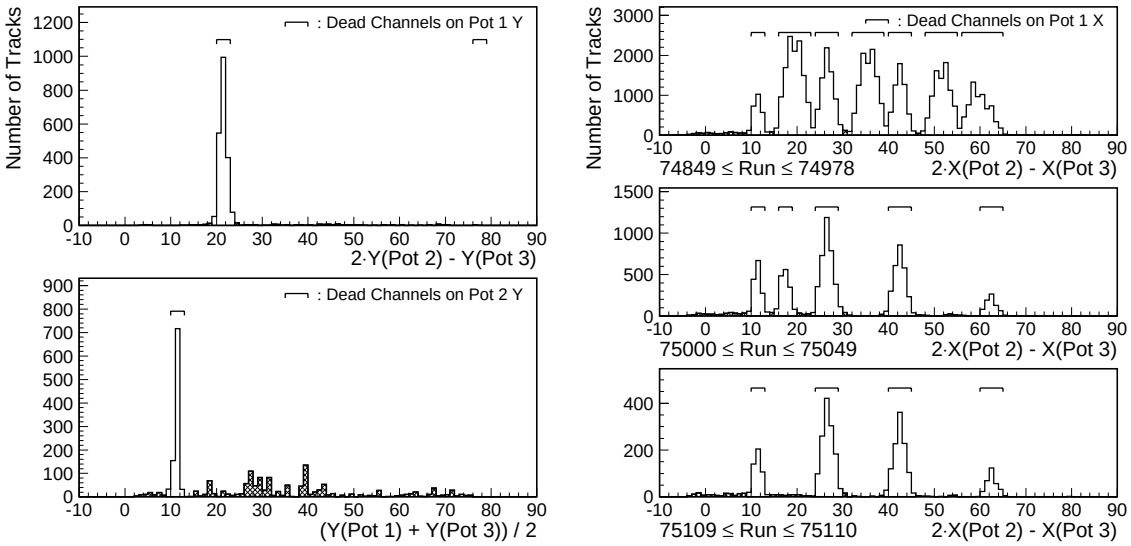

Figure 4.8: Distributions of *two-hit* Roman Pot tracks in the fiber detectors in which the reconstructed Roman Pot track does not have hits. The two-hit tracks are concentrated near the dead channels. The Roman Pot tracks in the cross-hatched regions do not point to any of the dead channels and are thus rejected since they are most likely due to detector noise.

west BBC and FCAL, indicating that they are dominated by non-diffractive events associated with beam halo particles. Events with $\theta_X^{RP} < 0$ are rejected from the diffractive data samples. This requirement does not remove any events from the region $0.035 \leq \xi \leq 0.095$ which is used in the following sections; events with $\theta_X^{RP} < 0$ always have $\xi < 0.035$.

Diffractive Variables ξ and t

The fractional momentum loss ξ and four-momentum transfer squared t of the antiproton are reconstructed from the Roman Pot track, the transport matrix between the Roman Pot spectrometer and the collision point, and z_{vtx} as described in Appendix A. Distributions of reconstructed ξ and $|t|$ are shown in Figure 4.11. Figure 4.12 shows distributions of inclusive single diffractive events as a function of ξ and $|t|$. Events with ξ and t within $0.035 \leq \xi \leq 0.095$ and $|t| \leq 1.0$ GeV^2 in the 1800

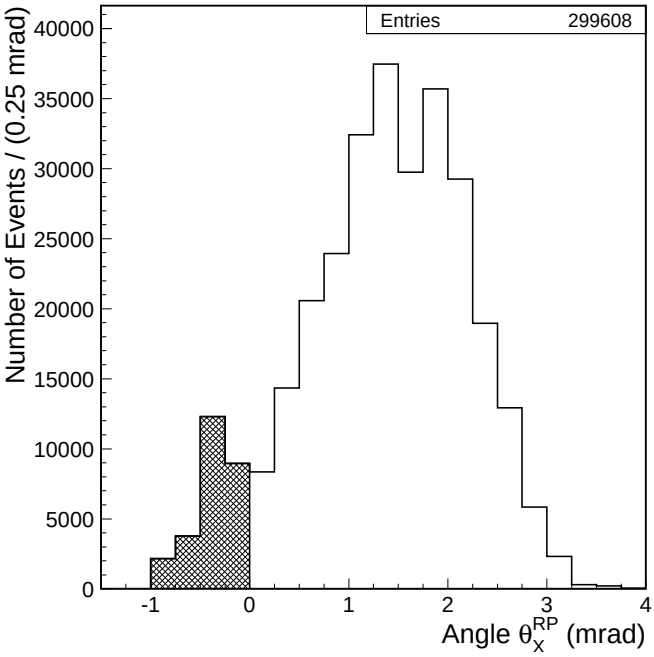

Figure 4.9: The distribution of the angle θ_X^{RP} of the reconstructed tracks with respect to the beam line in the horizontal direction. When the antiproton is bent toward the inside of the Tevatron ring, θ_X^{RP} is positive.

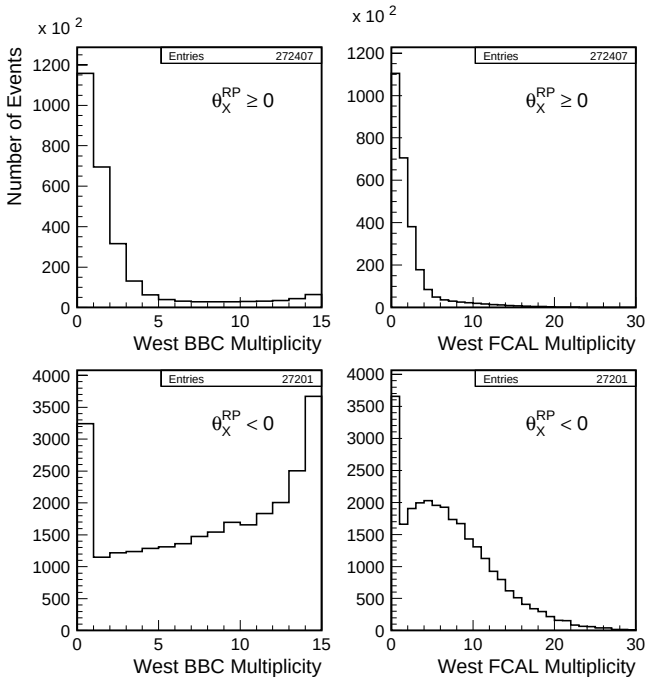

Figure 4.10: West BBC multiplicity (left) and FCAL tower multiplicity (right) distributions for events in the 630 GeV data sample with $\theta_X^{RP} \geq 0$ (top) and $\theta_X^{RP} < 0$ (bottom).

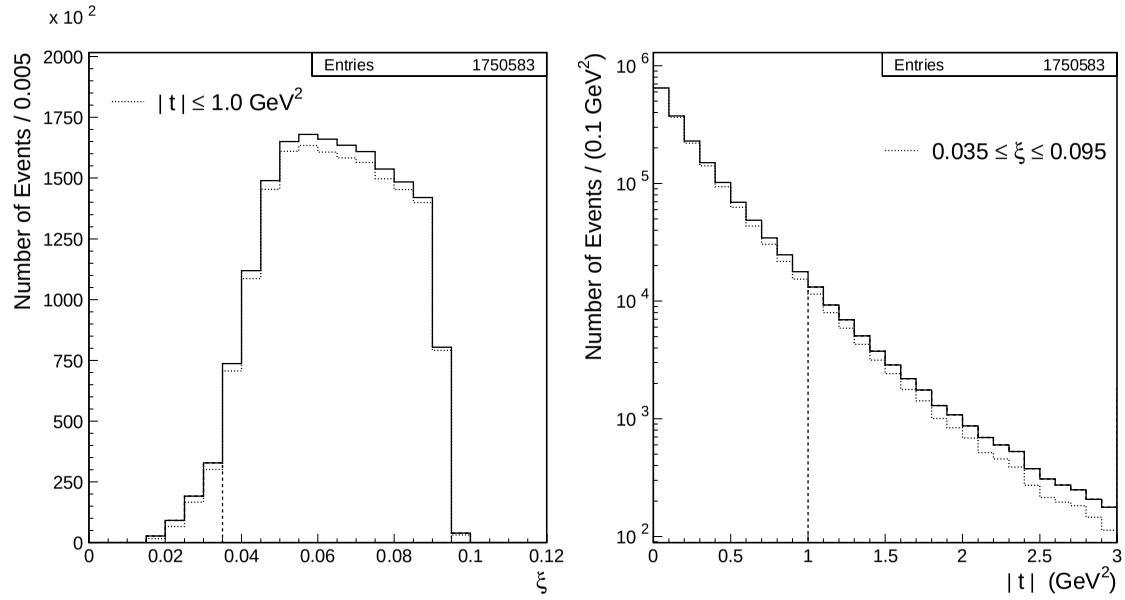

(a) 1800 GeV

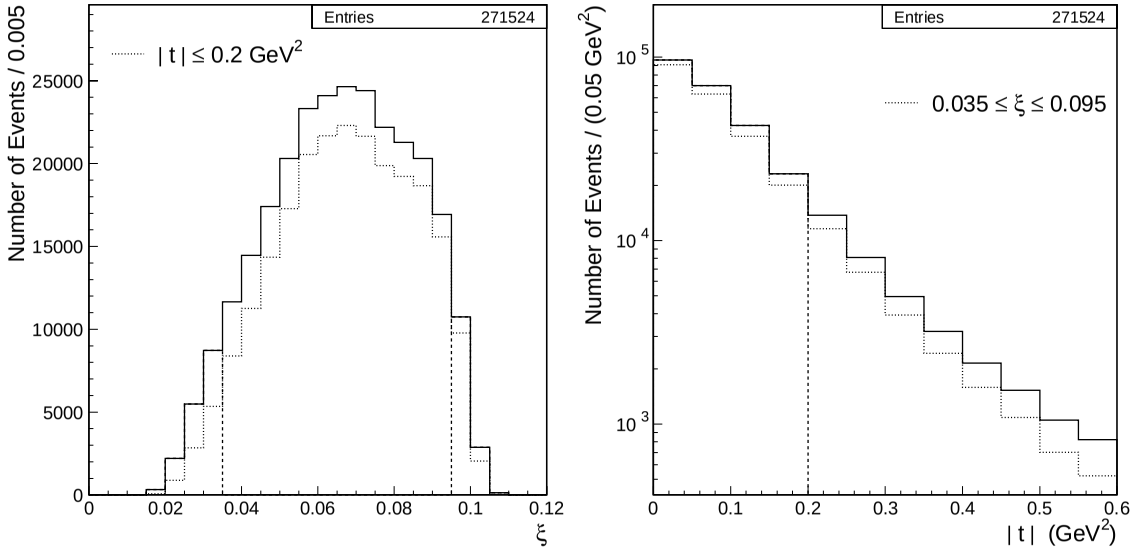

(b) 630 GeV

Figure 4.11: Reconstructed ξ (left) and $|t|$ (right) distributions for the (a) 1800 GeV and (b) 630 GeV data samples. The vertical dashed lines indicate the accepted regions of $0.035 \leq \xi \leq 0.095$ and $|t| \leq 1.0$ GeV^2 for the 1800 GeV data sample and $|t| \leq 0.2$ GeV^2 for the 630 GeV data sample. The dotted lines are ξ distributions after the t acceptance cut or t distributions after the ξ acceptance cut.

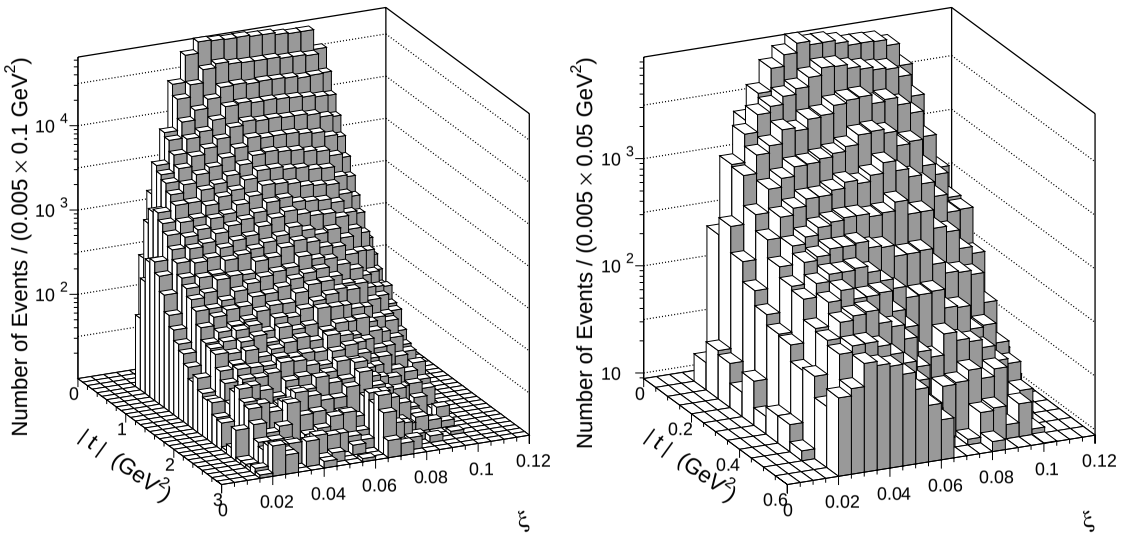

(a) 1800 GeV (b) 630 GeV

Figure 4.12: Distributions of inclusive single diffractive events as a function of ξ and $|t|$ in the (a) 1800 GeV and (b) 630 GeV data samples.

GeV data sample and within $0.035 \leq \xi \leq 0.095$ and $|t| \leq 0.2$ GeV^2 in the 630 GeV data sample are selected for further analysis. The 1800 GeV data sample is restricted to the region $|t| \leq 0.2$ GeV^2 when it is compared with the 630 GeV data sample in Section 5.4. Figure 4.13 shows ξ and $|t|$ distributions corrected for the Roman Pot acceptance.

Non-Diffractive Overlap Background

Despite the single vertex cut applied to both the 1800 and 630 GeV data samples to remove diffractive events overlapped by non-diffractive events occurring in the same bunch crossing, a small fraction of non-diffractive overlap background events still remains in the data samples. The 630 GeV data sample was collected at higher instantaneous luminosities than the 1800 GeV data sample and thus contains a larger fraction of residual non-diffractive overlap background events. The overlapping non-

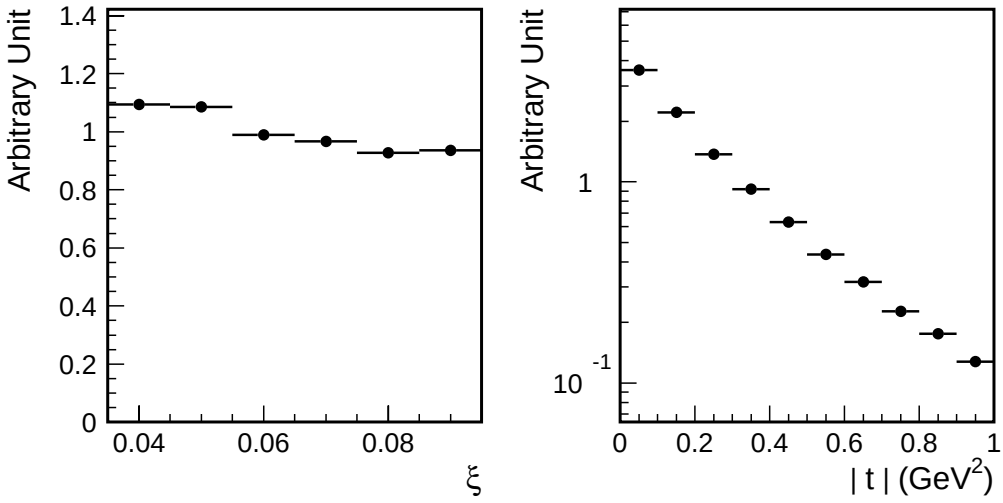

(a) 1800 GeV

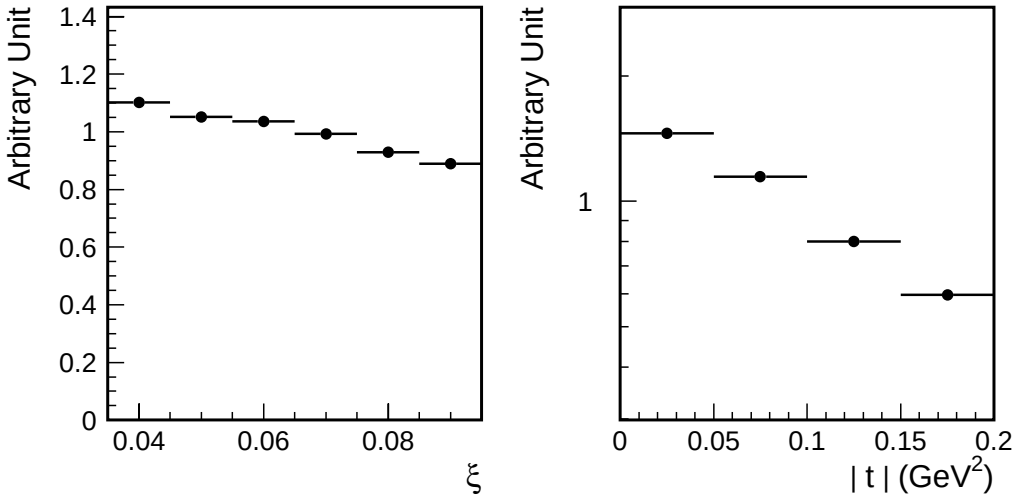

(b) 630 GeV

Figure 4.13: Distributions of ξ (left) and $|t|$ (right) for the (a) 1800 GeV and (b) 630 GeV diffractive inclusive samples. These distributions are corrected for the Roman Pot acceptance.

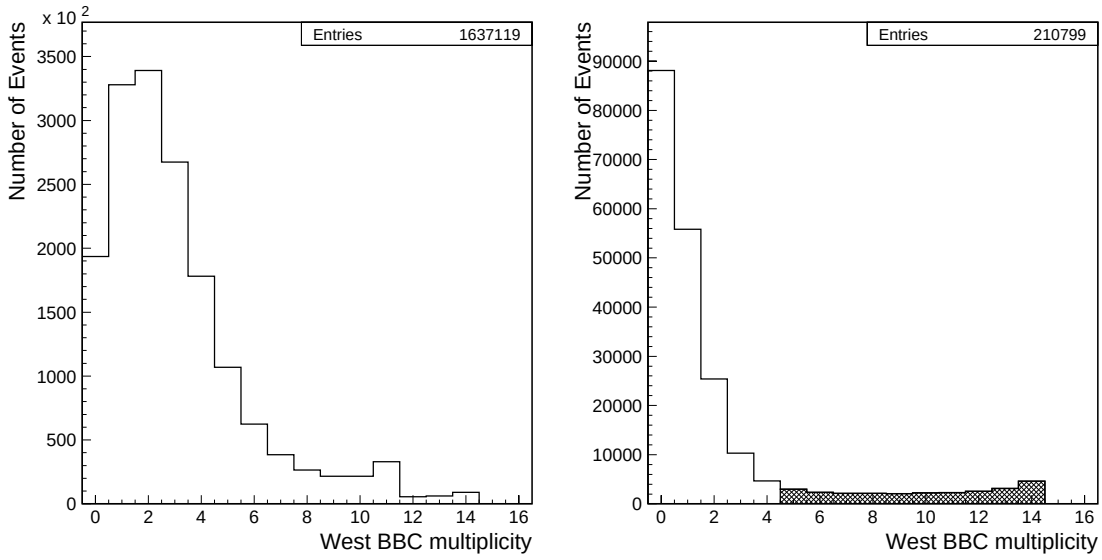

(a) 1800 GeV (b) 630 GeV

Figure 4.14: West BBC multiplicity distributions for the (a) 1800 GeV and (b) 630 GeV data samples. In the 630 GeV data sample, events with west BBC multiplicity ≥ 5 are removed from the data sample.

diffractive interactions spoil the rapidity gap signature expected in the forward region on the antiproton outgoing side (west side). Figure 4.14 shows west BBC multiplicity distributions. In 36 % (64 %) of events in the 1800 GeV data sample, two (five) counters of the west BBC and one (four) counter(s) of the east BBC were not read out. In the 630 GeV data sample, two counters of the west BBC and one counter of the east BBC were not read out. Therefore, although the west BBC array consists of 16 counters, the number of BBC hits does not reach 16 in Figure 4.14. For the 630 GeV data sample, in order to reduce the residual non-diffractive overlap background events, we remove events with west BBC multiplicity ≥ 5. For the 1800 GeV data sample, no selection cut is imposed on the west BBC multiplicity; however, each diffractive distribution in Chapter 5 is corrected for the residual background events by subtracting the corresponding non-diffractive distribution normalized to the non-diffractive over-

lap background fraction estimated from the analysis of the west BBC and forward calorimeter tower multiplicities in Section 4.3.2. Events which flow through the above selection criteria comprise the *diffractive inclusive samples.*

4.2.2 Non-Diffractive Inclusive Samples

Non-diffractive inclusive data samples collected with the minimum bias trigger are refined by the COSFLT filter, and the $\not\!\!E_T$ and z_{vtx} cuts. Figure 4.15 shows $\not\!\!E_T$ distributions for the minimum bias data samples. We select events with $\not\!\!E_T \leq 20$ GeV, as was done for the diffractive data samples. Figure 4.16 shows z_{vtx} distributions. The z_{vtx} cut, $|z_{vtx}| \leq 60$ cm, is applied to ensure that the event is well contained within the CDF detector. Approximately 0.3 million and 2.1 million events survive the selection criteria shown above in the 1800 and 630 GeV data samples, respectively. These events comprise the *non-diffractive inclusive samples.*

4.2.3 Jet Clustering Algorithm

The standard CDF jet clustering algorithm [64] is an *iterative cone algorithm* which uses a cone with a fixed radius in η-ϕ space to define a jet. The clustering is implemented in the standard CDF routine JETCLU. The clustering procedure consists of three steps: preclustering, clustering, and merging.

Preclustering

The clustering begins with creating a list of calorimeter towers with $E_T \geq 1.0$ GeV which are used as seed towers for jets. The seed towers are stored in order of decreasing E_T. The tower segmentation in azimuthal angle is 5° in the endplug and forward calorimeters, but it is 15° in the central and endwall calorimeters. Therefore, towers in

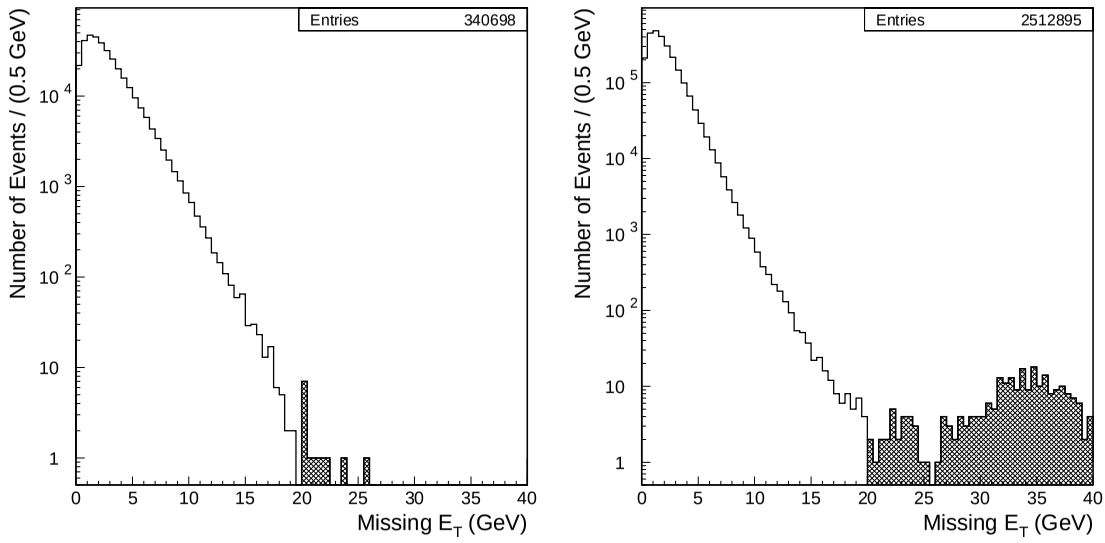

(a) 1800 GeV (b) 630 GeV

Figure 4.15: Distributions of $\not\!\!E_T$ for the (a) 1800 GeV and (b) 630 GeV minimum bias data samples. The events in the cross-hatched region are rejected by the selection cut $\not\!\!E_T \leq 20$ GeV.

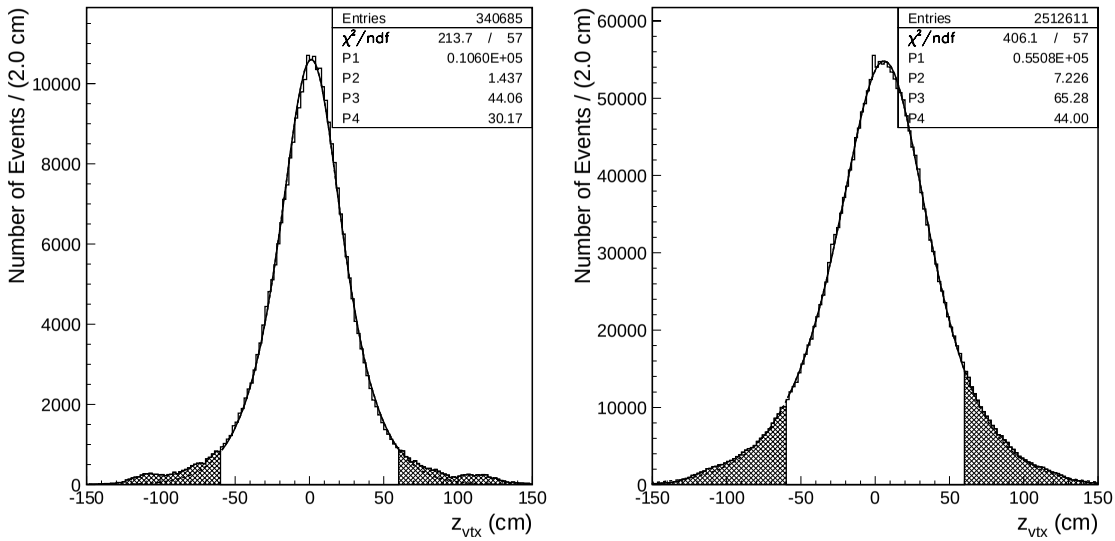

(a) 1800 GeV (b) 630 GeV

Figure 4.16: Distributions of z_{vtx} for the (a) 1800 GeV and (b) 630 GeV minimum bias data samples. The distributions are fitted to the form $C \cdot e^{\frac{-z^2}{2 \cdot \sigma_z^2}} \Big/ \left(1 + \frac{(z - z_{min})^2}{\beta^{*2}}\right)$, where $C = P1$, $z_{min} = P2$, $\sigma_z = P3$ and $\beta^* = P4$. The events in the cross-hatched region are removed by the selection cut $|z_{vtx}| \leq 60$ cm.

the endplug and forward regions are grouped together to have the same segmentation as the central and endwall calorimeters. Preclusters are formed by combining adjacent seed towers within a cone of radius R in η-ϕ space. A seed tower is incorporated into a precluster if it is within the radius R of a seed tower with higher E_T which is already assigned to the precluster. In this analysis, the radius R is set to 0.7 [2].

Clustering

Following the preclustering procedure, jet clustering is performed using the true tower segmentation. Jet clustering uses the E_T weighted centroid of a precluster $(\eta_{centroid}, \phi_{centroid})$,

$$\begin{aligned} \eta_{centroid} &= \frac{\sum_{i=1}^{n} E_T^i \eta^i}{\sum_{i=1}^{n} E_T^i}, \\ \phi_{centroid} &= \frac{\sum_{i=1}^{n} E_T^i \phi^i}{\sum_{i=1}^{n} E_T^i}, \end{aligned} \tag{4.1}$$

where the sums are carried out over all the seed towers in the precluster. The tower centroid (η^i, ϕ^i) is obtained by

$$\begin{aligned} \eta^i &= \frac{E_{T\,i}^{EM} \eta_i^{EM} + E_{T\,i}^{HA} \eta_i^{HA}}{E_T^i}, \\ \phi^i &= \frac{E_{T\,i}^{EM} \phi_i^{EM} + E_{T\,i}^{HA} \phi_i^{HA}}{E_T^i}, \end{aligned} \tag{4.2}$$

where $E_{T\,i}^{EM}$ and $E_{T\,i}^{HA}$ are transverse energies deposited in the electromagnetic (EM) and hadronic (HA) parts of a calorimeter tower with index i. $(\eta_i^{EM}, \phi_i^{EM})$ and $(\eta_i^{HA}, \phi_i^{HA})$ are the centroids of the electromagnetic and hadronic components of tower i, defined by a vector pointing from the event vertex to the center of the calorimeter tower (calculated at the depth that corresponds to shower maximum).

[2] In comparisons with results from the UA8 collaboration described in Section 5.7, a cone size of $R = 1.0$ is used to correspond to the cone size used by the UA8 collaboration.

We use Eq. (4.2) to determine η and ϕ of calorimeter towers, because event vertices are not necessarily positioned at the geometric center of the CDF detector, which is the position of $z = 0$ in the CDF coordinate system.

A cone of radius R in η-ϕ space is created around the centroid of a cluster. Then, all the towers with $E_T \geq 100$ MeV are incorporated into the cluster if the towers are within the cone. A new cluster centroid is determined from the towers within the cone using an E_T weighted centroid, and a new cone is created using the new cluster centroid. This process continues until the tower list remains unchanged.

Merging

At the stage of clustering, some towers may be shared by more than one cluster. If towers of one cluster are completely contained within another cluster, the smaller cluster is dropped. If two clusters partially overlap, an overlap fraction is computed by summing the E_T of the shared towers and dividing it by the E_T of the smaller cluster. If the fraction is above a cutoff value of 0.75, then the two clusters are merged. If the fraction is less than the cut threshold, the clusters are kept unchanged and the shared towers are assigned to the nearest cluster in η-ϕ space. After the towers are assigned uniquely to clusters, the centroid computation and tower shuffling are repeated until the tower lists stay unchanged.

4.2.4 Jet Energy Correction

The *uncorrected* energies of jets identified by the above iterative cone algorithm are different from the true energies of the partons which initiated the jets for a variety of reasons. Some of them result from physics processes:

- Energy of particles which do not originate from the hard scattering process is

included in the jet energy if the particles are located within the clustering cone of the jet. The energy of this source is often referred to as the *underlying event* energy.

- Some particles associated with the hard scattering which produced the jet may deposit energy outside the jet cone. The leaked energy is termed the *out-of-cone* energy.

Others are due to limitations in detector performance:

- The calorimeter response to charged pions shows a non-linearity for momenta below 10 GeV [64].

- Charged particles with $p_T \lesssim 400$ MeV curl in the tracking volume due to the solenoidal magnetic field and do not reach the calorimeters. At slightly higher p_T, the magnetic field may bend particles outside the jet cone.

- Particles which shower in boundary regions between calorimeter modules or regions between the central, endplug and forward calorimeters yield a smaller energy response than those in uniform calorimeter regions.

A jet correction function [64, 65] was constructed to take these effects into account. This function incorporates the following corrections:

Relative Correction

The relative jet correction takes into account non-uniformities in the calorimeter response as a function of jet η. The energies of jets in the endplug and forward regions are scaled to give the energy of the equivalent jet in the central calorimeter. The correction is derived from dijet events with at least one jet in the central region.

By requiring the p_T of the central jet and the p_T of the other jet to balance, the correction factor is obtained as a function of jet p_T and η.

Absolute Correction

The absolute jet correction aims at relating as closely as possible the energy of a clustered jet to the total true energy of particles inside the jet cone. The correction is derived using the Monte Carlo event generator ISAJET [66], which is based on the Field-Feynman parametrization of fragmentation [67]. After fragmentation, the generated events are passed through a CDF detector simulation called QFL. The QFL simulation is tuned to reproduce the response of the CDF calorimeters to individual particles using test beam results and *in situ* measurements of isolated pions in minimum bias events. After the generated events are processed with the QFL simulation, jets are reconstructed as if they were real jets in data. The uncorrected jet p_T is compared to the sum of the true p_T of all generated particles lying in a cone centered at the measured jet axis and originating from the primary partons. A quadratic polynomial fit is used to parametrize the mean jet response as a function of jet E_T.

Underlying Event Correction

The underlying event correction takes into account the energy due to the underlying event, i.e. the energy due to fragmentation of partons which are not associated with the hard scattering. In order to extract the jet energy originating from the hard scattering, the contribution of the underlying event to the jet energy must be subtracted. Since in diffractive events a large fraction of proton-antiproton interaction energy is carried away by the leading proton or antiproton, the underlying event energy is expected to be lower than in non-diffractive events.

The underlying event energy in dijet events is generally expected to be similar

Table 4.2: Underlying event E_T subtracted from jet E_T in this analysis.

	Diffractive		Non-diffractive	
	1800 GeV	630 GeV	1800 GeV	630 GeV
Underlying event E_T (GeV)	0.54	0.50	1.16	0.91

to the average energy level in soft interaction events. In this analysis, the underlying event E_T to be subtracted from the E_T of diffractive and non-diffractive jets is estimated by measuring the E_T in a randomly chosen cone with radius $R = 0.7$ in the diffractive and non-diffractive inclusive samples, respectively. Then, the E_T is multiplied by a canonical correction factor of 1.6 to account for the non-linearity of the CDF calorimeters in the low E_T region. The results are summarized in Table 4.2.

Out-of-Cone Correction

The out-of-cone correction accounts for energy that leaks outside the jet cone due to fragmentation effects and soft gluon radiation. In order to correct for out-of-cone energy, a small amount of energy which is parametrized as a function of jet p_T is added to the jet. The amount of energy is determined from the Monte Carlo event generator used to derive the absolute jet energy correction. For jets with radius of $R = 0.7$, the out-of-cone E_T is approximately 1.6 GeV at jet p_T of 7 GeV.

4.2.5 Dijet Event Samples

Events in the diffractive and non-diffractive inclusive samples are passed through the jet clustering routine JETCLU. Then, the jet correction function is applied to all the jets reconstructed by JETCLU. Fake jets due to calorimeter noise are removed using a *hot tower filter* (HTFLT), which is described in Appendix D. Diffractive and

non-diffractive dijet candidate event samples are selected from the diffractive and non-diffractive inclusive samples, respectively, by requiring the corrected E_T of the next-to-leading jet to be larger than 7 GeV. In the comparisons between 1800 GeV and 630 GeV results described in Section 5.4, an additional cut is imposed on the average E_T of the leading two jets, requiring $E_T^* = (E_T^{jet1} + E_T^{jet2})/2 \geq 10$ GeV, where E_T^{jet1} and E_T^{jet2} are the transverse energies of the leading and next-to-leading jets, respectively. Samples of events with two or more jets with $E_T \geq 10$ or 15 GeV are also used in this analysis.

These event selections are summarized in Tables 4.3 and 4.4. The diffractive dijet candidate events which pass all the selection requirements comprise the *diffractive dijet samples*, although these samples still contains a small fraction of non-diffractive overlap background events. The non-diffractive dijet candidate events comprise the *non-diffractive dijet samples*. Figures 4.17 and 4.18 show diffractive dijet candidate events in the CDF calorimeters and the Roman Pot spectrometer in the 1800 and 630 GeV data samples, respectively.

4.3 Background Fractions and Event Selection Efficiencies

When the single diffractive (SD) dijet samples are normalized to the corresponding cross section, the following background fractions and selection cut efficiencies must be taken into account:

- Beam-gas background.
- Non-diffractive overlap background.

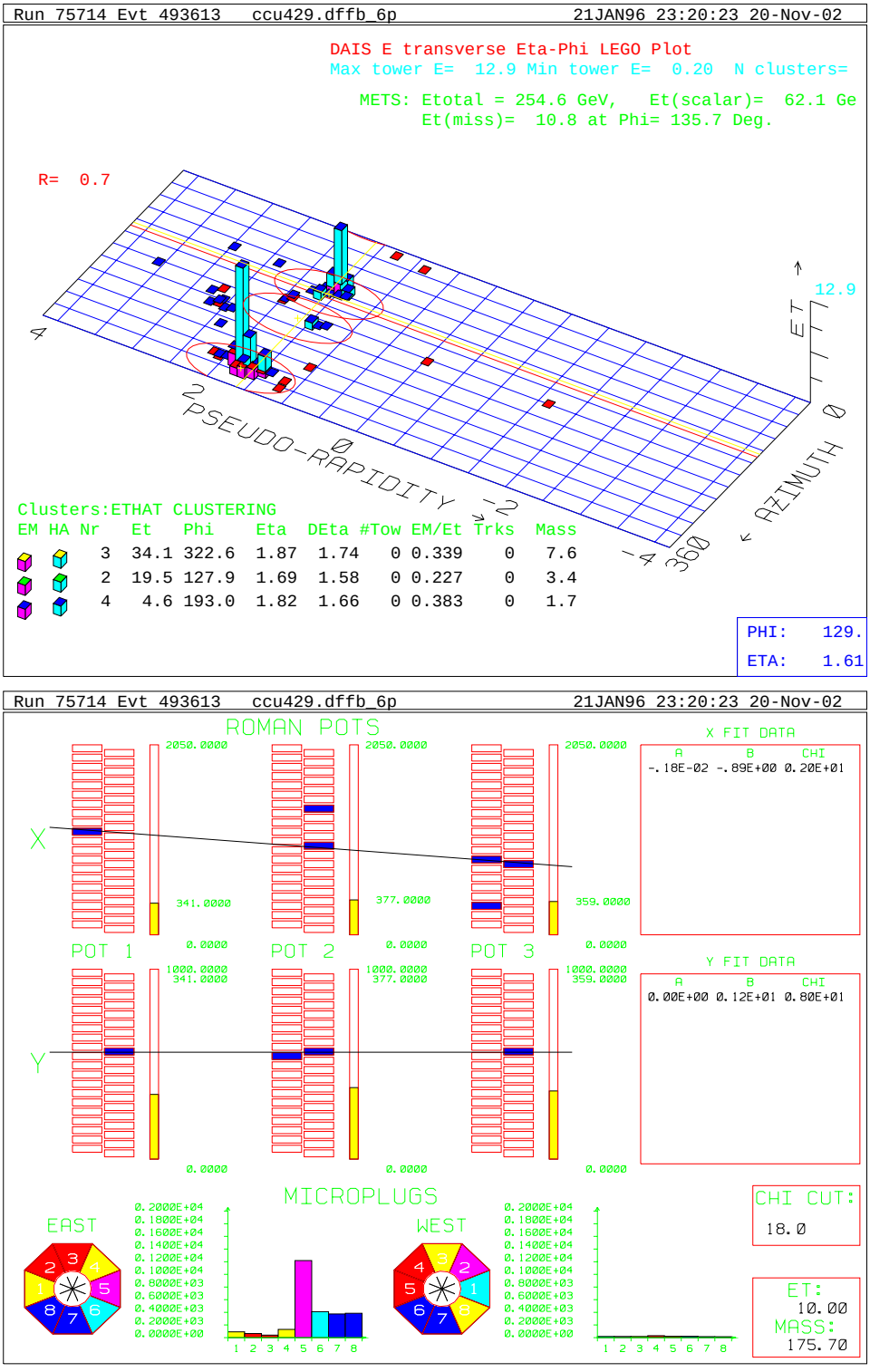

Figure 4.17: A diffractive dijet candidate event in the 1800 GeV data sample. In this event, the reconstructed ξ and t are $\xi = 0.072$ and $t = -0.01$ GeV^2, respectively. The west BBC multiplicity is one, and the west FCAL tower multiplicity is zero.

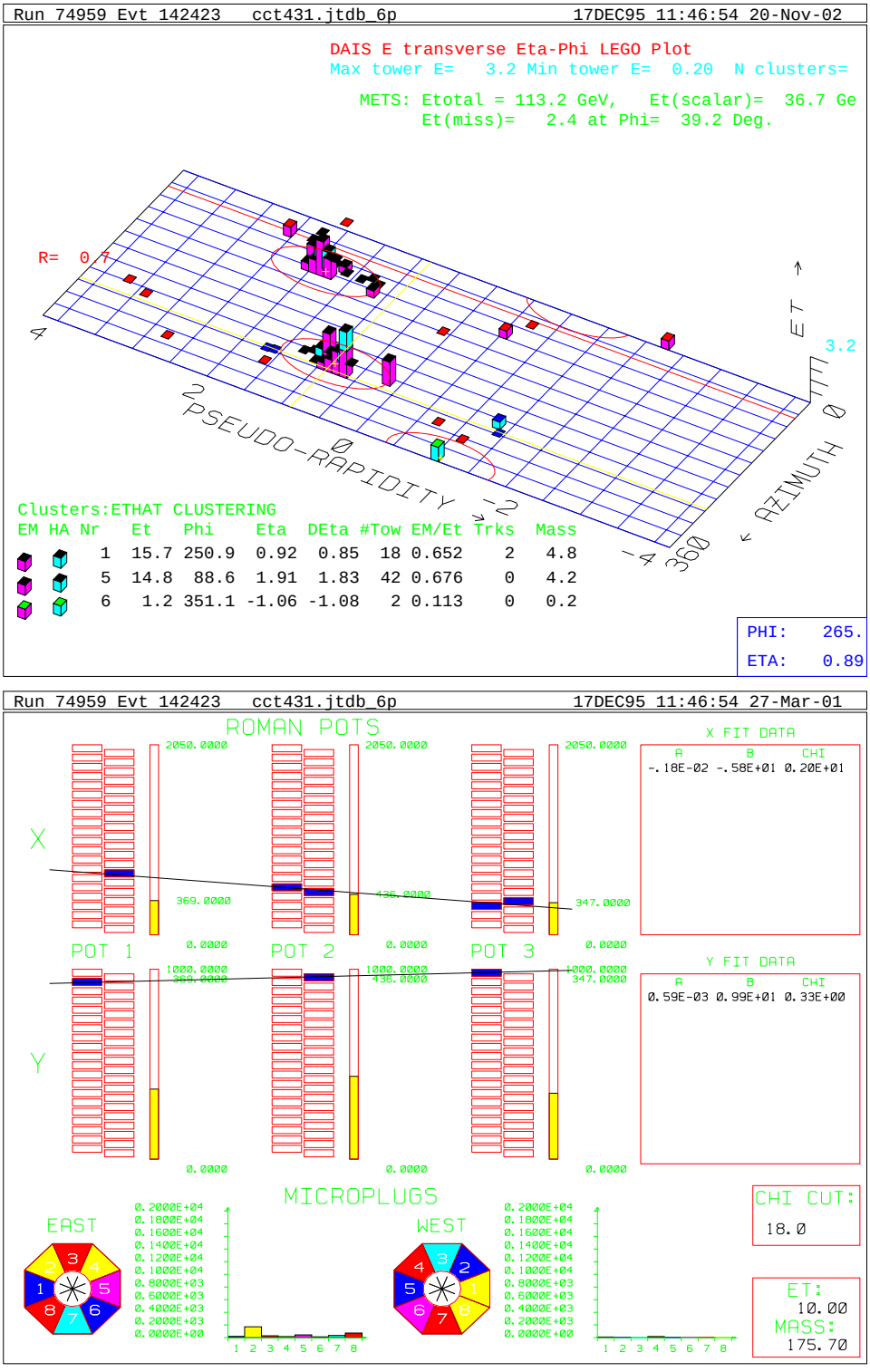

Figure 4.18: A diffractive dijet candidate event in the 630 GeV data sample. In this event, the reconstructed ξ and t are $\xi = 0.085$ and $t = -0.09$ GeV^2, respectively. The west BBC and FCAL tower multiplicities are both zero.

Table 4.3: Number of Roman Pot triggered events after each selection cut.

	Number of events	
	1800 GeV data	630 GeV data
Total triggered events	3,114,495	1,079,810
COSFLT	3,114,333	1,079,745
$\not\!\!E_T \leq 20$ GeV	3,114,317	1,079,713
Single vertex (class ≥ 5) cut	2,479,063	662,228
$\lvert z_{vtx} \rvert \leq 60$ cm	2,290,542	566,892
For Roman Pot track		
1 MIP cuts*	2,144,024	410,315
1 or 2 reconstructed tracks	1,819,551	335,891
Track hit pattern cut	1,758,879	299,608
$\theta_X^{RP} \geq 0$	1,750,829	272,407
For diffractive variables ξ and t		
ξ and t are reconstructed	1,750,583	271,524
Roman Pot acceptance cut**	1,638,695	210,799
Low multiplicity cut		
West BBC multiplicity ≤ 4	N/A	184,327
For jets		
Number of jets ≥ 2	132,971	7,256
Hot tower filter	108,680	7,211
≥ 2 jets with $E_T \geq 7$ GeV	30,410	1,186
$(E_T^{jet1} + E_T^{jet2})/2 \geq 10$ GeV	10,945	283
≥ 2 jets with $E_T \geq 10$ GeV	5,508	118
≥ 2 jets with $E_T \geq 15$ GeV	633	7

* Trigger counter $\text{ADC}_i \geq 250$, $\sum_i \text{ADC}_i \leq 1800$, $i = 1, 2$ and 3

** $0.035 \leq \xi \leq 0.095$, $\lvert t \rvert \leq 1.0$ (0.2) GeV^2 for the 1800 (630) GeV data sample

- West BBC multiplicity cut efficiency (only for the 630 GeV data).
- Single vertex cut efficiency.
- Hot tower filter efficiency.

These backgrounds and efficiencies are estimated from an analysis of multiplicities in forward detectors such as the BBC and forward calorimeter (FCAL). The FCAL tower multiplicity is obtained by counting the number of calorimeter towers with

Table 4.4: Number of non-diffractive events after each selection cut.

	Number of events	
	1800 GeV data	630 GeV data
Total triggered events	340,727	2,513,225
COSFLT filter	340,698	2,512,895
$\not\!\!E_T \leq 20$ GeV	340,685	2,512,611
$\lvert z_{vtx} \rvert \leq 60$ cm	299,959	2,050,428
For jets		
Number of jets ≥ 2	91,600	351,825
Hot tower filter	73,189	351,039
≥ 2 jets with $E_T \geq 7$ GeV	32,629	104,793
$(E_T^{jet1} + E_T^{jet2})/2 \geq 10$ GeV	17,134	34,887
≥ 2 jets with $E_T \geq 10$ GeV	10,514	16,866
≥ 2 jets with $E_T \geq 15$ GeV	1,489	1,129

E_T larger than the following η-dependent thresholds developed in the diffractive W analysis [18, 68],

$$E_T \text{ (GeV)} = \begin{cases} -0.143 \times |\eta| + 0.579 & (2.4 \leq |\eta| \leq 3.0), \\ -0.0625 \times |\eta| + 0.3375 & (3.0 < |\eta| \leq 4.2). \end{cases} \tag{4.3}$$

4.3.1 Beam-Gas Interaction Background

Figure 4.19 shows the east BBC and FCAL tower multiplicity distributions for the 1800 and 630 GeV single diffractive (SD) inclusive samples. The east BBC multiplicity distributions show an enhancement in the zero bin which is possibly due to beam-gas diffractive interactions and/or double pomeron exchange (DPE) interactions. In beam-gas diffractive interactions, an incoming antiproton is scattered quasielastically not by a beam proton but by a gas particle, and hits the Roman Pot spectrometer. Such interactions occurring in the downstream antiproton direction produce no particles hitting the east BBC and FCAL, and thus can provide an explanation for the enhancement in the zero bin of these distributions. The same is

true for DPE events that have a rapidity gap spanning the east BBC and FCAL. The beam-gas background fraction is estimated by extrapolating the straight line fitted at the high multiplicities (2−7) down to 0 and taking the fraction of events in the excess,

$$F_{GAS}^{SD\ incl}(1800\ \text{GeV}) = \frac{(127,234 \pm 357) - (42,537 \pm 258)}{1,638,695} = 5.17 \pm 0.03(\text{stat})\ \%,$$

$$F_{GAS}^{SD\ incl}(630\ \text{GeV}) = \frac{(10,101 \pm 101) - (5,657 \pm 98)}{184,327} = 2.41 \pm 0.08(\text{stat})\ \%.$$

In normalizing the data to the SD inclusive cross section, we apply a correction assuming that the enhancement is due to beam-gas interactions. A subsequent study [69] indicated that the enhancement in the zero bin is most likely due to DPE events, in which case no correction should have been made. Even if the entire correction factor were used as a systematic uncertainty and added in quadrature to the normalization uncertainty, the uncertainty would not increase by more than 1 %.

4.3.2 Non-Diffractive Overlap Background

Although a single vertex cut is applied to the single diffractive (SD) samples to select single interaction events, the samples still contain a certain fraction of non-diffractive (ND) overlap background events, which consist of ND interactions superimposed on a SD interaction. The overlap background fraction can be estimated from the west BBC multiplicity (N_{BBC}) and FCAL tower multiplicity (N_{FCAL}) distributions, since the SD events we use have a rapidity gap on the antiproton outgoing side (west side), while the overlapping ND events have particles over the entire phase space.

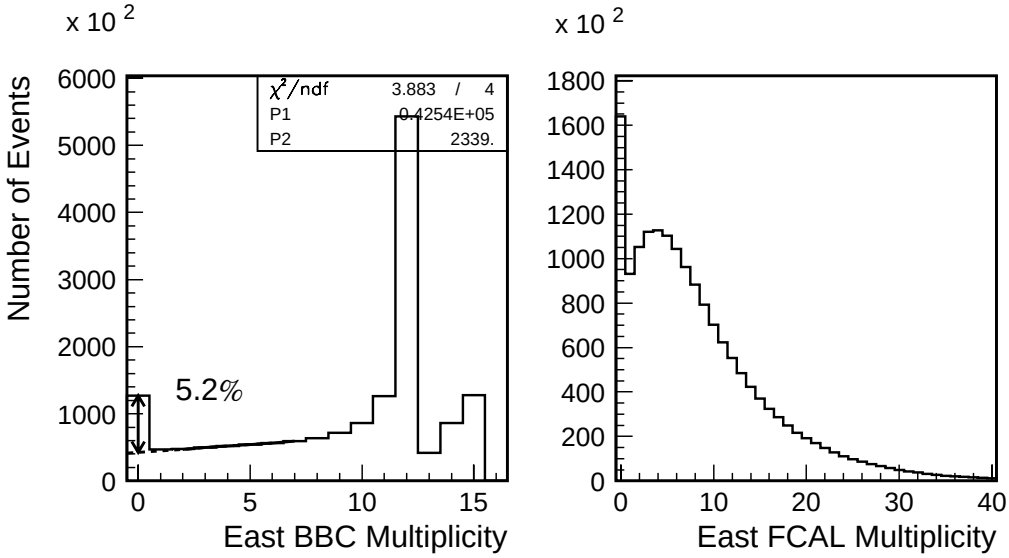

(a) 1800 GeV

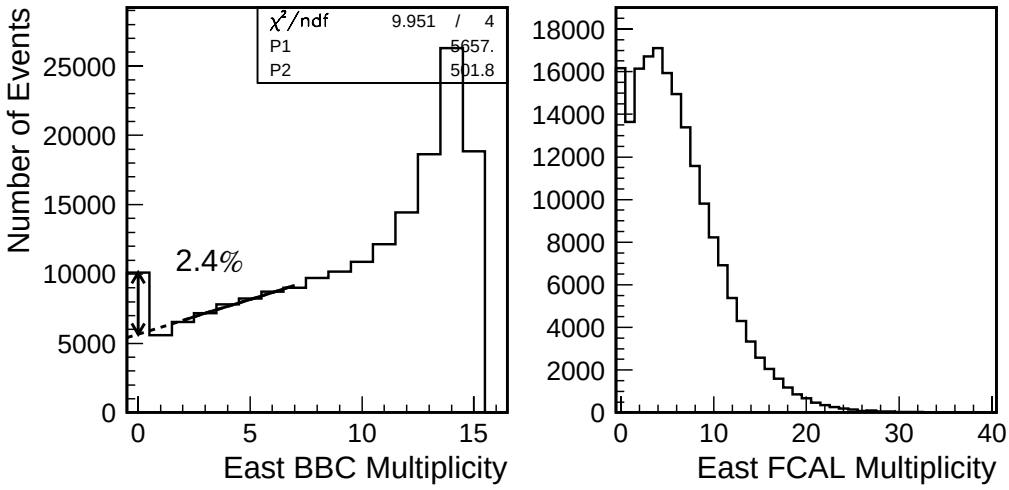

(b) 630 GeV

Figure 4.19: East BBC multiplicity (left) and FCAL tower multiplicity (right) distributions for the (a) 1800 GeV and (b) 630 GeV SD inclusive samples. The enhancement at the zero bin is possibly due to beam-gas diffractive interactions. The percentages in the left plots are the estimated beam-gas background fractions.

The 1800 GeV Diffractive Inclusive Sample

Figure 4.20 shows the west BBC (top) and FCAL tower (bottom) multiplicity distributions for 1800 GeV SD inclusive events in runs with a maximum number of west BBC hits of 14 (left) and 11 (right). To estimate the fraction of the ND overlap background, the west BBC and FCAL tower multiplicity distributions for the ND inclusive sample[3] are normalized to those for the SD inclusive sample at the maximum BBC bin (N_{BBC} = 14 or 11) and in the region $N_{FCAL} \geq 20$, where the ND overlap background is dominant. The estimated ND overlap background contributions are shown by the cross-hatched regions. The ND overlap background fraction can be estimated as

$$F_{SD\,incl}^{ND\,BG}(1800\text{ GeV}) = \frac{N_{SD\,incl}^{ND\,BG}(\text{Max WBBC=14}) + N_{SD\,incl}^{ND\,BG}(\text{Max WBBC=11})}{N_{SD}^{incl}(\text{Max WBBC=14}) + N_{SD}^{incl}(\text{Max WBBC=11})}, \tag{4.4}$$

where N_{SD}^{incl}(Max WBBC=14) and N_{SD}^{incl}(Max WBBC=11) are the numbers of diffractive inclusive events, and $N_{SD\,incl}^{ND\,BG}$(Max WBBC=14) and $N_{SD\,incl}^{ND\,BG}$(Max WBBC=11) are the estimated numbers of ND overlap background events in runs with a maximum number of west BBC hits of 14 and 11, respectively. From the BBC and FCAL tower multiplicity distributions, the ND overlap background fraction in the 1800 GeV SD inclusive sample is found to be

$$\begin{aligned} F_{SD\,incl}^{ND\,BG}(1800\text{ GeV, BBC}) &= \frac{(23,966 \pm 252) + (49,317 \pm 308)}{589,346 + 1,049,349} \\ &= 4.47 \pm 0.02(\text{stat})\ \%, \end{aligned}$$

[3]All the 1800 GeV ND inclusive events described in Section 4.1.2 were collected in runs with a maximum number of west BBC hits of 11. To estimate the ND overlap background fraction in the SD inclusive sample with a maximum number of west BBC hits of 15, about 428,000 minimum bias events collected in runs 75632−75643, in which the maximum number of west BBC hits is 15, are also used in this section.

$$F_{SD\,incl}^{ND\,BG}(1800\text{ GeV, FCAL}) = \frac{(14,159 \pm 213) + (10,698 \pm 177)}{589,346 + 1,049,349}$$
$$= 1.52 \pm 0.02(\text{stat})\ \%.$$

These two numbers are averaged, and the half of their difference is taken as a systematic uncertainty:

$$F_{SD\,incl}^{ND\,BG}(1800\text{ GeV}) = 3.0 \pm 1.5(\text{syst})\ \%.$$

The 1800 GeV Diffractive Dijet Samples

In the SD dijet samples, the ND overlap background fraction is larger, because the ND overlap background consists not only of events in which a soft ND event is superimposed on a SD dijet event, but also of events with a soft SD event superimposed on a ND dijet event. Figure 4.21 shows the west BBC and FCAL tower multiplicity distributions for the $E_T^{jet1,2} \geq 7$ GeV SD dijet sample. The ND overlap background contributions, estimated using the $E_T^{jet1,2} \geq 7$ GeV ND dijet sample, are indicated by the cross-hatched regions. The west BBC and FCAL tower multiplicity distributions for the ND dijet sample are normalized to those for the SD dijet sample at the maximum BBC bin ($N_{BBC} = 14$ or 11) and in the region $N_{FCAL} \geq 20$. The ND overlap background fraction can be estimated as

$$F_{SD\,jj}^{ND\,BG}(1800\text{ GeV}) = \frac{N_{SD\,jj}^{ND\,BG}(\text{Max WBBC=14}) + N_{SD\,jj}^{ND\,BG}(\text{Max WBBC=11})}{N_{SD}^{jj}(\text{Max WBBC=14}) + N_{SD}^{jj}(\text{Max WBBC=11})}, \tag{4.5}$$

where N_{SD}^{jj}(Max WBBC=14) and N_{SD}^{jj}(Max WBBC=11) are the numbers of diffractive dijet events, and $N_{SD\,jj}^{ND\,BG}$(Max WBBC=14) and $N_{SD\,jj}^{ND\,BG}$(Max WBBC=11) are the estimated numbers of ND overlap background events in runs with a maximum number of west BBC hits of 14 and 11, respectively. By averaging the ND overlap

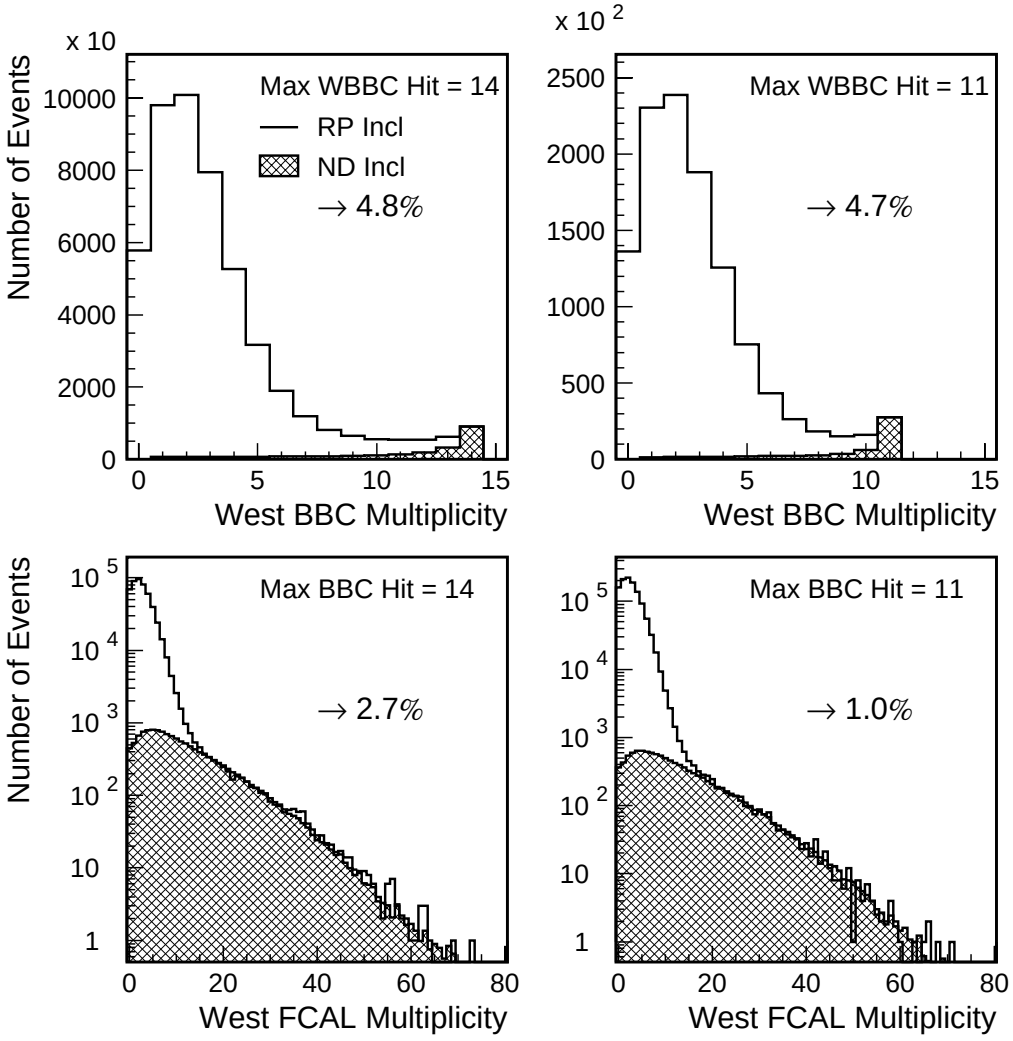

Figure 4.20: West BBC multiplicity (top) and FCAL tower multiplicity (bottom) distributions for the 1800 GeV SD inclusive sample (open histograms). Left (right) plots are for runs with a maximum west BBC hit = 14 (11). Distributions for the ND inclusive sample are normalized at the maximum BBC hit bin of 14 or 11, and in the region $N_{FCAL} \geq 20$ (cross-hatched histograms). The percentage in each plot is the estimated ND overlap background fraction.

background fractions extracted from the BBC and FCAL tower multiplicities, we obtain a fraction of 7.0 %, to which we assign a 10 % systematic uncertainty:

$$\begin{aligned} F_{SD\,jj}^{ND\,BG}(1800\text{ GeV, BBC}) &= \frac{(1,222.8 \pm 50.9) + (\ 977.9 \pm 37.9)}{11,605 + 18,805} \\ &= 7.2 \pm 0.2(\text{stat})\ \%, \\ F_{SD\,jj}^{ND\,BG}(1800\text{ GeV, FCAL}) &= \frac{(1,208.4 \pm 43.1) + (\ 818.7 \pm 33.9)}{11,605 + 18,805} \\ &= 6.7 \pm 0.2(\text{stat})\ \%, \end{aligned}$$

$$F_{SD\,jj}^{ND\,BG}(1800\text{ GeV}) = 7.0 \pm 0.7(\text{syst})\ \%.$$

Applying the same procedure to the $E_T^{jet1,2} \geq 10$ and $E_T^{jet1,2} \geq 15$ GeV SD dijet samples, we obtain $F_{SD\,jj}^{ND\,BG} = 9.4 \pm 0.9(\text{syst})$ % and $8.5 \pm 0.9(\text{syst})$ %, respectively.

The 630 GeV Diffractive Inclusive Sample

For the 630 GeV data samples, an additional selection cut is imposed on the west BBC multiplicity requiring it to be ≤ 4 to further reject ND overlap background events. The west BBC multiplicity cut rejects ≈ 80 % of the residual ND overlap background events; however, this cut also removes some single interaction events, i.e. SD events which are not associated with overlapping ND events. The residual ND overlap background fraction after the west BBC multiplicity cut and the west BBC multiplicity cut efficiency, defined as the fraction of single interaction events retained by the west BBC multiplicity cut, are estimated from the west BBC and FCAL tower multiplicity distributions below.

For the 1800 GeV data, the ND data sample with a single vertex of class ≥ 5 ($N_{vtx} = 1$) was used to estimate the ND overlap background contribution to the single vertex SD data sample; this method is referred to hereafter as *method A*. However, in the 630 GeV data, the west BBC multiplicity distribution for the single

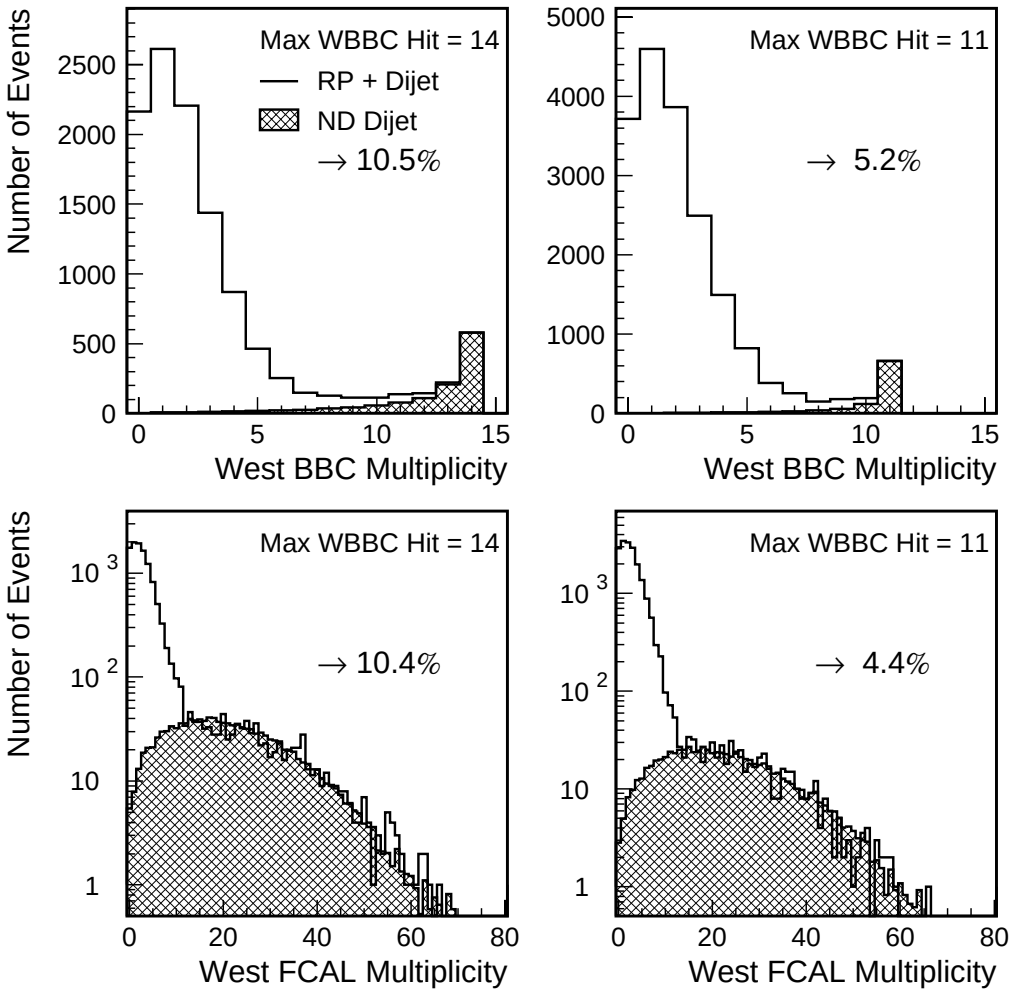

Figure 4.21: West BBC multiplicity (top) and FCAL tower multiplicity (bottom) distributions for the 1800 GeV SD dijet sample of $E_T^{jet1,2} \geq 7$ GeV (open histograms). Left (right) plots are for runs with a maximum BBC hit = 14 (11). Distributions for the ND dijet sample are normalized at the maximum BBC hit bin of 14 or 11, and in the region $N_{FCAL} \geq 20$ (cross-hatched histograms). The percentage in each plot is the estimated ND overlap background fraction.

vertex ND data sample does not match that for the SD data sample very well even in the region where the ND overlap background is dominant, in the case of the dijet events. Therefore, we also use the ND data sample with $N_{vtx} \geq 1$ to estimate the ND overlap background fraction; this method is referred to as *method B*. The average of the results from the two methods is then taken as our final result.

Figures 4.22(a−d) show the west BBC and FCAL tower multiplicity distributions for the SD inclusive sample and the ND overlap background contributions estimated using the ND inclusive samples with $N_{vtx} = 1$ and $N_{vtx} \geq 1$. In order to estimate the ND overlap background fraction from Figures 4.22(c) and (d), the west BBC multiplicity ≤ 4 cut is applied to both distributions; the resultant distributions are shown in Figures 4.22(e) and (f). From Figures 4.22(a) and (e), the residual ND overlap background fraction after the west BBC multiplicity cut is estimated to be

$$F_{SD\,incl}^{ND\,BG}(630\ \text{GeV},\ \text{BBC},\ \text{A}) = 3.75 \pm 0.06(\text{stat})\ \%,$$

$$F_{SD\,incl}^{ND\,BG}(630\ \text{GeV},\ \text{FCAL},\ \text{A}) = 2.67 \pm 0.03(\text{stat})\ \%.$$

From Figures 4.22(b) and (f),

$$F_{SD\,incl}^{ND\,BG}(630\ \text{GeV},\ \text{BBC},\ \text{B}) = 3.01 \pm 0.04(\text{stat})\ \%,$$

$$F_{SD\,incl}^{ND\,BG}(630\ \text{GeV},\ \text{FCAL},\ \text{B}) = 2.01 \pm 0.02(\text{stat})\ \%.$$

By taking the average of these four numbers, we obtain the ND overlap background fraction in the 630 GeV SD inclusive sample, and assign to it a systematic uncertainty which covers the four values within 1σ:

$$F_{SD\,incl}^{ND\,BG}(630\ \text{GeV}) = 2.9 \pm 0.9(\text{syst})\ \%.$$

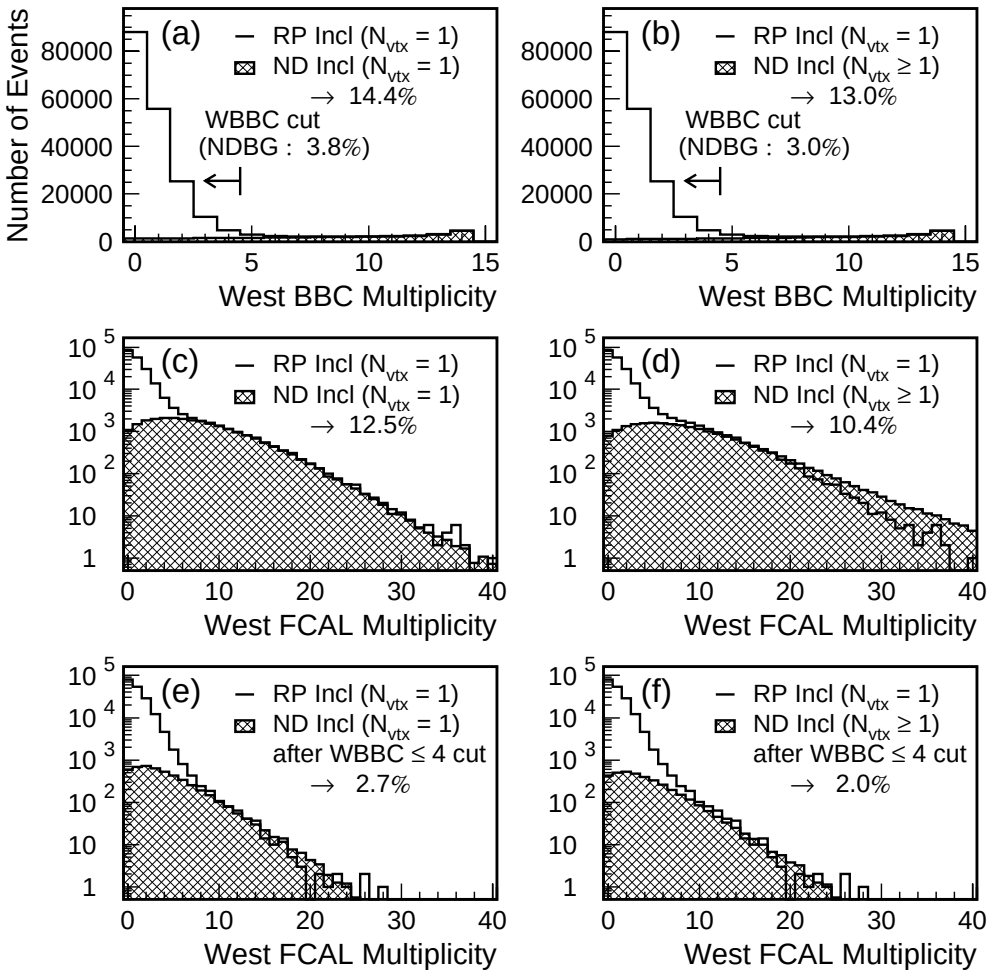

Figure 4.22: West BBC multiplicity (a,b) and FCAL tower multiplicity (c,d) distributions for the 630 GeV SD inclusive sample (open histograms). In order to estimate the ND overlap background contribution, ND distributions are normalized to the SD distributions at $N_{BBC} = 14$ and in the region $N_{FCAL} \geq 10$ (cross-hatched histograms). (e,f) West FCAL tower multiplicity distributions for the SD sample (open histograms) and ND overlap background (cross-hatched histograms) after the requirement of west BBC multiplicity ≤ 4. The percentages are the estimated ND overlap background fractions before or after the west BBC multiplicity cut.

The west BBC multiplicity cut efficiency is evaluated by dividing the number of SD inclusive events after the ND overlap background subtraction (i.e., in Figure 4.22(a) and (b), the number of events in the open histogram minus the cross-hatched histogram) with the west BBC multiplicity ≤ 4 cut by that without the west BBC multiplicity cut. Using the ND inclusive samples with $N_{vtx} = 1$ and $N_{vtx} \geq 1$, the efficiency $\epsilon_{SD\ incl}^{WBBC}$ is estimated to be $\epsilon_{SD\ incl}^{WBBC} = 98.3 \pm 0.2(\text{stat})$ % and $97.5 \pm 0.2(\text{stat})$ %, respectively. By taking the average of these two results, the west BBC multiplicity cut efficiency for the 630 GeV SD inclusive sample is obtained, to which one half of the difference between the two results is assigned as a systematic uncertainty:

$$\epsilon_{SD\ incl}^{WBBC}(630\ \text{GeV}) = 97.9 \pm 0.4(\text{syst})\ \%.$$

The 630 GeV Diffractive Dijet Samples

The ND overlap background fraction after the west BBC multiplicity cut and the west BBC multiplicity cut efficiency for the 630 GeV SD dijet samples are estimated in the same manner as for the 630 GeV SD inclusive sample. From Figures 4.23(a), (c) and (e), the residual ND overlap background fraction in the 630 GeV SD dijet sample of $E_T^{jet1,2} \geq 7$ GeV estimated using the single vertex ND dijet data sample is

$$F_{SD\ jj}^{ND\ BG}(630\ \text{GeV},\ \text{BBC},\ \text{A}) = \frac{101.4 \pm 4.1}{1,186} = 8.6 \pm 0.3(\text{stat})\ \%,$$

$$F_{SD\ jj}^{ND\ BG}(630\ \text{GeV},\ \text{FCAL},\ \text{A}) = \frac{91.6 \pm 3.9}{1,186} = 7.7 \pm 0.3(\text{stat})\ \%.$$

From Figures 4.23(b), (d) and (f), the residual ND background fraction estimated using the $N_{vtx} \geq 1$ ND dijet data sample is

$$F_{SD\ jj}^{ND\ BG}(630\ \text{GeV},\ \text{BBC},\ \text{B}) = \frac{59.6 \pm 2.4}{1,186} = 5.0 \pm 0.2(\text{stat})\ \%,$$

$$F_{SD\ jj}^{ND\ BG}(630\ \text{GeV},\ \text{FCAL},\ \text{B}) = \frac{53.3 \pm 2.3}{1,186} = 4.5 \pm 0.2(\text{stat})\ \%.$$

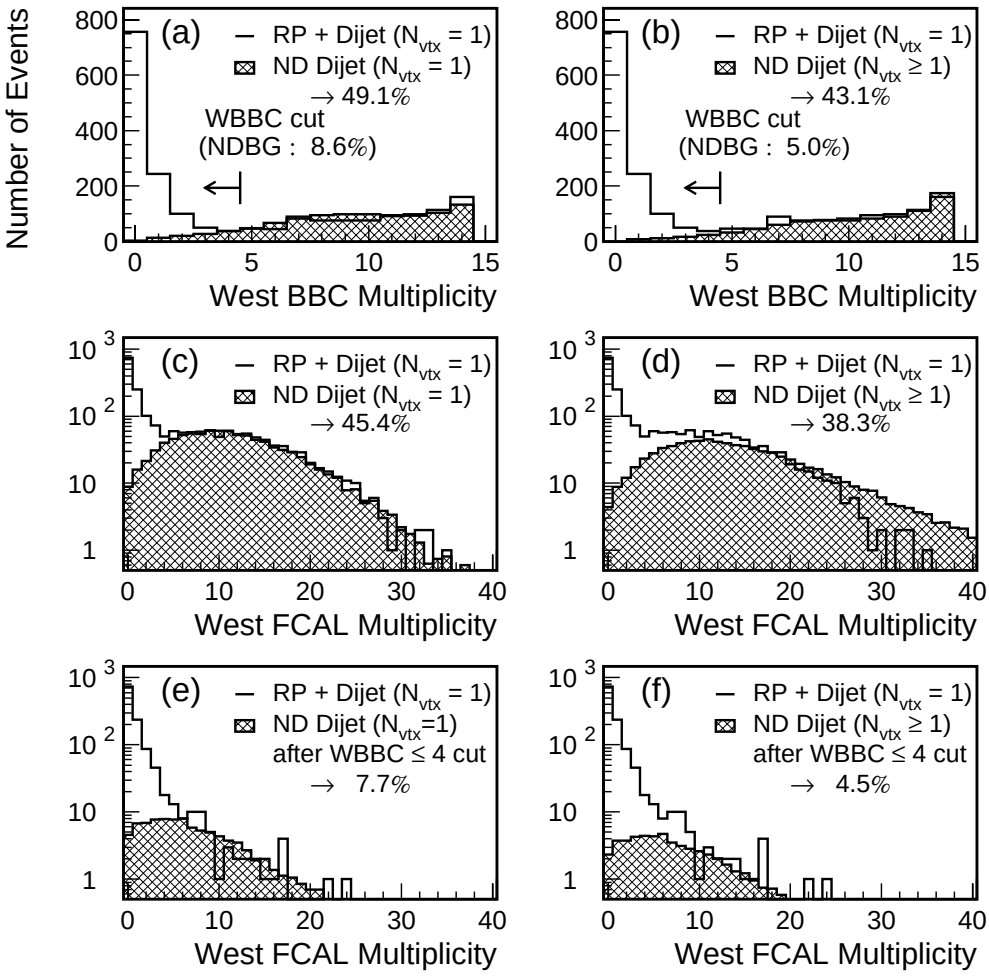

Figure 4.23: West BBC multiplicity (a,b) and FCAL tower multiplicity (c,d) distributions for the 630 GeV SD dijet sample of $E_T^{jet1,2} \geq 7$ GeV (open histograms). In order to estimate the ND overlap background contribution, ND distributions are normalized to the SD distributions in the regions $9 \leq N_{BBC} \leq 14$ and $N_{FCAL} \geq 10$ where the ND overlap background is dominant (cross-hatched histograms). (e,f) West FCAL tower multiplicity distributions for the SD sample (open histograms) and ND overlap background (cross-hatched histograms) after the requirement of west BBC multiplicity ≤ 4. The percentages are the estimated ND overlap background fractions before or after the west BBC multiplicity cut.

By taking the average of these four numbers, we obtain the ND overlap background fraction $F_{SD\,jj}^{ND\,BG}$, and assign to it a systematic uncertainty which covers the four values within 1σ:

$$F_{SD\,jj}^{ND\,BG}(630\ \text{GeV}) = 6.4 \pm 2.2(\text{syst})\ \%.$$

The west BBC multiplicity cut efficiency for the 630 GeV SD dijet sample of $E_T^{jet1,2} \geq 7$ GeV is evaluated by the same procedure as that used for the 630 GeV SD inclusive sample. Using the ND dijet samples with $N_{vtx} = 1$ and $N_{vtx} \geq 1$, the efficiency $\epsilon_{SD\,jj}^{WBBC}$ is estimated to be $\epsilon_{SD\,jj}^{WBBC} = 100 \pm 0.0(\text{stat})\ \%$ and $96.1 \pm 2.8(\text{stat})\ \%$, respectively. By taking the average of these two results, the west BBC multiplicity cut efficiency is obtained, to which one half of the difference between the two results is assigned as a systematic uncertainty:

$$\epsilon_{SD\,jj}^{WBBC}(630\ \text{GeV}) = 98.1 \pm 1.9(\text{syst})\ \%.$$

For the 630 GeV SD dijet sample of $E_T^{jet1,2} \geq 7$ GeV and $E_T^* = (E_T^{jet1} + E_T^{jet2})/2 \geq 10$ GeV, the residual ND overlap background fraction and the west BBC multiplicity cut efficiency are estimated to be $F_{SD\,jj}^{ND\,BG} = 8.3 \pm 2.8(\text{syst})\ \%$ and $\epsilon_{SD\,jj}^{WBBC} = 97.4 \pm 2.6(\text{syst})\ \%$, respectively.

4.3.3 Single Vertex Cut Efficiency

Although the single vertex cut is applied to the single diffractive (SD) samples to remove events containing multiple interactions or no interaction, it also removes some single interaction events with multiple vertices or zero vertices due to vertex reconstruction ambiguities. The single vertex cut efficiency, defined as the fraction of single interaction events retained by the single vertex cut, is evaluated below to take into account the removed single interaction events.

The 1800 GeV Diffractive Inclusive Sample

To evaluate the single vertex cut efficiency for the 1800 GeV data, we use only events in runs 75713−75738, which are not affected by vertex cuts at the trigger level. As shown in Figure 4.24(a), in runs 75713−75738, the numbers of single vertex events, zero vertex events and multiple vertex events are 722872, 206525 and 65396, respectively.

The top two plots of Figure 4.24(b) show the east BBC multiplicity distributions (solid lines) for the zero vertex events in runs with a maximum number of east BBC hits of 15 (left) and 12 (right). To estimate the fraction of single interaction events, the east BBC multiplicity distributions for the single vertex events, normalized at the maximum BBC bin, are superimposed (dotted lines).

The middle left plot of Figure 4.24(b) shows the east FCAL tower multiplicity distribution (solid line) for the zero vertex events in runs with a maximum number of east BBC hits of 15; the distribution for the single vertex events is superimposed (dotted line). In this case, the two distributions do not match in the high multiplicity region, where single interaction events are dominant; the single vertex events have higher multiplicities in this region. This is reasonable, since the multiplicities in the single vertex events are generally higher than those in the zero vertex events. (In the BBC case, because of the low granularity and resultant saturation, this effect is washed out.) To take into account the different shapes of the single vertex and zero vertex events, we form the ratio of the single vertex to zero vertex distributions and fit the distribution of the ratio to a straight line on a logarithmic scale in the region $9 \leq N_{FCAL} \leq 28$, as shown in the middle right plot of Figure 4.24(b). Then, for each multiplicity bin, we multiply the number of single vertex events by the value of the fitted line, including the regions $N_{FCAL} \leq 9$ and $N_{FCAL} \geq 29$, in which we use the

extrapolated fitted line. The result is shown in the bottom left plot of Figure 4.24(b). The number of single interaction events in the zero vertex event sample is taken as the number of events in the dotted line histogram. This number is 14679 ± 286 events, 27.0 % of the zero vertex events in runs with a maximum number of east BBC hits of 15. The same procedure was applied to events in runs with a maximum number of east BBC hits of 12; the result is shown in the bottom right plot of Figure 4.24(b).

Figure 4.24(c) shows the west BBC multiplicity (top) and FCAL tower multiplicity (bottom) distributions for the multiple vertex events (solid lines), and the distributions for the single vertex events (dotted lines) normalized in the regions $0 \leq N_{BBC} \leq 2$ and $0 \leq N_{FCAL} \leq 3$. These distributions are used to estimate the fraction of single interaction events in the multiple vertex event sample.

From the BBC and FCAL tower multiplicity distributions, the single vertex cut efficiency for the 1800 GeV SD inclusive sample is estimated to be

$$\begin{aligned}
&\epsilon^{1vtx}_{SD\,incl}(1800\text{ GeV}) \\
&= \frac{N^{1vtx}_{SD\,incl}}{N^{1vtx}_{SD\,incl} + \left(N^{1int}_{0vtx}(\text{Max EBBC=15}) + N^{1int}_{0vtx}(\text{Max EBBC=12})\right) + N^{1int}_{\geq 2vtx}},
\end{aligned} \tag{4.6}$$

$$\begin{aligned}
&\epsilon^{1vtx}_{SD\,incl}(1800\text{ GeV, BBC}) \\
&= \frac{722,872}{722,872 + ((13,548 \pm 227) + (38,208 \pm 291)) + (47,928 \pm 305)} \\
&= 87.88 \pm 0.05(\text{stat})\ \%,
\end{aligned}$$

$$\begin{aligned}
&\epsilon^{1vtx}_{SD\,incl}(1800\text{ GeV, FCAL}) \\
&= \frac{722,872}{722,872 + ((14,679 \pm 286) + (41,173 \pm 493)) + (44,805 \pm 257)} \\
&= 87.77 \pm 0.07(\text{stat})\ \%,
\end{aligned}$$

where $N^{1vtx}_{SD\,incl}$ is the number of SD inclusive events with $N_{vtx} = 1$, $N^{1int}_{\geq 2vtx}$ is the

estimated number of single interaction events in the multiple vertex event sample, and N_{0vtx}^{1int}(Max EBBC=15) and N_{0vtx}^{1int}(Max EBBC=12) are the estimated numbers of single interaction events in the zero vertex event samples collected in runs with a maximum number of east BBC hits of 15 and 12, respectively. By taking the average of the single vertex cut efficiencies obtained from the BBC and FCAL tower multiplicity analyses, we obtain an efficiency of $\epsilon_{SD\ incl}^{1vtx} = 87.8$ %, and to which 10 % of $(1 - \epsilon_{SD\ incl}^{1vtx})$ is assigned as a systematic uncertainty:

$$\epsilon_{SD\ incl}^{1vtx}(1800\ \text{GeV}) = 87.8 \pm 1.2(\text{syst})\ \%.$$

The 1800 GeV Diffractive Dijet Samples

For the SD dijet samples, we again use events in runs 75713−75738 only, as we did for the SD inclusive sample. After applying the dijet requirement of $E_T^{jet1,2} \geq 7$ GeV, the numbers of single vertex events and multiple vertex events are 12727 and 8339, respectively. The single interaction event fraction in dijet events with multiple vertices is found to be 36.7 % and 37.1 % from the BBC and FCAL tower multiplicities, as shown in Figure 4.25. The single vertex cut efficiency can be estimated as

$$\epsilon_{SD\ jj}^{1vtx} = \frac{N_{SD\ jj}^{1vtx}}{N_{SD\ jj}^{1vtx} + N_{\geq 2vtx}^{1int}}, \tag{4.7}$$

where $N_{SD\ jj}^{1vtx}$ is the number of SD dijet events with $N_{vtx} = 1$, and $N_{\geq 2vtx}^{1int}$ is the estimated number of single interaction events in dijet events with multiple vertices. The single vertex cut efficiencies estimated from the BBC and FCAL tower multiplicities are

$$\epsilon_{SD\ jj}^{1vtx}(1800\ \text{GeV},\ \text{BBC}) = \frac{12,727}{12,727 + (3,059.6 \pm 71.4)} = 80.6 \pm 0.4(\text{stat})\ \%,$$

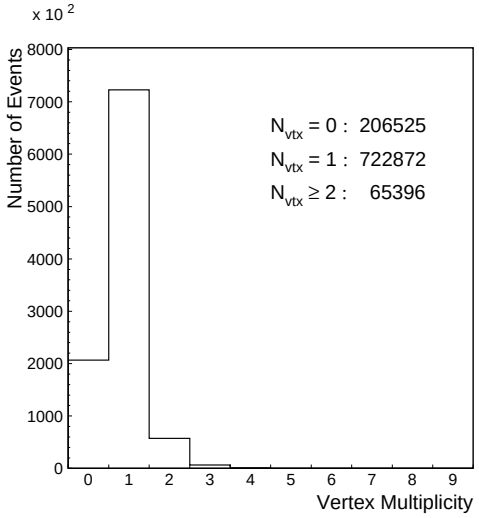

(a) Vertex multiplicity for the 1800 GeV SD inclusive subsample

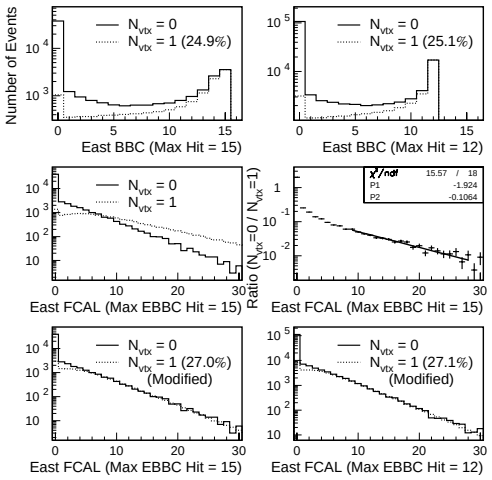

(b) East BBC/FCAL multiplicity for zero vertex events in the 1800 GeV SD inclusive subsample

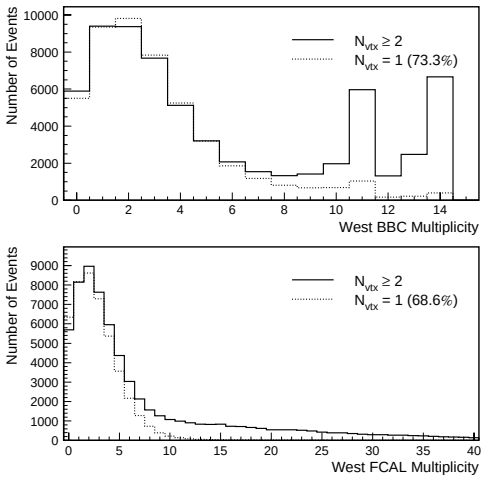

(c) West BBC/FCAL multiplicity for multiple vertex events in the 1800 GeV SD inclusive subsample

Figure 4.24: (a) Vertex multiplicity distribution for the 1800 GeV SD inclusive subsample without vertex cuts in the trigger. (b) East BBC and FCAL tower multiplicity distributions for zero vertex events in the 1800 GeV SD inclusive subsample (solid lines), and the single interaction event contributions estimated from the distributions for the single vertex events (dotted lines). (c) West BBC and FCAL tower multiplicity distributions for multiple vertex events in the 1800 GeV SD inclusive subsample (solid lines), and those for the single vertex events normalized in the regions $0 \leq N_{BBC} \leq 2$ and $0 \leq N_{FCAL} \leq 3$ (dotted lines). The percentages are the estimated single interaction event fractions in the zero vertex or multiple vertex event samples.

$$\epsilon^{1vtx}_{SD\ jj}(1800\ \text{GeV},\ \text{FCAL}) = \frac{12,727}{12,727 + (3,092.7 \pm 70.1)} = 80.4 \pm 0.4(\text{stat})\ \%.$$

By taking the average of these two results, the single vertex cut efficiency is estimated, to which 10 % of $(1 - \epsilon^{1vtx}_{SD\ incl})$ is assigned as a systematic uncertainty:

$$\epsilon^{1vtx}_{SD\ jj}(1800\ \text{GeV}) = 80.5 \pm 1.9(\text{syst})\ \%.$$

Using the same method, the single vertex cut efficiencies for the $E_T^{jet1,2} \geq 10$ and $E_T^{jet1,2} \geq 15$ GeV SD dijet samples are found to be $\epsilon^{1vtx}_{SD\ jj} = 77.8 \pm 2.2(\text{syst})$ % and $76.8 \pm 2.3(\text{syst})$ %, respectively.

The 630 GeV Diffractive Inclusive Sample

The single vertex cut efficiency for the 630 GeV SD inclusive sample is evaluated in a similar way to that used for the 1800 GeV SD inclusive sample. Figures 4.26(a) and (b) for the 630 GeV SD inclusive sample correspond to Figures 4.24(a) and (b) for the 1800 GeV SD inclusive sample, respectively. In the case of the 630 GeV SD inclusive sample, about 43 % of the zero vertex events are estimated to be single interaction events.

The fraction of single interaction events in the multiple vertex event sample for the 630 GeV data is estimated a little differently than for the 1800 GeV data. The top left plot of Figure 4.26(c) shows the west BBC multiplicity distribution for multiple vertex events. To estimate the number of multiple interaction events in the zero bin, a straight line is fitted in the region $7 \leq N_{BBC} \leq 12$ and extrapolated down to the zero bin. Then, the distribution for single vertex events, normalized in the zero bin to the solid line histogram minus the fitted (dashed) line, is superimposed to estimate the fraction of single interaction events in multiple vertex events.

The top right plot of Figure 4.26(c) shows the west FCAL tower multiplicity

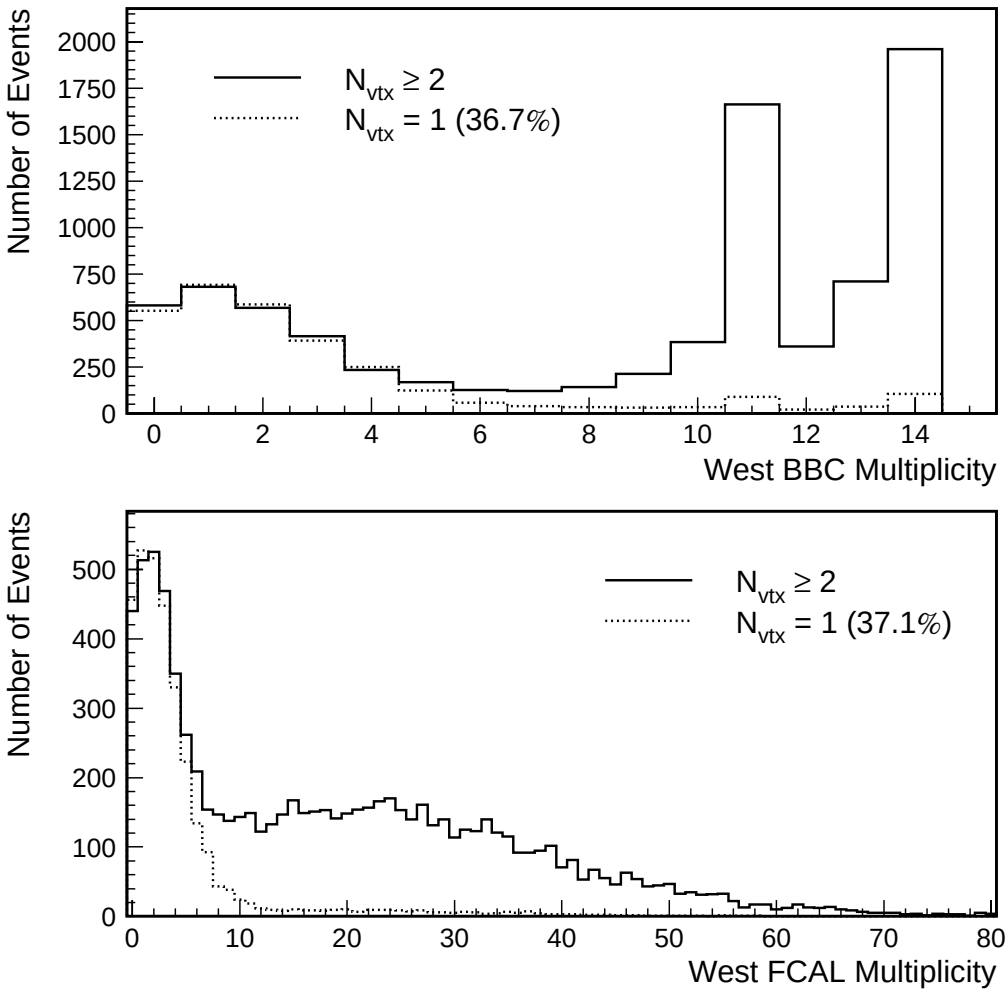

Figure 4.25: West BBC multiplicity (top) and FCAL tower multiplicity (bottom) distributions for multiple vertex events in the 1800 GeV SD dijet sample of $E_T^{jet1,2} \geq 7$ GeV (solid lines), and those for the single vertex events normalized in the regions $0 \leq N_{BBC} \leq 2$, and $0 \leq N_{FCAL} \leq 3$ (dotted lines). The percentage in each plot is the estimated single interaction event fraction in the multiple vertex events.

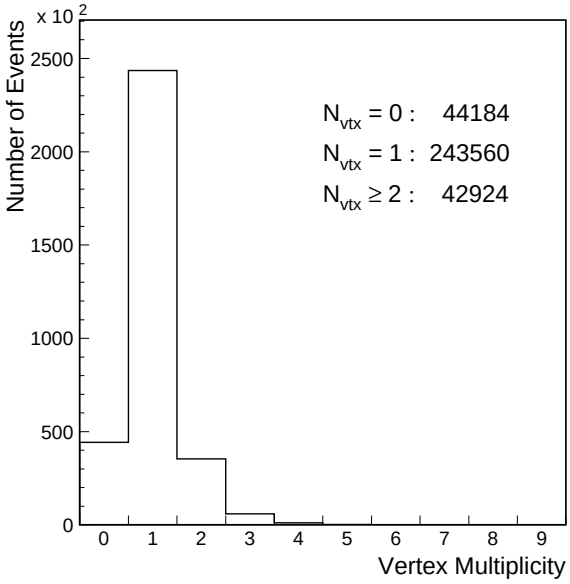

(a) Vertex multiplicity for the 630 GeV SD inclusive sample

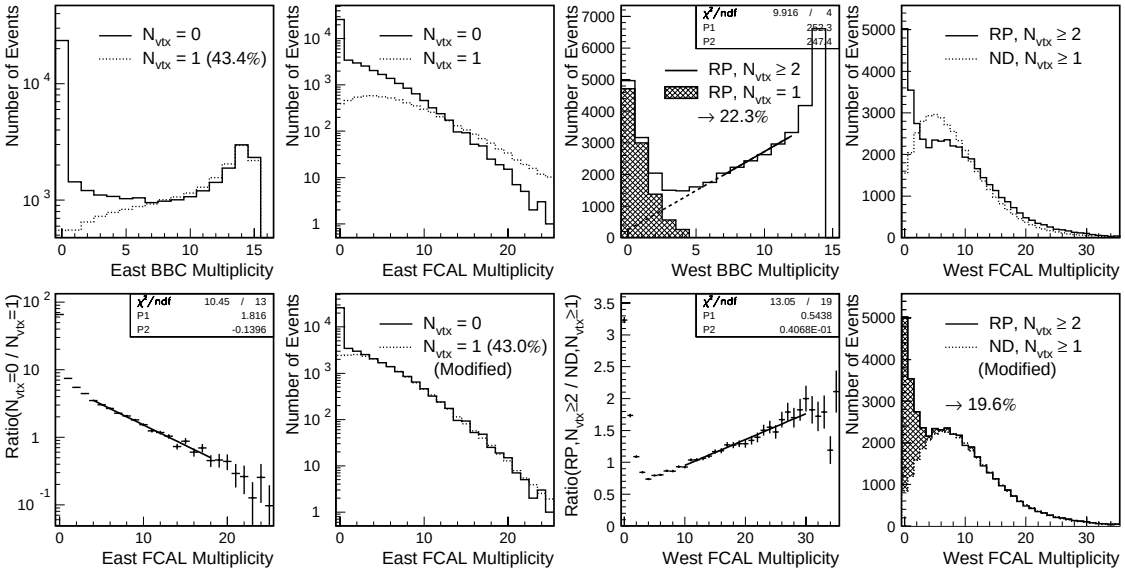

(b) East BBC/FCAL multiplicity for zero vertex events in the 630 GeV data

(c) West BBC/FCAL multiplicity for multiple vertex events in the 630 GeV data

Figure 4.26: (a) Vertex multiplicity distribution for the 630 GeV SD inclusive sample. (b) East BBC and FCAL tower multiplicity distributions for zero vertex events in the 630 GeV data (solid lines), and the single interaction event contributions estimated from the distributions for the single vertex events (dotted lines). (c) West BBC and FCAL tower multiplicity distributions for multiple vertex events in the 630 GeV data (solid lines), and the estimated single interaction event contributions (cross-hatched areas). The percentages are the estimated single interaction event fractions in the zero vertex or multiple vertex events.

distribution for the multiple vertex SD inclusive sample. To estimate the contribution of multiple interaction events, the distribution for the $N_{vtx} \geq 1$ non-diffractive (ND) inclusive sample is superimposed. However, the two distributions do not quite match at the high multiplicity region where multiple interaction events are dominant. Therefore, we form the ratio of the distribution for the multiple vertex SD inclusive sample to that for the $N_{vtx} \geq 1$ ND inclusive sample, and fit the ratio distribution to a straight line in the region $10 \leq N_{FCAL} \leq 30$ as shown in the bottom left plot of Figure 4.26(c). Then, for each multiplicity bin, we multiply the number of multiple vertex events by the value of the fitted line, including the regions $N_{FCAL} \leq 9$ and $N_{FCAL} \geq 31$, in which we use the extrapolated fitted line. The result is shown in the bottom right plot of Figure 4.26(c). The solid line histogram minus the dotted line histogram is estimated to be due to single interaction events.

Combining the above results, we obtain a single vertex cut efficiency for the 630 GeV SD inclusive sample of $\epsilon^{1vtx}_{SD\,incl} = 88.4$ %. This is the average of the values 88.1 % and 88.6 % obtained from the BBC and FCAL tower multiplicity distributions, respectively. To the single vertex cut efficiency $\epsilon^{1vtx}_{SD\,incl}$, 10 % of $(1-\epsilon^{1vtx}_{SD\,incl})$ is assigned as a systematic uncertainty:

$$\epsilon^{1vtx}_{SD\,incl}(630\ \text{GeV}) = 88.4 \pm 1.2(\text{syst})\ \%.$$

The 630 GeV Diffractive Dijet Samples

The single vertex cut efficiency for the 630 GeV SD dijet sample is evaluated in a similar way to that used for the 1800 GeV SD dijet sample. After applying the dijet requirement of $E_T^{jet1,2} \geq 7$ GeV, the numbers of single vertex events and multiple vertex events, for which the west BBC multiplicity ≤ 4 cut is not applied, are 2058 and 4466 events, respectively. Figures 4.27(a) and (c) show the west BBC and FCAL tower

multiplicity distributions for the multiple vertex SD dijet sample; the distributions for the $N_{vtx} \geq 1$ ND dijet sample are normalized to the SD distributions at $9 \leq N_{BBC} \leq 14$ and $N_{FCAL} \geq 10$ to estimate the contribution of multiple interaction events in the multiple vertex SD dijet sample. In the zero bins, the fraction of multiple interaction events (dotted line histogram) seems to be small. In Figures 4.27(b) and (d), the west BBC and FCAL tower multiplicity distributions for the single vertex SD dijet sample with $N_{WBBC} \leq 4$ are normalized in the zero bins to the solid line histograms minus the dotted line histograms shown in Figures 4.27(a) and (c) to estimate the fraction of single interaction events in the multiple vertex SD dijet sample. Using Eq. (4.7), the single vertex cut efficiency is estimated from the BBC and FCAL tower multiplicities to be

$$\epsilon^{1vtx}_{SD\,jj}(630 \text{ GeV, BBC}) = \frac{1,186}{1,186 + (169.7 \pm 15.7)} = 87.5 \pm 1.0(\text{stat}) \ \%,$$

$$\epsilon^{1vtx}_{SD\,jj}(630 \text{ GeV, FCAL}) = \frac{1,186}{1,186 + (153.5 \pm 14.0)} = 88.5 \pm 0.9(\text{stat}) \ \%.$$

By taking the average of these two values and assigning 10 % of $(1 - \epsilon^{1vtx}_{SD\,jj})$ as a systematic uncertainty to it, the single vertex cut efficiency for the 630 GeV SD dijet events with $E_T^{jet1,2} \geq 7$ GeV is estimated to be

$$\epsilon^{1vtx}_{SD\,jj}(630 \text{ GeV}) = 88.0 \pm 1.2(\text{syst}) \ \%.$$

For the 630 GeV SD dijet sample of $E_T^{jet1,2} \geq 7$ GeV and $E_T^* = (E_T^{jet1} + E_T^{jet2})/2 \geq 10$ GeV, the single vertex cut efficiency is estimated to be $\epsilon^{1vtx}_{SD\,jj} = 87.4 \pm 1.3(\text{syst}) \ \%$.

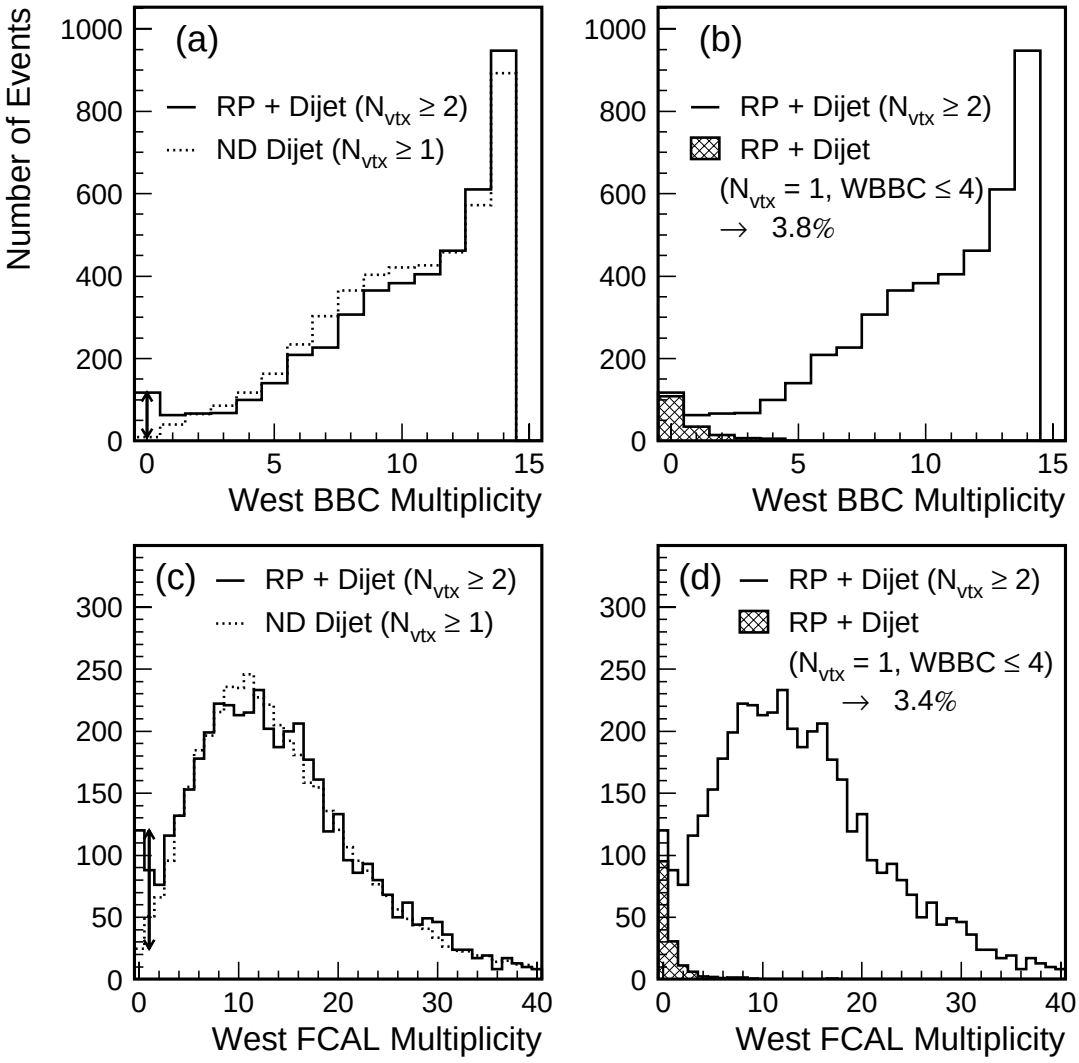

Figure 4.27: West BBC and FCAL tower multiplicity distributions for multiple vertex events in the 630 GeV SD dijet sample of $E_T^{jet1,2} \geq 7$ GeV (solid lines), the estimated multiple interaction event contributions (dotted lines), and the estimated single interaction event contributions (cross-hatched histograms). The percentages in the right plots are the estimated single interaction event fractions in the multiple vertex events.

4.4 Cross Sections

4.4.1 Diffractive Inclusive Samples

In this analysis, the diffractive data samples are normalized to the previously-measured single diffractive cross section; we do not attempt to derive an absolute cross section directly from our data, since it is very difficult to take into account all kinds of backgrounds, efficiencies, prescaling factors and so on.

Cross Sections from the CDF 1988−1989 Data

The CDF collaboration reported a measurement of differential cross sections of single diffractive dissociation at $\sqrt{s} = 1800$ and 546 GeV in Ref. [30]. Distributions of $x\ (= 1-\xi)$ were fitted to those for events generated by a Monte Carlo (MC) simulation which took into account the detector acceptance and the momentum resolution of the Roman Pot spectrometer. As an input to the MC simulation, the following formula was used:

$$\frac{d^2\sigma_{SD}^{incl}}{d\xi dt} = \frac{D}{\xi^{1+\epsilon}} e^{(b_0 - 2\alpha' \ln \xi)t} + I\xi^{\gamma} e^{b't}, \tag{4.8}$$

where the first and second terms on the right side represent the pomeron exchange cross section $\sigma_{I\!P}$ and the reggeon/pion exchange cross section[4] $\sigma_{I\!R}$, respectively. The slope of the pomeron trajectory α' was set to the value $\alpha' = 0.25$ GeV^{-2} in the fits. The remaining six parameters were determined from the fits.

Using Eq. (4.8)[5], we obtain for the single diffractive cross section at $\sqrt{s} = 1800$

[4] In Ref. [30], the second term of Eq. (4.8) is called "non-diffractive". In this analysis, we refer to "diffractive" as the cross section associated with a quasielastically-scattered antiproton (proton) and a forward rapidity gap. Therefore, the sum of the first and second terms of Eq. (4.8) is used to evaluate the diffractive inclusive cross section.

[5] We divide Eq. (4.8) by a factor of 2, since we are interested only in the cross section for $p + \bar{p} \to X + \bar{p}$, while in Ref. [30] both $p + \bar{p} \to p + X$ and $p + \bar{p} \to X + \bar{p}$ were taken into account.

GeV integrated over $0.035 \leq \xi \leq 0.095$ and $|t| \leq 1.0$ GeV^2,

$$\sigma_{SD\ incl}^{1800\ GeV}(\text{CDF fit}) = 0.78 \pm 0.08(\text{stat}) \text{ mb}$$

$$(\sigma_{I\!P} = 0.29 \text{ mb}, \sigma_{I\!R} = 0.49 \text{ mb}).$$

The integration was performed with the VEGAS program [70]. The 10 % statistical uncertainty in $\sigma_{SD\ incl}^{1800\ GeV}$(CDF fit) is estimated from the number of events within $0.035 \leq \xi \leq 0.095$ in Figure 15 of Ref. [30].

We extract the diffractive inclusive cross section at $\sqrt{s} = 630$ GeV integrated over $0.035 \leq \xi \leq 0.095$ and $|t| \leq 0.2$ GeV^2 by interpolating the CDF fit results for $\sigma_{I\!P}$ and $\sigma_{I\!R}$ at $\sqrt{s} = 1800$ and 546 GeV to $\sqrt{s} = 630$ GeV. In the region $0.035 \leq \xi \leq 0.095$ and $|t| \leq 0.2$ GeV^2, Eq. (4.8) yields $\sigma_{I\!P} = 0.199$ (0.220) mb and $\sigma_{I\!R} = 0.372$ (0.185) mb at $\sqrt{s} = 1800$ (546) GeV. Interpolating them to $\sqrt{s} = 630$ GeV by a power law in s, we obtain $\sigma_{I\!P} = 0.22$ mb and $\sigma_{I\!R} = 0.20$ mb, resulting in $\sigma_{SD\ incl}^{630\ GeV}$(CDF fit) = 0.42 mb. The diffractive inclusive cross section of 0.42 mb is mainly determined by the 546 GeV data which have about 600 events in the ξ region $0.035 \leq \xi \leq 0.095$ in Figure 13 of Ref. [30]. Therefore, we assign to this cross section a 4 % ($\approx \sqrt{600}/600$) statistical uncertainty:

$$\sigma_{SD\ incl}^{630\ GeV}(\text{CDF fit}) = 0.42 \pm 0.02(\text{stat}) \text{ mb}$$

$$(\sigma_{I\!P} = 0.22 \text{ mb}, \sigma_{I\!R} = 0.20 \text{ mb}).$$

Cross Sections from a Global Analysis of Hadronic Diffraction

As a cross check of the diffractive inclusive cross sections obtained from CDF data [30], we extract the diffractive inclusive cross section at $\sqrt{s} = 1800$ and 630 GeV from Ref. [71], in which a global analysis of hadronic diffraction was performed. In the global analysis, the following empirical expression is fitted to the Fermilab

fixed target, ISR and CDF 1988−1989 results at each energy:

$$\frac{d^2\sigma_{SD}^{incl}}{d\xi dt} = f_N(\xi,t)\sigma_T^{I\!Pp}(s\xi) + f_{\pi/p}(\xi,t)\sigma_T^{\pi p}(s\xi), \tag{4.9}$$

where $f_N(\xi,t)$ is the renormalized pomeron flux factor, $\sigma_T^{I\!Pp}(s\xi)$ is the $I\!Pp$ total cross section, $f_{\pi/p}(\xi,t)$ is the "reggeized" pion flux factor, and $\sigma_T^{\pi p}(s\xi)$ is the πp total cross section. The first and second terms on the right hand side of Eq. (4.9) are identified with the pomeron exchange cross section $\sigma_{I\!P}$ and the pion exchange cross section σ_π, respectively. The exact forms of these terms are

$$f_N(\xi,t) = \begin{cases} f_{I\!P/p}(\xi,t) & \text{if } N(s) < 1, \\ f_{I\!P/p}(\xi,t)/N(s) & \text{if } N(s) > 1, \end{cases} \tag{4.10}$$

$$f_{I\!P/p}(\xi,t) = \frac{\beta_{I\!Ppp}^2(t)}{16\pi}\xi^{1-2\alpha_{I\!P}(t)} = \frac{\beta_{I\!Ppp}^2(0)}{16\pi}\frac{F_1(t)^2}{\xi^{1+2\epsilon+2\alpha' t}}, \tag{4.11}$$

$$F_1(t) = \frac{4m_p^2 - 2.8t}{4m_p^2 - t}\left(\frac{1}{1 - t/(0.71\ \text{GeV}^2)}\right)^2 \tag{4.12}$$

$$N(s) = \int_{\xi_{min}}^{\xi_{max}}\int_{-\infty}^{0} f_{I\!P/p}(\xi,t)d\xi dt \approx 0.41 s^{2\epsilon}, \tag{4.13}$$

$$\sigma_T^{I\!Pp}(s\xi) = \beta_{I\!Ppp}(0)g(0)(s\xi)^\epsilon = \sigma_0^{I\!Pp}(s\xi)^\epsilon, \tag{4.14}$$

$$f_{\pi/p}(\xi,t) = \frac{1}{4\pi}\frac{g_{\pi pp}^2}{4\pi}\frac{|t|}{(t - m_\pi^2)^2}G_1(t)^2\xi^{1-2\alpha_\pi(t)}, \tag{4.15}$$

$$\sigma_T^{\pi p}(s\xi) = \frac{1}{2}(\sigma^{\pi^+ p} + \sigma^{\pi^- p}) = 10.83(s\xi)^{0.104} + 27.13(s\xi)^{-0.32} \quad \text{mb}, \tag{4.16}$$

$$G_1(t) = \frac{2.3\ \text{GeV}^2 - m_\pi^2}{2.3\ \text{GeV}^2 - t}, \tag{4.17}$$

where $f_{I\!P/p}(\xi,t)$ is the standard pomeron flux factor, $\beta_{I\!Ppp}(t)$ is the coupling of the pomeron to the proton, $\alpha_{I\!P}(t) = 1 + \epsilon + \alpha' t$ is the pomeron trajectory, $F_1(t)$ is the isoscalar electromagnetic form factor of the proton, $\xi_{min} = 1.5\ \text{GeV}^2/s$ is the effective diffractive threshold, $\xi_{max} = 0.1$, $g(t)$ is the triple-pomeron coupling, $g_{\pi pp}$ is the on mass-shell coupling of the pion to the proton with $g_{\pi pp}^2/4\pi \approx 14.6\ \text{GeV}^{-2}$,

$\alpha_\pi(t) = 0.9\ \mathrm{GeV}^{-2}\, t$ is the pion trajectory, and $G_1(t)$ is a pion form factor introduced to account for off mass-shell corrections. In Eqs. (4.13), (4.14) and (4.16), s is in units of GeV^2. Only $g(0)$ is treated as a free parameter in the fit. With $\epsilon = 0.104$, $\alpha' = 0.25\ \mathrm{GeV}^{-2}$ and $\beta_{I\!Ppp}(0) = 6.57\ \mathrm{GeV}^{-1}$, the fit yields $g(0) = 1.1\ \mathrm{GeV}^{-1}$, and thus $\sigma_0^{I\!Pp} = \beta_{I\!Ppp}(0)g(0) = 2.8$ mb.

From the global fit result, we obtain

$$\sigma_{SD\ incl}^{1800\ GeV}(\text{global fit}) = 0.59 \pm 0.06(\text{syst})\ \text{mb}$$

$$(\sigma_{I\!P} = 0.32\ \text{mb},\ \sigma_\pi = 0.27\ \text{mb})$$

for the diffractive inclusive cross section at $\sqrt{s} = 1800$ GeV integrated over $0.035 \leq \xi \leq 0.095$ and $|t| \leq 1.0\ \mathrm{GeV}^2$, and

$$\sigma_{SD\ incl}^{630\ GeV}(\text{global fit}) = 0.41 \pm 0.04(\text{syst})\ \text{mb}$$

$$(\sigma_{I\!P} = 0.24\ \text{mb},\ \sigma_\pi = 0.17\ \text{mb})$$

at $\sqrt{s} = 630$ GeV for the region $0.035 \leq \xi \leq 0.095$ and $|t| \leq 0.2\ \mathrm{GeV}^2$.

Summary of Diffractive Inclusive Cross Section

The value of $\sigma_{SD\ incl}^{1800\ GeV}$(global fit) obtained from the global fit is lower than that of $\sigma_{SD\ incl}^{1800\ GeV}$(CDF fit) obtained from the CDF fit by 2.4 σ. However, we note that (a) the cross section from the CDF fit at $\sqrt{s} = 1800$ GeV could have a sizable systematic uncertainty due to the relatively large background subtraction (see Table 1 of Ref. [30]), and (b) the global fit prediction agrees within a few % with the measured CDF cross section at $\sqrt{s} = 546$ GeV, where the subtracted background is substantially lower. With these considerations, we use the cross section from the CDF fit, but assign to it an overall 20 % uncertainty:

$$\sigma_{SD\ incl}^{1800\ GeV}(0.035 \leq \xi \leq 0.095,\ |t| \leq 1.0\ \mathrm{GeV}^2) = 0.78 \pm 0.16\ \text{mb}.$$

At $\sqrt{s} = 630$ GeV, we obtain $\sigma_{SD\ incl}^{630\ GeV}$(global fit) $= 0.41 \pm 0.04$(syst) mb of diffractive inclusive cross section for the region $0.035 \leq \xi \leq 0.095$ and $|t| \leq 0.2$ GeV^2, which is comparable to $\sigma_{SD\ incl}^{630\ GeV}$(CDF fit) $= 0.42 \pm 0.02$(stat) mb. Again, we use the cross section of 0.42 mb from the CDF fit and assign to it an uncertainty of 0.04 mb:

$$\sigma_{SD\ incl}^{630\ GeV}(0.035 \leq \xi \leq 0.095,\ |t| \leq 0.2\ \text{GeV}^{-2}) = 0.42 \pm 0.04\ \text{mb}.$$

4.4.2 Diffractive Dijet Samples

The selected diffractive dijet events must be normalized to the corresponding cross sections when we evaluate the ratio of diffractive dijet to non-diffractive dijet production rates in Chapter 5. The diffractive dijet cross section is evaluated from the ratio of the number of diffractive dijet events to the number of diffractive inclusive events whose cross section was obtained in Section 4.4.1.

Diffractive Dijet Cross Sections at $\sqrt{s} = 1800$ GeV

For the 1800 GeV data sample, the cross section σ_{SD}^{jj} is obtained as

$$\sigma_{SD}^{jj} = R_{\frac{jj}{incl}}^{SD} \times \sigma_{SD}^{incl}, \tag{4.18}$$

$$R_{\frac{jj}{incl}}^{SD} = \left[\frac{N_{SD}^{jj} \cdot (1 - F_{SD\,jj}^{ND\,BG})}{\epsilon_{SD\,jj}^{HTFLT} \cdot \epsilon_{SD\,jj}^{1vtx}} \ / \ \frac{N_{SD}^{incl} \cdot (1 - F_{SD\,incl}^{ND\,BG}) \cdot (1 - F_{SD\,incl}^{GAS})}{\epsilon_{SD\,incl}^{1vtx}} \right], \tag{4.19}$$

where σ_{SD}^{incl} is the diffractive inclusive cross section, N_{SD}^{incl} and N_{SD}^{jj} are the numbers of diffractive inclusive and diffractive dijet events, $F_{SD\,incl}^{GAS}$ is the beam-gas background fraction in the diffractive inclusive sample, $F_{SD\,incl}^{ND\,BG}$ and $F_{SD\,jj}^{ND\,BG}$ are the fractions of non-diffractive overlap background in the diffractive inclusive and diffractive dijet samples, $\epsilon_{SD\,incl}^{1vtx}$ and $\epsilon_{SD\,jj}^{1vtx}$ are the single vertex cut efficiencies (fraction of single interaction events retained by the single vertex cut) for the diffractive inclusive and

Table 4.5: Number of events, efficiencies and background fractions for the 1800 GeV diffractive dijet and diffractive inclusive samples.

SD inclusive events	N_{SD}^{incl}	$1,638,695 \pm 1,280$
after RP acceptance correction		$2,086,088 \pm 1,726$
ND overlap background fraction	$F_{SD\,incl}^{ND\,BG}$	3.0 ± 1.5 %
Beam-gas background fraction	$F_{SD\,incl}^{GAS}$	5.2 %
Single vertex cut efficiency	$\epsilon_{SD\,incl}^{1vtx}$	87.8 ± 1.2 %
SD dijet events ($E_T^{jet1,2} \geq 7$ GeV)	N_{SD}^{jj}	$30,410 \pm 174.4$
after RP acceptance correction		$38,138.7 \pm 230.5$
ND overlap background fraction	$F_{SD\,jj}^{ND\,BG}$	7.0 ± 0.7 %
Single vertex cut efficiency	$\epsilon_{SD\,jj}^{1vtx}$	80.5 ± 1.9 %
Hot tower filter efficiency	$\epsilon_{SD\,jj}^{HTFLT}$	97.1 ± 0.5 %
SD dijet events ($E_T^{jet1,2} \geq 10$ GeV)	N_{SD}^{jj}	$5,508 \pm 74.2$
after RP acceptance correction		$6,854.5 \pm 97.2$
ND overlap background fraction	$F_{SD\,jj}^{ND\,BG}$	9.4 ± 0.9 %
Single vertex cut efficiency	$\epsilon_{SD\,jj}^{1vtx}$	77.8 ± 2.2 %
Hot tower filter efficiency	$\epsilon_{SD\,jj}^{HTFLT}$	97.1 ± 0.5 %
SD dijet events ($E_T^{jet1,2} \geq 15$ GeV)	N_{SD}^{jj}	633 ± 25.2
after RP acceptance correction		805.0 ± 33.8
ND overlap background fraction	$F_{SD\,jj}^{ND\,BG}$	8.5 ± 0.9 %
Single vertex cut efficiency	$\epsilon_{SD\,jj}^{1vtx}$	76.8 ± 2.3 %
Hot tower filter efficiency	$\epsilon_{SD\,jj}^{HTFLT}$	97.1 ± 0.5 %

diffractive dijet samples, and $\epsilon_{SD\,jj}^{HTFLT}$ is the hot tower filter efficiency. All values needed to evaluate $R_{\frac{incl}{jj}}^{SD}$ from Eq. (4.19) are summarized in Table 4.5. First, ignoring the difference in the Roman Pot acceptance between the diffractive inclusive and dijet samples, we obtain a cross section of 16.5 ± 0.1(stat) μb for diffractive dijet events with $E_T^{jet1,2} \geq 7$ GeV.

The Roman Pot acceptance for the 1800 GeV data sample is shown in Figure 3.16 as a function of ξ and t in steps of $\Delta\xi = 0.005$ and $\Delta t = 0.10$ GeV^2. In order to correct the number of diffractive inclusive and diffractive dijet events for the Roman Pot acceptance, each event is weighted by $1/A(\xi_i, t_i)$, where $A(\xi_i, t_i)$ is the Roman

Pot acceptance for the ξ-t bin of the event, and the statistical error is evaluated as $\sqrt{\sum_{i=1}^{N_{SD}} (1/A(\xi_i, t_i))^2}$. This procedure yields $N_{SD}^{incl} = 2086088 \pm 1726$ and $N_{SD}^{jj} = 38138.7 \pm 230.5$ for diffractive inclusive events and for diffractive dijet events with $E_T^{jet1,2} \geq 7$ GeV. From these numbers, a cross section of 16.3 ± 0.1(stat) μb is obtained for diffractive dijet events with $E_T^{jet1,2} \geq 7$ GeV. Similarly, cross sections of 2.95 ± 0.04(stat) μb and 0.355 ± 0.015(stat) μb are obtained for diffractive dijet events with $E_T^{jet1,2} \geq 10$ and 15 GeV, respectively.

Diffractive Dijet Cross Sections at $\sqrt{s} = 630$ GeV

For the 630 GeV data sample, an additional cut is imposed on the west BBC multiplicity. Therefore, the efficiencies of the west BBC multiplicity cut, $\epsilon_{SD\,jj}^{WBBC}$ and $\epsilon_{SD\,incl}^{WBBC}$, have to be taken into account to get the ratio $R_{\frac{jj}{incl}}^{SD}$. The hot tower filter efficiency is set to 100 % in the 630 GeV data analysis, as described in Appendix D.2, and thus can be ignored. The ratio $R_{\frac{jj}{incl}}^{SD}$ is given by

$$R_{\frac{jj}{incl}}^{SD} = \left[\frac{N_{SD}^{jj} \cdot (1 - F_{SD\,jj}^{ND\,BG})}{\epsilon_{SD\,jj}^{1vtx} \cdot \epsilon_{SD\,jj}^{WBBC}} \;/\; \frac{N_{SD}^{incl} \cdot (1 - F_{SD\,incl}^{ND\,BG}) \cdot (1 - F_{SD\,incl}^{GAS})}{\epsilon_{SD\,incl}^{1vtx} \cdot \epsilon_{SD\,incl}^{WBBC}} \right]. \qquad (4.20)$$

All values needed in Eq. (4.20) are summarized in Table 4.6. When the difference in the Roman Pot acceptance between the diffractive inclusive and dijet samples is ignored, a cross section of 2.67 ± 0.08(stat) μb is obtained for diffractive dijet events with $E_T^{jet1,2} \geq 7$ GeV, and 0.63 ± 0.04(stat) μb for diffractive dijet events with $E_T^{jet1,2} \geq 7$ GeV and $E_T^* = (E_T^{jet1} + E_T^{jet2})/2 \geq 10$ GeV.

When the Roman Pot acceptance is taken into account on an event-by-event basis, a cross section of 2.54 ± 0.08(stat) μb is obtained for diffractive dijet events with $E_T^{jet1,2} \geq 7$ GeV, and 0.60 ± 0.04(stat) μb for diffractive dijet events with $E_T^{jet1,2} \geq 7$ GeV and $E_T^* = (E_T^{jet1} + E_T^{jet2})/2 \geq 10$ GeV.

Table 4.6: Number of events, efficiencies and background fractions for the 630 GeV diffractive dijet and diffractive inclusive samples.

SD inclusive events	N_{SD}^{incl}	$184,327 \pm 429$
after RP acceptance correction		$304,117 \pm 771$
Beam-gas background fraction	$F_{SD\,incl}^{GAS}$	2.4 %
ND overlap background fraction	$F_{SD\,incl}^{ND\,BG}$	2.9 ± 0.9 %
West BBC multiplicity cut efficiency	$\epsilon_{SD\,incl}^{WBBC}$	97.9 ± 0.4 %
Single vertex cut efficiency	$\epsilon_{SD\,incl}^{1vtx}$	88.4 ± 1.2 %
SD dijet events ($E_T^{jet1,2} \geq 7$ GeV)	N_{SD}^{jj}	$1,186 \pm 34.4$
after RP acceptance correction		$1,860.3 \pm 57.8$
ND overlap background fraction	$F_{SD\,jj}^{ND\,BG}$	6.4 ± 2.2 %
West BBC multiplicity cut efficiency	$\epsilon_{SD\,jj}^{WBBC}$	98.1 ± 1.9 %
Single vertex cut efficiency	$\epsilon_{SD\,jj}^{1vtx}$	88.0 ± 1.2 %
SD dijet events ($(E_T^{jet1} + E_T^{jet2})/2 \geq 10$ GeV)	N_{SD}^{jj}	283 ± 16.8
after RP acceptance correction		443.2 ± 28.5
ND overlap background fraction	$F_{SD\,jj}^{ND\,BG}$	8.3 ± 2.8 %
West BBC multiplicity cut efficiency	$\epsilon_{SD\,jj}^{WBBC}$	97.4 ± 2.6 %
Single vertex cut efficiency	$\epsilon_{SD\,jj}^{1vtx}$	87.4 ± 1.3 %

The diffractive dijet cross sections and the non-diffractive dijet cross sections discussed in Section 4.4.3 have a sizable systematic uncertainty mainly due to jet energy calibration and jet energy resolution effects, since the jet E_T distributions for both diffractive dijet and non-diffractive dijet events are falling sharply with increasing jet E_T, as shown later in Figure 4.29. The systematic uncertainties in the absolute cross sections for diffractive dijet and non-diffractive dijet events are not quoted in this dissertation. These uncertainties cancel out to some extent in the ratio of the diffractive dijet to non-diffractive dijet cross sections, since the jet E_T distributions for diffractive dijet and non-diffractive dijet events are very similar. The systematic uncertainties in the ratio of diffractive dijet to non-diffractive dijet event rates are discussed in Section 4.4.4.

4.4.3 Non-Diffractive Dijet Samples

The selected non-diffractive dijet events are normalized to the corresponding cross sections as

$$\sigma_{ND}^{jj} = \frac{N_{ND}^{jj}}{N_{ND}^{incl} \cdot \langle N \rangle \cdot \epsilon_{ND}^{z_{vtx}}} \cdot \sigma_{BBC}, \tag{4.21}$$

where N_{ND}^{incl} and N_{ND}^{jj} are the numbers of non-diffractive inclusive and non-diffractive dijet events, respectively, $\langle N \rangle$ is the average number of interactions in each minimum bias (MB) event, $\epsilon_{ND}^{z_{vtx}}$ is the efficiency of the cut $|z_{vtx}| \leq 60$ cm, and σ_{BBC} is the effective BBC cross section. The effective BBC cross section is $\sigma_{BBC} = 51.15 \pm 1.60$ mb at $\sqrt{s} = 1800$ GeV [59], and $\sigma_{BBC} = 39.9 \pm 1.2$ mb at $\sqrt{s} = 630$ GeV [60]. For the non-diffractive inclusive events, the z_{vtx} cut is not applied in this case in order to retain events without a reconstructed vertex due to vertex reconstruction ambiguities.

The value of $\langle N \rangle$ is obtained as follows. The average number of minimum bias interactions per bunch crossing during the 1800 and 630 GeV runs is given by

$$n = \frac{\mathcal{L}_{inst} \cdot \sigma_{BBC} \cdot C_{acc}(\mathcal{L}_{inst})}{f_0}, \tag{4.22}$$

where $f_0 = 286.278$ kHz is the frequency of bunch crossings at the Tevatron, $\mathcal{L}_{inst}$ is the instantaneous luminosity in units of 10^{30} cm^{-2}s^{-1}, and $C_{acc}(\mathcal{L}_{inst})$ is a correction factor for $\mathcal{L}_{inst}$ due to accidental BBC east-west coincidences This factor is $C_{acc}(\mathcal{L}_{inst}) = 1 - 0.002704 \cdot \mathcal{L}_{inst}$ for the 1800 GeV data, and is set to $C_{acc}(\mathcal{L}_{inst}) = 1$ for the 630 GeV data. The number of minimum bias interactions per bunch crossing obeys Poisson statistics, i.e. $P(i) = e^{-n} n^i / i!$. Therefore, the average number of minimum bias interactions in each minimum bias event triggered by a BBC east-west coincidence is given by

$$\langle N \rangle = \frac{\sum_{i=1}^{\infty} P(i) \cdot i}{\sum_{i=1}^{\infty} P(i)} = \frac{n}{1 - e^{-n}}. \tag{4.23}$$

By taking the average of Eq. (4.23) weighted over the entire data sample, $\langle N \rangle = 1.045$ (1.074) is obtained for the 1800 (630) GeV data.

The value of $\epsilon_{ND}^{z_{vtx}}$ is evaluated as follows. The z_{vtx} distribution in minimum bias events fits the form:

$$\frac{d\mathcal{L}}{dz} \propto e^{-\frac{z^2}{2\sigma_z^2}} \Big/ \left(1 + \frac{(z - z_{min})^2}{\beta^{*2}}\right), \tag{4.24}$$

where z_{min} is the mean of the z_{vtx} distribution, β^* is the Tevatron β parameter, and σ_z is the longitudinal beam bunch length. Results of fits in the region $|z_{vtx}| \leq 60$ cm are shown in Figure 4.16. The efficiency can be evaluated by calculating $\epsilon_{ND}^{z_{vtx}} = \int_{-60\text{ cm}}^{+60\text{ cm}} \mathcal{L}dz / \int_{-\infty}^{\infty} \mathcal{L}dz$. This calculation yields the value $\epsilon_{ND}^{z_{vtx}} = 95.7$ (86.1) % for the 1800 (630) GeV data, to which we assign a 2 % uncertainty [72, 73].

Using Eq. (4.21), non-diffractive dijet cross sections of 5.04 ± 0.03(stat) mb, 1.63 ± 0.02(stat) mb and 0.230 ± 0.006(stat) mb are obtained for dijet events with $E_T^{jet1,2} \geq 7$, 10 and 15 GeV, respectively, and 2.65 ± 0.02(stat) mb for dijet events with $E_T^{jet1,2} \geq 7$ GeV and $E_T^* = (E_T^{jet1} + E_T^{jet2})/2 \geq 10$ GeV, all at $\sqrt{s} = 1800$ GeV.

Similarly, at $\sqrt{s} = 630$ GeV, non-diffractive dijet cross sections of 1.800 ± 0.006(stat) mb are obtained for dijet events with $E_T^{jet1,2} \geq 7$, and 0.599 ± 0.003(stat) mb for dijet events with $E_T^{jet1,2} \geq 7$ GeV and $E_T^* = (E_T^{jet1} + E_T^{jet2})/2 \geq 10$ GeV.

4.4.4 Ratio of Diffractive Dijet to Non-Diffractive Dijet Cross Sections

From the single diffractive (SD) dijet and non-diffractive (ND) dijet cross sections obtained in Sections 4.4.2 and 4.4.3, the ratio of the SD dijet to ND dijet cross sections (event rates) can be obtained. The systematic uncertainties associated with the normalization of this ratio are discussed below.

Uncertainty due to Jet Energy Scale

In addition to the uncertainties associated with the background fractions and the selection cut efficiencies, which have already been discussed, the uncertainty due to the jet energy scale has to be considered. The jet energy scale uncertainty is estimated to be [74, 75]

$$\delta E_T^{jet} = \begin{cases} \pm 5.6\ \% & (|\eta^{jet}| < 2.4), \\ \pm 6.1\ \% & (|\eta^{jet}| \geq 2.4) \end{cases}$$

for the dijet event samples of $E_T^{jet1,2} \geq 7$ and 10 GeV, and

$$\delta E_T^{jet} = \begin{cases} \pm 4.1\ \% & (|\eta^{jet}| < 2.4), \\ \pm 4.8\ \% & (|\eta^{jet}| \geq 2.4) \end{cases}$$

for the dijet event samples of $E_T^{jet1,2} \geq 15$ GeV.

By changing the jet E_T scale by $\pm\delta E_T$ in the 1800 GeV SD dijet and ND dijet event samples simultaneously, we observe a variation of $^{+7.3}_{-8.2}$, $^{+5.3}_{-4.0}$ and $^{+6.0}_{-4.2}$ % in the SD/ND ratio for the dijet event samples of $E_T^{jet1,2} \geq 7$, $E_T^{jet1,2} \geq 10$ and $E_T^{jet1,2} \geq 15$ GeV, respectively. In a conservative approach, we choose the larger of the two values, yielding uncertainties in the SD/ND dijet event ratio of ± 8.2 %, ± 5.3 % and ± 6.0 % for the 1800 GeV dijet event samples of $E_T^{jet1,2} \geq 7$, $E_T^{jet1,2} \geq 10$ and $E_T^{jet1,2} \geq 15$ GeV. Similarly, the uncertainties in the SD/ND dijet event ratio are estimated to be ± 10 % for the 630 GeV dijet event samples of $E_T^{jet1,2} \geq 7$ GeV and ± 12 % for $E_T^{jet1,2} \geq 7$ GeV and $E_T^* = (E_T^{jet1} + E_T^{jet2})/2 \geq 10$ GeV.

Uncertainty due to Underlying Event Correction

The uncertainty due to the underlying event subtraction is mainly due to the uncertainty in the difference in underlying event E_T between SD and ND events. Changing the underlying event E_T to be subtracted from ND (SD) jet E_T by $\pm$

30 % results in a variation of $^{+13.8}_{-12.2}$ % ($^{+11.1}_{-9.7}$ %) in the SD/ND ratio for the dijet event samples of $E_T^{jet1,2} \geq 7$ GeV. For the $E_T^{jet1,2} \geq 10$ GeV dijet event samples, the resulting variation is $^{+15.7}_{-14.0}$ % ($^{+9.0}_{-9.0}$ %), and for the $E_T \geq 15$ GeV dijet event samples $^{+14.3}_{-14.8}$ % ($^{+4.0}_{-6.8}$ %). Again, by conservatively choosing the larger of the two values, the uncertainty in the SD/ND dijet event ratio is estimated to be 14 %, 16 % and 15 % for the 1800 GeV dijet event samples of $E_T^{jet1,2} \geq 7$, $E_T^{jet1,2} \geq 10$ and $E_T^{jet1,2} \geq 15$ GeV, respectively. Similarly, for the 630 GeV data, the uncertainty in the SD/ND dijet event ratio is estimated to be 18 % for the 630 GeV dijet event samples of $E_T^{jet1,2} \geq 7$ GeV, and of $E_T^{jet1,2} \geq 7$ GeV and $E_T^* = (E_T^{jet1} + E_T^{jet2})/2 \geq 10$ GeV.

Summary of the SD/ND Ratio

These uncertainties are added in quadrature to the uncertainty in the SD/ND dijet event ratio stemming from the separate uncertainties in the SD and ND data samples. The systematic uncertainties associated with the normalization of the ratio are summarized in Table 4.7 for the 1800 GeV data and in Table 4.8 for the 630 GeV data. The overall systematic uncertainty in the SD/ND dijet event ratio is 26 %, 27 % and 26 % for the 1800 GeV dijet event samples of $E_T^{jet1,2} \geq 7$, $E_T^{jet1,2} \geq 10$ and $E_T^{jet1,2} \geq 15$ GeV, respectively. Including systematic uncertainties, the ratios of the SD dijet to ND dijet cross sections in the region $0.035 \leq \xi \leq 0.095$ and $|t| \leq 1.0$ GeV^2 for 1800 GeV dijet events with $E_T^{jet1,2} \geq 7$, 10 and 15 GeV are

$$R_{\frac{SD}{ND}}^{1800\ GeV}(E_T^{jet1,2} \geq 7\ \text{GeV}) = 0.323 \pm 0.003(\text{stat}) \pm 0.085(\text{syst})\ \%,$$

$$R_{\frac{SD}{ND}}^{1800\ GeV}(E_T^{jet1,2} \geq 10\ \text{GeV}) = 0.182 \pm 0.003(\text{stat}) \pm 0.048(\text{syst})\ \%,$$

$$R_{\frac{SD}{ND}}^{1800\ GeV}(E_T^{jet1,2} \geq 15\ \text{GeV}) = 0.154 \pm 0.008(\text{stat}) \pm 0.040(\text{syst})\ \%.$$

The overall systematic uncertainty in the SD/ND dijet event ratio is 23 % and 24 % for the 630 GeV dijet event samples of $E_T^{jet1,2} \geq 7$ GeV and of $E_T^{jet1,2} \geq 7$ GeV

and $E_T^* = (E_T^{jet1} + E_T^{jet2})/2 \geq 10$ GeV, respectively. The ratio of the SD dijet to ND dijet cross sections in the region $0.035 \leq \xi \leq 0.095$ and $|t| \leq 0.2$ GeV^2 for 630 GeV dijet events with $E_T^{jet1,2} \geq 7$ GeV is

$$R_{\frac{SD}{ND}}^{630\ GeV}(E_T^{jet1,2} \geq 7\ \text{GeV}) = 0.141 \pm 0.004(\text{stat}) \pm 0.014(\text{syst})\ \%,$$

and for dijet events with $E_T^{jet1,2} \geq 7$ GeV and $E_T^* = (E_T^{jet1} + E_T^{jet2})/2 \geq 10$ GeV,

$$R_{\frac{SD}{ND}}^{630\ GeV}(E_T^{jet1,2} \geq 7\ \text{GeV}, E_T^* \geq 10\ \text{GeV}) = 0.100 \pm 0.006(\text{stat}) \pm 0.011(\text{syst})\ \%.$$

The measured ratios at $\sqrt{s} = 1800$ GeV are smaller than the ratio $R_{\frac{SD}{ND}}^{1800\ GeV}(E_T^{jet1,2} \geq 20\ \text{GeV}) = 0.75 \pm (\text{stat}) \pm 0.09(\text{syst})\ \%$ from a previous measurement by the CDF collaboration for dijet events with $E_T^{jet1,2} \geq 20$ GeV, $1.8 < |\eta^{jet1,2}| < 3.5$ and $\eta^{jet1}\eta^{jet2} > 0$ collected at $\sqrt{s} = 1800$ GeV [19]. This is expected from the difference in the jet η range used in the two measurements. In this analysis, all CDF calorimeters covering $-4.2 < \eta < 4.2$ are used, while in the previous CDF measurement, the two leading jets in an event are restricted to the region $1.8 < |\eta^{jet1,2}| < 3.5$. Since jets in SD events are shifted toward the forward direction on the opposite side of the rapidity gap and/or the quasielastically-scattered particles, while jets in ND events are symmetric with respect to $\eta = 0$ as shown later in Figure 4.31, the ratio of SD dijet to ND dijet events is expected to be higher in the forward direction than in the whole η region.

4.5 Comparison of Diffractive Inclusive and Diffractive Dijet Event Kinematics

The top two plots of Figures 4.28(a) and (b) show ξ and t distributions for the diffractive inclusive and diffractive dijet samples collected at $\sqrt{s} = 1800$ and 630

Table 4.7: Systematic uncertainties in the normalization of the single diffractive (SD) dijet to non-diffractive (ND) dijet cross section ratio at $\sqrt{s} = 1800$ GeV.

Source	Systematic uncertainty (%)		
SD sample			
inclusive			
σ_{SD}^{incl}		20 %	
$F_{SD\,incl}^{ND\,BG}$		1.5 %	
$\epsilon_{SD\,incl}^{1vtx}$		1.4 %	
dijets $E_T^{jet1,2}$ threshold	7 GeV	10 GeV	15 GeV
$F_{SD\,jj}^{ND\,BG}$	0.7 %	0.9 %	0.9 %
$\epsilon_{SD\,jj}^{1vtx}$	2.4 %	2.8 %	3.0 %
$\epsilon_{SD\,jj}^{HTFLT}$	2.0 %*	2.0 %*	2.0 %*
Total in SD	20.4 %	20.4 %	20.4 %
ND sample			
σ_{ND}^{incl}, effective BBC cross section		3.1 %	
$\langle N \rangle$, average number of interactions per MB event		1.0 %	
$\epsilon_{ND\,incl}^{z_{vtx}}$		2.1 %	
Total in ND		3.9 %	
SD/ND uncertainty from jet energy			
Absolute jet energy scale	8.2 %	5.3 %	6.0 %
Underlying event subtraction	14 %	16 %	15 %
Total in SD/ND	26 %	27 %	26 %

* A 2 % systematic uncertainty is assigned to account for a possible difference in the hot tower filter efficiency between diffractive and non-diffractive events.

Table 4.8: Systematic uncertainties in the normalization of the single diffractive (SD) dijet to non-diffractive (ND) dijet cross section ratio at $\sqrt{s} = 630$ GeV.

Source	Systematic uncertainty	
SD sample		
inclusive		
σ_{SD}^{incl}	9.5 %	
$F_{SD\ incl}^{ND\ BG}$	0.9 %	
$\epsilon_{SD\ incl}^{1vtx}$	1.4 %	
$\epsilon_{SD\ incl}^{WBBC}$	0.4 %	
dijet	$E_T^{jet1,2} \geq 7$ GeV	+ $E_T^* \geq 10$ GeV
$F_{SD\ jj}^{ND\ BG}$	2.4 %	3.1 %
$\epsilon_{SD\ jj}^{1vtx}$	1.4 %	1.5 %
$\epsilon_{SD\ jj}^{WBBC}$	2.0 %	2.7 %
Total in SD	10.2 %	10.6 %
ND sample		
σ_{ND}^{incl}, effective BBC cross section	3.0 %	
$\langle N \rangle$, average number of interactions per MB event	0.9 %	
$\epsilon_{ND\ incl}^{z_{vtx}}$	2.3 %	
Total in ND	3.9 %	
SD/ND uncertainty from jet energy		
Absolute jet energy scale	10 %	12 %
Underlying event subtraction	18 %	18 %
Total in SD/ND	23 %	24 %

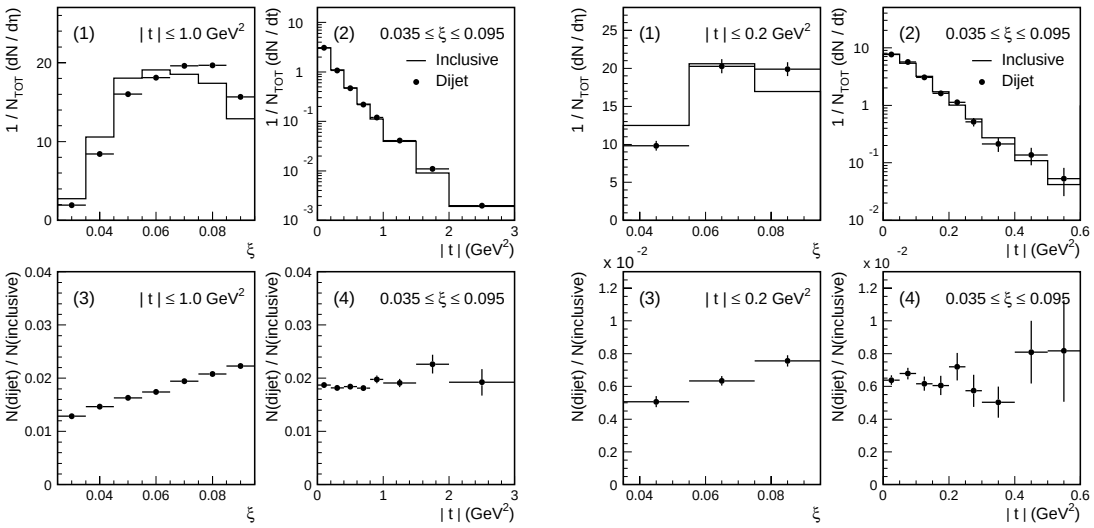

(a) 1800 GeV (b) 630 GeV

Figure 4.28: Distributions of (1) ξ and (2) $|t|$ for the diffractive inclusive (histograms) and diffractive dijet (points) data samples, and the ratio of diffractive dijet events to diffractive inclusive events as a function of (3) ξ and (4) $|t|$ for the (a) 1800 GeV and (b) 630 GeV data samples. The dijet data samples are selected by requiring at least two jets with $E_T \geq 7$ GeV in an event.

GeV. The ratio of diffractive dijet events to diffractive inclusive events is shown as a function of ξ and t in the bottom two plots of Figures 4.28(a) and (b).

The distributions for the 1800 and 630 GeV data samples show similar trends, which are summarized below.

- The diffractive dijet events favor larger ξ values relative to the diffractive inclusive events.

- The ratio of diffractive dijet events to diffractive inclusive events has an approximately flat t-dependence.

4.6 Comparison of Diffractive Dijet and Non-Diffractive Dijet Kinematics

In this section, jet kinematic properties are compared between diffractive dijet and non-diffractive dijet events. Figure 4.29 shows distributions of E_T of the leading two jets and of the mean E_T of the leading two jets, $E_T^* = (E_T^{jet1} + E_T^{jet2})/2$, for the $E_T^{jet1,2} \geq 7$ GeV diffractive dijet and non-diffractive dijet samples collected at $\sqrt{s} = 1800$ and 630 GeV. It is found that jet E_T distributions for diffractive dijet events are similar to, but somewhat steeper than those for non-diffractive dijet events. The steeper jet E_T spectrum of diffractive dijet events may indicate that the x-dependence of the diffractive structure function of the antiproton is steeper than that of the usual non-diffractive one. The x-dependence of the diffractive structure function relative to the non-diffractive one is studied in Chapter 5. At high E_T ($E_T \gtrsim 15$ GeV), the E_T spectra for diffractive jets and non-diffractive jets become similar, as shown in Figure 4.30. This result is consistent with results from a study of diffractive dijet production by the DØ collaboration [20].

Figure 4.31 shows distributions of the pseudorapidity η of the leading two jets and of the mean η of the leading two jets, $\eta^* = (\eta^{jet1} + \eta^{jet2})/2$, for the $E_T^{jet1,2} \geq 7$ GeV diffractive dijet and non-diffractive dijet samples collected at $\sqrt{s} = 1800$ and 630 GeV. It is seen that the η of jets in diffractive dijet events is boosted toward the proton outgoing (positive η) direction.

Figure 4.32 shows distributions of the azimuthal angle difference $\Delta\phi_{jj}$ between the leading two jets for diffractive dijet and non-diffractive dijet events with $E_T^{jet1,2} \geq 7$ GeV. The $\Delta\phi_{jj}$ distributions show a back-to-back structure; however, they have a relatively long tail toward $\Delta\phi_{jj} = 0$, which may be due to either the contribution of

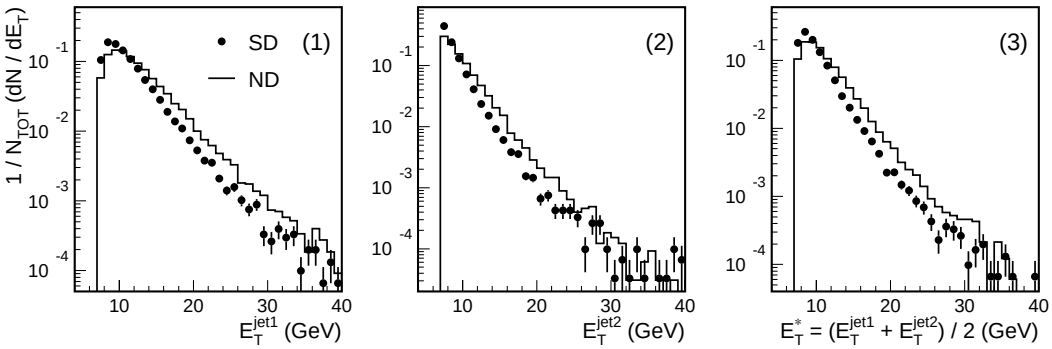

(a) 1800 GeV

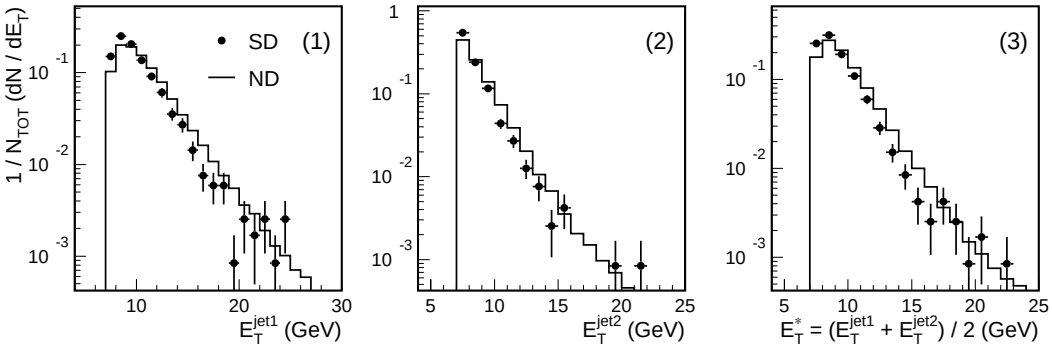

(b) 630 GeV

Figure 4.29: Distributions of (1) the leading jet E_T (E_T^{jet1}), (2) the next-to-leading jet E_T (E_T^{jet2}), and (3) the mean E_T of the leading two jets, $E_T^* = (E_T^{jet1} + E_T^{jet2})/2$, for the $E_T^{jet1,2} \geq 7$ GeV diffractive dijet (points) and non-diffractive dijet (histograms) samples collected at (a) $\sqrt{s} = 1800$ GeV and (b) $\sqrt{s} = 630$ GeV.

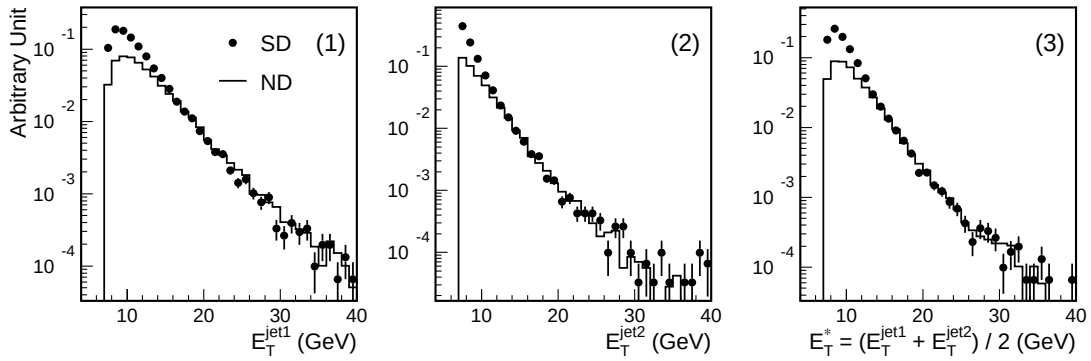

(a) 1800 GeV

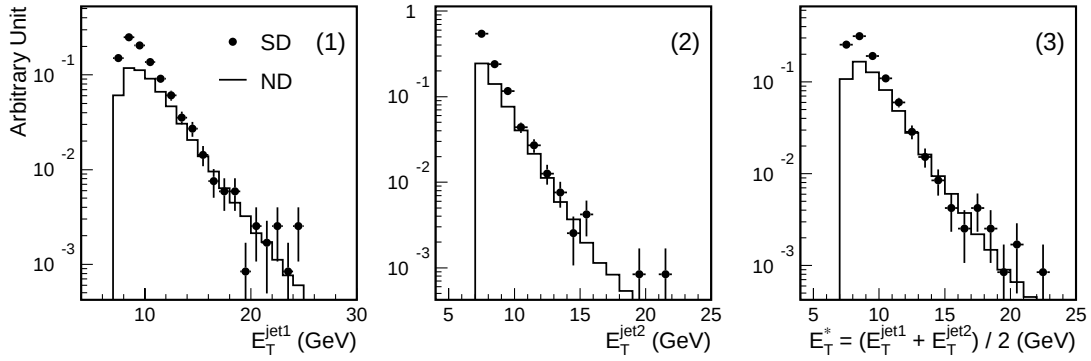

(b) 630 GeV

Figure 4.30: Distributions of (1) the leading jet E_T (E_T^{jet1}), (2) the next-to-leading jet E_T (E_T^{jet2}), and (3) the mean E_T of the leading two jets, $E_T^* = (E_T^{jet1} + E_T^{jet2})/2$, for the $E_T^{jet1,2} \geq 7$ GeV diffractive dijet (points) and non-diffractive dijet (histograms) samples collected at (a) $\sqrt{s} = 1800$ GeV and (b) $\sqrt{s} = 630$ GeV. The non-diffractive distributions are normalized to the diffractive distributions at high E_T ($E_T \geq 15$ GeV).

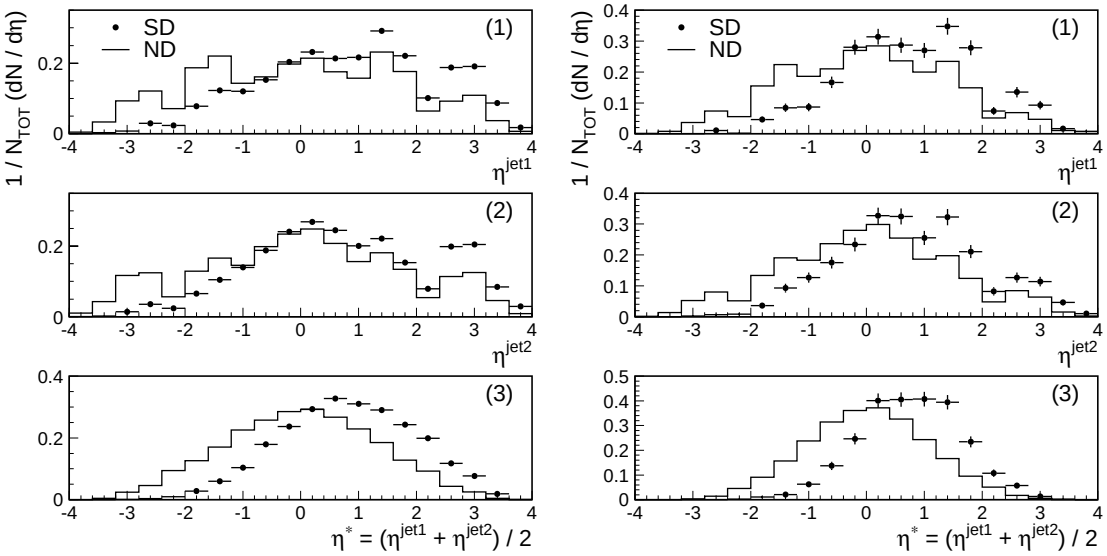

(a) 1800 GeV (b) 630 GeV

Figure 4.31: Distributions of (1) the leading jet η (η^{jet1}), (2) the next-to-leading jet η (η^{jet2}), and (3) the mean η of the leading two jets, $\eta^* = (\eta^{jet1} + \eta^{jet2})/2$, for the $E_T^{jet1,2} \geq 7$ GeV diffractive dijet (points) and non-diffractive dijet (histograms) samples collected at (a) $\sqrt{s} = 1800$ GeV and (b) $\sqrt{s} = 630$ GeV.

higher order QCD processes, or the interference of the underlying event fluctuation. Figure 4.33 shows $\Delta\phi_{jj}$ distributions for dijet events with higher jet E_T values. It is seen that the $\Delta\phi_{jj}$ distribution is more back-to-back for dijet events with higher jet E_T values.

Diffractive dijets are found to be more back-to-back than non-diffractive dijets in both the 1800 and 630 GeV data samples. This feature may be due to the reduced energy available for diffractive dijet events relative to that for non-diffractive dijet events.

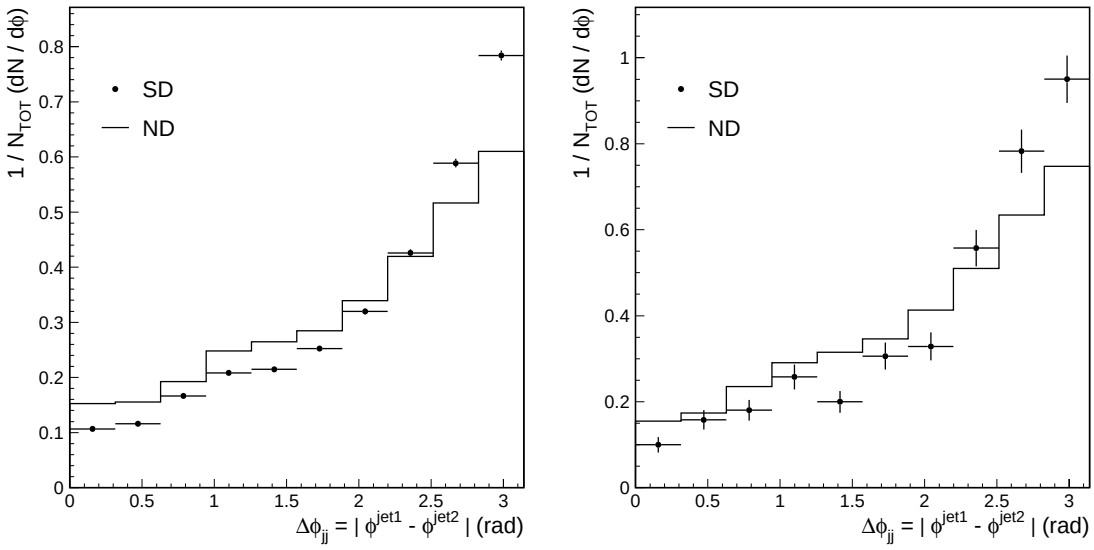

(a) 1800 GeV (b) 630 GeV

Figure 4.32: Distributions of the azimuthal angle difference $\Delta\phi_{jj}$ between the leading two jets for the $E_T^{jet1,2} \geq 7$ GeV diffractive dijet (points) and non-diffractive dijet (histograms) samples collected at (a) $\sqrt{s} = 1800$ GeV and (b) $\sqrt{s} = 630$ GeV.

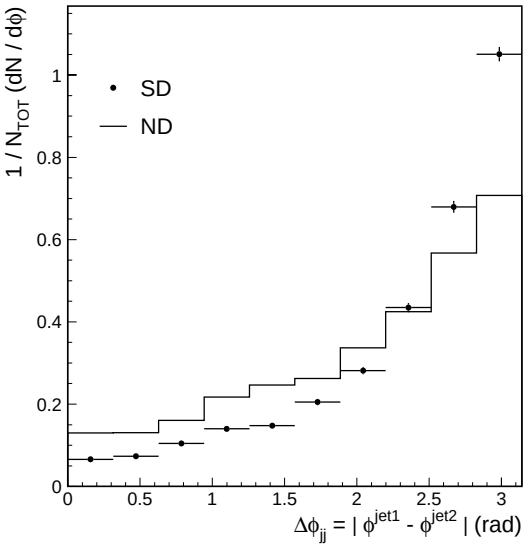

(a) $\sqrt{s} = 1800$ GeV, $E_T^{jet1,2} \geq 7$ GeV, $E_T^* = (E_T^{jet1} + E_T^{jet2})/2 \geq 10$ GeV

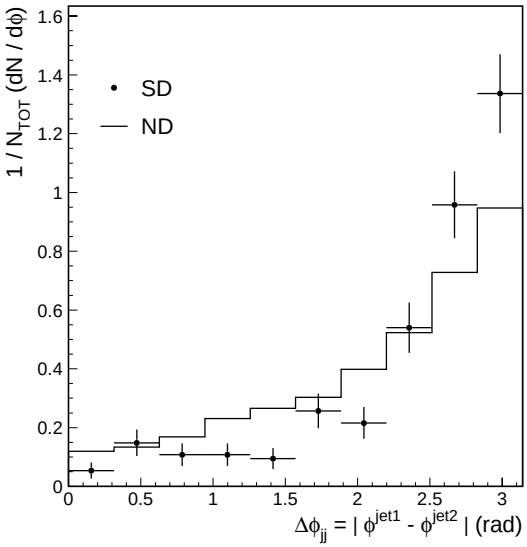

(b) $\sqrt{s} = 630$ GeV, $E_T^{jet1,2} \geq 7$ GeV, $E_T^* = (E_T^{jet1} + E_T^{jet2})/2 \geq 10$ GeV

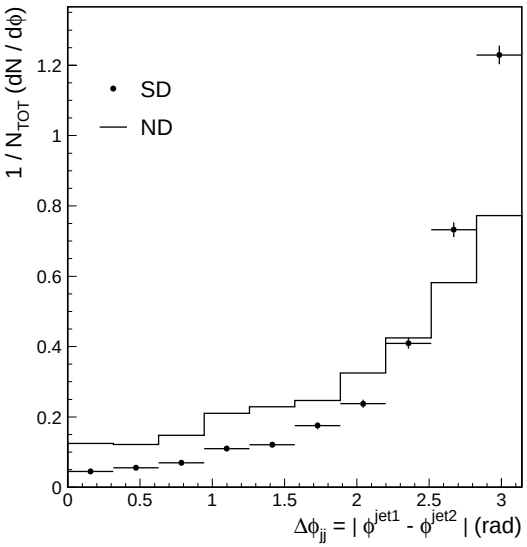

(c) $\sqrt{s} = 1800$ GeV, $E_T^{jet1,2} \geq 10$ GeV

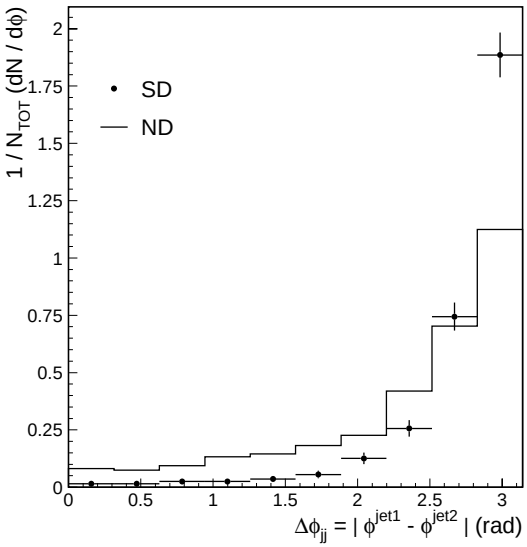

(d) $\sqrt{s} = 1800$ GeV, $E_T^{jet1,2} \geq 15$ GeV

Figure 4.33: Distributions of the azimuthal angle difference $\Delta\phi_{jj}$ between the leading two jets for diffractive dijet (points) and non-diffractive dijet (histograms) events with $E_T^{jet1,2} \geq 7$ GeV and $E_T^* = (E_T^{jet1} + E_T^{jet2})/2 \geq 10$ GeV collected at (a) $\sqrt{s} = 1800$ GeV and (b) $\sqrt{s} = 630$ GeV, and with (c) $E_T^{jet1,2} \geq 10$ GeV and (d) $E_T^{jet1,2} \geq 15$ GeV collected at $\sqrt{s} = 1800$ GeV.

Chapter 5

Measurement of the Diffractive Structure Function

In this chapter, a measurement of the diffractive structure function F_{jj}^D [1] is presented based on the ratio $R_{\frac{SD}{ND}}$ of single diffractive (SD) dijet to non-diffractive (ND) dijet event rates. Section 5.1 presents the ratio $R_{\frac{SD}{ND}}(x_{\bar{p}})$ of SD dijet to ND dijet event rates as a function of x-Bjorken of the antiproton $x_{\bar{p}}$, measured using the 1800 GeV data samples for SD events with a quasielastically-scattered leading antiproton. In Section 5.2, based on the measured $R_{\frac{SD}{ND}}(x_{\bar{p}})$, the diffractive structure function $F_{jj}^D(\beta)$ of the antiproton is extracted as a function of $\beta = x_{\bar{p}}/\xi$, where ξ is the fractional momentum loss of the antiproton. The dependence of $R_{\frac{SD}{ND}}(x_{\bar{p}})$ and $F_{jj}^D(\beta)$ on ξ is also discussed in Sections 5.1 and 5.2, respectively. Then, several comparisons are made to test QCD factorization in diffraction processes. In Section 5.3, the measured $F_{jj}^D(\beta)$ is compared with expectations based on results obtained in diffractive deep inelastic

[1] The diffractive structure function F_{jj}^D and the non-diffractive structure function F_{jj} referred to in this chapter are *effective* structure functions defined in Section 2.3.3. For simplicity, the word "effective" is mostly omitted in this chapter.

scattering experiments at HERA [9, 12]. Section 5.4 presents results on $R_{\frac{SD}{ND}}(x_{\bar{p}})$ and $F_{jj}^{D}(\beta)$ obtained from the 630 GeV data samples, and compares them with results from the 1800 GeV data samples. In Section 5.5, comparisons are made between $R_{\frac{SD}{ND}}(x_{\bar{p}})$ and $R_{\frac{DPE}{SD}}(x_p)$, the ratio of the dijet production rate by double pomeron exchange (DPE) to the SD dijet production rate as a function of x-Bjorken of the proton x_p. In Section 5.6, results on SD dijet production obtained in this analysis are compared with results from a previous analysis of SD J/ψ production [22], in which SD events are identified using the signature of a forward rapidity gap instead of a quasielastically-scattered leading particle. Finally, results on SD dijet production in $p\bar{p}$ collisions at $\sqrt{s} = 630$ GeV and the pomeron structure function obtained by the UA8 collaboration [4] are compared with results from our 630 GeV SD dijet data.

5.1 Ratio of Diffractive Dijet to Non-Diffractive Dijet Rates : $R_{\frac{SD}{ND}}$

In this section, a measurement of the ratio of single diffractive (SD) dijet to non-diffractive (ND) dijet event rates as a function of x-Bjorken $x_{\bar{p}}$ of the antiproton is presented, using the 1800 GeV data samples for SD events with a quasielastically-scattered leading antiproton. For each event, $x_{\bar{p}}$ is evaluated from the E_T and η of the jets using the equation

$$x_{\bar{p}} = \frac{1}{\sqrt{s}} \sum_{i=1}^{n} E_T^i e^{-\eta^i}, \tag{5.1}$$

where E_T^i and η^i are the E_T and η of the i-th highest E_T jet in an event. The sum is carried out over the two leading jets plus the next highest E_T jet if there is one with $E_T \geq 5$ GeV.

Measuring the ratio of SD dijet to ND dijet event rates as a function of $x_{\bar{p}}$ has advantages from both physics and experimental points of view.

- From a physics point of view, the ratio is important because, in leading order QCD, it is approximately equal to the ratio of the diffractive structure function F_{jj}^D to the non-diffractive structure function F_{jj} of the antiproton as a function of $x_{\bar{p}}$. This was discussed in more detail in Section 2.3.3.

- From an experimental point of view, systematic uncertainties due to jet energy reconstruction and detector effects are likely to cancel out in the ratio, because, for a fixed $x_{\bar{p}}$, jets of the same E_T come from similar η regions for both SD and ND events, and thus calorimeter non-uniformity effects are reduced.

Figure 5.1(a) shows $x_{\bar{p}}$ distributions, on a logarithmic scale[2] with a bin width of $\Delta(\log x_{\bar{p}}) = 0.1$, for SD dijet events with $E_T^{jet1,2} \geq 7$ GeV, $0.035 \leq \xi \leq 0.095$ and $|t| \leq 1.0$ GeV^2, along with the estimated ND overlap background contribution. The SD distribution is corrected for the Roman Pot acceptance by weighting each event by $1/A(\xi_i, t_i)$, where $A(\xi_i, t_i)$ is the Roman Pot acceptance in the ξ-t bin of the event. The statistical error on the SD distribution in each bin is evaluated as $\sqrt{\sum_i \left(1/A(\xi_i, t_i)\right)^2}$, where the sum is carried out over the SD dijet events in the bin. The ND overlap background contribution is obtained from the distribution for the ND dijet sample by normalizing it to the background fraction estimated in Section 4.3.2. The statistical error on the ND overlap background distribution is evaluated as the square-root of the number of events after the distribution is normalized to the background fraction of the SD dijet sample. The $x_{\bar{p}}$ distribution for ND dijet events with the same jet E_T cut is shown in Figure 5.1(b). The shape of the $x_{\bar{p}}$ distribution is compared between

[2]Distributions shown as a function of $x_{\bar{p}}$, x_p or β are plotted versus $\log x_{\bar{p}}$, $\log x_p$ or $\log \beta$ and shown versus $x_{\bar{p}}$, x_p or β on a logarithmic scale, unless otherwise stated.

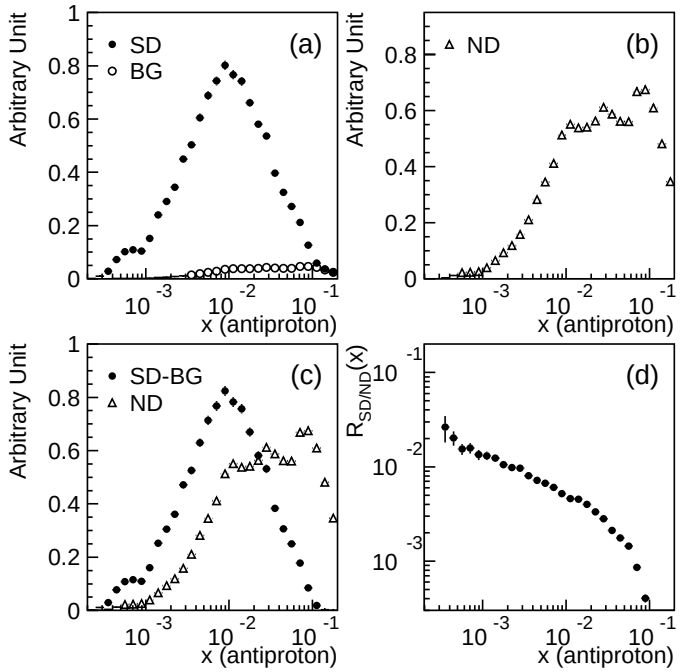

Figure 5.1: (a) Distributions of $x_{\bar{p}}$ for the $E_T^{jet1,2} \geq 7$ GeV SD dijet sample and the estimated ND overlap background contribution. (b) The $x_{\bar{p}}$ distribution for the $E_T^{jet1,2} \geq 7$ GeV ND dijet sample. (c) Shape comparison of $x_{\bar{p}}$ distributions for the SD dijet and ND dijet samples. (d) The ratio of SD to ND event rates for dijet events with $E_T^{jet1,2} \geq 7$ GeV as a function of $x_{\bar{p}}$.

the SD and ND data samples in Figure 5.1(c). In this figure, the estimated ND overlap background contribution is subtracted from the distribution for the SD dijet data sample. Figure 5.1(d) shows the ratio $R_{\frac{SD}{ND}}(x_{\bar{p}})$ of the SD to ND distributions as a function of $x_{\bar{p}}$. The SD and ND distributions were normalized to the corresponding event rates prior to forming the $R_{\frac{SD}{ND}}(x_{\bar{p}})$ distribution. It is seen that the ratio of SD dijet to ND dijet events increases with decreasing $x_{\bar{p}}$.

Figure 5.2 is the same as Figure 5.1(d), i.e. shows the ratio of SD to ND event rates for dijet events with $E_T^{jet1,2} \geq 7$ GeV as a function of $x_{\bar{p}}$ for SD events with a leading antiproton in the region $0.035 \leq \xi \leq 0.095$ and $|t| \leq 1.0$ GeV^2. In the region of $x_{\bar{p}}$ between 0.001 and $0.5 \times \xi_{min} = 0.0175$, the distribution is well fit by

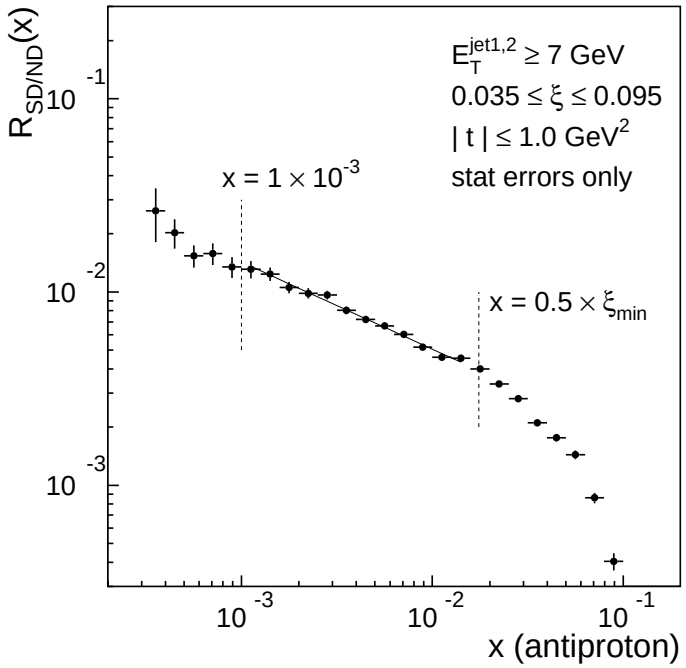

Figure 5.2: The ratio of SD to ND event rates for dijet events with $E_T^{jet1,2} \geq 7$ GeV as a function of $x_{\bar{p}}$ for SD events in the region $0.035 \leq \xi \leq 0.095$ and $|t| \leq 1.0$ GeV^2. The distribution is fitted to the power law form $R_{\frac{SD}{ND}}(x_{\bar{p}}) = R_0(x_{\bar{p}}/0.0065)^{-r}$ in the indicated region.

a power law, where ξ_{min} denotes the minimum value of the ξ range used to make the distribution. Note that, for $x_{\bar{p}} < 0.001$, the jets tend to be close to the detector edge on the high positive η side, and therefore this region is excluded from the fit to avoid detector bias. The "drop-off" of the ratio in the region $x_{\bar{p}} > \xi_{min}$ is expected, since only events with $\xi > x_{\bar{p}}$ contribute to the the ratio at a given $x_{\bar{p}}$. The fit to the power law form $R_{\frac{SD}{ND}}(x_{\bar{p}}) = R_0(x_{\bar{p}}/0.0065)^{-r}$ in the region $-3.0 \leq \log x_{\bar{p}} < -1.8$ ($0.001 \leq x_{\bar{p}} \lesssim 0.0175$) yields $R_0 = (6.1 \pm 0.1) \times 10^{-3}$ and $r = 0.45 \pm 0.02$ with a reduced χ^2 of $\chi^2/d.o.f. = 0.76$. The value of 0.0065 in the power law form used in the fit was chosen to correspond to the center of the $x_{\bar{p}}$ distribution in order to reduce the correlation between the two fit parameters R_0 and r.

Table 5.1: Fit parameters R_0 and r, and $\chi^2/d.o.f.$ for different event samples and different numbers of jets included in the $x_{\bar{p}}$ determination.

Event sample : number of jets	R_0	r	$\chi^2/d.o.f.$
All dijet events :			
only leading two jets	$(4.8 \pm 0.1) \times 10^{-3}$	0.33 ± 0.02	1.21
up to three jets with $E_T \geq 5$ GeV	$(6.1 \pm 0.1) \times 10^{-3}$	0.45 ± 0.02	0.76
up to four jets with $E_T \geq 5$ GeV	$(7.0 \pm 0.1) \times 10^{-3}$	0.48 ± 0.02	0.74
Dijet events with $E_T^{jet3} < 5$ GeV :			
only leading two jets	$(9.6 \pm 0.2) \times 10^{-3}$	0.31 ± 0.03	1.18

Dependence on Number of Jets Used in Evaluating $x_{\bar{p}}$

For each event, $x_{\bar{p}}$ is evaluated from the E_T and η of jets in the event using Eq. (5.1). Therefore, the value of $x_{\bar{p}}$ depends on the number of jets in the event over which the sum is carried out. In this analysis, unless otherwise stated, $x_{\bar{p}}$ is determined by summing over the two leading jets plus the next highest E_T jet if there is one with $E_T \geq 5$ GeV. To study the sensitivity of our results to the number of jets included in the determination of $x_{\bar{p}}$, we also quote results obtained by determining $x_{\bar{p}}$ using only the two leading jets, and by using the two leading jets plus up to two extra jets with $E_T \geq 5$ GeV. Results are presented in Figure 5.3 and Table 5.1. The power r varies by $^{+0.03}_{-0.12}$ and the normalization parameter R_0 by $^{+15}_{-21}$ % when the number of jets included in the determination of $x_{\bar{p}}$ is changed. Results obtained from dijet exclusive events with $E_T^{jet1,2} \geq 7$ GeV and $E_T^{jet3} < 5$ GeV are also presented in Figure 5.3 and Table 5.1.

Dependence on Jet E_T Threshold

Figure 5.4 is similar to Figures 5.1 and 5.2, but is for dijet events with $E_T^{jet1,2} \geq 10$ and 15 GeV. The figures on the right side of Figure 5.4 show the ratio $R_{\frac{SD}{ND}}(x_{\bar{p}})$ for dijet events with $E_T^{jet1,2} \geq 10$ and 15 GeV. Fits of these distributions to the power law

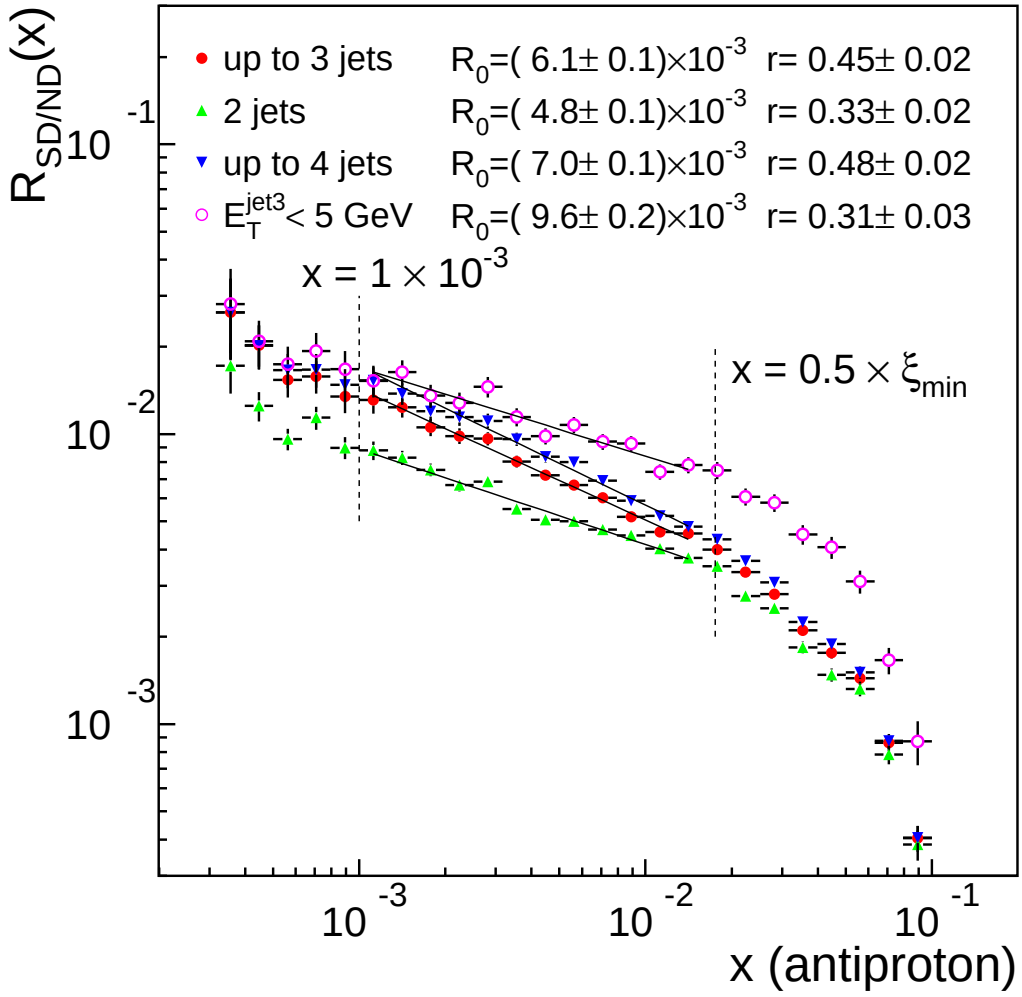

Figure 5.3: Ratios of SD to ND event rates for dijet events with $E_T^{jet1,2} \geq 7$ GeV as a function of $x_{\bar{p}}$, in which up to three jets with $E_T \geq 5$ GeV are used in evaluating $x_{\bar{p}}$ (filled circles), only the leading two jets are used (upward triangles), up to four jets with $E_T \geq 5$ GeV are used (downward triangles), and only the leading two jets are used for dijet exclusive events with $E_T^{jet3} < 5$ GeV (open circles). All distributions are fitted to the power law form $R_{\frac{SD}{ND}}(x_{\bar{p}}) = R_0(x_{\bar{p}}/0.0065)^{-r}$ in the indicated regions.

Table 5.2: Fit parameters R_0 and r and $\chi^2/d.o.f.$ for the dijet samples of $E_T^{jet1,2} \geq 7$, 10 and 15 GeV in the region $0.035 \leq \xi \leq 0.095$.

$E_T^{jet1,2}$ threshold	R_0	r	$\chi^2/d.o.f.$
7 GeV	$(6.1 \pm 0.1) \times 10^{-3}$	0.45 ± 0.02	0.76
10 GeV	$(4.1 \pm 0.1) \times 10^{-3}$	0.48 ± 0.05	2.16
15 GeV	$(4.6 \pm 0.4) \times 10^{-3}$	0.54 ± 0.16	0.87

form $R_{\frac{SD}{ND}}(x_{\bar{p}}) = R_0(x_{\bar{p}}/0.0065)^{-r}$ yield the parameters R_0 and r listed in Table 5.2, where they are compared with the parameters obtained from the fit to the distribution for dijet events with $E_T^{jet1,2} \geq 7$ GeV. In Figure 5.5, the ratios $R_{\frac{SD}{ND}}(x_{\bar{p}})$ for the dijet event samples of $E_T^{jet2} \geq 7$, 10 and 15 GeV are superimposed. Figure 5.5(a) is for all dijet events, and Figure 5.5(b) is for events with no third jet with $E_T \geq 5$ GeV.

It is seen that the shape of the $R_{\frac{SD}{ND}}(x_{\bar{p}})$ distribution does not depend on the jet E_T threshold. For all three jet E_T thresholds, the power r is consistent within the quoted statistical errors. As for the normalization of the distribution, the data of $E_T^{jet1,2} \geq 7$ GeV lie above the higher E_T data samples when no third jet E_T requirement is imposed, while for events selected with the $E_T < 5$ GeV requirement on a third jet, the data of all three jet E_T thresholds fall on top of one another.

Dependence on ξ

In soft single diffraction, in addition to pomeron exchange, contributions from reggeon exchange are also expected in the ξ region of the data samples used in this analysis, i.e. $0.035 \leq \xi \leq 0.095$. According to the result of a global fit to the pp and $p\bar{p}$ SD cross sections [71], the fraction of the cross section due to reggeon exchange at $\sqrt{s} = 1800$ GeV varies from ≈ 20 % at $\xi = 0.04$ to ≈ 60 % at $\xi = 0.09$. In hard diffraction, if the pomeron had a different structure than the reggeon, a

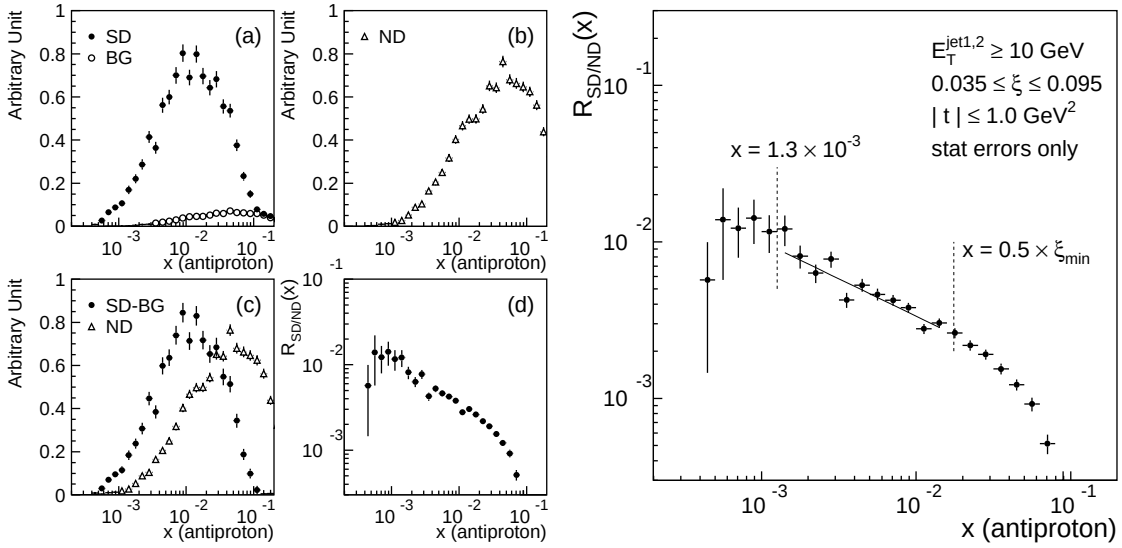

(a) Dijet events with $E_T^{jet1,2} \geq 10$ GeV

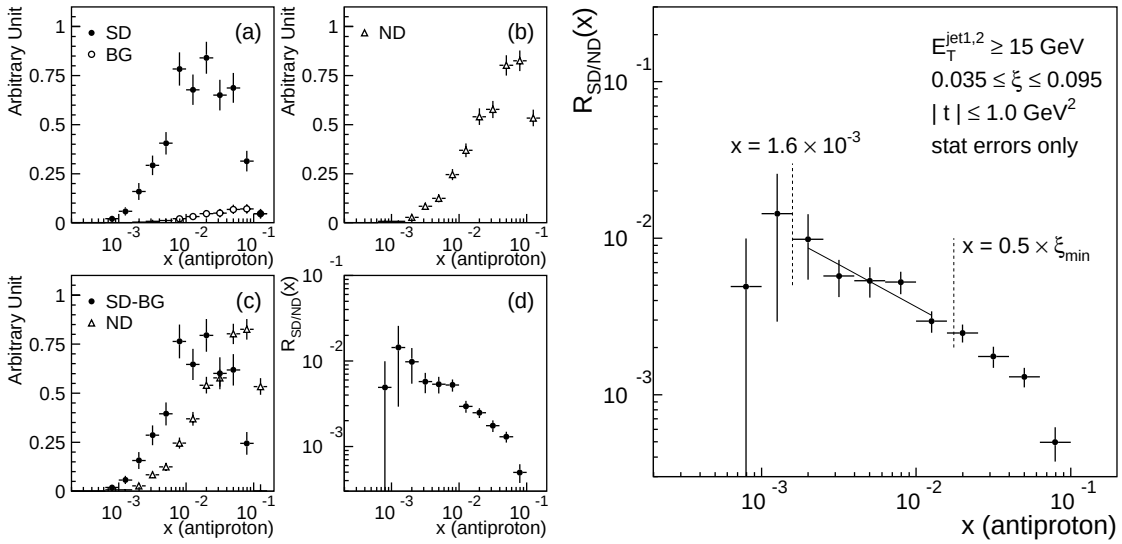

(b) Dijet events with $E_T^{jet1,2} \geq 15$ GeV

Figure 5.4: Distributions of $x_{\bar{p}}$ for the SD dijet sample, ND overlap background events, and ND dijet sample (top two plots in the left side sets), shape comparison of $x_{\bar{p}}$ distributions for the SD dijet and ND dijet samples (bottom left plot in the left side sets), and the ratio of SD dijet to ND dijet event rates as a function of $x_{\bar{p}}$ (bottom right plot in the left side sets and enlarged versions in the right side plots) for the dijet samples of (a) $E_T^{jet1,2} \geq 10$ GeV and (b) $E_T^{jet1,2} \geq 15$ GeV. In the right side plots, the distributions are fitted to the power law form $R_{\frac{SD}{ND}}(x_{\bar{p}}) = R_0(x_{\bar{p}}/0.0065)^{-r}$ in the indicated regions.

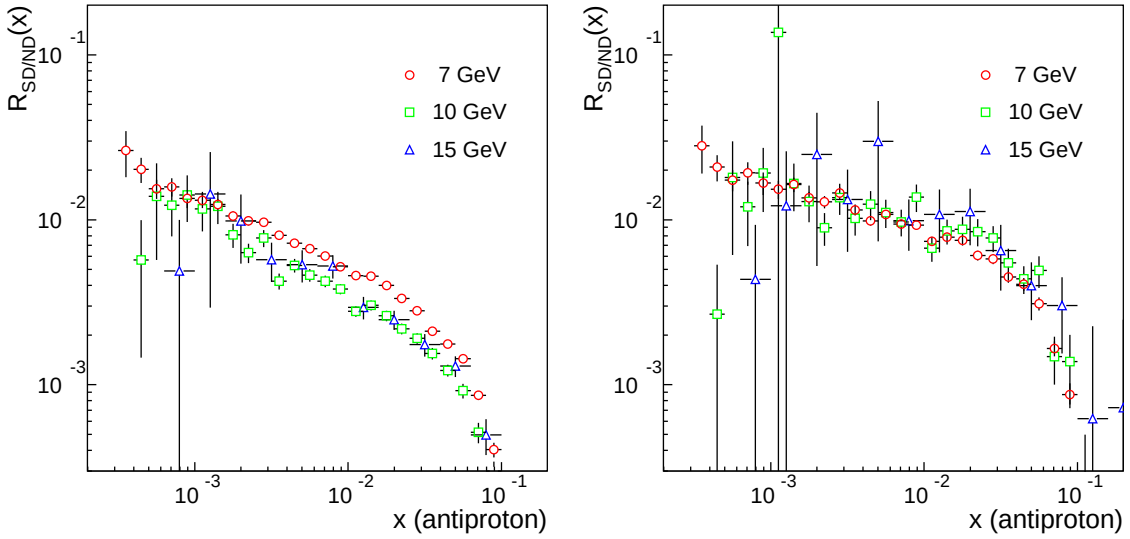

(a) Without $E_T^{jet3} < 5$ GeV requirement

(b) With $E_T^{jet3} < 5$ GeV requirement

Figure 5.5: The ratio of SD to ND event rates as a function of $x_{\bar{p}}$ for the dijet samples of three jet E_T thresholds, $E_T^{jet1,2} \geq 7$ (circles), 10 (squares) and 15 (triangles) GeV (a) without a requirement on the third jet and (b) with a $E_T^{jet3} < 5$ GeV requirement.

change in the relative contribution between the pomeron and reggeon would lead to a change in the shape of the SD dijet to ND dijet event ratio as a function of $x_{\bar{p}}$. Figure 5.6 shows the ratio $R_{\frac{SD}{ND}}(x_{\bar{p}})$ in the region $x_{\bar{p}} \geq 0.001$ for six ξ intervals of width $\Delta\xi = 0.01$ centered at 0.04 to 0.09. The lines represent fits of the power law form $R_{\frac{SD}{ND}}(x_{\bar{p}}) = R_0(x_{\bar{p}}/0.0065)^{-r}$ performed in the region $0.001 \leq x_{\bar{p}} \lesssim 0.5 \times \xi_{min}$, where ξ_{min} is the lower value of the ξ interval. The results of the fits are presented in Table 5.3, where the errors quoted are statistical only. No significant dependence on ξ is observed, either in shape or in normalization.

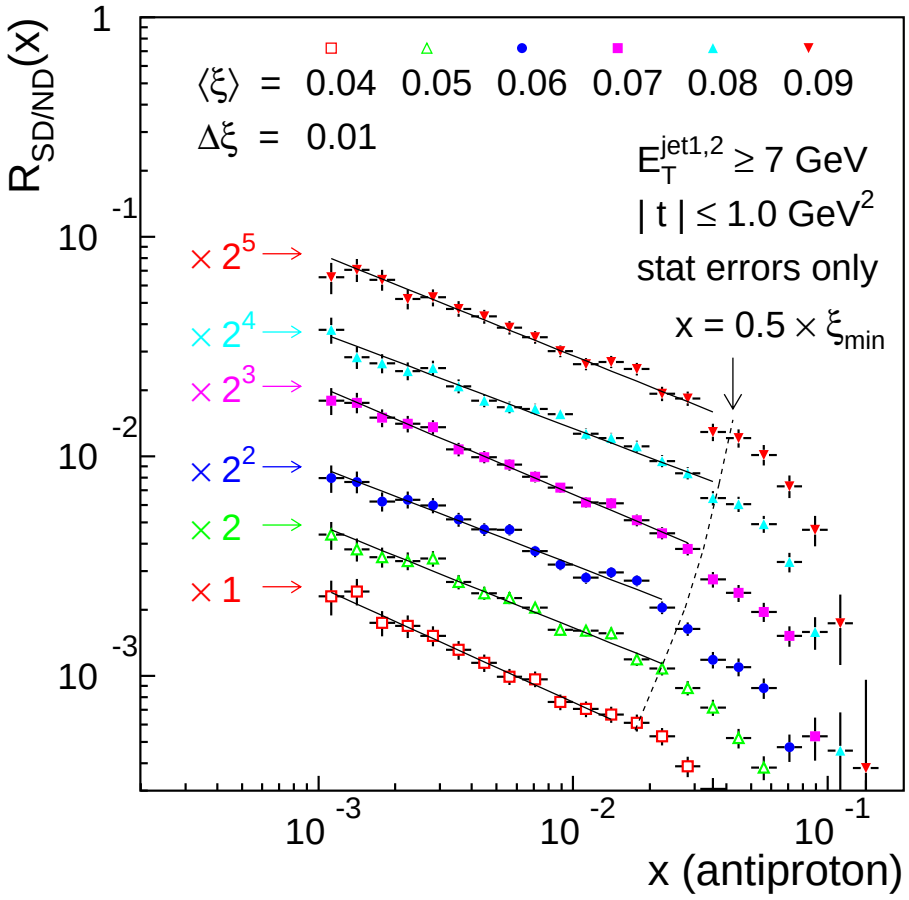

Figure 5.6: The ratio of SD to ND event rates for dijet events with $E_T^{jet1,2} \geq 7$ GeV as a function of $x_{\bar{p}}$ in the region $x_{\bar{p}} \geq 0.001$ for six ξ intervals of width $\Delta\xi = 0.01$ centered at 0.04 to 0.09. The distributions are fitted to the power law form $R_{\frac{SD}{ND}}(x_{\bar{p}}) = R_0(x_{\bar{p}}/0.0065)^{-r}$ in the indicated regions. For presentation purposes, the ratios are multiplied by the factors indicated in the figure.

Table 5.3: Fit parameters R_0 and r and $\chi^2/d.o.f.$ for six ξ intervals.

$\langle\xi\rangle$	R_0	r	$\chi^2/d.o.f.$
0.04	$(0.95 \pm 0.03) \times 10^{-3}$	0.53 ± 0.04	0.30
0.05	$(1.01 \pm 0.02) \times 10^{-3}$	0.47 ± 0.02	0.88
0.06	$(0.97 \pm 0.02) \times 10^{-3}$	0.45 ± 0.02	1.18
0.07	$(1.04 \pm 0.02) \times 10^{-3}$	0.49 ± 0.02	0.42
0.08	$(1.01 \pm 0.02) \times 10^{-3}$	0.44 ± 0.02	1.21
0.09	$(1.10 \pm 0.02) \times 10^{-3}$	0.47 ± 0.02	1.16

5.2 Measurement of the Diffractive Structure Function : F_{jj}^D

5.2.1 Definition of F_{jj}^D

In the approximation leading to an effective subprocess matrix element in leading order (LO) QCD [38], the single diffractive (SD) dijet to non-diffractive (ND) dijet production ratio is equal to the ratio of the corresponding effective structure functions of the antiproton,

$$R_{\frac{SD}{ND}}(x_{\bar{p}}, \xi) = \frac{F_{jj}^D(x_{\bar{p}}, \xi)}{F_{jj}(x_{\bar{p}})}, \tag{5.2}$$

where the incoming antiproton is assumed to be scattered quasielastically in SD dijet events. The structure functions F_{jj}^D and F_{jj} are defined in Section 2.3.3. The Q^2-dependence of the structure functions is ignored in Eq. (5.2). In this analysis, the SD dijet event rate is always integrated over a certain t region, and so is the diffractive structure function F_{jj}^D. The diffractive structure function F_{jj}^D can be evaluated by multiplying the ratio of SD dijet to ND dijet event rates by the non-diffractive proton structure function F_{jj},

$$F_{jj}^D(x_{\bar{p}}, \xi) = R_{\frac{SD}{ND}}(x_{\bar{p}}, \xi) \times F_{jj}(x_{\bar{p}}). \tag{5.3}$$

Evaluated in terms of the variables $\beta = x_{\bar{p}}/\xi$ and ξ, the diffractive structure function of the antiproton $F_{jj}^D(\beta, \xi)$ may lead to the effective structure function of the exchanged object (pomeron and/or reggeon).

The parton distribution functions (PDFs) of the proton are determined from global fits to experimental data from a variety of hard scattering processes in different kinematic ranges. A variety of PDFs of the proton are presently available. For the results

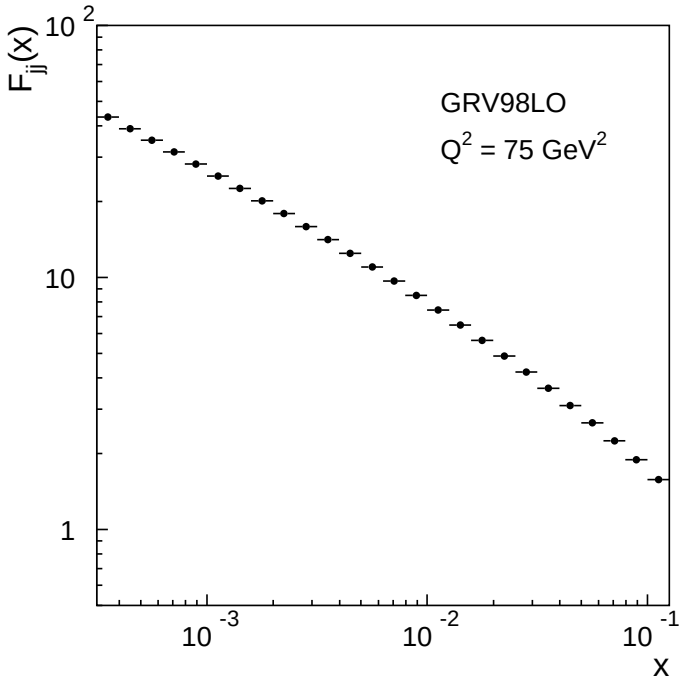

Figure 5.7: The distribution of $F_{jj}(x)$ evaluated using GRV98LO at $Q^2 = 75$ GeV^2.

presented in this dissertation, the GRV98LO [40] PDF set is used. The $F_{jj}(x)$ function derived from the GRV98LO PDF set at $Q^2 = 75$ GeV^2 is shown in Figure 5.7. The $F_{jj}(x)$ distribution shows a behavior similar to a power law in the x region mostly considered in this analysis, i.e. $0.001 \lesssim x \lesssim 0.02$. Choosing different PDF sets results in small differences in the resultant $F_{jj}^D(\beta)$ distribution, as shown in Figure 5.8.

For the SD dijet sample of $E_T^{jet1,2} \geq 7$ GeV, the scaling variable Q^2 is set to 75 GeV^2 which approximately corresponds to the average value of $(E_T^{jet})^2$. Figure 5.9 shows distributions of $(E_T^*)^2 = \left((E_T^{jet1} + E_T^{jet2})/2\right)^2$ for the SD dijet and ND dijet samples of $E_T^{jet1,2} \geq 7$ GeV. Changing Q^2 from 49 to 150 GeV^2 results in small differences in the resultant $F_{jj}^D(\beta)$ distribution, as shown in Figure 5.10.

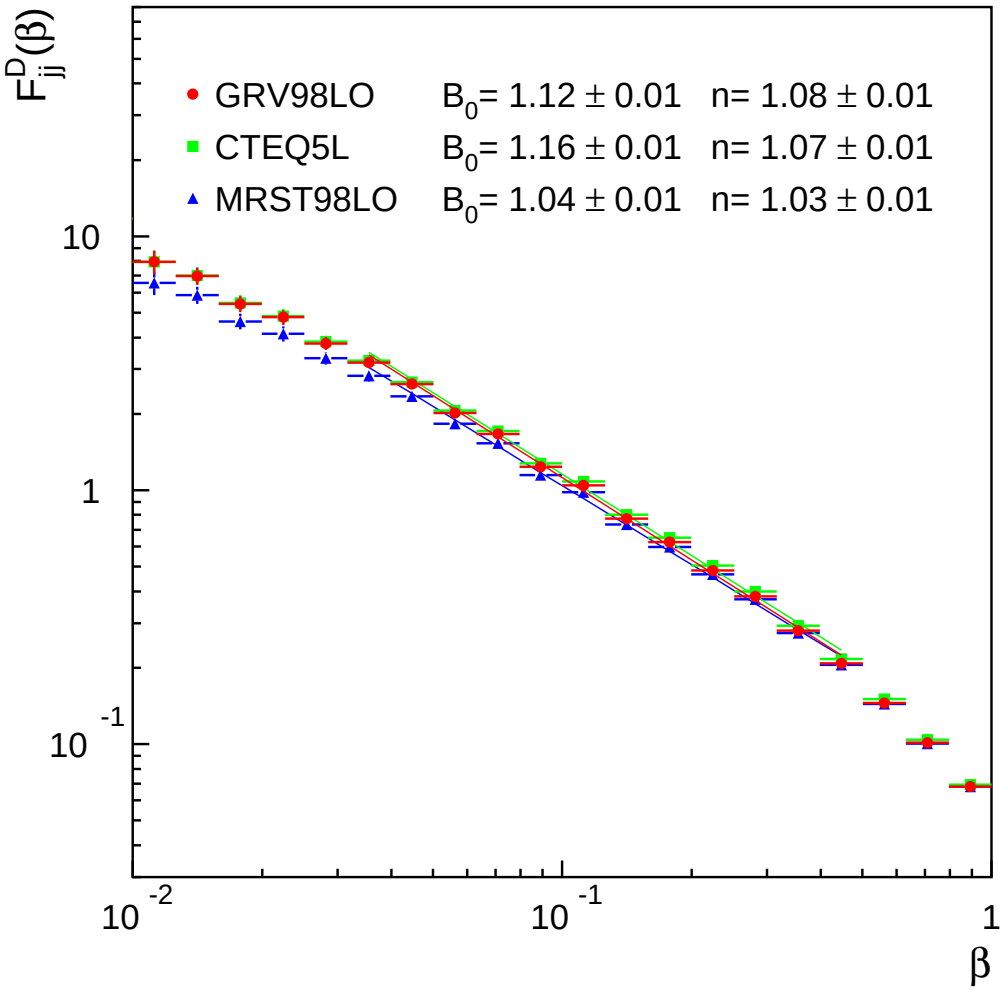

Figure 5.8: Distributions of $F_{jj}^{D}(\beta)$ extracted from dijet events with $E_T^{jet1,2} \geq 7$ GeV using the GRV98LO [40] (circles), CTEQ5L [41] (squares) and MRST98LO [42] (triangles) PDF sets. The distributions are fitted to the power law form $F_{jj}^{D}(\beta) = B_0(\beta/0.1)^{-n}$.

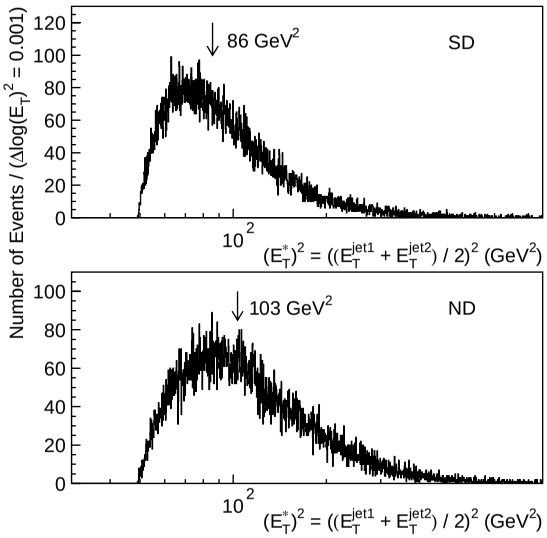

Figure 5.9: Distributions of the leading two jet mean E_T squared, $(E_T^*)^2 = \left((E_T^{jet1} + E_T^{jet2})/2\right)^2$, for (a) SD dijet and (b) ND dijet events with $E_T^{jet1,2} \geq 7$ GeV. The arrows point at the *median* values of 86 and 103 GeV^2 for the SD and ND events, respectively, which are the values of $(E_T^*)^2$ dividing the event samples into two halves with equal numbers of events.

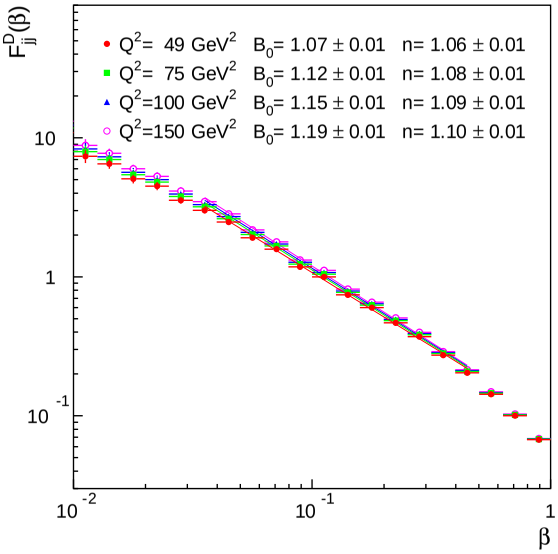

Figure 5.10: Distributions of $F_{jj}^D(\beta)$ extracted from dijet events with $E_T^{jet1,2} \geq 7$ GeV using the non-diffractive structure function F_{jj} evaluated at $Q^2 = 49$ (filled circles), 75 (squares), 100 (triangles), and 150 GeV^2 (open circles). The distributions are fitted to the power law form $F_{jj}^D(\beta) = B_0(\beta/0.1)^{-n}$.

5.2.2 Extraction of F_{jj}^{D}

The following procedure is used to extract $F_{jj}^{D}(\beta)$ integrated over a certain ξ region. Implementing this procedure separately for several ξ intervals leads to $F_{jj}^{D}(\beta, \xi)$.

1. Obtain $x_{\bar{p}}$ and $\beta = x_{\bar{p}}/\xi$ values using Eq. (5.1).

2. Form histograms versus $\log x_{\bar{p}}$ of the number of SD dijet events with a leading antiproton in a given ξ-t region, the ND overlap background contribution in the SD dijet events, and ND dijet events. The number of SD dijet events, $N_{SD}^{jj}(x_{\bar{p}})$, is corrected for the Roman Pot acceptance by weighting each event by $1/A(\xi_i, t_i)$, where $A(\xi_i, t_i)$ is the Roman Pot acceptance in the ξ-t bin of the event. These histograms are then normalized to the corresponding event rates.

3. Evaluate the ratio $R_{\frac{SD}{ND}}(x_{\bar{p}})$ of SD dijet to ND dijet event rates versus $\log x_{\bar{p}}$, as shown in Figure 5.2. The ND overlap background contribution is subtracted from the SD dijet events when the distribution $R_{\frac{SD}{ND}}(x_{\bar{p}})$ is formed.

4. Form a histogram of the non-diffractive structure function $F_{jj}(x_{\bar{p}})$ versus $\log x_{\bar{p}}$ using a chosen PDF set.

5. Form a histogram of the diffractive structure function $F_{jj}^{D}(x_{\bar{p}})$ versus $\log x_{\bar{p}}$ by multiplying the ratio $R_{\frac{SD}{ND}}(x_{\bar{p}})$ obtained in step 3 by the non-diffractive structure function $F_{jj}(x_{\bar{p}})$ obtained in step 4.

6. For each SD dijet event, which is assigned index i, evaluate a weight factor

$$W(x_{\bar{p},i}) = \frac{F_{jj}^{D}(x_{\bar{p},i})}{N_{SD}^{jj}(x_{\bar{p},i})}, \tag{5.4}$$

where $N_{SD}^{jj}(x_{\bar{p},i})$ and $F_{jj}^{D}(x_{\bar{p},i})$ are the number of SD dijet events and the value of the diffractive structure function F_{jj}^{D} in the $\log x_{\bar{p}}$ bin corresponding to the

$x_{\bar{p}}$ value of the event i, respectively. Recall that $N_{SD}^{jj}(x_{\bar{p}})$ obtained in step 2 is corrected for the Roman Pot acceptance.

7. Fill a histogram versus $\log\beta$ with the weight $W(x_{\bar{p},i})/A(\xi_i,t_i)$, where $A(\xi_i,t_i)$ is the Roman Pot acceptance in the ξ-t bin of the event i. The result represents $F_{jj}^{D}(\beta)$ on a logarithmic β scale.

8. Divide the $F_{jj}^{D}(\beta)$ distribution by the used ξ range in order to obtain the $F_{jj}^{D}(\beta)$ distribution per unit ξ.

9. The statistical error on $F_{jj}^{D}(\beta)$ in a $\log\beta$ bin of index k, $\delta F_{jj}^{D}(\beta_k)$, is given by

$$\delta F_{jj}^{D}(\beta_k) = \sqrt{\sum_{i=1}^{N_{SD}^{jj}(\beta_k)} \left(\frac{W(x_{\bar{p},i})}{A(\xi_i,t_i)}\right)^2 + \sum_{j=1}^{N_{x_{\bar{p}}\text{-}bin}} \left(N_{SD}^{jj}(\beta_k,x_{\bar{p},j})\delta W(x_{\bar{p},j})\right)^2}, \quad (5.5)$$

where the first sum is carried out over the SD dijet events, $N_{SD}^{jj}(\beta_k)$, in the $\log\beta$ bin of index k, and the second sum is carried out over all the $x_{\bar{p}}$ bins, $N_{x_{\bar{p}}\text{-}bin}$. The number of SD dijet events in the $\log\beta$ bin of index k and in the $\log x_{\bar{p}}$ bin of index j is denoted by $N_{SD}^{jj}(\beta_k,x_{\bar{p},j})$, and $\delta W(x_{\bar{p},j})$ denotes the error on $W(x_{\bar{p}})$ in the $\log x_{\bar{p}}$ bin of index j contributed by the statistical errors of the ND dijet events and the ND overlap background events. Thus, the first sum in the square-root of Eq. (5.5) represents the error due to the statistical error of SD dijet events, and the second term represents the error due to the statistical error of ND dijet events and the error of the ND overlap background events.

10. To obtain the $F_{jj}^{D}(\beta)$ distribution on a linear β scale, in steps 7−9 multiply the factor $W(x_{\bar{p},i})/A(\xi_i,t_i)$ by $d\beta/d(\log\beta) = \beta\ln 10$, and fill a histogram versus β.

5.2.3 F_{jj}^D as a Function of β

Recalling that $F_{jj}^D(x_{\bar{p}})$ exhibits a power law dependence on $x_{\bar{p}}$, and noting that the non-diffractive proton structure shows a behavior similar to a power law in the $x_{\bar{p}}$ range considered here, a power law dependence on β is also expected for $F_{jj}^D(\beta)$:

$$R_{\frac{SD}{ND}}(x_{\bar{p}},\xi) \propto 1/x_{\bar{p}}^r \quad \text{and} \quad F_{jj}(x_{\bar{p}}) \propto 1/x_{\bar{p}}^k \quad \Rightarrow \quad F_{jj}^D(x_{\bar{p}},\xi) \propto 1/x_{\bar{p}}^{r+k},$$

$$\beta = x_{\bar{p}}/\xi \quad \Rightarrow \quad F_{jj}^D(\beta,\xi) \propto 1/\beta^{n\approx r+k} \cdot 1/\xi^{m\approx r+k}.$$

Figure 5.11 displays the $F_{jj}^D(\beta)$ distribution on a logarithmic β scale, extracted from dijet events with $E_T^{jet1,2} \geq 7$ GeV for the region $0.035 \leq \xi \leq 0.095$ and $|t| \leq 1.0$ GeV^2, and Figure 5.12 displays it on a linear β scale. As expected, a power law is observed in the kinematic region of $\beta \lesssim 0.5$. A fit to the power law form $F_{jj}^D(\beta) = B_0(\beta/0.1)^{-n}$ in the region $-1.5 \leq \log\beta < -0.3$ ($0.03 \lesssim \beta \lesssim 0.5$) in Figure 5.11 yields $B_0 = 1.12 \pm 0.01$ and $n = 1.08 \pm 0.01$ with $\chi^2/d.o.f. = 1.7$. The value of 0.1 in the power law form used in the fit corresponds approximately to the center of the $F_{jj}^D(\beta)$ distribution on a logarithmic scale in order to reduce the correlation between the two fit parameters B_0 and n.

The interesting question as to whether $F_{jj}^D(\beta)$ drops to zero at $\beta = 1$, as expected for real particles, is difficult to answer conclusively from these results, since the extracted $F_{jj}^D(\beta)$ distributions are, in the region near $\beta = 1$, sensitive to systematic uncertainties and resolution effects in E_T^{jet}, η^{jet} and β.

As in the case of the $R_{\frac{SD}{ND}}(x_{\bar{p}})$ distribution, one of the main uncertainties in the $F_{jj}^D(\beta)$ distribution comes from the number of jets used in evaluating $x_{\bar{p}}$ and $\beta = x_{\bar{p}}/\xi$. This is studied in Figure 5.13. Results of power law fits to $F_{jj}^D(\beta)$ distributions obtained with various requirements on jets are presented in Table 5.4.

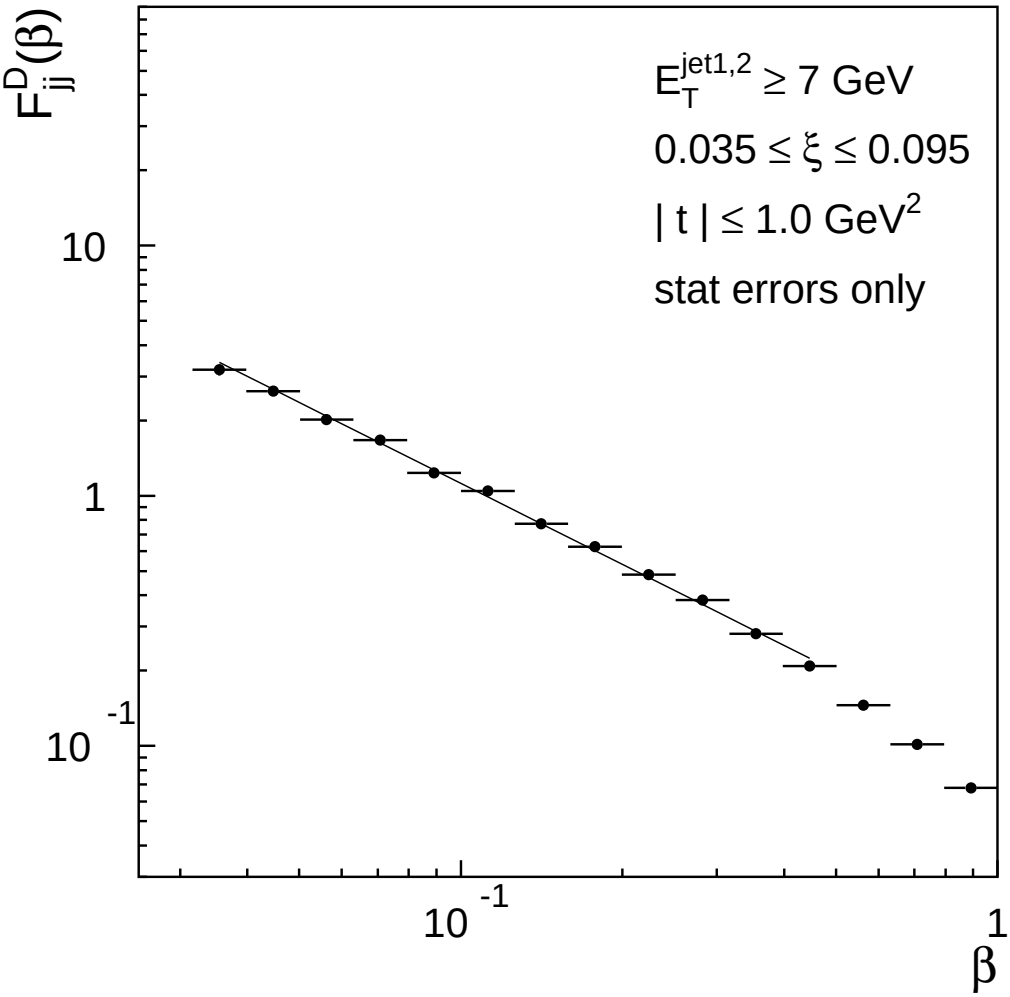

Figure 5.11: The distribution of $F_{jj}^{D}(\beta)$ on a logarithmic scale extracted from dijet events with $E_T^{jet1,2} \geq 7$ GeV for the region $0.035 \leq \xi \leq 0.095$ and $|t| \leq 1.0$ GeV^2 normalized per unit ξ. The distribution is fitted to the power law form $F_{jj}^{D}(\beta) = B_0(\beta/0.1)^{-n}$ in the region $-1.5 \leq \log\beta < -0.3$.

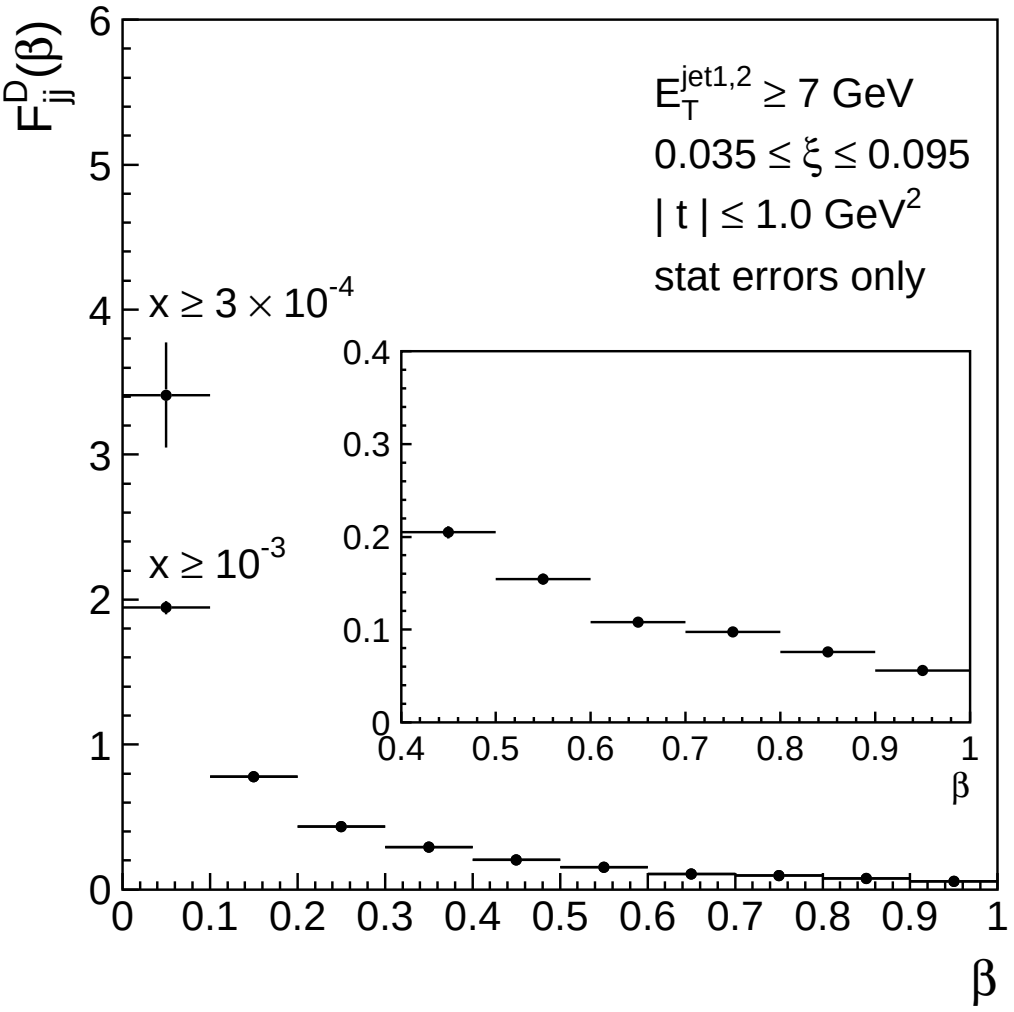

Figure 5.12: The distribution of $F_{jj}^{D}(\beta)$ on a linear scale extracted from dijet events with $E_T^{jet1,2} \geq 7$ GeV for the region $0.035 \leq \xi \leq 0.095$ and $|t| \leq 1.0$ GeV^2 normalized per unit ξ. The two points in the lowest β bin are evaluated using events with $x_{\bar{p}} \geq 0.001$ and 0.0003, respectively. The inset is a close-up view of the region $0.4 \leq \beta \leq 1.0$.

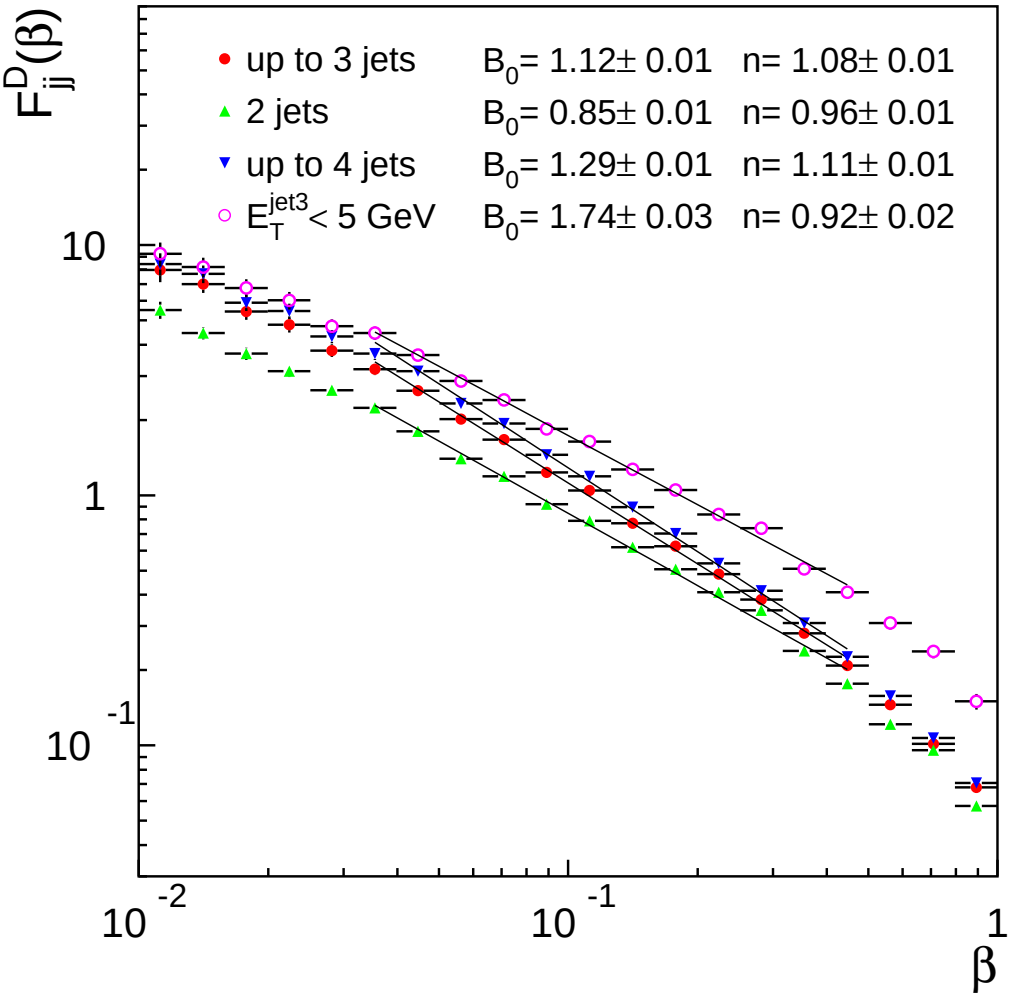

Figure 5.13: Distributions of $F_{jj}^{D}(\beta)$ extracted from dijet events with $E_T^{jet1,2} \geq 7$ GeV, in which up to three jets with $E_T \geq 5$ GeV are used in evaluating β (filled circles), only the leading two jets are used (upward triangles), up to four jets with $E_T \geq 5$ GeV are used (downward triangles), and only the leading two jets are used for dijet exclusive events with $E_T^{jet3} < 5$ GeV (open circles). All distributions are fitted to the power law form $F_{jj}^{D}(\beta) = B_0(\beta/0.1)^{-n}$.

Table 5.4: Fit parameters B_0 and n, and $\chi^2/d.o.f.$ for different event samples and different numbers of jets included in the β determination.

Event sample : number of jets	B_0	n	$\chi^2/d.o.f.$
All dijet events :			
only leading two jets	0.85 ± 0.01	0.96 ± 0.01	3.9
up to three jets with $E_T \geq 5$ GeV	1.12 ± 0.01	1.08 ± 0.01	1.7
up to four jets with $E_T \geq 5$ GeV	1.29 ± 0.01	1.11 ± 0.01	1.8
Dijet events with $E_T^{jet3} < 5$ GeV :			
only leading two jets	1.74 ± 0.03	0.92 ± 0.02	1.0

Table 5.5: Fit parameters B_0 and n, and $\chi^2/d.o.f.$ for six ξ intervals.

$\langle\xi\rangle$	B_0	n	$\chi^2/d.o.f.$
0.04	1.64 ± 0.05	1.07 ± 0.04	0.3
0.05	1.33 ± 0.03	1.02 ± 0.02	1.6
0.06	1.05 ± 0.02	1.04 ± 0.02	1.6
0.07	0.96 ± 0.02	1.08 ± 0.02	1.8
0.08	0.82 ± 0.01	1.02 ± 0.02	1.7
0.09	0.79 ± 0.01	1.05 ± 0.02	2.1

5.2.4 F_{jj}^D as a Function of β and ξ

Figure 5.14 shows $F_{jj}^D(\beta)$ distributions for six ξ intervals. The lines in the region $0.001/\xi_{min} \lesssim \beta \lesssim 0.5$ represent fits to the power law form $F_{jj}^D(\beta) = B_0(\beta/0.1)^{-n}$, where ξ_{min} is the lower value of the ξ interval. The results of the fits are presented in Table 5.5.

The exponent n is almost constant over the measured ξ region. This is displayed in Figure 5.15(a), which shows the exponents n determined by the fits as a function of ξ. A one-parameter fit to the six exponents n in this plot indicated by the dashed line yields

$$n = 1.04 \pm 0.01(\text{stat})$$

with $\chi^2/d.o.f. = 1.6$. This observed β-ξ factorization of the diffractive structure

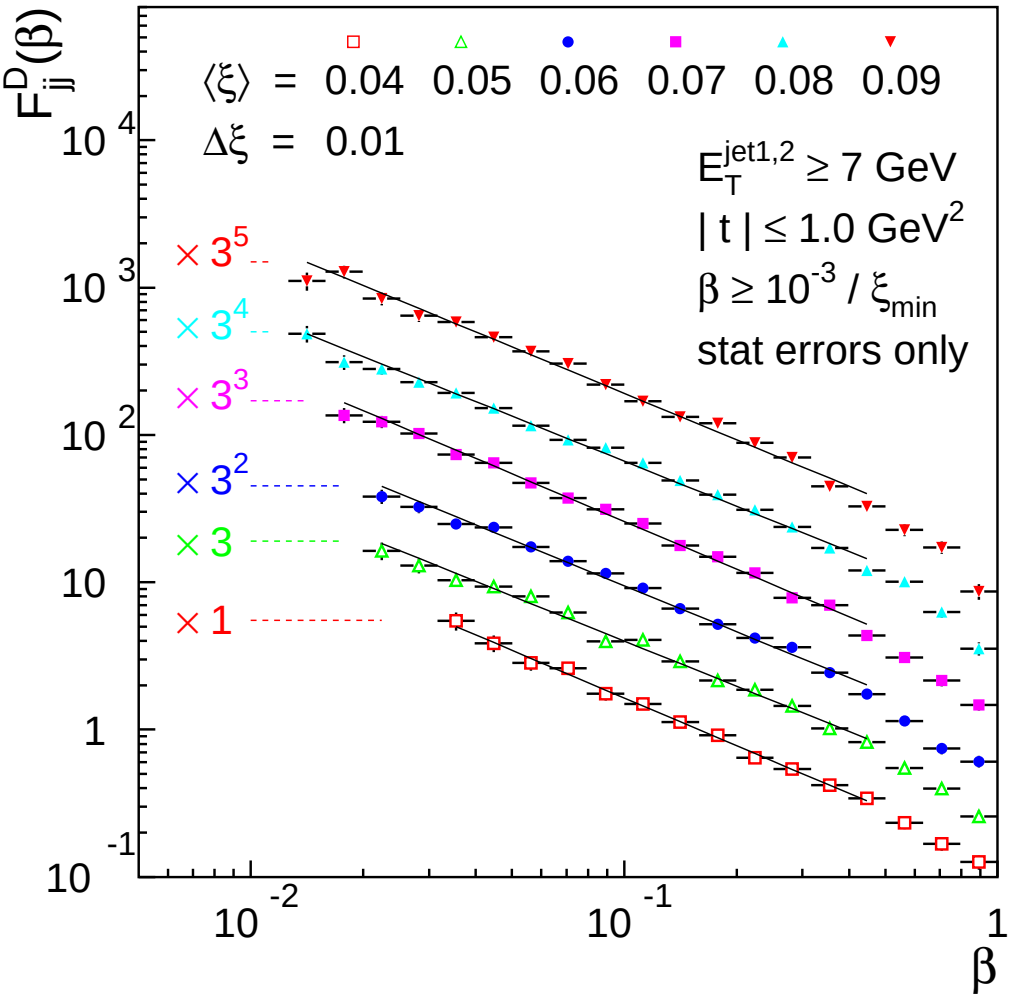

Figure 5.14: Distributions of $F_{jj}^{D}(\beta)$ extracted from dijet events with $E_T^{jet1,2} \geq 7$ GeV for six ξ intervals of width $\Delta\xi = 0.1$. Each distribution is normalized per unit ξ and fitted to the power law form $F_{jj}^{D}(\beta) = B_0(\beta/0.1)^{-n}$. For presentation purposes, the distributions are multiplied by the factors indicated in the figure.

function F_{jj}^D in terms of the variables β and ξ in the region $0.001/\xi < \beta < 0.5$ is in contradiction with models in which two exchanges, such as the pomeron and reggeon, with different structure function (β-dependence) and flux-factor (ξ-dependence) contribute to $F_{jj}^D(\beta)$.

Figure 5.15(b) displays the values of $B_0 = F_{jj}^D(\beta,\xi)|_{\beta=0.1}$ for six ξ intervals. A fit of $B_0 = F_{jj}^D(\beta,\xi)|_{\beta=0.1}$ to the power law form $C\xi^{-m}$ yields

$$m = 0.92 \pm 0.02(\text{stat})$$

with $\chi^2/d.o.f. = 4.1$. The fitted curve displays a steeper dependence than the ξ-dependence of the SD inclusive events.

Systematic Uncertainties in n and m

The errors in n and m quoted above were obtained from the power law fits to the values of n and B_0 shown in Table 5.5. The errors in n and B_0 in this table are from the power law fits of the $F_{jj}^D(\beta)$ distributions shown in Figure 5.14; in those fits, only the statistical errors on the $F_{jj}^D(\beta)$ distributions are taken into account. Thus, the errors in n and m quoted above are statistical.

To estimate the systematic uncertainties in n and m, we studied the sensitivity of n and m to the number of jets used in evaluating β and the requirement on extra jets in an event. The results are shown in Table 5.6. Based on these results, we assign to both n and m a systematic uncertainty of 0.1, which spans all values in Table 5.6:

$$\begin{aligned} n &= 1.0 \pm 0.1, \\ m &= 0.9 \pm 0.1, \end{aligned}$$

and the diffractive structure function $F_{jj}^D(\beta,\xi)$ measured in the region $0.001/\xi < \beta < 0.5$, $0.035 \le \xi \le 0.095$ and $|t| \le 1.0$ GeV^2 at $\sqrt{s} = 1800$ GeV is well represented by

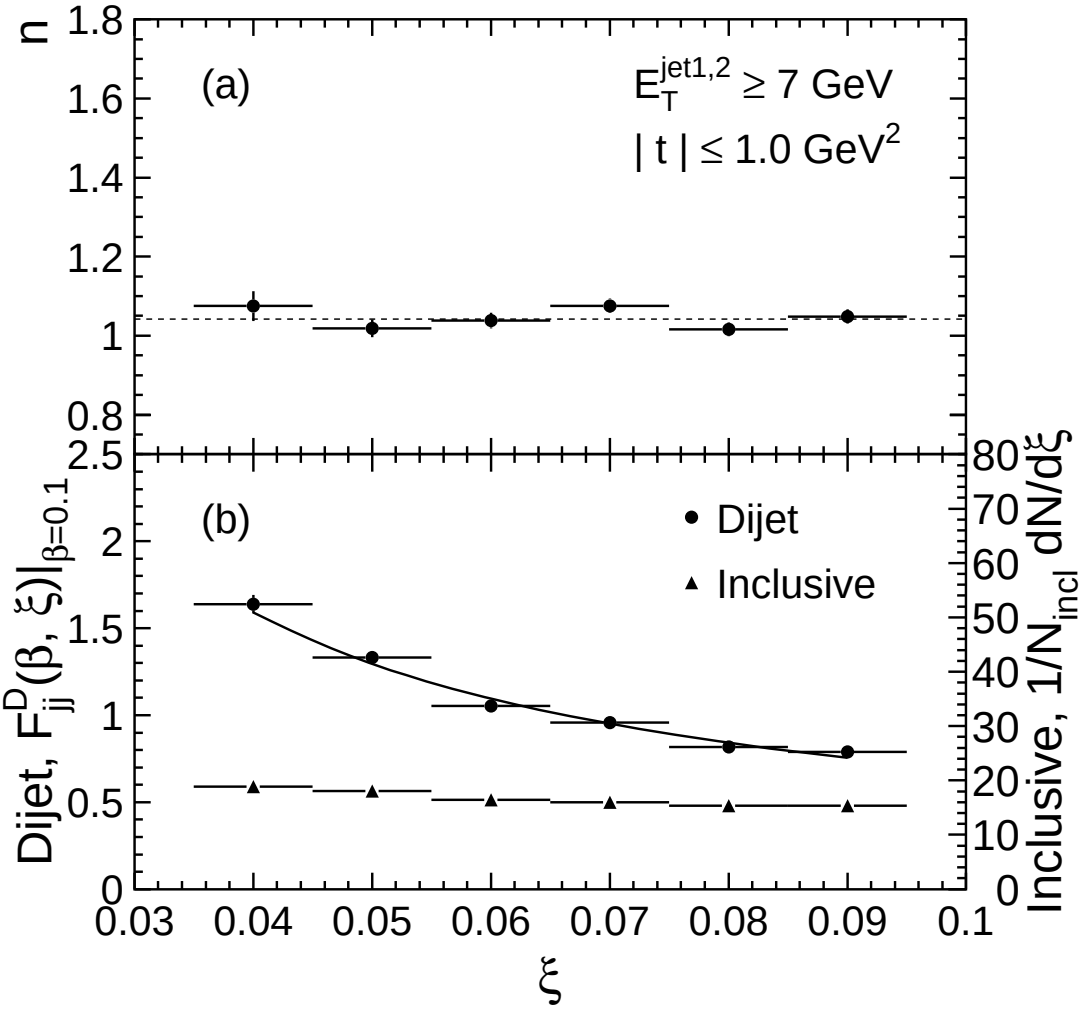

Figure 5.15: (a) Values of the exponent n from fits with $F_{jj}^D(\beta) = B_0(\beta/0.1)^{-n}$ to the $F_{jj}^D(\beta)$ distributions extracted from dijet events with $E_T^{jet2} \geq 7$ GeV for six ξ intervals. The fit of n to a constant number is indicated by the dashed line. (b) Values of the parameter B_0 from fits with $F_{jj}^D(\beta) = B_0(\beta/0.1)^{-n}$ to the $F_{jj}^D(\beta)$ distributions extracted from dijet events with $E_T^{jet1,2} \geq 7$ GeV for six ξ intervals (circles), and $1/N_{incl}\, dN/d\xi$ for SD inclusive events (triangles). The fit of $B_0 = F_{jj}^D(\beta, \xi)|_{\beta=0.1}$ to the form $C\xi^{-m}$ is indicated by the solid curve.

Table 5.6: Fit parameters n and m for different event samples and different numbers of jets included in the β determination.

Event sample : number of jets	n ($\chi^2/d.o.f.$)	m ($\chi^2/d.o.f.$)
All dijet events :		
only leading two jets	0.94 ± 0.01 (1.8)	0.80 ± 0.02 (3.3)
up to three jets with $E_T \geq 5$ GeV	1.04 ± 0.01 (1.6)	0.92 ± 0.02 (4.1)
up to four jets with $E_T \geq 5$ GeV	1.07 ± 0.01 (4.4)	0.95 ± 0.01 (14.)
Dijet events with $E_T^{jet3} < 5$ GeV :		
only leading two jets	0.89 ± 0.01 (0.8)	0.86 ± 0.04 (0.9)

the form:

$$F_{jj}^D(\beta, \xi) \propto \frac{1}{\beta^{1.0 \pm 0.1}} \frac{1}{\xi^{0.9 \pm 0.1}}. \tag{5.6}$$

Figure 5.16 is similar to Figure 5.14, but shows the $F_{jj}^D(\beta)$ distributions over a wider β region, including the unphysical region of $\beta > 1$. The data at $\beta > 1$ are due to systematic uncertainties and resolution effects in the β reconstruction. The observed overflows are relatively small and are neglected in the other figures presented in this dissertation. The region $\beta < 0.001/\xi$, which is equivalent to $x_{\bar{p}} < 0.001$, is sensitive to detector edge effects and, for this reason, data points in the region $\beta < 0.001/\xi_{min}$ are also not shown in the other figures.

Dependence of F_{jj}^D on ξ at High β

In the region $0.001/\xi < \beta < 0.5$, $0.035 \leq \xi \leq 0.095$ and $|t| \leq 1.0$ GeV^2 at $\sqrt{s} =$ 1800 GeV, the measured diffractive structure function $F_{jj}^D(\beta, \xi)$ is well represented by the form of Eq. (5.6). Another subject of interest is the ξ-dependence of F_{jj}^D at $\beta \geq 0.5$, where the measured F_{jj}^D does not exhibit a power law behavior in β. Figure 5.17 shows the $F_{jj}^D(\xi)$ distributions fitted to the power law form $C\xi^{-m}$ in the eight $\log\beta$ intervals of width $\Delta(\log\beta) = 0.2$ centered at -1.5 to -0.1. The values of

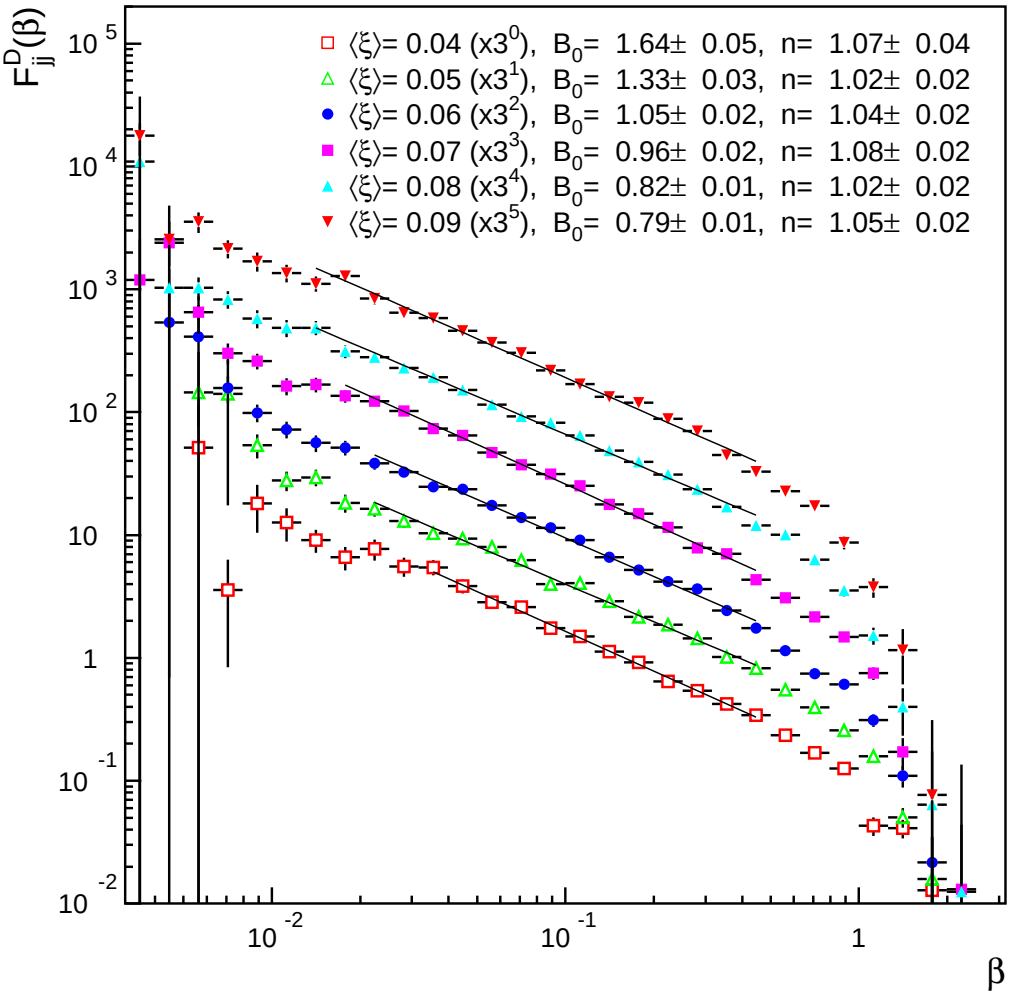

Figure 5.16: Distributions of $F_{jj}^{D}(\beta)$ extracted from dijet events with $E_T^{jet1,2} \geq 7$ GeV for six ξ intervals. This figure is similar to Figure 5.14, but shows a wider β region. Each distribution is fitted to the power law form $F_{jj}^{D}(\beta) = B_0(\beta/0.1)^{-n}$. For presentation purposes, the distributions are multiplied by the factors indicated in the figure.

m obtained from these fits are shown in Figure 5.17 and presented as a function of β in Figure 5.18. We observe that:

- The average value of m is approximately 1.
- m shows a rise at the high β region.

These features are consistent with results obtained in the analysis of diffractive deep inelastic scattering by the H1 collaboration [76].

5.3 Comparison with HERA Results

5.3.1 Results from the H1 1994 Data

The H1 collaboration reported [9] a measurement of the diffractive deep inelastic scattering (DIS) cross section and the differential diffractive F_2 structure function of the proton, $F_2^D(\beta, Q^2, \xi)$, over the kinematic region of $4.5 < Q^2 < 75$ GeV^2, based on the data of an integrated luminosity ≈ 2.0 pb^{-1} collected in 1994. In the H1 analysis, the ξ-dependence of $F_2^D(\beta, Q^2, \xi)$ was found to depend on β, which contradicts the Regge factorization assumption given by Eq. (2.30) with a leading pomeron exchange only. This finding was accommodated in Ref. [9] by introducing a subleading reggeon (ρ, ω, f, A_2 etc.) exchange, which has a different ξ-dependence than pomeron exchange. With the subleading reggeon exchange, $F_2^D(\beta, Q^2, \xi)$ can be expressed as

$$F_2^D(\beta, Q^2, \xi) = f_{I\!P/p}(\xi) F_2^{I\!P}(\beta, Q^2) + f_{I\!R/p}(\xi) F_2^{I\!R}(\beta, Q^2), \tag{5.7}$$

where $I\!P$ and $I\!R$ denote the pomeron and reggeon, $f_{I\!P/p}(\xi)$ and $f_{I\!R/p}(\xi)$ are the pomeron and reggeon flux factors, and $F_2^{I\!P}(\beta, Q^2)$ and $F_2^{I\!R}(\beta, Q^2)$ may be interpreted as the F^2 structure functions of the pomeron and reggeon, respectively. In Eq. (5.7),

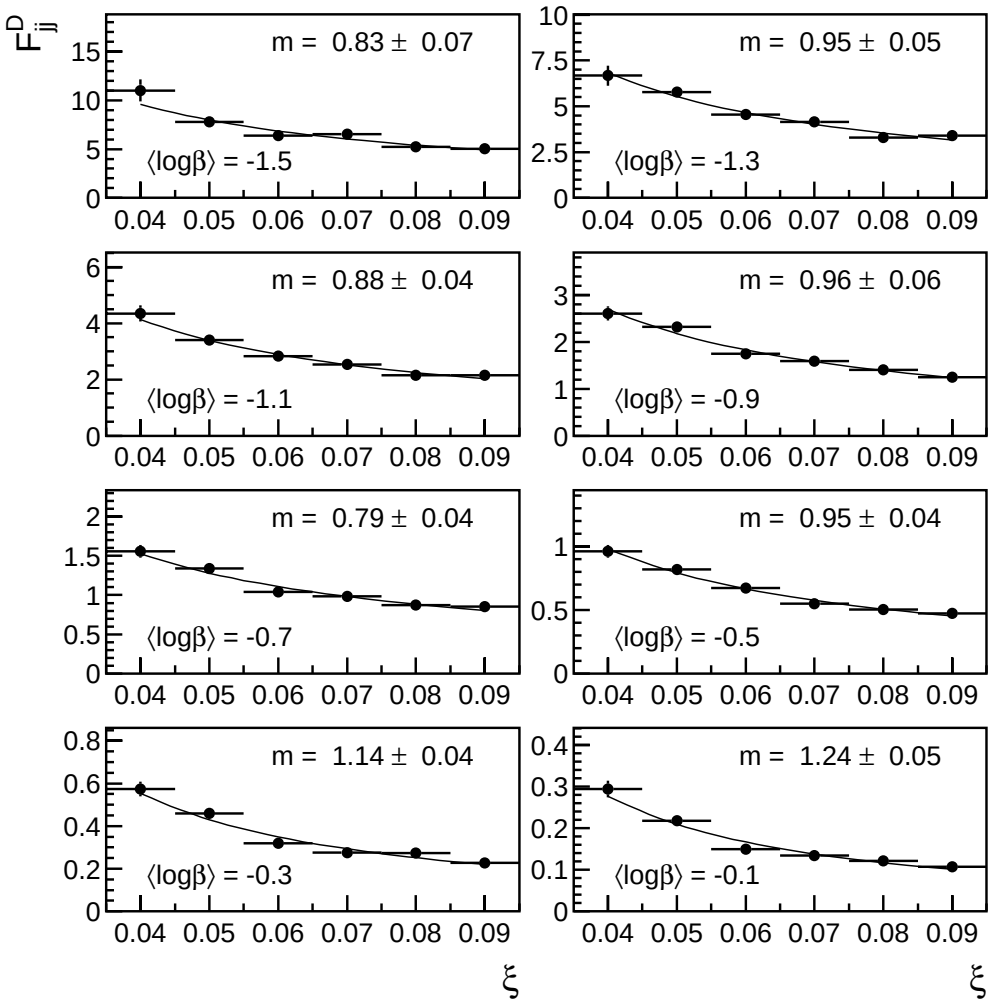

Figure 5.17: Distributions of $F_{jj}^D(\beta, \xi)$ versus ξ obtained using dijet events with $E_T^{jet1,2} \geq 7$ GeV for eight $\log\beta$ intervals of width $\Delta(\log\beta) = 0.2$ centered at -1.5 to -0.1. The distributions are fitted to the power law form $C\xi^{-m}$.

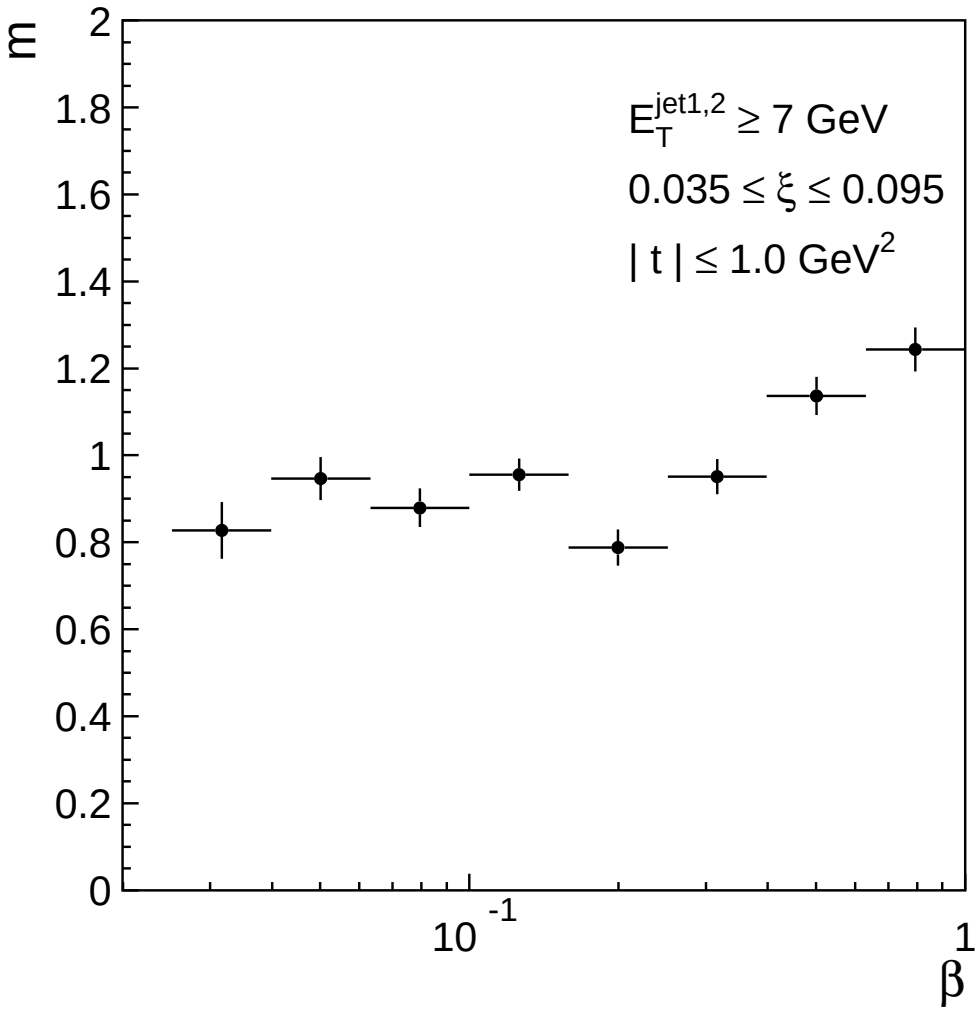

Figure 5.18: The exponent m from fits with $C\xi^{-m}$ to $F_{jj}^D(\beta,\xi)$ extracted from dijet events with $E_T^{jet1,2} \geq 7$ GeV for the region $0.035 \leq \xi \leq 0.095$ and $|t| \leq 1.0$ GeV^2, as a function of β on a logarithmic scale.

a possible interference between the pomeron exchange and the reggeon exchange is ignored. Since the extracted $F_2^{I\!P}(\beta, Q^2)$ was found to evolve with Q^2 as expected in the DGLAP evolution equations, QCD fits were performed to $F_2^{I\!P}(\beta, Q^2)$ to extract the parton distribution functions of the pomeron. The results showed that the fraction of the pomeron momentum carried by gluons is $F_g^D \approx 0.9$ at $Q^2 = 4.5$ GeV^2 and $F_g^D \approx 0.8$ at $Q^2 = 75$ GeV^2.

In Figure 5.19, the $F_{jj}^D(\beta)$ distribution extracted in this analysis is compared with expectations from the H1 results [9]. The expectations from the H1 results are obtained using the following form for the diffractive structure function $F_{jj}^D(\beta)$:

$$F_{jj}^D(\beta) = \sum_{i=I\!P, I\!R} \int_{t=-1.0\ \mathrm{GeV}^2}^{t=t_{min}} \int_{\xi=0.035}^{\xi=0.095} f_{i/p}(\xi, t) F_{jj}^i(\beta) d\xi dt, \tag{5.8}$$

where $-t_{min} \approx m_p^2 \xi^2/(1-\xi)$ [3] is the minimum kinematically allowed value of $-t$, and $F_{jj}^{I\!P}(\beta)$ and $F_{jj}^{I\!R}(\beta)$ denote the effective structure functions of the pomeron and reggeon, respectively. For the pomeron, we use parton distributions from the H1 fits[4] [77], and for the reggeon, we use the Owens pion structure function [78] multiplied by a coefficient of $C_{I\!R} = 16.0$ (15.9) [79] for the H1 fit 2 (fit 3), as was done by the H1 collaboration. For the flux factors, we use the form:

$$f_{i/p}(\xi, t) = \frac{e^{b_i t}}{\xi^{2\alpha_i(t)-1}} \quad (i = I\!P, I\!R) \tag{5.9}$$

with $\alpha_{I\!P}(t) = 1.20 + 0.26t$, $\alpha_{I\!R}(t) = 0.57 + 0.9t$, $b_{I\!P} = 4.6$ GeV^{-2}, and $b_{I\!R} = 2.0$ GeV^{-2} [9].

[3] The value of t_{min} is very close to 0 ($t_{min} \approx -0.001$ GeV^2 at $\xi = 0.035$, and $t_{min} \approx -0.009$ GeV^2 at $\xi = 0.095$). Therefore, it is usually omitted throughout this dissertation.

[4] In Refs. [9, 77], the parton distribution functions of the pomeron are normalized such that they represent ξ times the parton distribution functions multiplied by the pomeron flux factor at $\xi = 0.003$ integrated over t in the region -1.0 GeV$^2 < t < t_{min}$. Therefore, these distributions must be multiplied by $1/\left(0.003 \cdot f_{I\!P/\bar{p}}(\xi = 0.003)\right) = 0.746$ to obtain the "true" diffractive parton distributions.

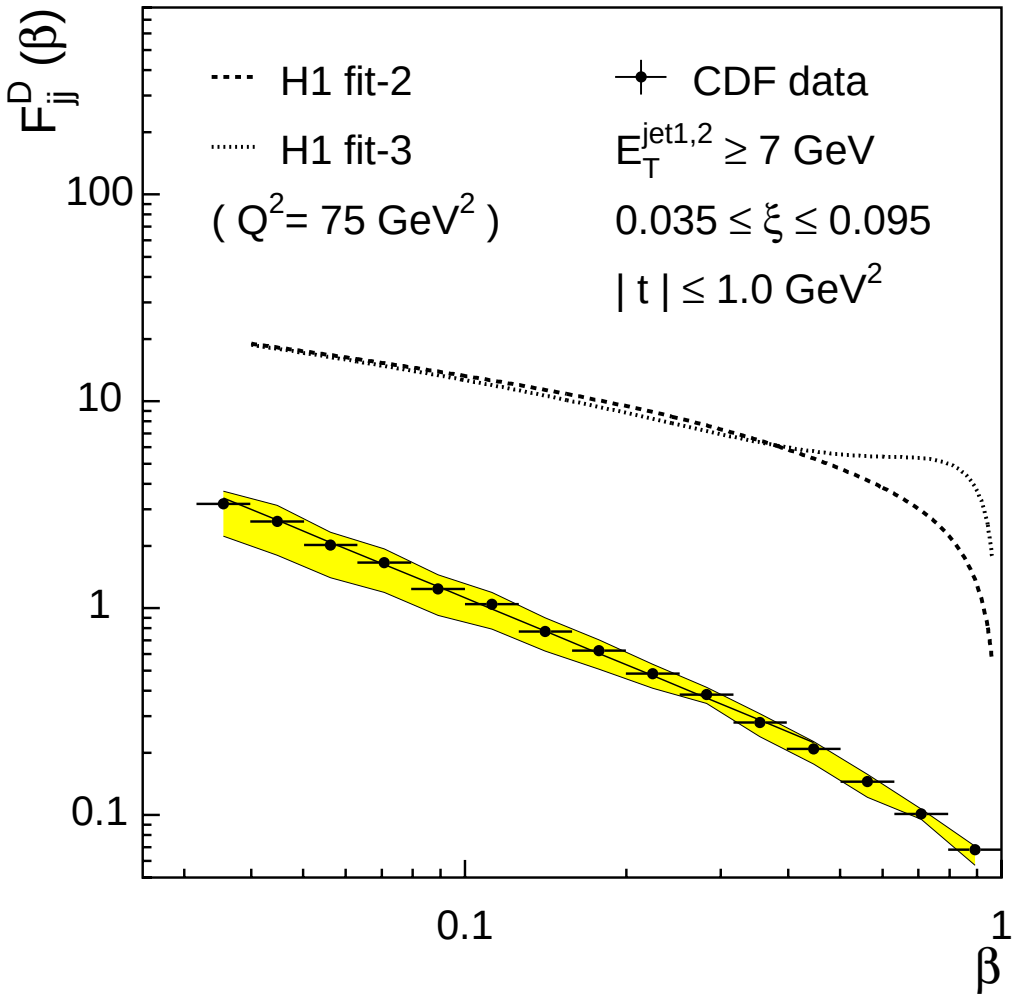

Figure 5.19: The distribution of $F_{jj}^D(\beta)$ (points) extracted from dijet events with $E_T^{jet1,2} \geq 7$ GeV for the region $0.035 \leq \xi \leq 0.095$ and $|t| \leq 1.0$ GeV^2, compared with expectations from the diffractive parton distributions in the proton extracted from diffractive deep inelastic scattering by the H1 collaboration [9]. The solid line is a fit to the data of the power law form $F_{jj}^D(\beta) = B_0(\beta/0.1)^{-n}$. The lower (upper) boundary of the filled band represents the $F_{jj}^D(\beta)$ distribution obtained using only the leading two jets (up to four jets of $E_T > 5$ GeV) in evaluating β. The dashed (dotted) curve is the expectation from the H1 fit 2 (fit 3). The systematic uncertainty in the normalization of the measured $F_{jj}^D(\beta)$ distribution is ± 26 % (see Table 4.7).

The $F_{jj}^D(\beta)$ determined from the H1 fit 2 and fit 3 of the pomeron structure disagree with our results both in normalization and shape. To quantify the discrepancy in normalization, we define a discrepancy factor D as the ratio of the integral over β from $\beta = 10^{-1.4} \approx 0.04$ to 1 of our measurement divided by the expectation from the H1 results:

$$D = \frac{\int_{\beta=10^{-1.4}\approx 0.04}^{\beta=1} F_{jj}^D(\beta;\ \mathrm{CDF}) d\beta}{\int_{\beta=10^{-1.4}\approx 0.04}^{\beta=1} F_{jj}^D(\beta;\ \mathrm{H1}) d\beta} = \frac{\int_{\log\beta=-1.4}^{\log\beta=0} F_{jj}^D(\beta;\ \mathrm{CDF})(\beta \ln 10) d(\log\beta)}{\int_{\log\beta=-1.4}^{\log\beta=0} F_{jj}^D(\beta;\ \mathrm{H1})(\beta \ln 10) d(\log\beta)}. \tag{5.10}$$

From the data and curves presented in Figure 5.19, the discrepancy factor is found to be $D = 0.06 \pm 0.02$ and 0.05 ± 0.02 for the H1 fit 2 and fit 3, respectively.

The actual determination of D is performed as follows. For the 14 CDF data points above $\beta = 0.04$ [5], we multiply the value of each point by the Jacobian of $d\beta/d(\log\beta) = \beta \ln 10$ and sum up the results. The same operation is performed for the H1 fit 2 and fit 3 expectations in steps of $\Delta(\log\beta) = 0.04$, and the factor D is determined as the ratio of the CDF to H1 results. The ratio D is sensitive to the number of jets used in evaluating β. Using the $F_{jj}^D(\beta)$ distributions obtained with only the leading two jets or up to four jets of $E_T \geq 5$ GeV, which are shown in Figure 5.19, results in a variation of $^{+13}_{-20}$ % in D. The uncertainty of 26 % in the ratio of single diffractive (SD) dijet to non-diffractive (ND) dijet event rates shown in Table 4.7 also contributes to the uncertainty in D. Adding these two uncertainties in quadrature, the resulting uncertainty in D is ± 0.02 for both the H1 fit 2 and fit 3

[5] We do not use the CDF point below $\beta = 0.04$, since the H1 results are applicable only above $\beta = 0.04$ [9, 77].

comparisons:

$$D = \begin{cases} 0.06 \pm 0.02 & \text{for the H1 fit-2,} \\ 0.05 \pm 0.02 & \text{for the H1 fit-3.} \end{cases}$$

The disagreement between the $F_{jj}^{D}(\beta)$ extracted in this analysis and expectations from the H1 results on diffractive DIS indicates a breakdown of QCD factorization in diffraction processes. Note that a similar discrepancy was observed previously in the comparison between the SD W, dijet and b-quark production rates measured by the CDF collaboration [18, 19, 21] and expectations based on results obtained by the ZEUS collaboration from diffractive DIS and dijet photoproduction at HERA [5, 15].

5.3.2 Results from the H1 1997 Data

Recently, the H1 collaboration reported [12] new results obtained from a data set of an integrated luminosity 10.6 pb^{-1} collected in 1997, which is about a factor of five larger than the data set used in the previous H1 analysis [9]. For data in the kinematic region of $6.5 \leq Q^2 \leq 120$ GeV^2, $0.01 \leq \beta \leq 0.9$ and $0.0001 \lesssim \xi < 0.05$, QCD fits were performed to extract the diffractive parton distribution functions, and an assessment of the experimental and theoretical uncertainties on the resulting diffractive parton distributions was made. In Figure 5.20, the $F_{jj}^{D}(\beta)$ distribution extracted in this analysis is compared with expectations from the recent [12] and previous [9] leading order QCD fits by the H1 collaboration. It is found that the expectations from the recent H1 analysis are closer to the distribution extracted in this analysis in shape than the expectations from the previous H1 analysis; however, a large discrepancy of approximately one order of magnitude in normalization still remains, indicating a breakdown of QCD factorization in normalization. It may be worth mentioning that, in the recent H1 results, the fraction of the pomeron momentum carried by gluons is

estimated to be $F_g^D = 0.75 \pm 0.15$ at $Q^2 = 10$ GeV^2, which is closer to $F_g^D = 0.54^{+0.16}_{-0.14}$ obtained in the SD W, dijet and b-quark analyses [18, 19, 21] than the previous H1 result of $F_g^D \approx 0.9$ (0.8) at $Q^2 = 4.5$ (75) GeV^2.

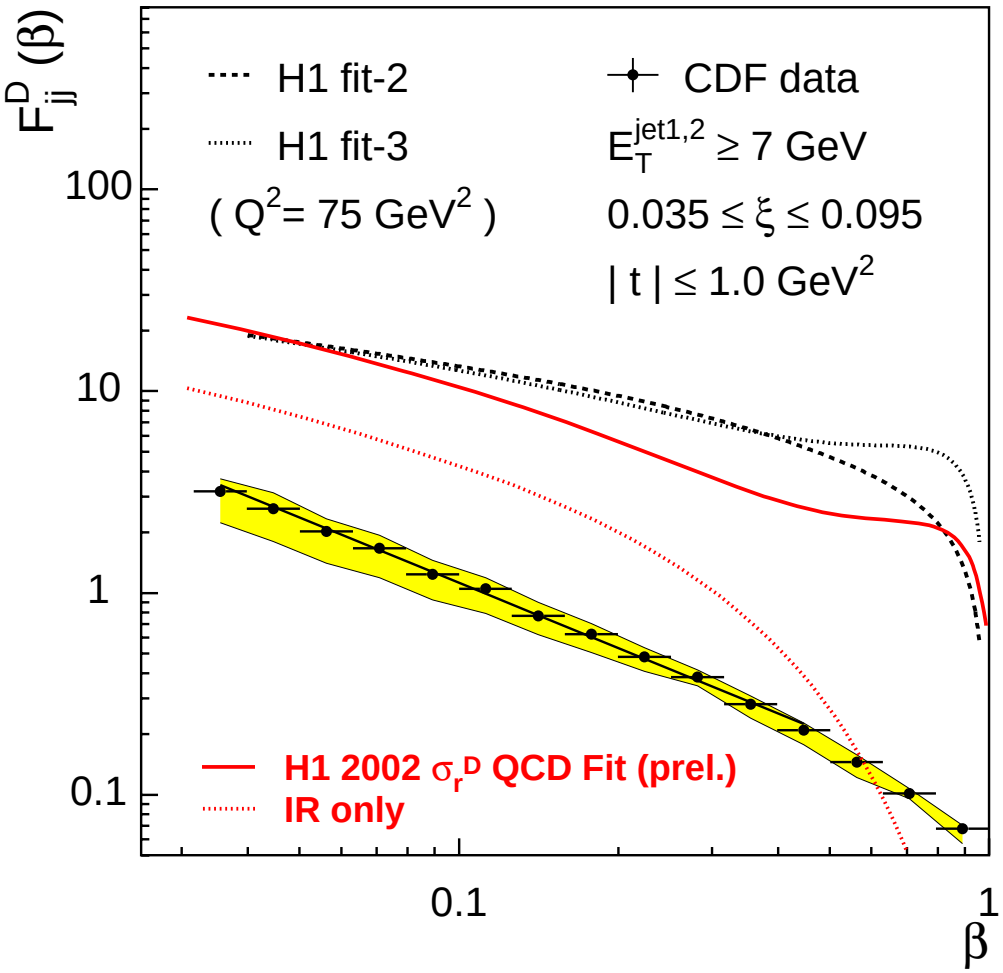

Figure 5.20: The distribution of $F_{jj}^D(\beta)$ extracted from dijet events with $E_T^{jet1,2} \geq 7$ GeV in this analysis for the region $0.035 \leq \xi \leq 0.095$ and $|t| \leq 1.0$ GeV^2 compared with predictions from the recent (2002) [12] and previous [9] leading order QCD fits by the H1 collaboration. This figure is adapted from Figure 20 in Ref. [12].

5.4 Comparison between $\sqrt{s} = 630$ and 1800 GeV

In this section, the ratio $R_{\frac{SD}{ND}}(x_{\bar{p}})$ of single diffractive (SD) dijet to non-diffractive (ND) dijet event rates as a function of $x_{\bar{p}}$ and the diffractive structure function $F_{jj}^{D}(\beta)$ extracted from the 630 GeV data samples are presented and compared with results from the 1800 GeV data samples. In the 630 GeV SD data sample, the range in t is restricted to $|t| \leq 0.2$ GeV^2, as discussed in Section 4.2.1. To make comparisons in the same ξ-t region between $\sqrt{s} = 630$ and 1800 GeV, the 1800 GeV SD data sample is also restricted to the region $|t| \leq 0.2$ GeV^2 in this section. Also, for comparisons between $\sqrt{s} = 630$ and 1800 GeV, in addition to the jet requirement of $E_T^{jet1,2} \geq 7$ GeV used mainly in Sections 5.1 and 5.2, another cut is imposed on the average E_T of the leading two jets requiring $E_T^* = (E_T^{jet1} + E_T^{jet2})/2 \geq 10$ GeV. The numbers of events, background fractions, and selection cut efficiencies are estimated with these new requirements. The results are summarized in Table 5.4.

Table 5.7: Number of events, efficiencies and background fractions for the 1800 GeV SD dijet and inclusive samples in the region $0.035 \leq \xi \leq 0.095$ and $|t| \leq 0.2$ GeV^2.

SD inclusive events	N_{SD}^{incl}	$1,010,335 \pm 1,005$
after RP acceptance correction		$1,237,210 \pm 1,312$
ND overlap background	$F_{SD\,incl}^{ND\,BG}$	3.3 ± 1.7 %
Beam-gas background	$F_{SD\,incl}^{GAS}$	5.1 %
Single vertex cut efficiency	$\epsilon_{SD\,incl}^{1vtx}$	87.9 ± 1.2 %
SD dijet events ($(E_T^{jet1} + E_T^{jet2})/2 \geq 10$ GeV)	N_{SD}^{jj}	$6,719 \pm 82.0$
after RP acceptance correction		8031.2 ± 103.5
ND overlap background	$F_{SD\,jj}^{ND\,BG}$	9.7 ± 1.0 %
Single vertex cut efficiency	$\epsilon_{SD\,jj}^{1vtx}$	76.8 ± 2.3 %
Hot tower filter efficiency	$\epsilon_{SD\,jj}^{HTFLT}$	97.1 ± 0.5 %

5.4.1 Comparison in Terms of $R_{\frac{SD}{ND}}$

Figure 5.21 is similar to Figure 5.1, but is for the 630 GeV SD dijet and ND dijet samples of $E_T^{jet1,2} \geq 7$ GeV and $E_T^* = (E_T^{jet1} + E_T^{jet2})/2 \geq 10$ GeV; the SD events are in the region $0.035 \leq \xi \leq 0.095$ and $|t| \leq 0.2$ GeV^2. For the 630 GeV data sample, an additional selection cut requiring the west BBC multiplicity to be equal to or less than 4 is imposed to reduce the ND overlap background; therefore, the SD distribution is corrected for the residual ND overlap background contribution after the west BBC multiplicity cut is applied. Figure 5.21(d) shows that the ratio of SD dijet to ND dijet event rates increases with decreasing $x_{\bar{p}}$, which is consistent with the result obtained at $\sqrt{s} = 1800$ GeV.

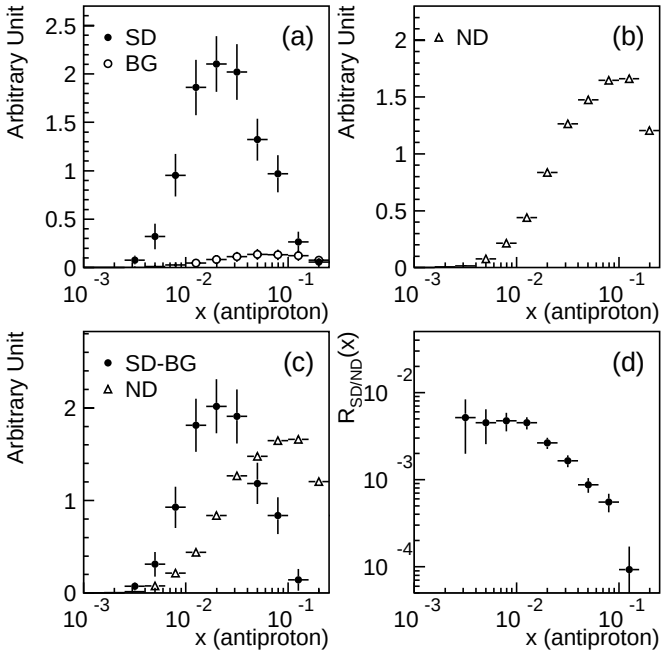

Figure 5.21: (a) Distributions of $x_{\bar{p}}$ for the 630 GeV SD dijet sample of $E_T^{jet1,2} \geq 7$ GeV and $E_T^* = (E_T^{jet1} + E_T^{jet2})/2 \geq 10$ GeV, and the estimated ND overlap background contribution. (b) The $x_{\bar{p}}$ distribution for the ND dijet sample. (c) Shape comparison of $x_{\bar{p}}$ distributions for the SD dijet and ND dijet samples. (d) The ratio of the SD dijet to ND dijet event rates as a function of $x_{\bar{p}}$.

In Figure 5.22, the measured ratio $R_{\frac{SD}{ND}}(x_{\bar{p}})$ is compared between $\sqrt{s} = 630$ and 1800 GeV. In this figure, the leading two jets plus the next highest E_T jet is used in evaluating $x_{\bar{p}}$ if there is one with $E_T \geq 5$ GeV. The shape of the distribution at $\sqrt{s} = 630$ GeV is very similar to that at $\sqrt{s} = 1800$ GeV. However, the 630 GeV data points lie consistently above the 1800 GeV ones. This result implies that the normalization of the diffractive structure function $F_{jj}^{D}(\beta)$ measured in $p\bar{p}$ collisions at $\sqrt{s} = 630$ is higher than that at $\sqrt{s} = 1800$ GeV, since the ratio $R_{\frac{SD}{ND}}(x_{\bar{p}})$ is, in leading order QCD, approximately equal to the ratio of the diffractive to non-diffractive effective structure functions, and the effective non-diffractive structure function does not depend on the s value at which the structure function is measured.

Number of Jets Used in Evaluating $x_{\bar{p}}$

An uncertainty in the $R_{\frac{SD}{ND}}(x_{\bar{p}})$ distribution arises from the sensitivity of the ratio $R_{\frac{SD}{ND}}(x_{\bar{p}})$ to the number of jets used in evaluating the value of $x_{\bar{p}}$. The $R_{\frac{SD}{ND}}(x_{\bar{p}})$ distributions in which different numbers of jets are used in evaluating $x_{\bar{p}}$ are shown in Figures 5.23(a) and (b) for $\sqrt{s} = 630$ and 1800 GeV, respectively. Also, the $R_{\frac{SD}{ND}}(x_{\bar{p}})$ distribution is compared between $\sqrt{s} = 630$ and 1800 GeV in Figures 5.24(a) and (b), in which only the leading two jets are used in evaluating $x_{\bar{p}}$ and the leading two jets plus up to two extra jets with $E_T \geq 5$ GeV are included in the $x_{\bar{p}}$ evaluation, respectively. In all cases, the $R_{\frac{SD}{ND}}(x_{\bar{p}})$ distribution is falling with increasing $x_{\bar{p}}$ at both $\sqrt{s} = 630$ and 1800 GeV. Also, the 630 GeV data points lie above the 1800 GeV points or the 630 and 1800 GeV data points lie almost on top of each other. The ratio of the 630 to 1800 GeV data is quantitatively evaluated in Section 5.4.2.

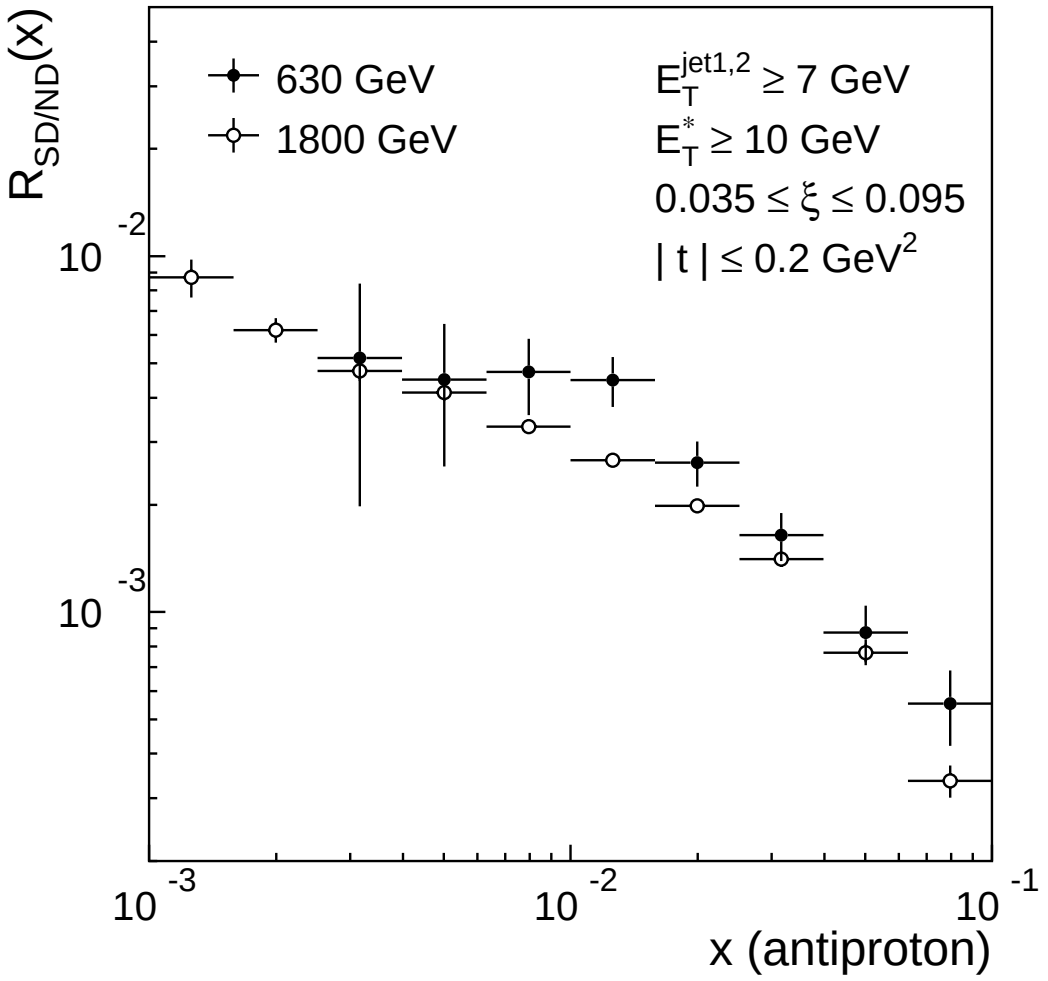

Figure 5.22: The ratio of SD dijet to ND dijet event rates as a function of $x_{\bar{p}}$ measured at $\sqrt{s} = 630$ (filled circles) and 1800 GeV (open circles), in the region $0.035 \leq \xi \leq 0.095$ and $|t| \leq 0.2$ GeV^2 for the SD data sample. Dijet events are selected by requiring $E_T^{jet1,2} \geq 7$ GeV and $E_T^* = (E_T^{jet1} + E_T^{jet2})/2 \geq 10$ GeV. Up to three jets with $E_T \geq 5$ GeV are used in evaluating $x_{\bar{p}}$.

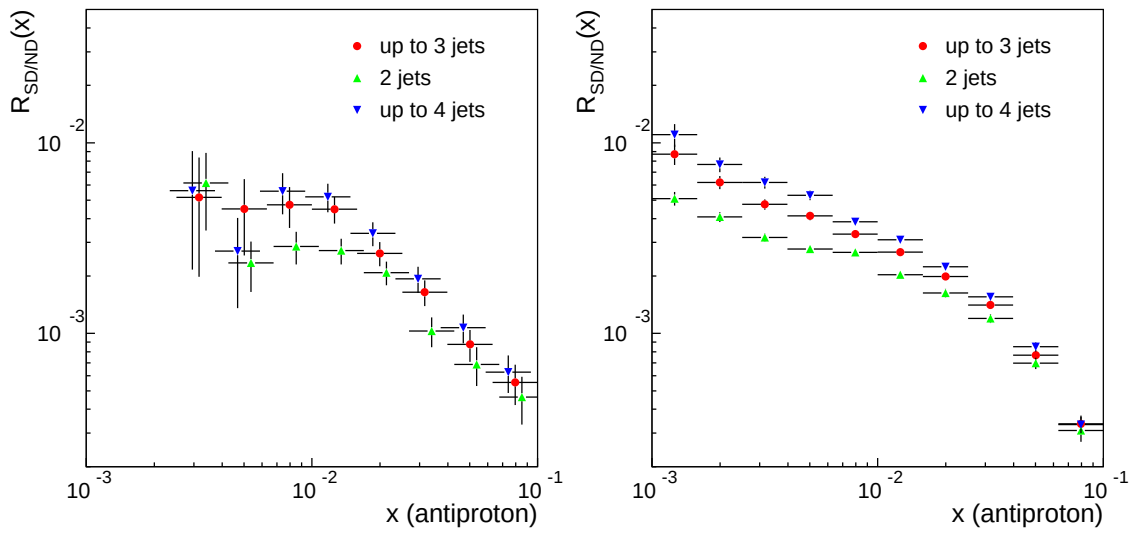

(a) 630 GeV (b) 1800 GeV

Figure 5.23: The ratio of SD dijet to ND dijet event rates as a function $x_{\bar{p}}$ measured at (a) $\sqrt{s} = 630$ GeV and (b) $\sqrt{s} = 1800$ GeV; in evaluating $x_{\bar{p}}$, up to three jets with $E_T \geq 5$ GeV are used (circles), only the leading two jets are used (upward triangles), and up to four jets with $E_T \geq 5$ GeV are included (downward triangles). For presentation purposes, the upward and downward triangles in (a) are shifted to the right and left, respectively, by $\Delta(\log x_{\bar{p}}) = 0.03$.

5.4.2 Comparison in Terms of F_{jj}^D

Figure 5.25 shows the $F_{jj}^D(\beta)$ distributions, normalized per unit ξ, for the 630 and 1800 GeV data samples. The distributions are fitted to the power law form $F_{jj}^D(\beta) = B_1(\beta/0.3)^{-n}$ in the region $-1.0 \leq \log\beta < -0.2$ ($0.1 \leq \beta \lesssim 0.6$). The value of 0.3 in the power law form corresponds approximately to the center of the $F_{jj}^D(\beta)$ distribution obtained at $\sqrt{s} = 630$ GeV on a logarithmic scale. The lower β limit is imposed to avoid detector (calorimeter) edge effects in the 630 GeV data. The upper limit of $\beta = 0.6$ is the value below which the $F_{jj}^D(\beta)$ distributions follow a power law. The fit of the $F_{jj}^D(\beta)$ distributions to the form $F_{jj}^D(\beta) = B_1(\beta/0.3)^{-n}$ yields $B_1 = 0.262 \pm 0.030$ and $n = 1.4 \pm 0.2$ with $\chi^2/d.o.f. = 1.6$ at $\sqrt{s} = 630$ GeV,

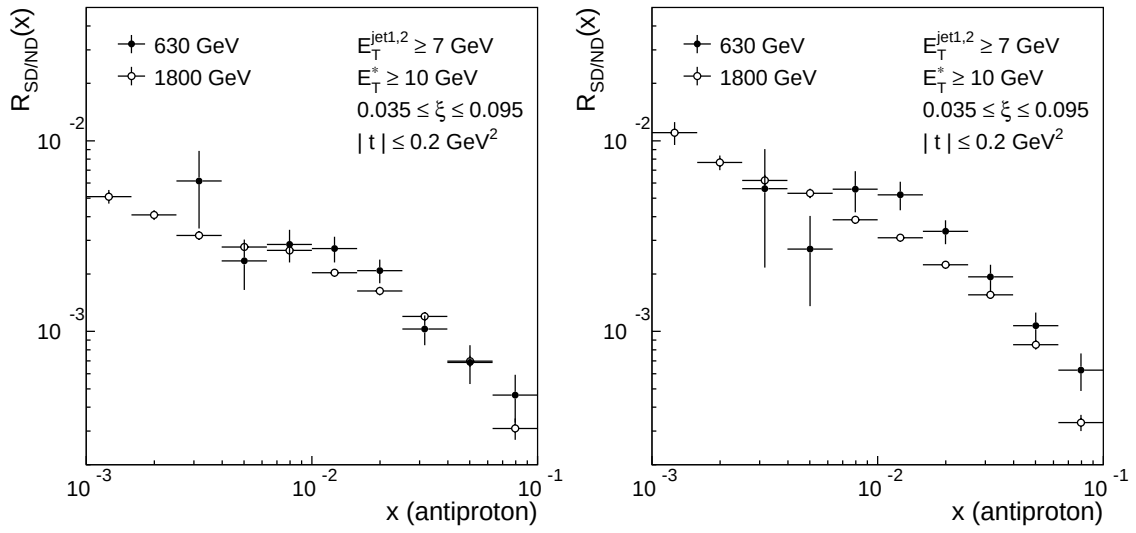

(a) Only the leading two jets are used in evaluating $x_{\bar{p}}$.

(b) Up to four jets with $E_T \geq 5$ GeV are used in evaluating $x_{\bar{p}}$.

Figure 5.24: The ratio of SD dijet to ND dijet event rates as a function of $x_{\bar{p}}$ measured at $\sqrt{s} = 630$ (filled circles) and 1800 GeV (open circles), in the region $0.035 \leq \xi \leq 0.095$ and $|t| \leq 0.2$ GeV^2 for the SD data samples.

and $B_1 = 0.193 \pm 0.005$ and $n = 1.2 \pm 0.04$ with $\chi^2/d.o.f. = 1.9$ at $\sqrt{s} = 1800$ GeV, respectively. Since the power n is consistent between the two energies, the $F_{jj}^D(\beta)$ distributions are fitted with the same n value at both energies in order to evaluate the ratio of the normalization factor of $F_{jj}^D(\beta)$ between the two energies. Fitting the 630 GeV distribution with the power $n = 1.2$ obtained from the fit of the higher statistics 1800 GeV data yields $B_1 = 0.255 \pm 0.029$ with $\chi^2/d.o.f. = 1.4$. Therefore, the ratio of 630 to 1800 GeV in the parameter B_1 is found to be

$$\begin{aligned} R_{\frac{630}{1800}} &= \frac{0.255 \pm 0.029}{0.193 \pm 0.005} \\ &= 1.32 \pm 0.15(\text{stat}). \end{aligned}$$

The systematic uncertainty in the ratio $R_{\frac{630}{1800}}$ is discussed below.

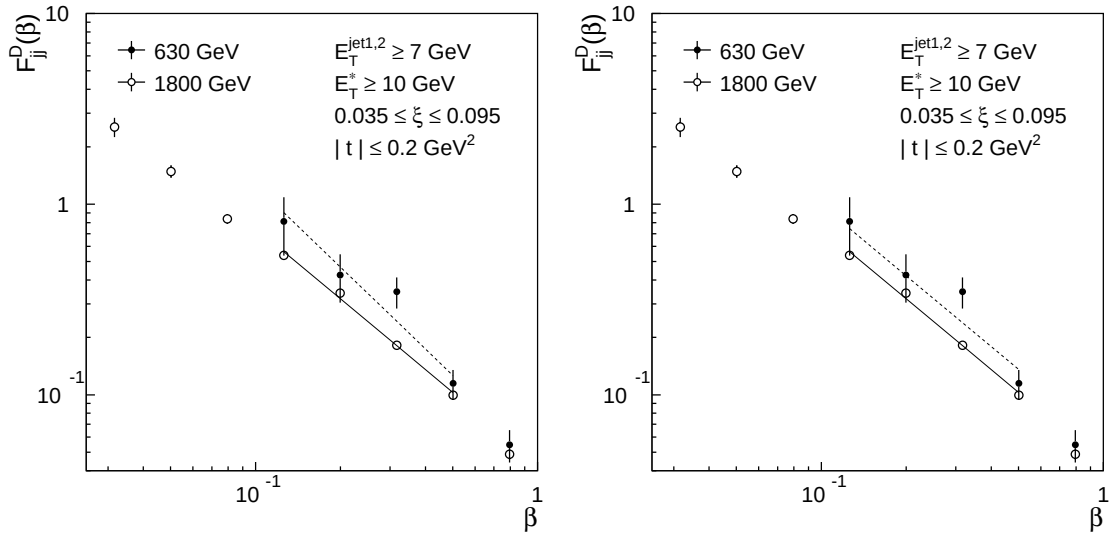

(a) The 630 and 1800 GeV distributions are fitted independently.

(b) The 630 GeV distribution is fitted with the n value obtained from the fit of the 1800 GeV distribution.

Figure 5.25: Distributions of $F_{jj}^D(\beta)$ extracted from dijet events with $E_T^{jet1,2} \geq 7$ GeV and $E_T^* = (E_T^{jet1} + E_T^{jet2})/2 \geq 10$ GeV for the region $0.035 \leq \xi \leq 0.095$ and $|t| \leq 0.2$ GeV^2 at $\sqrt{s} = 630$ (filled circles) and 1800 GeV (open circles). The leading two jets plus the next highest E_T jet are used in evaluating β if there is a third jet with $E_T \geq 5$ GeV. Each distribution is fitted to the power law form $F_{jj}^D(\beta) = B_1(\beta/0.3)^{-n}$.

Systematic Uncertainties in the Ratio $R_{\frac{630}{1800}}$

The dominant systematic uncertainties in the ratio $R_{\frac{630}{1800}}$ are due to

- the sensitivity of the ratio $R_{\frac{630}{1800}}$ to the number of jets used in evaluating $x_{\bar{p}}$ and $\beta = x_{\bar{p}}/\xi$, and
- uncertainties in the SD inclusive cross section σ_{SD}^{incl} and the BBC cross section σ_{BBC}.

The uncertainty arising from each source is discussed below.

Number of Jets Used in Evaluating β

The $F_{jj}^D(\beta)$ distributions vary when different numbers of jets are included in the

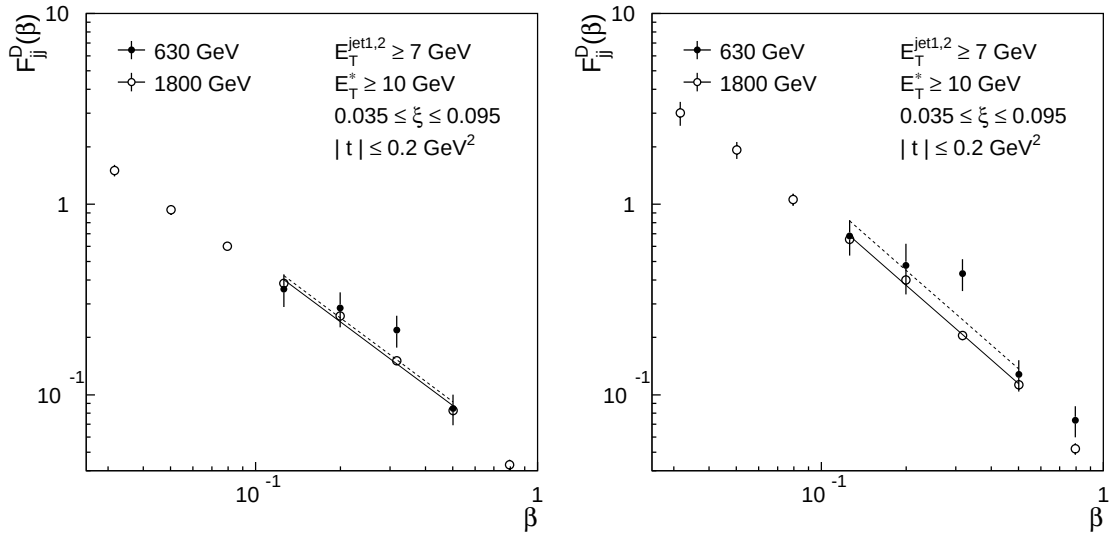

(a) Only the leading two jets are used in evaluating β.

(b) Up to four jets with $E_T^{jet} \geq 5$ GeV are used in evaluating β.

Figure 5.26: Distributions of $F_{jj}^D(\beta)$ extracted from dijet events with $E_T^{jet1,2} \geq 7$ GeV and $E_T^* = (E_T^{jet1} + E_T^{jet2})/2 \geq 10$ GeV for the region $0.035 \leq \xi \leq 0.095$ and $|t| \leq 0.2$ GeV^2 at $\sqrt{s} = 630$ (filled circles) and 1800 GeV (open circles). Each distribution is fitted to the power law form $F_{jj}^D(\beta) = B_1(\beta/0.3)^{-n}$. The 630 GeV distributions are fitted with the n value obtained from the fit of the corresponding 1800 GeV distributions.

evaluation of β. In Figure 5.25, up to three jets with $E_T \geq 5$ GeV are used in evaluating $x_{\bar{p}}$ and β, while in Figures 5.26(a) and (b), only the leading two jets are used in evaluating β and up to four jets with $E_T \geq 5$ GeV are included in the evaluation of β, respectively. In these three cases, the ratio $R_{\frac{630}{1800}}$ is,

$$R_{\frac{630}{1800}} = \begin{cases} 1.32 \pm 0.15(\text{stat}) & \text{up to three jets with } E_T \geq 5 \text{ GeV}, \\ 1.05 \pm 0.11(\text{stat}) & \text{only leading two jets}, \\ 1.20 \pm 0.14(\text{stat}) & \text{up to four jets with } E_T \geq 5 \text{ GeV}. \end{cases}$$

We use the ratio $R_{\frac{630}{1800}}$ obtained using up to three jets, and assign to it an asymmetric uncertainty so that all the ratios shown above are included within 1σ:

$$R_{\frac{630}{1800}} = 1.32^{+0.00}_{-0.27}.$$

Uncertainty in Normalization

In the comparison between 630 and 1800 GeV results, four different data sets are used: (a) SD inclusive data collected at $\sqrt{s} = 630$ and (b) 1800 GeV, (c) minimum bias data collected at $\sqrt{s} = 630$ and (d) 1800 GeV. The normalization of the SD dijet sample which is selected from the SD inclusive data is obtained from the SD inclusive cross section σ_{SD}^{incl}, as shown in Eq. (4.18). The normalization of the ND dijet sample which is selected from the minimum bias data is determined from the effective BBC cross section σ_{BBC}, as shown in Eq. (4.21). The SD inclusive cross section at $\sqrt{s} = 630$ GeV in the region $0.035 \leq \xi \leq 0.095$ and $|t| \leq 0.2$ GeV^2, which was evaluated in Section 4.4.1, and the effective BBC cross sections at $\sqrt{s} = 630$ and 1800 GeV are

$$\sigma_{SD\ incl}^{630\ GeV}(0.035 \leq \xi \leq 0.095, |t| \leq 0.2\ \text{GeV}^2) = 0.42 \pm 0.02\ \text{mb},$$

$$\sigma_{BBC}^{630\ GeV} = 39.9 \pm 1.2\ \text{mb},$$

$$\sigma_{BBC}^{1800\ GeV} = 51.15 \pm 1.60\ \text{mb}.$$

We evaluate the SD inclusive cross section at $\sqrt{s} = 1800$ GeV in the region $0.035 \leq \xi \leq 0.095$ and $|t| \leq 0.2$ GeV^2 in a similar manner to that used for the SD inclusive cross section at $\sqrt{s} = 1800$ GeV in the region $0.035 \leq \xi \leq 0.095$ and $|t| \leq 1.0$ GeV^2, as documented in Section 4.4.1. Using Eq. (4.8) from Ref. [30], we obtain for the SD cross section at $\sqrt{s} = 1800$ GeV integrated over $0.035 \leq \xi \leq 0.095$ and $|t| \leq 0.2$ GeV^2, $\sigma_{SD\ incl}^{1800\ GeV}(\text{CDF fit}) = 0.57 \pm 0.03(\text{stat})$ mb ($\sigma_{I\!P} = 0.29$ mb, $\sigma_{I\!R} = 0.49$ mb). From the result of a global fit to the pp and $p\bar{p}$ SD cross sections [71], we obtain $\sigma_{SD\ incl}^{1800\ GeV}(\text{global fit}) = 0.40 \pm 0.04(\text{syst})$ mb ($\sigma_{I\!P} = 0.19$ mb, $\sigma_{\pi} = 0.21$ mb). We use the CDF-measured value of $\sigma_{SD\ incl}^{1800\ GeV}(\text{CDF fit})$, but assign to it an asymmetric

systematic uncertainty so that the -1σ value reaches the value of $\sigma_{SD\ incl}^{1800\ GeV}$(global fit):

$$\begin{aligned}\sigma_{SD\ incl}^{1800\ GeV}(0.035 \leq \xi \leq 0.095, |t| \leq 0.2\ \mathrm{GeV}^2) &= 0.57 \pm 0.03(\mathrm{stat}) \pm {}^{+0.00}_{-0.17}(\mathrm{syst})\ \mathrm{mb} \\ &= 0.57^{+0.03}_{-0.17}\ \mathrm{mb}.\end{aligned}$$

The uncertainties in $\sigma_{SD\ incl}^{630\ GeV}$, $\sigma_{SD\ incl}^{1800\ GeV}$, $\sigma_{BBC}^{630\ GeV}$ and $\sigma_{BBC}^{1800\ GeV}$ are propagated to the uncertainty in the ratio $R_{\frac{630}{1800}}$ using the standard error propagation formula, yielding

$$\begin{aligned}R_{\frac{630}{1800}} &= 1.32 \pm 0.04(\sigma_{BBC}^{630\ GeV}) \pm 0.04(\sigma_{BBC}^{1800\ GeV}) \pm 0.05(\sigma_{SD\ incl}^{630\ GeV})^{+0.40}_{-0.07}(\sigma_{SD\ incl}^{1800\ GeV}) \\ &= 1.32^{+0.41}_{-0.10},\end{aligned}$$

where the symbols in the parentheses show the source of the uncertainty.

Summary of the Ratio $R_{\frac{630}{1800}}$

Adding these uncertainties in quadrature, the ratio $R_{\frac{630}{1800}}$ is estimated to be

$$R_{\frac{630}{1800}} = 1.3 \pm 0.2(\mathrm{stat})^{+0.4}_{-0.3}(\mathrm{syst}).$$

Although the ratio is consistent with unity within the error, its central value is higher than unity, which may indicate a breakdown of factorization.

Comparison with Predictions from Phenomenological Models

Several phenomenological models which explain the suppression of the diffractive structure function measured at the Tevatron relative to that obtained at HERA, such as the pomeron flux renormalization model [31], the soft color exchange model [48], and the rapidity gap survival probability model [43, 44], predict that the normalization factor of the diffractive structure function is higher at $\sqrt{s} = 630$ GeV than at $\sqrt{s} = 1800$ GeV. With a pomeron intercept of $\alpha_{I\!P}(0) = 1.104$ [27], the pomeron flux renormalization model predicts $R_{\frac{630}{1800}} = (1800/630)^{4(\alpha_{I\!P}(0)-1)} = 1.55$. The rapidity gap survival probability model predicts $R_{\frac{630}{1800}} = 1.8$ [80]. The measured ratio

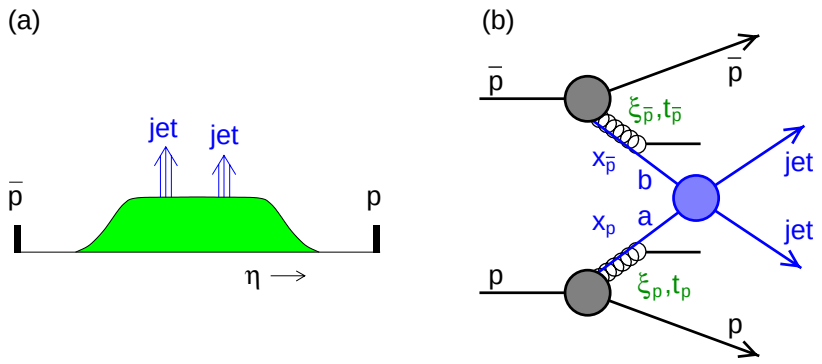

Figure 5.27: Illustrations of (a) event topology in pseudorapidity η and (b) diagram for dijet production in double pomeron exchange.

$R_{\frac{630}{1800}} = 1.3 \pm 0.2(\text{stat})^{+0.4}_{-0.3}(\text{syst})$ is compatible with the factorization expectation of unity, but also with predictions from the pomeron flux renormalization model and the rapidity gap survival probability model.

5.5 Comparison with Results from Double Pomeron Exchange Dijet Events

Double pomeron exchange (DPE) events are characterized by quasielastically-scattered leading proton and antiproton, which are separated from the diffractive mass system X by large rapidity gaps. The first observation of dijet production by DPE was reported by the CDF collaboration in $p\bar{p}$ collisions at $\sqrt{s} = 1800$ GeV [25]. The process of dijet production in events with a DPE event topology is shown schematically in Figure 5.27.

As mentioned in Section 2.3.3, the ratio $R_{\frac{SD}{ND}}(x_{\bar{p}})$ of single diffractive (SD) dijet to non-diffractive (ND) dijet production rates as a function of $x_{\bar{p}}$ is, in leading order QCD, approximately equal to the ratio of the diffractive structure function F^D_{jj} to the non-diffractive structure function F_{jj} of the antiproton. Assuming QCD factorization

for diffraction processes, the cross section for DPE dijet production can be expressed in terms of the diffractive parton distribution functions of the proton and antiproton as

$$\frac{d^7\sigma^{jj}_{DPE}}{dx_p dx_{\bar{p}} d\xi_p d\xi_{\bar{p}} dt_p dt_{\bar{p}} d\hat{t}} = \sum_{a,b} f^D_{a/p}(x_p, Q^2, \xi_p, t_p) f^D_{b/\bar{p}}(x_{\bar{p}}, Q^2, \xi_{\bar{p}}, t_{\bar{p}}) \frac{d\hat{\sigma}_{ab\to jj}}{d\hat{t}}. \quad (5.11)$$

The variables ξ_p and $\xi_{\bar{p}}$ are the fractional momentum loss of the proton and antiproton, and t_p and $t_{\bar{p}}$ are the four-momentum transfer at the $I\!Pp$ and $I\!P\bar{p}$ vertices. Using the diffractive structure function $F^D_{jj}(x, Q^2, \xi, t)$ of the proton or antiproton defined by Eq. (2.43), the DPE dijet cross section is given by

$$\frac{d^7\sigma^{jj}_{DPE}}{dx_p dx_{\bar{p}} d\xi_p d\xi_{\bar{p}} dt_p dt_{\bar{p}} d\hat{t}} \approx \frac{F^D_{jj}(x_p, Q^2, \xi_p, t_p)}{x_p} \frac{F^D_{jj}(x_{\bar{p}}, Q^2, \xi_{\bar{p}}, t_{\bar{p}})}{x_{\bar{p}}} \frac{d\hat{\sigma}_{gg\to jj}}{d\hat{t}}. \quad (5.12)$$

From Eqs. (2.44) and (5.12), the ratio of DPE dijet to SD dijet production rates is

$$\begin{aligned} & R_{\frac{DPE}{SD}}(x_p, \xi_p, t_p) \\ & \approx \frac{\int dx_{\bar{p}} \int d\xi_{\bar{p}} \int dt_{\bar{p}} \int d\hat{t} \frac{F^D_{jj}(x_p, Q^2, \xi_p, t_p)}{x_p} \frac{F^D_{jj}(x_{\bar{p}}, Q^2, \xi_{\bar{p}}, t_{\bar{p}})}{x_{\bar{p}}} \frac{d\hat{\sigma}_{gg\to jj}}{d\hat{t}}}{\int dx_{\bar{p}} \int d\xi_{\bar{p}} \int dt_{\bar{p}} \int d\hat{t} \frac{F_{jj}(x_p, Q^2)}{x_p} \frac{F^D_{jj}(x_{\bar{p}}, Q^2, \xi_{\bar{p}}, t_{\bar{p}})}{x_{\bar{p}}} \frac{d\hat{\sigma}_{gg\to jj}}{d\hat{t}}} \quad (5.13) \\ & = \frac{F^D_{jj}(x_p, \xi_p, t_p)}{F_{jj}(x_p)}, \quad (5.14) \end{aligned}$$

where the Q^2-dependence of the structure functions is ignored. When the ratio $R_{\frac{DPE}{SD}}(x_p, \xi_p, t_p)$ is integrated over ξ_p and t_p, the ratio $R_{\frac{DPE}{SD}}$ is given by

$$R_{\frac{DPE}{SD}}(x_p) = F^D_{jj}(x_p)/F_{jj}(x_p). \quad (5.15)$$

Therefore, QCD factorization can be tested by comparing the ratios $R_{\frac{SD}{ND}}(x_{\bar{p}})$ and $R_{\frac{DPE}{SD}}(x_p)$.

Dijet events with a DPE event topology have been studied at $\sqrt{s} = 1800$ GeV by the CDF collaboration [25] using the same data sample as that used for the single

diffractive dijet analysis described in this dissertation. The events were collected by triggering on a leading antiproton detected in the Roman Pot spectrometer. In the SD data sample, a DPE signal is searched for by requiring a rapidity gap in the forward calorimeter and BBC on the proton outgoing side (positive η in the CDF coordinate system). Since the quasielastically scattered leading proton is not detected, the fractional momentum loss of the proton ξ_p is determined from the information of final state particles in the diffractive mass system X, based on the formula [81]:

$$\xi_p = \frac{1}{\sqrt{s}} \sum_i E_T^i e^{\eta^i}. \tag{5.16}$$

In practice, the sum is carried out over all hits in the BBCs and calorimeter towers above noise level. The ξ_p value reconstructed by this method is calibrated by comparing the value of $\xi_{\bar{p}}$ obtained by the above procedure[6] with that determined by the Roman Pot spectrometer. Events without hits in the forward calorimeter and BBC on the proton outgoing side are concentrated in the region $0.01 < \xi_p < 0.03$.

To test QCD factorization in diffraction processes, the ratio $R_{\frac{DPE}{SD}}(x_p)$ is compared with the ratio $R_{\frac{SD}{ND}}(x_{\bar{p}})$ as a function of $x\,(\equiv x_p = x_{\bar{p}})$ in Figure 5.28, where the ratios $R_{\frac{DPE}{SD}}(x_p)$ and $R_{\frac{SD}{ND}}(x_{\bar{p}})$ are normalized per unit ξ. For this comparison, the data are restricted to the regions $7 < E_T^{jet1,2} < 10$ GeV, $|t_{\bar{p}}| < 1$ GeV^2, $0.035 < \xi_{\bar{p}} < 0.095$, and for DPE $0.01 < \xi_p < 0.03$. In the chosen ξ_p region of $0.01 < \xi_p < 0.03$, the SD background in the DPE candidate event sample is negligibly small. The vertical dashed lines mark the DPE kinematic boundary (left) and the value of $x = \xi_{p,min} = 0.01$ (right), where $\xi_{p,min}$ is the minimum value of the ξ_p range used. The weighted average of the $R_{\frac{DPE}{SD}}(x_p)$ and $R_{\frac{SD}{ND}}(x_p)$ data points in the region between the vertical

[6] The sign in the exponent of Eq. (5.16) should be reversed for $\xi_{\bar{p}}$.

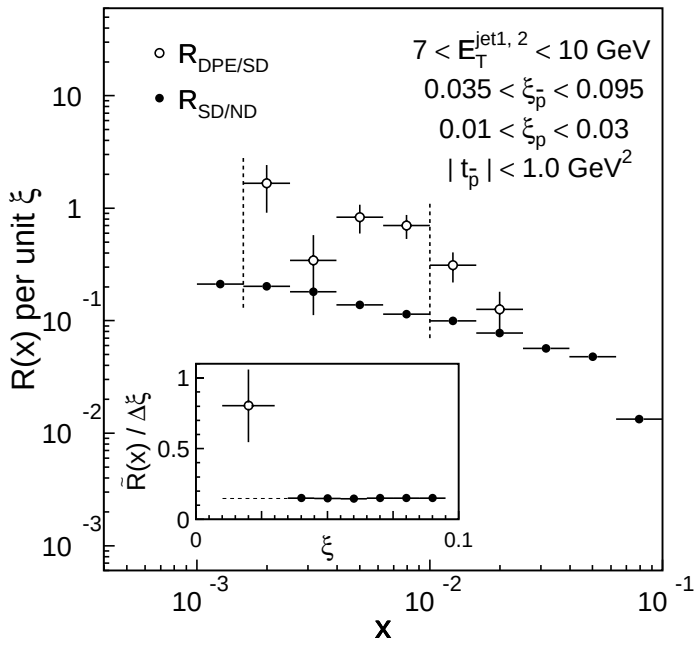

Figure 5.28: Ratios of DPE to SD (SD to ND) dijet event rates per unit ξ, shown as open (filled) circles, as a function of x-Bjorken of the struck parton in the proton (antiproton). The errors are statistical only. The SD/ND ratio has a normalization uncertainty of ± 20 %. The inset shows $\tilde{R}(x)$ per unit ξ versus ξ, where the tilde over the R indicates the weighted average of the $R(x)$ points in the region of x within the vertical dashed lines. This figure is adapted from Figure 4 in Ref. [25].

dashed lines is

$$\tilde{R}_{\frac{DPE}{SD}} = 0.80 \pm 0.26,$$

$$\tilde{R}_{\frac{SD}{ND}} = 0.14 \pm 0.01,$$

where the tilde over R indicates the weighted average of the points in the region of x within the vertical dashed lines in the main figure of Figure 5.28. The ratios $\tilde{R}_{\frac{DPE}{SD}}$ and $\tilde{R}_{\frac{SD}{ND}}$ have to be compared in the same ξ regions to test factorization. However, the ξ_p region where $\tilde{R}_{\frac{DPE}{SD}}$ is evaluated is $0.01 < \xi_p < 0.03$, which does not overlap with the $\xi_{\bar{p}}$ region of $0.035 < \xi_{\bar{p}} < 0.095$ where $\tilde{R}_{\frac{DPE}{SD}}$ is evaluated. The ξ-dependence of the ratios $\tilde{R}_{\frac{DPE}{SD}}(\xi_p)$ and $\tilde{R}_{\frac{SD}{ND}}(\xi_{\bar{p}})$ is examined in the inset in Figure 5.28. The ratio $\tilde{R}_{\frac{SD}{ND}}(\xi_p)$ is approximately flat in $\xi_{\bar{p}}$. The extrapolation of a straight line fit to the six

$\tilde{R}_{\frac{SD}{ND}}$ ratios to $\xi_p = 0.02$ yields

$$\tilde{R}_{\frac{SD}{ND}} = 0.15 \pm 0.02.$$

The double ratio of $\tilde{R}_{\frac{SD}{ND}}$ to $\tilde{R}_{\frac{DPE}{SD}}$ is found to be

$$D \equiv \tilde{R}_{\frac{SD}{ND}} / \tilde{R}_{\frac{DPE}{SD}} = 0.19 \pm 0.07.$$

The deviation of D from unity indicates a breakdown of QCD factorization in diffraction processes.

5.6 Comparison with Results from Hard Single Diffraction with Rapidity Gaps

In the analysis described in this dissertation, single diffractive (SD) events are identified by detecting a leading antiproton. However, the CDF collaboration has previously studied hard SD processes, such as SD W [18], dijet [19], b-quark [21] and J/ψ production [22], by identifying SD events using a rapidity gap signature in the forward detectors, such as the forward calorimeters and BBCs.

In the analysis of SD J/ψ production by the CDF collaboration, J/ψ events associated with at least one jet were studied in terms of the x-Bjorken of the struck parton in the proton or antiproton associated with the detected rapidity gap, in a similar manner to that used in the SD dijet analysis described in this dissertation. In events containing a J/ψ meson associated with at least one jet, the values of x-Bjorken of partons in the proton (x_p) and antiproton ($x_{\bar{p}}$) participating in J/ψ production can be evaluated based on the formula:

$$x = \frac{p_T^{J/\psi} e^{\pm \eta^{J/\psi}} + E_T^{jet} e^{\pm \eta^{jet}}}{\sqrt{s}}, \tag{5.17}$$

where the + (−) sign in the exponents is for x_p ($x_{\bar{p}}$). In practice, since the E_T of the leading jet is expected to be balanced by the E_T of the J/ψ, and $p_T^{J/\psi}$ is more accurately measured by the tracking detectors than E_T^{jet} measured by the calorimeters, $p_T^{J/\psi}$ is used instead of E_T^{jet} in the determination of x,

$$x = \frac{p_T^{J/\psi}(e^{\pm\eta^{J/\psi}} + e^{\pm\eta^{jet}})}{\sqrt{s}}. \tag{5.18}$$

The fractional momentum loss ξ of the proton or antiproton associated with the detected rapidity gap is determined as is done in the analysis of DPE dijet events described in Section 5.5.

The ratio of SD to ND event rates for J/ψ production $R^{J/\psi}_{\frac{SD}{ND}}(x)$, normalized per unit ξ, is compared with that for dijet production $R^{jj}_{\frac{SD}{ND}}(x)$ as a function of x in Figure 5.29. The ratio $R^{J/\psi}_{\frac{SD}{ND}}(x)$ is divided by a factor of 2 when it is compared with the ratio $R^{jj}_{\frac{SD}{ND}}(x)$ from the analysis of SD dijet events with a leading antiproton, since in the J/ψ case, rapidity gaps on both the positive and negative η sides are considered. The ratio is evaluated in the region $0.01 \leq \xi \leq 0.03$ for J/ψ production, and in the region $0.035 \leq \xi \leq 0.095$ for dijet production. The vertical dashed lines in Figure 5.29 show the kinematic boundaries. The upper bound corresponds to the minimum ξ value ξ_{min} of the SD J/ψ event sample and ensures that all ξ values within $0.01 \leq \xi \leq 0.03$ contribute to the x distribution, while the lower bound x_{min} is imposed to avoid detector edge effects. Both the J/ψ and dijet distributions exhibit similar behavior.

As shown in Eq. (2.44), the ratio $R^{jj}_{\frac{SD}{ND}}(x)$ of the SD dijet event rate in a certain ξ-t region to the ND dijet event rate as a function of x-Bjorken of the particle which is scattered quasielastically in the SD event is related to the diffractive and usual

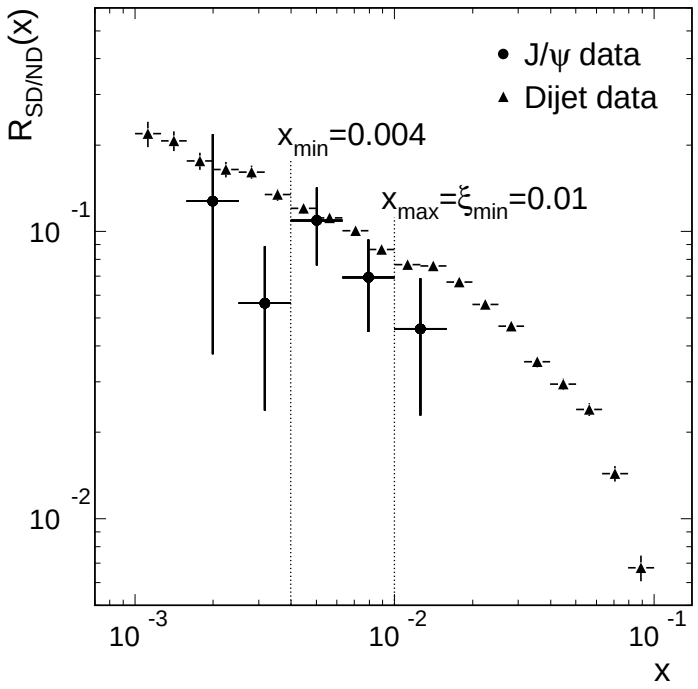

Figure 5.29: Ratios of SD to ND J/ψ (circles) and dijet (triangles) event rates per unit ξ as a function of x-Bjorken of the struck parton in the proton (antiproton) associated with the rapidity gap. This figure is adapted from Figure 4 in Ref. [22].

non-diffractive parton distribution functions as

$$R^{jj}_{\frac{SD}{ND}}(x) \approx \frac{f^D_g(x) + \frac{C_F}{C_A}\sum_i \left(f^D_{q_i}(x) + f^D_{\bar{q}_i}(x)\right)}{f_g(x) + \frac{C_F}{C_A}\sum_i \left(f_{q_i}(x) + f_{\bar{q}_i}(x)\right)}, \tag{5.19}$$

where $C_F = 4/3$ and $C_A = 3$ are color factors and the Q^2-dependence of the parton distribution functions is ignored. The diffractive parton distribution functions are integrated over the given ξ-t region. For simplicity, hereafter we denote the sum of the diffractive quark distribution functions and the sum of the usual non-diffractive quark distribution functions by $f^D_q(x) = \sum_i \left(f^D_{q_i}(x) + f^D_{\bar{q}_i}(x)\right)$ and $f_q(x) = \sum_i \left(f_{q_i}(x) + f_{\bar{q}_i}(x)\right)$, respectively. In high energy $p\bar{p}$ collisions, J/ψ mesons are produced dominantly by gluon-gluon interactions. Therefore, the ratio $R^{J/\psi}_{\frac{SD}{ND}}(x)$

of SD to ND J/ψ event rates may be approximated as

$$R^{J/\psi}_{\frac{SD}{ND}}(x) \approx \frac{f_g^D(x)}{f_g(x)}. \tag{5.20}$$

From Eqs. (5.19) and (5.20), the ratio of $R^{jj}_{\frac{SD}{ND}}(x)$ to $R^{J/\psi}_{\frac{SD}{ND}}(x)$ is given by

$$\frac{R^{jj}_{\frac{SD}{ND}}(x)}{R^{J/\psi}_{\frac{SD}{ND}}(x)} \approx \frac{1+\frac{4}{9}\frac{f_q^D(x)}{f_g^D(x)}}{1+\frac{4}{9}\frac{f_q(x)}{f_g(x)}}. \tag{5.21}$$

Evaluating this ratio of ratios by integrating the $R^{jj}_{\frac{SD}{ND}}(x)$ and $R^{J/\psi}_{\frac{SD}{ND}}(x)$ distributions in the region $0.004 \leq x \leq 0.01$ in Figure 5.29 yields

$$R^{jj}_{\frac{SD}{ND}}/R^{J/\psi}_{\frac{SD}{ND}} = 1.17 \pm 0.27(\text{stat}) \pm 0.13(\text{syst}),$$

where the systematic uncertainty includes in quadrature only the uncertainties associated with the J/ψ measurement.

It is worth mentioning here that the ξ region in the SD J/ψ measurement does not overlap with that in the SD dijet measurement. However, since no significant ξ-dependence of the ratio $R^{jj}_{\frac{SD}{ND}}(x)$ is observed in the region $0.035 \leq \xi \leq 0.095$, as described in Section 5.1, we assume that $R_{\frac{SD}{ND}}(x)$ does not depend on ξ down to $\xi = 0.01$. Also, the t region is different between the SD J/ψ measurement and the SD dijet measurement. In the J/ψ analysis, the value of t is not measured, and the measurement is integrated over all t values, while the dijet analysis is performed in the region $|t| \leq 1.0$ GeV^2. Since the t distribution falls very rapidly, as shown in Eqs. (2.14) and (2.15) and in Figure 4.13, the difference in the t region between the J/ψ measurement and the dijet measurement is ignored in the following argument.

Using, in Eq. (5.21), the measured value of the ratio $R^{jj}_{\frac{SD}{ND}}/R^{J/\psi}_{\frac{SD}{ND}} = 1.17 \pm 0.27(\text{stat}) \pm 0.13(\text{syst})$ and the ratio of $f_q(x)/f_g(x) = 0.274$ at $x = 0.0063$ and

$Q^2 = 36$ GeV^2 extracted from the GRV98LO PDF set, the gluon fraction in the diffractive exchange $F_g^D \equiv f_g^D/(f_g^D + f_q^D)$ is found to be[7]

$$\begin{aligned} F_g^D &= 0.59 \pm 0.24(\text{stat}) \pm 0.11(\text{syst}) \\ &= 0.59 \pm 0.26, \end{aligned}$$

where the quoted systematic uncertainty is due to only the uncertainties associated with the J/ψ measurement. The measured value of $F_g^D = 0.59 \pm 0.26$ is consistent with the gluon fraction of $F_g^D = 0.54^{+0.16}_{-0.14}$ obtained by combining results on SD W, dijet and b-quark production [18, 19, 21].

As presented in Section 5.1, one of the main uncertainties in the normalization of the ratio $R^{jj}_{\frac{SD}{ND}}(x)$ for dijet production, which arises from the sensitivity of the ratio $R^{jj}_{\frac{SD}{ND}}(x)$ to the number of jets included in the x determination, is about $^{+15}_{-21}$ %. Another uncertainty, which is due to the uncertainty in the normalization of the SD data sample, is about ± 26 % as shown in Table 4.7. These uncertainties in the ratio $R_{\frac{SD}{ND}}(x)$ contribute an additional uncertainty to F_g^D of $^{+0.34}_{-0.31}$.

5.7 Comparison with UA8 Results

5.7.1 Summary of UA8 Results

The UA8 collaboration has studied single diffractive (SD) dijet production in $p\bar{p}$ collisions at $\sqrt{s} = 630$ GeV using data from the 1988−1989 $Sp\bar{p}S$ collider run [4]. In Ref. [4], an intensive study of the structure of the pomeron is made using mainly a variable x(2-jet) which is, in the absence of gluon radiation, jet-clustering and detector

[7] In Ref. [22], the errors in the ratio $R^{jj}_{\frac{SD}{ND}}/R^{jj}_{\frac{SD}{ND}}$ were not fully propagated to the errors in the gluon fraction F_g^D. The errors shown here are corrected errors, which are larger than those in Ref. [22] by a factor of about 1.7.

effects, related to the parton momenta in the pomeron and proton by

$$x(\text{2-jet}) = \beta - x_p, \tag{5.22}$$

where the antiproton is assumed to be scattered quasielastically. Figure 5.30(a) (Figure 4(a) of Ref. [4]) shows the x(2-jet) distribution observed in the UA8 data together with Monte Carlo predictions based on hard and soft pomeron structure functions. The hard and soft pomeron structure functions are defined as $\beta f(\beta) = 6\beta(1-\beta)$ and $\beta f(\beta) = 6(1-\beta)^5$, respectively, where $f(\beta)$ is the parton distribution function of the pomeron. It was found that the data distribution has a component at high x(2-jet), which is harder than the prediction from the hard pomeron structure function. Therefore, a super-hard pomeron structure function of the form $\beta f(\beta) = \delta(\beta - 1)$ was introduced, in which all the momentum of the pomeron enters into the hard scattering. The x(2-jet) distribution expected for the super-hard pomeron structure function is shown in Figure 5.30(b) (Figure 4(b) of Ref. [4]). A fit of the data x(2-jet) distribution to a sum of predictions for the soft, hard and super-hard pomeron structure functions yielded a pomeron structure function consisting of

$$\beta f(\beta) = \begin{cases} \delta(\beta-1) & \text{(super-hard)} & 30\ \%, \\ 6\beta(1-\beta) & \text{(hard)} & 57\ \%, \\ 6(1-\beta)^5 & \text{(soft)} & 13\ \%. \end{cases}$$

5.7.2 Comparing Data

In this section, we re-analyze our CDF 630 GeV SD data *à la* UA8, and compare the x(2-jet) distribution between the UA8 and CDF data. The following changes are made from our original CDF 630 GeV data analysis described in the preceding sections:

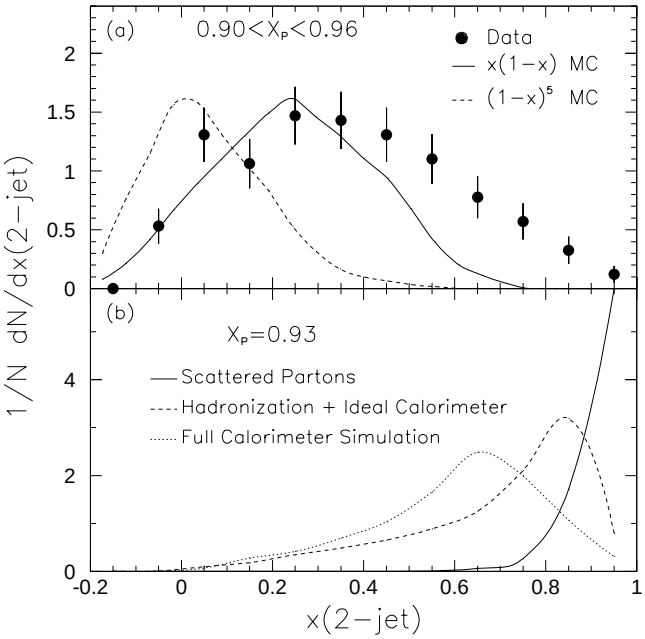

Figure 5.30: (a) Observed x(2-jet) distribution for the UA8 data in the region $0.04 < \xi < 0.10$. The two curves show the expected distributions for the hard and soft structure functions with arbitrary normalizations. (b) Results of x(2-jet) calculation in PYTHIA for $\xi = 0.07$, assuming the entire momentum of the pomeron participates in the hard scattering. The solid line is the scattered parton distribution before hadronization. The dashed curve is after hadronization and assuming an idealized calorimeter. The dotted curve shows the result of a full detector simulation. This figure is adapted from Figure 4 in Ref. [4].

- $0.04 \leq \xi \leq 0.10$. ($\leftarrow$ $0.035 \leq \xi \leq 0.095$.)
- Jet cone radius $R = 1.0$. ($\leftarrow$ $R = 0.7$.)
- Neither underlying event nor out-of-cone corrections are applied. ($\leftarrow$ Both corrections are applied.)
- $E_T^{jet1,2} \geq 8$ GeV. ($\leftarrow$ $E_T^{jet1,2} \geq 7$ GeV.)
- $|\eta^{jet1,2}| \leq 2$. ($\leftarrow$ No restriction.)
- $\Delta\phi_{jj} \geq 135°$. ($\leftarrow$ No restriction.)

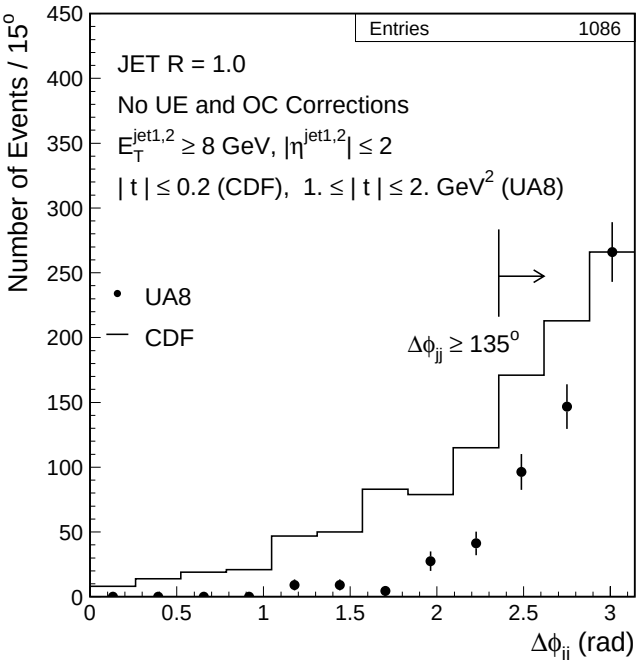

Figure 5.31: The azimuthal angle difference $\Delta\phi_{jj}$ between the leading two jets for the UA8 (points) and CDF (histogram) data samples.

The descriptions in the parentheses are the ones used originally in the preceding sections.

In Figure 5.31, the distribution of the azimuthal angle difference $\Delta\phi_{jj}$ between the leading two jets to which the $\Delta\phi_{jj} \geq 135^\circ$ cut has not yet been applied is compared between the UA8 and CDF data. It is found that the CDF distribution is broader and has a longer tail toward smaller $\Delta\phi_{jj}$ values than the UA8 distribution. However, the x(2-jet) distribution is almost the same for events with $\Delta\phi_{jj} \geq 135^\circ$ and $\Delta\phi_{jj} < 135^\circ$, as shown in Figure 5.32. Therefore, we ignore the difference in the $\Delta\phi_{jj}$ distribution and apply the $\Delta\phi_{jj} \geq 135^\circ$ cut to both the UA8 and CDF data. Figure 5.33 shows a comparison of the x(2-jet) distributions for the UA8 and CDF data. The CDF x(2-jet) distribution is similar to, but has a somewhat larger soft component than the UA8 distribution. This may be explained by the difference in the ξ distribution; the UA8 data have more events in the low ξ region than the CDF data, as shown in

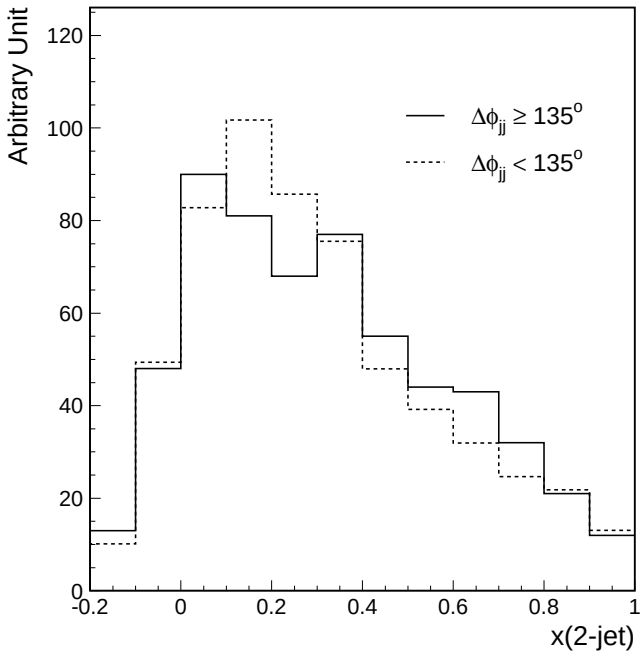

Figure 5.32: Distributions of x(2-jet) for SD dijet events with $\Delta\phi_{jj} \geq 135^\circ$ (solid line) and $\Delta\phi_{jj} < 135^\circ$ (dashed line) in the CDF data.

Table 5.8. Figure 5.34(a) shows that events with low ξ values favor higher x(2-jet) values as expected from kinematics: when a pomeron is emitted with low momentum, the event is required to have a higher x(2-jet) value in order to produce jets. By weighting events in the CDF data so that the ξ distribution becomes similar to that for the UA8 data, we obtain the x(2-jet) distribution shown in Figure 5.34(b). This figure shows good agreement between the UA8 and CDF distributions. From this result, we conclude that the x(2-jet) distributions for the CDF and UA8 data are compatible.

Table 5.8: Number of events in the UA8 and CDF data samples in three ξ intervals.

Experiment	ξ-ranges			Total
	0.04−0.06	0.06−0.08	0.08−0.10	
UA8	86	86	77	249
CDF	150	286	214	650

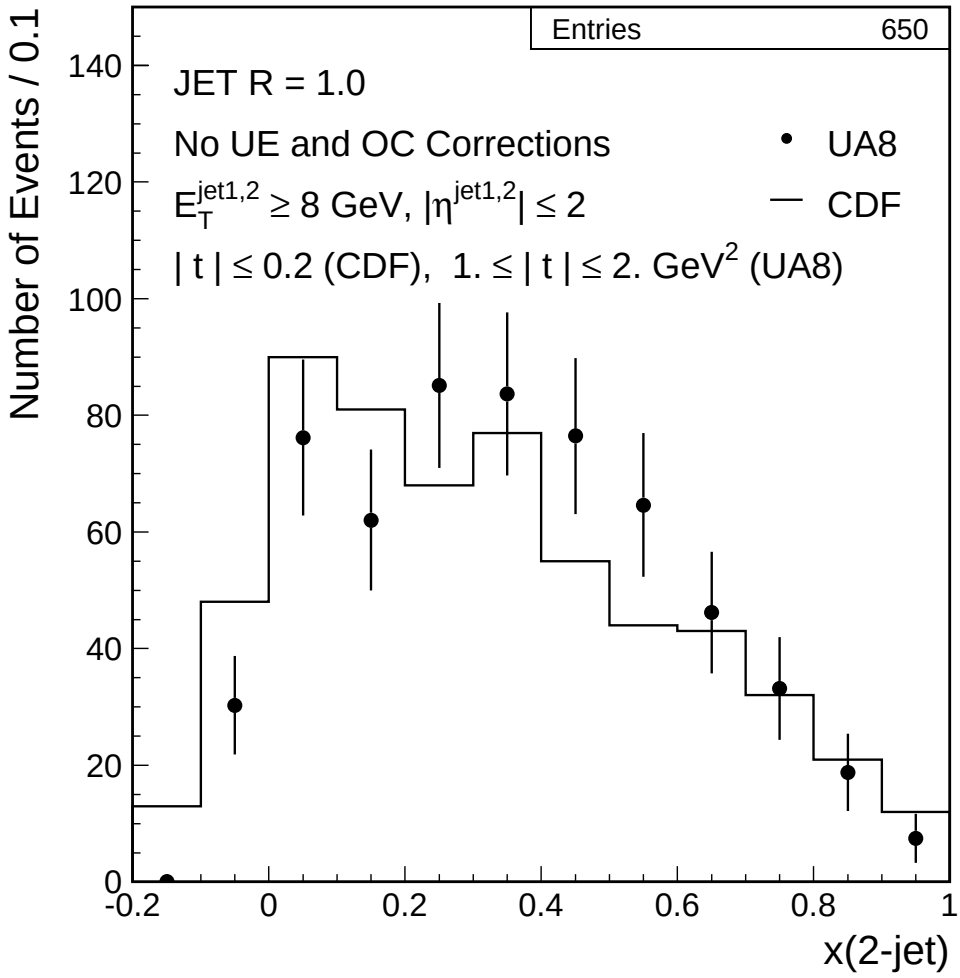

Figure 5.33: Distributions of x(2-jet) for SD dijet events in the UA8 (points) and CDF (histogram) data samples.

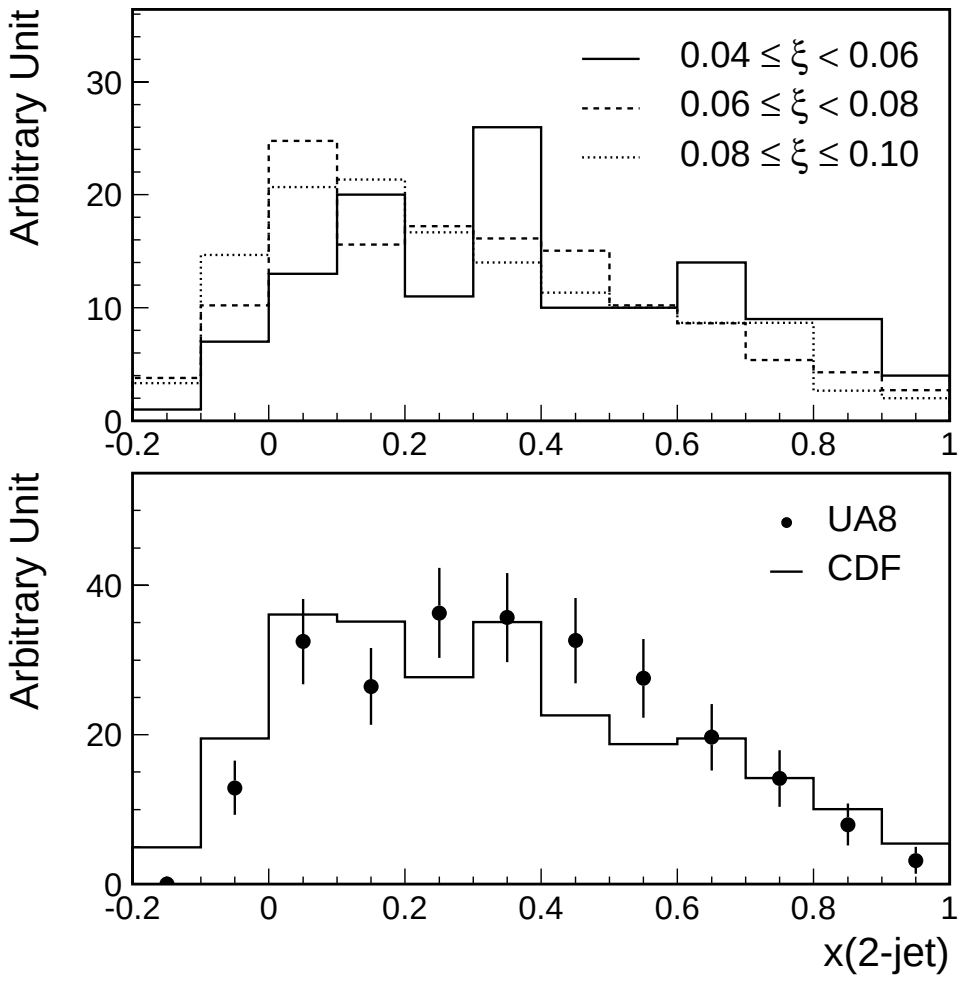

Figure 5.34: (a) Distributions of x(2-jet) for SD dijet events with $0.04 \le \xi < 0.06$ (solid line), $0.06 \le \xi < 0.08$ (dashed line), and $0.08 \le \xi \le 0.10$ (dotted line). (b) Distributions of x(2-jet) for SD dijet events in the UA8 (points) and CDF (histogram) data samples. In the CDF distribution, events are weighted so that the ξ distribution becomes similar to that of the UA8 data.

Although the UA8 and CDF data samples look consistent, the interpretations in terms of the structure function of the pomeron are very different. What is causing the difference? Since the UA2 calorimeter used in the UA8 experiment had a pseudorapidity coverage of $|\eta| < 3$, a cut was imposed on jet η requiring $|\eta^{jet1,2}| \leq 2$ in the UA8 analysis, and the cut was used also for the CDF data in the above comparisons. The CDF calorimeter has a pseudorapidity coverage of $|\eta| < 4.2$, which is much wider than the UA2 calorimeter coverage of $|\eta| < 3$. The x(2-jet) distributions for the CDF data with and without the $|\eta^{jet1,2}| \leq 2$ cut are shown in Figure 5.35. It is found that events removed by the $|\eta^{jet1,2}| \leq 2$ cut have lower x(2-jet) values relative to events with $|\eta^{jet1,2}| \leq 2$, indicating that the CDF data are more sensitive to the low x(2-jet) region and consequently to the low β region of the pomeron structure function. Presumably, the UA8 data were not sensitive to the "low-β peak" of the pomeron structure function found in the CDF data.

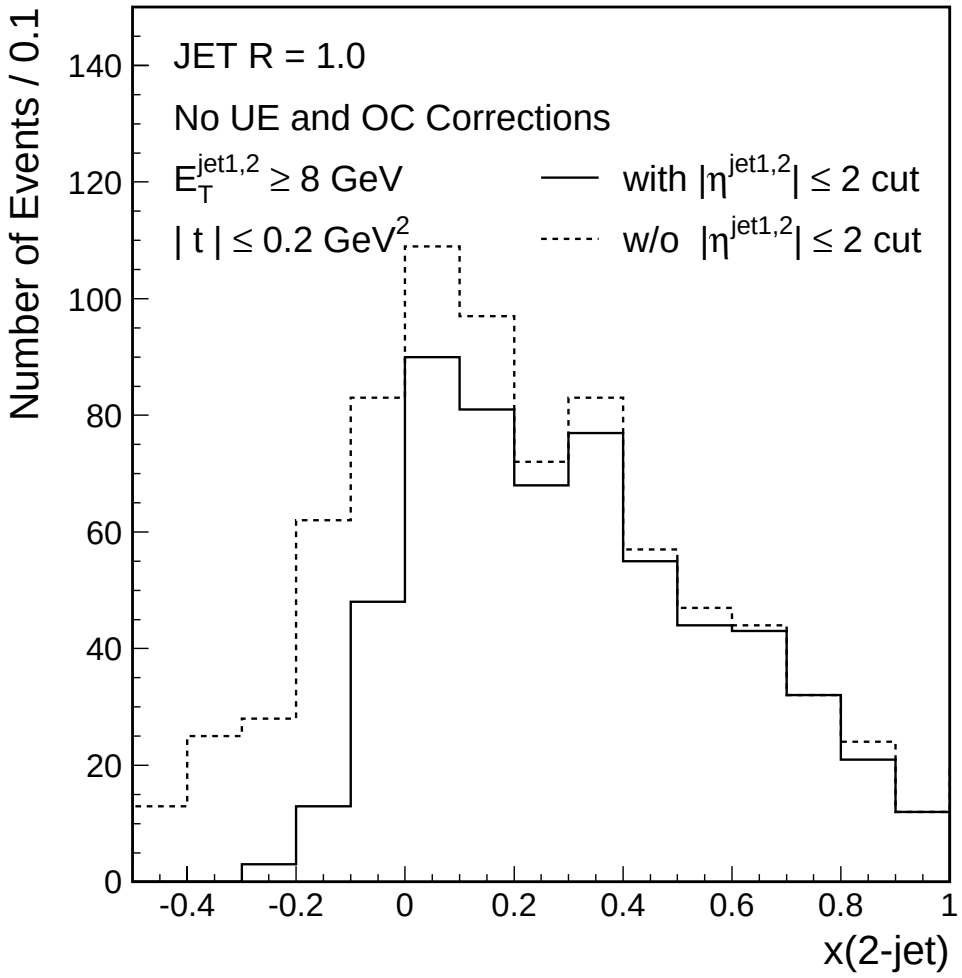

Figure 5.35: Distributions of x(2-jet) for the CDF SD dijet events with (solid line) and without (dashed line) the $|\eta^{jet1,2}| \leq 2$ cut.

Chapter 6

Summary and Conclusions

In this dissertation, a measurement of the effective diffractive structure function F_{jj}^D of the antiproton was presented. The F_{jj}^D was measured using single diffractive dijet events produced in association with a leading antiproton in $p\bar{p}$ collisions at $\sqrt{s}$ = 1800 and 630 GeV at the Fermilab Tevatron. To test QCD factorization in diffraction processes, i.e. universality of the diffractive structure function, the measured F_{jj}^D was compared between $\sqrt{s} = 1800$ and 630 GeV, and with expectations based on results from diffractive deep inelastic scattering studies at HERA [9, 12], as well as with results from a study of dijet production in double pomeron exchange events at the Tevatron [25].

6.1 Measurement of F_{jj}^D

The measurement is based on two inclusive event samples: single diffractive events, $p+\bar{p} \to X+\bar{p}$, collected by triggering on a quasielastically-scattered leading antiproton detected in a Roman Pot spectrometer, and non-diffractive events collected with a minimum bias trigger requiring a coincidence between two forward beam-beam

counter arrays. Using events containing two or more jets in these samples, the ratio $R_{\frac{SD}{ND}}(x_{\bar{p}})$ of single diffractive dijet to non-diffractive dijet event rates was measured as a function of the Bjorken scaling variable of the struck parton in the antiproton $x_{\bar{p}}$. The ratio $R_{\frac{SD}{ND}}(x_{\bar{p}})$ was found to decrease with increasing $x_{\bar{p}}$.

Based on the measured ratio $R_{\frac{SD}{ND}}$, an effective leading order diffractive structure function F_{jj}^{D} of the antiproton was extracted. In the kinematic region of antiproton fractional momentum loss $0.035 \leq \xi \leq 0.095$, four-momentum transfer squared $|t| \leq 1.0$ GeV^2 and $\beta = x_{\bar{p}}/\xi < 0.5$, $F_{jj}^{D}(\beta,\xi)$, measured at $\sqrt{s} = 1800$ GeV using dijet events with $E_T^{jet1,2} \geq 7$ GeV, was found to have the form $F_{jj}^{D}(\beta,\xi) \propto \beta^{-1.0\pm0.1}\xi^{-0.9\pm0.1}$. The observed ξ-dependence of F_{jj}^{D} shows that pomeron-exchange-like behavior of $\lesssim 1/\xi$ extends to relatively high ξ values, where the ξ-dependence of soft single diffraction is rather flat due to a reggeon exchange contribution of $\lesssim \xi$ [71] in addition to the pomeron exchange contribution.

6.2 Comparison with HERA Results

To address the question of QCD factorization in diffraction processes, several comparisons were made on the measured F_{jj}^{D}. Compared to expectations based on results obtained by the H1 collaboration at HERA from studies of diffractive deep inelastic scattering [9, 12], $e + p \rightarrow e + X + p$, F_{jj}^{D} measured in this analysis was found to be smaller than the expectations by approximately an order of magnitude, indicating a breakdown of QCD factorization in diffraction processes. This result is similar to that previously found in the comparison between the single diffractive W, dijet and b-quark production rates measured by the CDF collaboration [18, 19, 21] and expectations based on results obtained by the ZEUS collaboration from diffractive

DIS and dijet photoproduction at HERA [5, 15].

6.3 Comparison between $\sqrt{s} = 630$ and 1800 GeV

Some phenomenological models [31, 43, 44, 48] attribute the breakdown of QCD factorization observed in comparisons between Tevatron and HERA diffraction results to a suppression of the diffractive cross section at the Tevatron resulting from partonic exchanges, in addition to the diffractive exchange, which spoil the diffractive signature of rapidity gaps. These models also predict that the hadron-hadron diffraction cross section is more suppressed at higher collision energies, i.e. the normalization of the diffractive structure function measured at $\sqrt{s} = 630$ GeV is higher than that at $\sqrt{s} = 1800$ GeV. In this dissertation, comparisons were made between results on F_{jj}^D, extracted from dijet events with $E_T^{jet1,2} \geq 7$ GeV and average E_T of the leading two jets $E_T^* = (E_T^{jet1} + E_T^{jet2})/2 \geq 10$ GeV produced in $p\bar{p}$ collisions at $\sqrt{s} = 630$ and 1800 GeV with a leading antiproton in the kinematic region of $0.035 \leq \xi \leq 0.095$ and $|t| \leq 0.2$ GeV^2. The β-dependence of F_{jj}^D measured at $\sqrt{s} = 630$ GeV was found to be in general agreement with that at $\sqrt{s} = 1800$ GeV. The ratio of F_{jj}^D measured at $\sqrt{s} = 630$ GeV to that at $\sqrt{s} = 1800$ GeV in the region $0.1 \leq \beta \lesssim 0.6$ was found to be $R_{\frac{630}{1800}} = 1.3 \pm 0.2(\text{stat})^{+0.4}_{-0.3}(\text{syst})$. While this ratio is compatible with the predictions of 1.55 and 1.8 of the pomeron flux renormalization model [31] and rapidity gap survival probability model [44, 80], it is also compatible within errors with the factorization expectation of unity, so that no firm conclusions about QCD factorization can be drawn from this comparison alone.

6.4 Comparison with Results from Double Pomeron Exchange Dijet Events

Comparisons were also made with results from a study of dijet production in double pomeron exchange events, $p+\bar{p} \rightarrow p+X+\bar{p}$, obtained by the CDF collaboration at $\sqrt{s} = 1800$ GeV [25]. The ratio $R_{\frac{SD}{ND}}(x_{\bar{p}})$ was compared with the ratio $R_{\frac{DPE}{SD}}(x_p)$ of dijet production in double pomeron exchange events to that in single diffractive events associated with a leading antiproton as a function of the x-Bjorken. The ratio of $R_{\frac{SD}{ND}}$ to $R_{\frac{DPE}{SD}}$ was found to be $D = 0.19 \pm 0.07$. The deviation of the ratio D from unity also indicates a breakdown of QCD factorization in diffraction processes. The normalization of the diffractive structure function measured in dijet events by double pomeron exchange is larger than that measured in single diffractive dijet events by approximately a factor of 5. Thus, in double pomeron exchange events, the diffractive structure function is not as suppressed as in single diffractive events. A plausible reason for this is that, when the proton or antiproton scatters quasielastically in $p\bar{p}$ collisions, there is no additional partonic exchange, so that the other incoming particle escapes intact from the collision more easily.

6.5 Comparison with Results from Single Diffractive J/ψ Events

Results on single diffractive dijet production were also compared with results obtained by the CDF collaboration [22] from a study of single diffractive events containing a J/ψ meson, which is dominantly produced by gluon-gluon interactions. By combining these results, the gluon fraction of the diffractive exchange was found to be

$F_g^D = 0.59 \pm 0.26$ [1], which is compatible with (a) $F_g^D = 0.54^{+0.16}_{-0.14}$ obtained by the CDF collaboration by combining results on single diffractive W, dijet and b-quark production [18, 19, 21], (b) $F_g^D = 0.3-0.8$ obtained by the ZEUS collaboration by combining results on diffractive deep inelastic scattering and dijet photoproduction [5, 15], and (c) $F_g^D = 0.75 \pm 0.15$ at $Q^2 = 10$ GeV^2 obtained by the H1 collaboration from scaling violations observed in diffractive deep inelastic scattering [12]. This agreement indicates that, although the diffractive structure function measured at the Tevatron is different from that measured at HERA in normalization, the gluon fraction of the diffractive exchange at the Tevatron is approximately the same as that at HERA.

6.6 Comparison with UA8 Results

Comparisons with results on single diffractive dijet events obtained by the UA8 collaboration in $p\bar{p}$ collisions at $\sqrt{s} = 630$ GeV [4] were also presented. Using the same selection cuts for the CDF 630 GeV data as those used in the UA8 analysis, the distribution of x(2-jet) $(= \beta - x_p)$ for the CDF data becomes compatible with the x(2-jet) distribution obtained in the UA8 analysis. The CDF data are more sensitive to low β and low x(2-jet) values because of the wider acceptance of the CDF calorimeters than the calorimeters used by the UA8 collaboration.

6.7 Suggestions for the Future

The CDF collaboration is presently collecting data from $p\bar{p}$ collisions at $\sqrt{s} = 1960$ GeV using the upgraded CDF II detector [82] at the Tevatron. The upgraded detector

[1] The systematic uncertainties in the ratio of single diffractive dijet to non-diffractive dijet event rates yield an additional uncertainty of $^{+0.34}_{-0.31}$.

contains, in addition to the Roman Pot spectrometer used during the 1995−1996 run, two very forward MiniPlug calorimeters [83] and two beam shower counter (BSC) arrays, covering the pseudorapidity regions of $5.5 < |\eta| < 7.5$ and $3.6 < |\eta| < 5.1$, respectively. These new detectors are crucial for extending diffraction studies into the areas discussed below.

6.7.1 Q^2-Dependence of F_{jj}^D

In some analyses of diffractive deep inelastic scattering at HERA [9, 12], the diffractive parton distribution functions of the proton were extracted based on the Q^2-dependence of the diffractive F_2 structure function using the DGLAP equations [37]. The validity of the DGLAP evolution in diffraction processes is a subject of great interest, so that checking it at the Tevatron would provide valuable information. In the analysis described in this dissertation, dijet events with $E_T^{jet1,2} \geq 7$ GeV were mainly used to extract F_{jj}^D. Due to the limited statistics of diffractive dijet events at high E_T values in the data used, the dependence of F_{jj}^D on jet E_T, which is related to the Q^2-dependence of F_{jj}^D, could not be studied in detail. Such a study would be feasible using the higher statistics Run 2 data.

6.7.2 F_{jj}^D at Low ξ

In this analysis, F_{jj}^D was measured in the ξ region of $0.035 \leq \xi \leq 0.095$, where in soft single diffraction there are contributions from reggeon exchange in addition to pomeron exchange according to Regge theory. It would be interesting to measure F_{jj}^D over a wider ξ range, especially in the region of $\xi \lesssim 0.035$ not accessible in the present measurement, where pomeron exchange is expected to become more dominant. Single

diffractive events with low ξ ($\xi \lesssim 0.035$) can be collected by triggering on events which have no hit in the BSC arrays on the proton or antiproton outgoing side. In such events, the value of ξ could be evaluated in a similar manner to that used in the analyses of dijet production by double pomeron exchange [25] and single diffractive J/ψ production [22] by using information from calorimetry including the MiniPlug calorimeters.

6.7.3 Dijet Production by Double Pomeron Exchange

The results from a study of dijet production by double pomeron exchange [25], which were compared with results on single diffractive dijet production in Section 5.5, were based on about 100 double pomeron exchange dijet events and thus had sizable statistical uncertainties in the ratio $R_{\frac{DPE}{SD}}$ of double pomeron exchange dijet to single diffractive dijet event rates. It would be interesting to study double pomeron exchange dijet events using the higher statistics Run 2 data, which will allow us to better understand the mechanism of production of events with multiple rapidity gaps.

The CDF Collaboration

D. Acosta,[14] T. Affolder,[25] H. Akimoto,[51] M. G. Albrow,[13] D. Ambrose,[37] D. Amidei,[28] K. Anikeev,[27] J. Antos,[1] G. Apollinari,[13] T. Arisawa,[51] A. Artikov,[11] T. Asakawa,[49] W. Ashmanskas,[10] F. Azfar,[35] P. Azzi-Bacchetta,[36] N. Bacchetta,[36] H. Bachacou,[25] W. Badgett,[13] S. Bailey,[18] P. de Barbaro,[41] A. Barbaro-Galtieri,[25] V. E. Barnes,[40] B. A. Barnett,[21] S. Baroiant,[5] M. Barone,[15] G. Bauer,[27] F. Bedeschi,[38] S. Behari,[21] S. Belforte,[48] W. H. Bell,[17] G. Bellettini,[38] J. Bellinger,[52] D. Benjamin,[12] J. Bensinger,[4] A. Beretvas,[13] J. Berryhill,[10] A. Bhatti,[42] M. Binkley,[13] D. Bisello,[36] M. Bishai,[13] R. E. Blair,[2] C. Blocker,[4] K. Bloom,[28] B. Blumenfeld,[21] S. R. Blusk,[41] A. Bocci,[42] A. Bodek,[41] G. Bolla,[40] A. Bolshov,[27] Y. Bonushkin,[6] D. Bortoletto,[40] J. Boudreau,[39] A. Brandl,[31] C. Bromberg,[29] M. Brozovic,[12] E. Brubaker,[25] N. Bruner,[31] J. Budagov,[11] H. S. Budd,[41] K. Burkett,[18] G. Busetto,[36] K. L. Byrum,[2] S. Cabrera,[12] P. Calafiura,[25] M. Campbell,[28] W. Carithers,[25] J. Carlson,[28] D. Carlsmith,[52] W. Caskey,[5] A. Castro,[3] D. Cauz,[48] A. Cerri,[38] L. Cerrito,[20] A. W. Chan,[1] P. S. Chang,[1] P. T. Chang,[1] J. Chapman,[28] C. Chen,[37] Y. C. Chen,[1] M.-T. Cheng,[1] M. Chertok,[5] G. Chiarelli,[38] I. Chirikov-Zorin,[11] G. Chlachidze,[11] F. Chlebana,[13] L. Christofek,[20] M. L. Chu,[1] J. Y. Chung,[33] W.-H. Chung,[52] Y. S. Chung,[41] C. I. Ciobanu,[33] A. G. Clark,[16] M. Coca,[41] A. P. Colijn,[13] A. Connolly,[25]

M. Convery,[42] J. Conway,[44] M. Cordelli,[15] J. Cranshaw,[46] R. Culbertson,[13] D. Dagenhart,[4] S. D'Auria,[17] S. De Cecco,[43] F. DeJongh,[13] S. Dell'Agnello,[15] M. Dell'Orso,[38] S. Demers,[41] L. Demortier,[42] M. Deninno,[3] D. De Pedis,[43] P. F. Derwent,[13] T. Devlin,[44] C. Dionisi,[43] J. R. Dittmann,[13] A. Dominguez,[25] S. Donati,[38] M. D'Onofrio,[38] T. Dorigo,[36] N. Eddy,[20] K. Einsweiler,[25] E. Engels, Jr.,[39] R. Erbacher,[13] D. Errede,[20] S. Errede,[20] R. Eusebi,[41] Q. Fan,[41] H.-C. Fang,[25] S. Farrington,[17] R. G. Feild,[53] J. P. Fernandez,[40] C. Ferretti,[28] R. D. Field,[14] I. Fiori,[3] B. Flaugher,[13] L. R. Flores-Castillo,[39] G. W. Foster,[13] M. Franklin,[18] J. Freeman,[13] J. Friedman,[27] Y. Fukui,[23] I. Furic,[27] S. Galeotti,[38] A. Gallas,[32] M. Gallinaro,[42] T. Gao,[37] M. Garcia-Sciveres,[25] A. F. Garfinkel,[40] P. Gatti,[36] C. Gay,[53] D. W. Gerdes,[28] E. Gerstein,[9] S. Giagu,[43] P. Giannetti,[38] K. Giolo,[40] M. Giordani,[5] P. Giromini,[15] V. Glagolev,[11] D. Glenzinski,[13] M. Gold,[31] N. Goldschmidt,[28] J. Goldstein,[13] G. Gomez,[8] M. Goncharov,[45] I. Gorelov,[31] A. T. Goshaw,[12] Y. Gotra,[39] K. Goulianos,[42] C. Green,[40] A. Gresele,[36] G. Grim,[5] C. Grosso-Pilcher,[10] M. Guenther,[40] G. Guillian,[28] J. Guimaraes da Costa,[18] R. M. Haas,[14] C. Haber,[25] S. R. Hahn,[13] E. Halkiadakis,[41] C. Hall,[18] T. Handa,[19] R. Handler,[52] F. Happacher,[15] K. Hara,[49] A. D. Hardman,[40] R. M. Harris,[13] F. Hartmann,[22] K. Hatakeyama,[42] J. Hauser,[6] J. Heinrich,[37] A. Heiss,[22] M. Hennecke,[22] M. Herndon,[21] C. Hill,[7] A. Hocker,[41] K. D. Hoffman,[10] R. Hollebeek,[37] L. Holloway,[20] S. Hou,[1] B. T. Huffman,[35] R. Hughes,[33] J. Huston,[29] J. Huth,[18] H. Ikeda,[49] C. Issever,[7] J. Incandela,[7] G. Introzzi,[38] M. Iori,[43] A. Ivanov,[41] J. Iwai,[51] Y. Iwata,[19] B. Iyutin,[27] E. James,[28] M. Jones,[37] U. Joshi,[13] H. Kambara,[16] T. Kamon,[45] T. Kaneko,[49] J. Kang,[28] M. Karagoz Unel,[32] K. Karr,[50] S. Kartal,[13] H. Kasha,[53] Y. Kato,[34] T. A. Keaffaber,[40] K. Kelley,[27] M. Kelly,[28] R. D. Kennedy,[13] R. Kephart,[13] D. Khazins,[12] T. Kikuchi,[49] B. Kilminster,[41] B. J. Kim,[24] D. H. Kim,[24] H. S. Kim,[20]

M. J. Kim,[9] S. B. Kim,[24] S. H. Kim,[49] T. H. Kim,[27] Y. K. Kim,[25] M. Kirby,[12] M. Kirk,[4] L. Kirsch,[4] S. Klimenko,[14] P. Koehn,[33] K. Kondo,[51] J. Konigsberg,[14] A. Korn,[27] A. Korytov,[14] K. Kotelnikov,[30] E. Kovacs,[2] J. Kroll,[37] M. Kruse,[12] V. Krutelyov,[45] S. E. Kuhlmann,[2] K. Kurino,[19] T. Kuwabara,[49] N. Kuznetsova,[13] A. T. Laasanen,[40] N. Lai,[10] S. Lami,[42] S. Lammel,[13] J. Lancaster,[12] K. Lannon,[20] M. Lancaster,[26] R. Lander,[5] A. Lath,[44] G. Latino,[31] T. LeCompte,[2] Y. Le,[21] J. Lee,[41] S. W. Lee,[45] N. Leonardo,[27] S. Leone,[38] J. D. Lewis,[13] K. Li,[53] C. S. Lin,[13] M. Lindgren,[6] T. M. Liss,[20] J. B. Liu,[41] T. Liu,[13] Y. C. Liu,[1] D. O. Litvintsev,[13] O. Lobban,[46] N. S. Lockyer,[37] A. Loginov,[30] J. Loken,[35] M. Loreti,[36] D. Lucchesi,[36] P. Lukens,[13] S. Lusin,[52] L. Lyons,[35] J. Lys,[25] R. Madrak,[18] K. Maeshima,[13] P. Maksimovic,[21] L. Malferrari,[3] M. Mangano,[38] G. Manca,[35] M. Mariotti,[36] G. Martignon,[36] M. Martin,[21] A. Martin,[53] V. Martin,[32] J. A. J. Matthews,[31] P. Mazzanti,[3] K. S. McFarland,[41] P. McIntyre,[45] M. Menguzzato,[36] A. Menzione,[38] P. Merkel,[13] C. Mesropian,[42] A. Meyer,[13] T. Miao,[13] R. Miller,[29] J. S. Miller,[28] H. Minato,[49] S. Miscetti,[15] M. Mishina,[23] G. Mitselmakher,[14] Y. Miyazaki,[34] N. Moggi,[3] E. Moore,[31] R. Moore,[28] Y. Morita,[23] T. Moulik,[40] M. Mulhearn,[27] A. Mukherjee,[13] T. Muller,[22] A. Munar,[38] P. Murat,[13] S. Murgia,[29] J. Nachtman,[6] V. Nagaslaev,[46] S. Nahn,[53] H. Nakada,[49] I. Nakano,[19] R. Napora,[21] F. Niell,[28] C. Nelson,[13] T. Nelson,[13] C. Neu,[33] M. S. Neubauer,[27] D. Neuberger,[22] C. Newman-Holmes,[13] C.-Y. P. Ngan,[27] T. Nigmanov,[39] H. Niu,[4] L. Nodulman,[2] A. Nomerotski,[14] S. H. Oh,[12] Y. D. Oh,[24] T. Ohmoto,[19] T. Ohsugi,[19] R. Oishi,[49] T. Okusawa,[34] J. Olsen,[52] W. Orejudos,[25] C. Pagliarone,[38] F. Palmonari,[38] R. Paoletti,[38] V. Papadimitriou,[46] D. Partos,[4] J. Patrick,[13] G. Pauletta,[48] M. Paulini,[9] T. Pauly,[35] C. Paus,[27] D. Pellett,[5] A. Penzo,[48] L. Pescara,[36] T. J. Phillips,[12] G. Piacentino,[38] J. Piedra,[8] K. T. Pitts,[20] A. Pompoš,[40] L. Pondrom,[52] G. Pope,[39] T. Pratt,[35] F. Prokoshin,[11] J. Proudfoot,[2]

F. Ptohos,[15] O. Pukhov,[11] G. Punzi,[38] J. Rademacker,[35] A. Rakitine,[27] F. Ratnikov,[44] H. Ray,[28] D. Reher,[25] A. Reichold,[35] P. Renton,[35] M. Rescigno,[43] A. Ribon,[36] W. Riegler,[18] F. Rimondi,[3] L. Ristori,[38] M. Riveline,[47] W. J. Robertson,[12] T. Rodrigo,[8] S. Rolli,[50] L. Rosenson,[27] R. Roser,[13] R. Rossin,[36] C. Rott,[40] A. Roy,[40] A. Ruiz,[8] D. Ryan,[50] A. Safonov,[5] R. St. Denis,[17] W. K. Sakumoto,[41] D. Saltzberg,[6] C. Sanchez,[33] A. Sansoni,[15] L. Santi,[48] S. Sarkar,[43] H. Sato,[49] P. Savard,[47] A. Savoy-Navarro,[13] P. Schlabach,[13] E. E. Schmidt,[13] M. P. Schmidt,[53] M. Schmitt,[32] L. Scodellaro,[36] A. Scott,[6] A. Scribano,[38] A. Sedov,[40] S. Seidel,[31] Y. Seiya,[49] A. Semenov,[11] F. Semeria,[3] T. Shah,[27] M. D. Shapiro,[25] P. F. Shepard,[39] T. Shibayama,[49] M. Shimojima,[49] M. Shochet,[10] A. Sidoti,[36] J. Siegrist,[25] A. Sill,[46] P. Sinervo,[47] P. Singh,[20] A. J. Slaughter,[53] K. Sliwa,[50] F. D. Snider,[13] R. Snihur,[26] A. Solodsky,[42] J. Spalding,[13] T. Speer,[16] M. Spezziga,[46] P. Sphicas,[27] F. Spinella,[38] M. Spiropulu,[10] L. Spiegel,[13] J. Steele,[52] A. Stefanini,[38] J. Strologas,[20] F. Strumia, [16] D. Stuart,[7] A. Sukhanov,[14] K. Sumorok,[27] T. Suzuki,[49] T. Takano,[34] R. Takashima,[19] K. Takikawa,[49] P. Tamburello,[12] M. Tanaka,[49] B. Tannenbaum,[6] M. Tecchio,[28] R. J. Tesarek,[13] P. K. Teng,[1] K. Terashi,[42] S. Tether,[27] A. S. Thompson,[17] E. Thomson,[33] R. Thurman-Keup,[2] P. Tipton,[41] S. Tkaczyk,[13] D. Toback,[45] K. Tollefson,[29] D. Tonelli,[38] M. Tonnesmann,[29] H. Toyoda,[34] W. Trischuk,[47] J. F. de Troconiz,[18] J. Tseng,[27] D. Tsybychev,[14] N. Turini,[38] F. Ukegawa,[49] T. Unverhau,[17] T. Vaiciulis,[41] J. Valls,[44] A. Varganov,[28] E. Vataga,[38] S. Vejcik III,[13] G. Velev,[13] G. Veramendi,[25] R. Vidal,[13] I. Vila,[8] R. Vilar,[8] I. Volobouev,[25] M. von der Mey,[6] D. Vucinic,[27] R. G. Wagner,[2] R. L. Wagner,[13] W. Wagner,[22] N. B. Wallace,[44] Z. Wan,[44] C. Wang,[12] M. J. Wang,[1] S. M. Wang,[14] B. Ward,[17] S. Waschke,[17] T. Watanabe,[49] D. Waters,[26] T. Watts,[44] M. Weber,[25] H. Wenzel,[22] W. C. Wester III,[13] B. Whitehouse,[50] A. B. Wicklund,[2] E. Wicklund,[13] T. Wilkes,[5]

H. H. Williams,[37] P. Wilson,[13] B. L. Winer,[33] D. Winn,[28] S. Wolbers,[13] D. Wolinski,[28] J. Wolinski,[29] S. Wolinski,[28] M. Wolter,[50] S. Worm,[44] X. Wu,[16] F. Würthwein,[27] J. Wyss,[38] U. K. Yang,[10] W. Yao,[25] G. P. Yeh,[13] P. Yeh,[1] K. Yi,[21] J. Yoh,[13] C. Yosef,[29] T. Yoshida,[34] I. Yu,[24] S. Yu,[37] Z. Yu,[53] J. C. Yun,[13] L. Zanello,[43] A. Zanetti,[48] F. Zetti,[25] and S. Zucchelli[3]

[1] *Institute of Physics, Academia Sinica, Taipei, Taiwan 11529, Republic of China*

[2] *Argonne National Laboratory, Argonne, Illinois 60439*

[3] *Istituto Nazionale di Fisica Nucleare, University of Bologna, I-40127 Bologna, Italy*

[4] *Brandeis University, Waltham, Massachusetts 02254*

[5] *University of California at Davis, Davis, California 95616*

[6] *University of California at Los Angeles, Los Angeles, California 90024*

[7] *University of California at Santa Barbara, Santa Barbara, California 93106*

[8] *Instituto de Fisica de Cantabria, CSIC-University of Cantabria, 39005 Santander, Spain*

[9] *Carnegie Mellon University, Pittsburgh, PA 15218*

[10] *Enrico Fermi Institute, University of Chicago, Chicago, Illinois 60637*

[11] *Joint Institute for Nuclear Research, RU-141980 Dubna, Russia*

[12] *Duke University, Durham, North Carolina 27708*

[13] *Fermi National Accelerator Laboratory, Batavia, Illinois 60510*

[14] *University of Florida, Gainesville, Florida 32611*

[15] *Laboratori Nazionali di Frascati, Istituto Nazionale di Fisica Nucleare, I-00044 Frascati, Italy*

[16] *University of Geneva, CH-1211 Geneva 4, Switzerland*

[17] *Glasgow University, Glasgow G12 8QQ, United Kingdom*

[18] *Harvard University, Cambridge, Massachusetts 02138*

[19] *Hiroshima University, Higashi-Hiroshima 724, Japan*

[20] *University of Illinois, Urbana, Illinois 61801*

[21] *The Johns Hopkins University, Baltimore, Maryland 21218*

[22] *Institut für Experimentelle Kernphysik, Universität Karlsruhe, 76128 Karlsruhe, Germany*

[23] *High Energy Accelerator Research Organization (KEK), Tsukuba, Ibaraki 305, Japan*

[24] *Center for High Energy Physics: Kyungpook National University, Taegu 702-701; Seoul National University, Seoul 151-742; and SungKyunKwan University, Suwon 440-746; Korea*

[25] *Ernest Orlando Lawrence Berkeley National Laboratory, Berkeley, California 94720*

[26] *University College London, London WC1E 6BT, United Kingdom*

[27] *Massachusetts Institute of Technology, Cambridge, Massachusetts 02139*

[28] *University of Michigan, Ann Arbor, Michigan 48109*

[29] *Michigan State University, East Lansing, Michigan 48824*

[30] *Institution for Theoretical and Experimental Physics, ITEP, Moscow 117259, Russia*

[31] *University of New Mexico, Albuquerque, New Mexico 87131*

[32] *Northwestern University, Evanston, Illinois 60208*

[33] *The Ohio State University, Columbus, Ohio 43210*

[34] *Osaka City University, Osaka 588, Japan*

[35] *University of Oxford, Oxford OX1 3RH, United Kingdom*

[36] *Universita di Padova, Istituto Nazionale di Fisica Nucleare, Sezione di Padova, I-35131 Padova, Italy*

[37] *University of Pennsylvania, Philadelphia, Pennsylvania 19104*

[38] *Istituto Nazionale di Fisica Nucleare, University and Scuola Normale Superiore of Pisa, I-56100 Pisa, Italy*

[39] *University of Pittsburgh, Pittsburgh, Pennsylvania 15260*

[40] *Purdue University, West Lafayette, Indiana 47907*

[41] *University of Rochester, Rochester, New York 14627*

[42] *Rockefeller University, New York, New York 10021*

[43] *Instituto Nazionale de Fisica Nucleare, Sezione di Roma, University di Roma I, "La Sapienza," I-00185 Roma, Italy*

[44] *Rutgers University, Piscataway, New Jersey 08855*

[45] *Texas A&M University, College Station, Texas 77843*

[46] *Texas Tech University, Lubbock, Texas 79409*

[47] *Institute of Particle Physics, University of Toronto, Toronto M5S 1A7, Canada*

[48] *Istituto Nazionale di Fisica Nucleare, University of Trieste/ Udine, Italy*

[49] *University of Tsukuba, Tsukuba, Ibaraki 305, Japan*

[50] *Tufts University, Medford, Massachusetts 02155*

[51] *Waseda University, Tokyo 169, Japan*

[52] *University of Wisconsin, Madison, Wisconsin 53706*

[53] *Yale University, New Haven, Connecticut 06520*

Appendix A

Reconstruction of ξ and t from a Roman Pot Track

For single diffractive events containing a quasielastically-scattered leading antiproton detected in the Roman Pot (RP) spectrometer, the antiproton fractional momentum loss ξ and four-momentum transfer squared t can be determined from (a) the position and angle of the leading antiproton detected in the Roman Pot spectrometer relative to the beam line, (b) the position of the $p\bar{p}$ interaction point, and (c) the beam transport matrix between the interaction point and the Roman Pot spectrometer.

The position of a $p\bar{p}$ interaction in the Z direction is evaluated based on the Z-position of a vertex reconstructed using primarily the information provided by the Vertex detector (VTX). The beam transport matrix is obtained from information on accelerator elements. The accelerator elements between the CDF nominal collision point and the Roman Pot detector stations are shown in Table A.1. In this analysis, the beam transport matrix was calculated up to next-to-leading order using the TRANSPORT program [84]. An arbitrary charged particle can be represented by a

five-dimensional vector $\boldsymbol{X}$,

$$\boldsymbol{X} = (X, dX, Y, dY, -\xi),$$

where X (Y) is the position and dX (dY) are the angle of the particle relative to the beam line in the X (Y) direction. The variable ξ is the fractional difference of the momentum of the particle to that of the beam, i.e. $\xi = (p_{beam} - p_{particle})/p_{beam}$. The five-dimensional vector $\boldsymbol{X}$ of a leading recoil antiproton at the Roman Pot position is related to that of the leading recoil antiproton at the interaction point by the beam transport matrix,

$$\boldsymbol{X}_{CDF}^{recoil\,\bar{p}} = \mathcal{M}_{RP\to CDF}\boldsymbol{X}_{RP}^{recoil\,\bar{p}}, \tag{A.1}$$

where $\boldsymbol{X}_{CDF}^{recoil\,\bar{p}}$ ($\boldsymbol{X}_{RP}^{recoil\,\bar{p}}$) is the five-dimensional vector $\boldsymbol{X}$ for the quasielastically-scattered recoil antiproton at the interaction point (Roman Pot position), and $\mathcal{M}_{RP\to CDF}$ is the transport matrix from the Roman Pot position to the interaction point at CDF. Four elements of Eq. (A.1) can be expressed as

$$X_{CDF}^{recoil\,\bar{p}} = F_1(X_{RP}^{recoil\,\bar{p}}, dX_{RP}^{recoil\,\bar{p}}, Y_{RP}^{recoil\,\bar{p}}, dY_{RP}^{recoil\,\bar{p}}, \xi), \tag{A.2a}$$

$$dX_{CDF}^{recoil\,\bar{p}} = F_2(X_{RP}^{recoil\,\bar{p}}, dX_{RP}^{recoil\,\bar{p}}, Y_{RP}^{recoil\,\bar{p}}, dY_{RP}^{recoil\,\bar{p}}, \xi), \tag{A.2b}$$

$$Y_{CDF}^{recoil\,\bar{p}} = F_3(X_{RP}^{recoil\,\bar{p}}, dX_{RP}^{recoil\,\bar{p}}, Y_{RP}^{recoil\,\bar{p}}, dY_{RP}^{recoil\,\bar{p}}, \xi), \tag{A.2c}$$

$$dY_{CDF}^{recoil\,\bar{p}} = F_4(X_{RP}^{recoil\,\bar{p}}, dX_{RP}^{recoil\,\bar{p}}, Y_{RP}^{recoil\,\bar{p}}, dY_{RP}^{recoil\,\bar{p}}, \xi). \tag{A.2d}$$

The functions F_1, F_2, F_3 and F_4 can be determined from the transport matrix $\mathcal{M}_{RP\to CDF}$. The variables $X_{RP}^{recoil\,\bar{p}}$, $dX_{RP}^{recoil\,\bar{p}}$, $Y_{RP}^{recoil\,\bar{p}}$ and $dY_{RP}^{recoil\,\bar{p}}$ are measured by the Roman Pot spectrometer. The variable $X_{CDF}^{recoil\,\bar{p}}$ ($Y_{CDF}^{recoil\,\bar{p}}$) is the same as X_{CDF}^{beam} (Y_{CDF}^{beam}), which is the position of the antiproton beam at the interaction point in the X (Y) direction. The average position and angle of the beam in the X and Y directions are measured by the Silicon Vertex detector (SVX). Given the values of

$X_{CDF}^{recoil\,\bar{p}}$, $X_{RP}^{recoil\,\bar{p}}$, $dX_{RP}^{recoil\,\bar{p}}$, $Y_{RP}^{recoil\,\bar{p}}$ and $dY_{RP}^{recoil\,\bar{p}}$, Eq. (A.2a) is an equation of the variable ξ. The value of ξ is obtained by solving this equation, which is generally a quartic equation of ξ.

The value of the four-momentum transfer squared t can be reconstructed using the formula:

$$t = 2m_p^2 - 2E_{beam}E_{recoil\,\bar{p}} + 2p_{beam}p_{recoil\,\bar{p}}\cos\theta, \tag{A.3}$$

$$\cos\theta = \frac{1}{\sqrt{1 + (dX_{CDF}^{recoil\,\bar{p}} - dX_{CDF}^{beam})^2 + (dY_{CDF}^{recoil\,\bar{p}} - dY_{CDF}^{beam})^2}},$$

where θ is the angle between the initial beam antiproton and quasielastically-scattered recoil antiproton, $m_{\bar{p}}$ is the antiproton mass, and E_{beam} ($E_{recoil\,\bar{p}}$) and p_{beam} ($p_{recoil\,\bar{p}}$) are the energy and momentum of the initial beam antiproton (recoil antiproton), respectively. The values of $dX_{CDF}^{recoil\,\bar{p}}$ and $dY_{CDF}^{recoil\,\bar{p}}$ are determined using Eqs. (A.2b), (A.2c) and (A.2d). The values of dX_{CDF}^{beam} and dY_{CDF}^{beam} were measured by the SVX detector on a run-by-run basis, and can be extracted from the SVXBPO database. The value of t is determined by inserting these values into Eq. (A.3).

Table A.1: Tevatron configuration from the CDF nominal collision point (BØ) to the position of the Roman Pot detector stations. "Drift" is a free space, "Quad" is a quadrupole magnet, "Dipole" is a dipole magnet which bends beam particles toward the inside of the Tevatron ring, and "Vsep" and "Hsep" are vertical and horizontal beam separators, respectively. In the "Parameters" column, "Grad" means the gradient of the quadrupole magnet, "Volt" and "Dist" are the voltage and distance between the electrode plates of the beam separator, respectively, and "Angle" means the angle at which the beam line is bent by the dipole magnet. The quadrupole magnets with positive (negative) gradient focus antiprotons in the horizontal (vertical) direction. The vertical beam separators bend antiprotons upward, and the horizontal beam separator bends antiprotons toward the outside of the Tevatron ring.

Elements	Effective length (m) (Distance from BØ)	Parameters 630 GeV run	Parameters 1800 GeV run
Drift	7.633 (0.)		
Quad (Q1)	3.353 (7.633)	Grad = 437.5224 (kGauss/m)	Grad = 1255.1807
Drift	0.876 (10.986)		
Quad (Q2)	5.893 (11.863)	Grad = −433.2981	Grad = −1241.3511
Drift	0.876 (17.755)		
Quad (Q3)	3.353 (18.632)	Grad = 437.5224	Grad = 1255.1807
Drift	1.413 (21.984)		
Vsep (VS1)	2.572 (23.397)	Volt = 107.216 (kV) Dist = 0.05 (m)	Volt = 129.834
Drift	0.187 (25.969)		
Vsep (VS2)	2.572 (26.156)	Volt = 107.216	Volt = 129.834
Drift	0.187 (28.728)		
Hsep (HS)	2.572 (28.915)	Volt = 117.726	Volt = 140.27
Drift	0.847 (31.487)		
Dipole (CD)	0.762 (32.334)	X: 5.761×10^{-5} (rad) Y: 1.1522×10^{-5} (rad)	3.3408×10^{-5} (rad) 2.88×10^{-5} (rad)
Drift	0.847 (33.096)		
Quad (Q4)	1.402 (33.943)	Grad = −8.1884	Grad = −24.9062
Drift	0.307 (35.345)		
Dipole (D1)	6.121 (35.652)	Angle = 0.00811781 (rad)	
Drift	0.279 (41.773)		
Dipole (D2)	6.121 (42.052)	Angle = 0.00811781	
Drift	0.279 (48.174)		
Dipole (D3)	6.121 (48.453)	Angle = 0.00811781	
Drift	2.186 (54.575)		
RP1	0. (56.761)		

Appendix B

Roman Pot Acceptance

To evaluate the acceptance of the Roman Pot spectrometer, a Monte Carlo simulation was used which generates single diffractive events according to the previously-measured ξ and t distributions and projects quasielastically-scattered recoil antiprotons from the interaction point at CDF to the position of the Roman Pot detector stations. The Monte Carlo simulation program was originally written by H. Nakada for the study of the Roman Pot triggered data collected at $\sqrt{s} = 1800$ GeV [75], and was subsequently modified to generate single diffractive events also at $\sqrt{s} = 630$ GeV. The Roman Pot acceptance is evaluated from the fraction of single diffractive events with a recoil antiproton which does not collide with the beam pipe and electrostatic beam separators and passes through the Roman Pot fiducial region. The Roman Pot acceptance study for the 1800 GeV data is described in detail elsewhere [75]. This appendix describes the acceptance evaluation only for the 630 GeV data.

Before evaluating the Roman Pot acceptance, distributions of the position and angle of Roman Pot tracks, reconstructed ξ, t and the azimuthal angle $\phi_{\bar{p}}$ of recoil antiprotons are compared between data and Monte Carlo simulation to ensure that

the Monte Carlo simulation is reliable.

B.1 Antiproton Beam Characteristics

In this section, the spatial spread and angular spread of the antiproton beam are studied. This information is used as input to the Monte Carlo simulation. First, distributions of reconstructed primary vertices with respect to the average beam position are measured using tracks in the Silicon Vertex detector (SVX), and the transverse profile of the antiproton beam is estimated.

The following selection cuts are used for vertex reconstruction:

- Number of three-dimensional tracks for vertex reconstruction ≥ 3.
- χ^2 of vertex fit < 20.
- p_T of each SVX track > 0.6 GeV.
- Number of hits in the SVX for each SVX track ≥ 4.

Figure B.1 shows distributions of reconstructed vertices on the X-Y plane with respect to the average beam position for diffractive events in run 75020. The measured position variation of reconstructed vertices is gaussian and circular, indicating that the profile of the proton and antiproton beams is also gaussian and circular. Figure B.2 shows the standard deviation σ of the vertex distribution as a function of run number for the diffractive and non-diffractive data. The spread of vertices is very stable during the runs used in this analysis. The diffractive and non-diffractive data show consistent results.

When a proton beam with spatial spread of $\sigma_{p\text{-}beam}$ collides with an antiproton beam with spatial spread of $\sigma_{\bar{p}\text{-}beam}$, the spread of interaction points, which is pre-

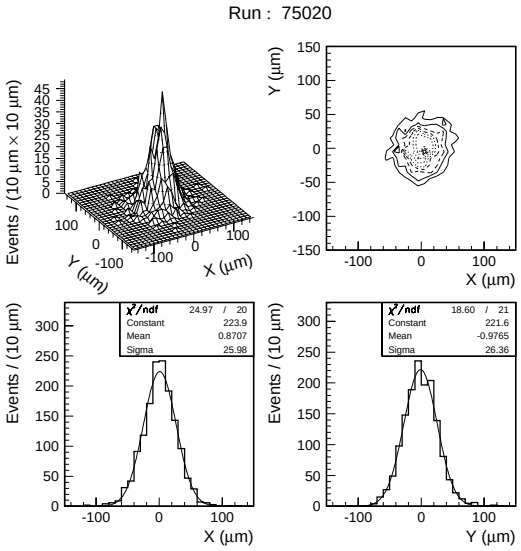

Figure B.1: The upper two plots show two-dimensional distributions of reconstructed vertices on the X-Y plane for run 75020. The lower two plots show the projection in the X and Y directions, respectively. A fit to a gaussian distribution is superimposed.

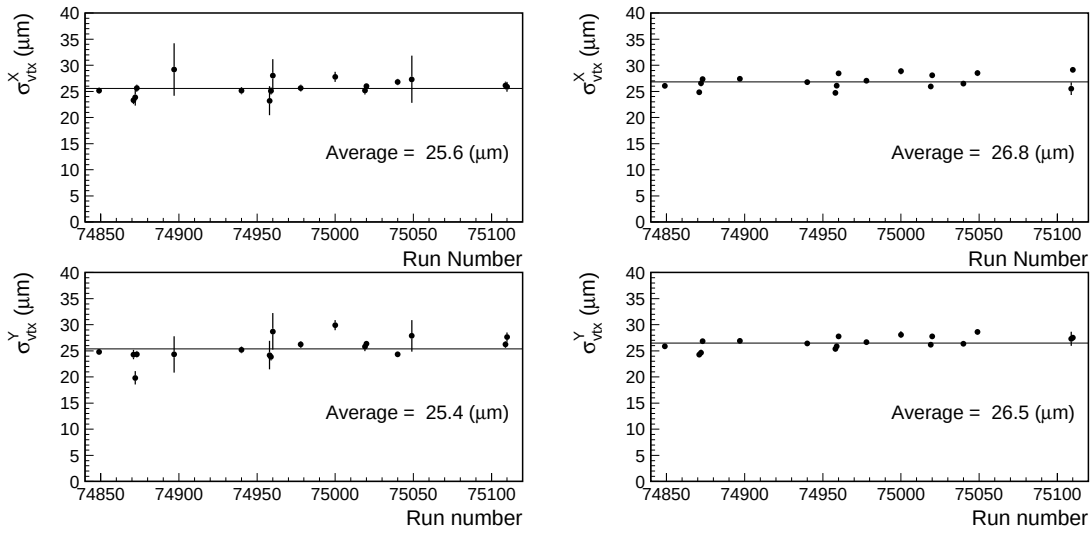

(a) Diffractive data (b) Non-diffractive data

Figure B.2: The standard deviation σ of the vertex distribution as a function of run number in X (top) and Y (bottom) directions for the (a) diffractive and (b) non-diffractive data samples.

sumably similar to the spread of reconstructed vertices σ_{vtx}, is related to $\sigma_{\bar{p}\text{-}beam}$ and $\sigma_{\bar{p}\text{-}beam}$ by $\left(\frac{1}{\sigma_{vtx}}\right)^2 = \left(\frac{1}{\sigma_{p\text{-}beam}}\right)^2 + \left(\frac{1}{\sigma_{\bar{p}\text{-}beam}}\right)^2$. Assuming that the $\sigma_{p\text{-}beam}$ and $\sigma_{\bar{p}\text{-}beam}$ are the same, $\sigma_{\bar{p}\text{-}beam} = \sigma_{vtx} \times \sqrt{2} \approx 37.8$ μm. The spatial spread of a beam σ can be written as

$$\sigma = \sqrt{\beta^* \cdot \frac{\epsilon}{6\beta\gamma}}, \tag{B.1}$$

where β^* is the Tevatron β parameter, ϵ is the 95 % normalized emittance, and $\beta\gamma$ $(= p/m_p)$ is the relativistic momentum of the beam. In the 630 GeV run, $\beta^* = 0.44$ m and $\beta\gamma = 315/m_p = 335.7$, resulting in an emittance of $\epsilon = 5.97 \times 10^{-6}$ $(\pi \cdot \mathrm{m} \cdot \mathrm{rad})$.

The angular spread of a beam σ^{ang} is given by

$$\sigma^{ang} = \sqrt{\frac{\epsilon}{6\beta\gamma} \;/\; \beta^*}. \tag{B.2}$$

Therefore, the angular spread of the antiproton beam is estimated to be $\sigma^{ang}_{\bar{p}\text{-}beam} =$ 0.0859 mrad.

B.2 Comparison between Data and Monte Carlo Simulation

In this section, distributions of the position and angle of Roman Pot tracks, reconstructed ξ, t, and the azimuthal angle $\phi_{\bar{p}}$ of recoil antiprotons are compared between data and Monte Carlo (MC) simulation to check the reliability of the MC simulation. The algorithm of the MC simulation is described in Ref. [75]. For the study of the 630 GeV data, the ξ and t distributions obtained in the global fit of hadronic diffraction [71] are used as inputs to the MC simulation. During the 630 GeV run, the Roman Pot tracking detectors had many dead channels, as shown in Table 4.1. Those Roman Pot channels were also assumed to be dead in the MC simulation.

For the data, events in the diffractive inclusive sample with a Roman Pot track having three hits in both X and Y directions are used. The Roman Pot acceptance cuts of $0.035 \leq \xi \leq 0.095$ and $|t| \leq 0.2$ GeV^2 are not applied to these events.

For the MC simulation, three separate sets of events are generated; one is for runs 74849−74978, another for runs 75000−75049, and the other for runs 75109−75110, since the number of Roman Pot dead channels is different among these three sets of runs, resulting in different distributions of the position and angle of Roman Pot tracks and so on.

Figures B.3−B.9 show distributions of the position and angle of Roman Pot tracks, reconstructed ξ, t and $\phi_{\bar{p}}$ for the data and the MC simulation. Data distributions are shown separately for the 17 runs used in this analysis; the corresponding MC distributions are superimposed. Distributions for the data and the MC simulation are in general agreement. Figure B.10 shows distributions of the Roman Pot hit pattern for the data and the MC simulation. In these distributions, events which have hits only in two Roman Pot tracking detectors in either the X or Y direction are also included. "Class=0" is for tracks which have hits in three Roman Pots both in X and Y directions, and "Class=1 (2)" is for tracks which have hits in three Roman Pots in X (Y) and in two Roman Pots in Y (X). The data have a smaller fraction of events with a Roman Pot track of class=1 and 2 than the MC simulation, which is probably because some Roman Pot tracks of class=1 and 2 are spoiled due to noise hits in the data. The ratios of the data to the MC simulation in the class=1 and 2 bins can be considered as the efficiencies for the reconstruction of class=1 and 2 Roman Pot tracks. The ratios of the data to the MC simulation in the class=1 and 2 bins are shown in Figure B.11 as a function of run number. Fits of a constant number to the distributions in Figure B.11 yield efficiencies of 45 % and 75 % for the

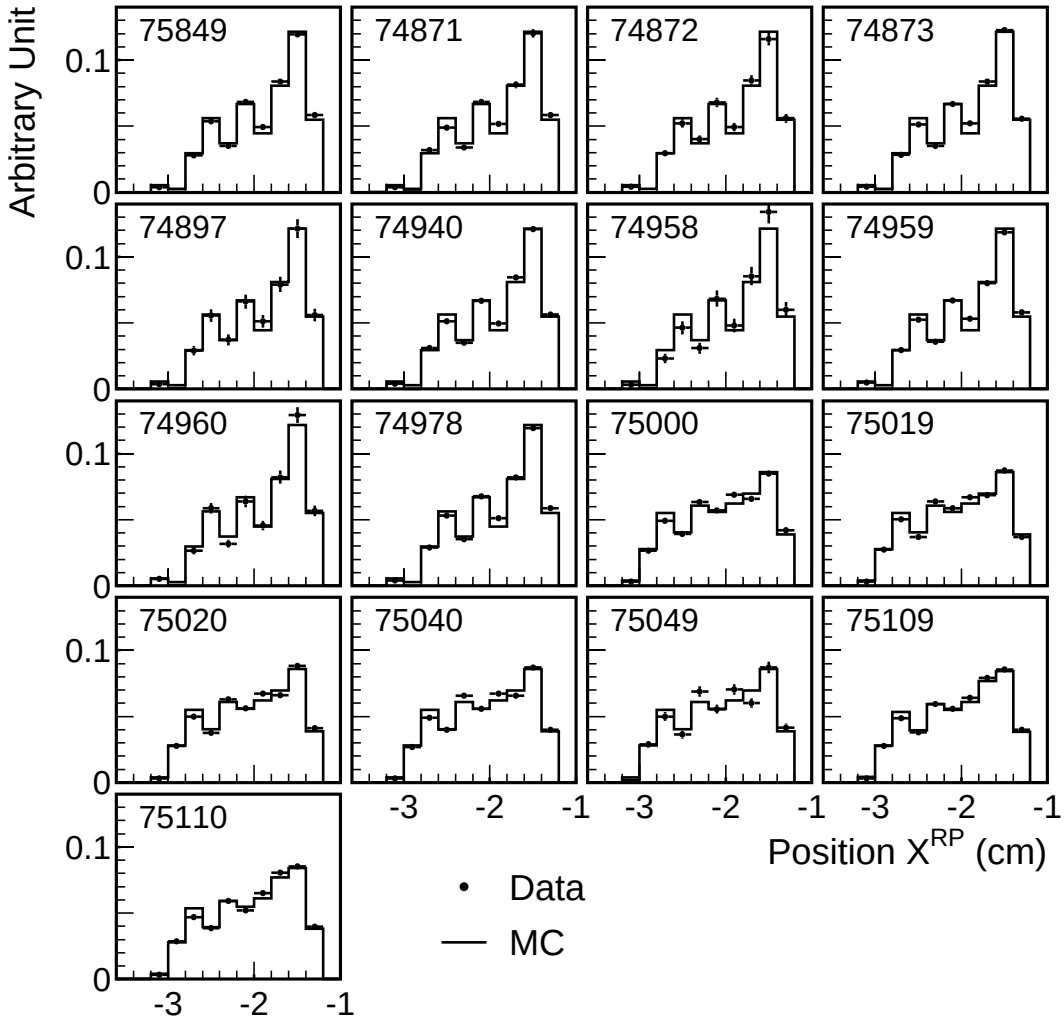

Figure B.3: Distributions of the position X^{RP} of reconstructed Roman Pot tracks in the horizontal direction relative to the center of the beam pipe for the data (points) and the MC simulation (histogram) for each run.

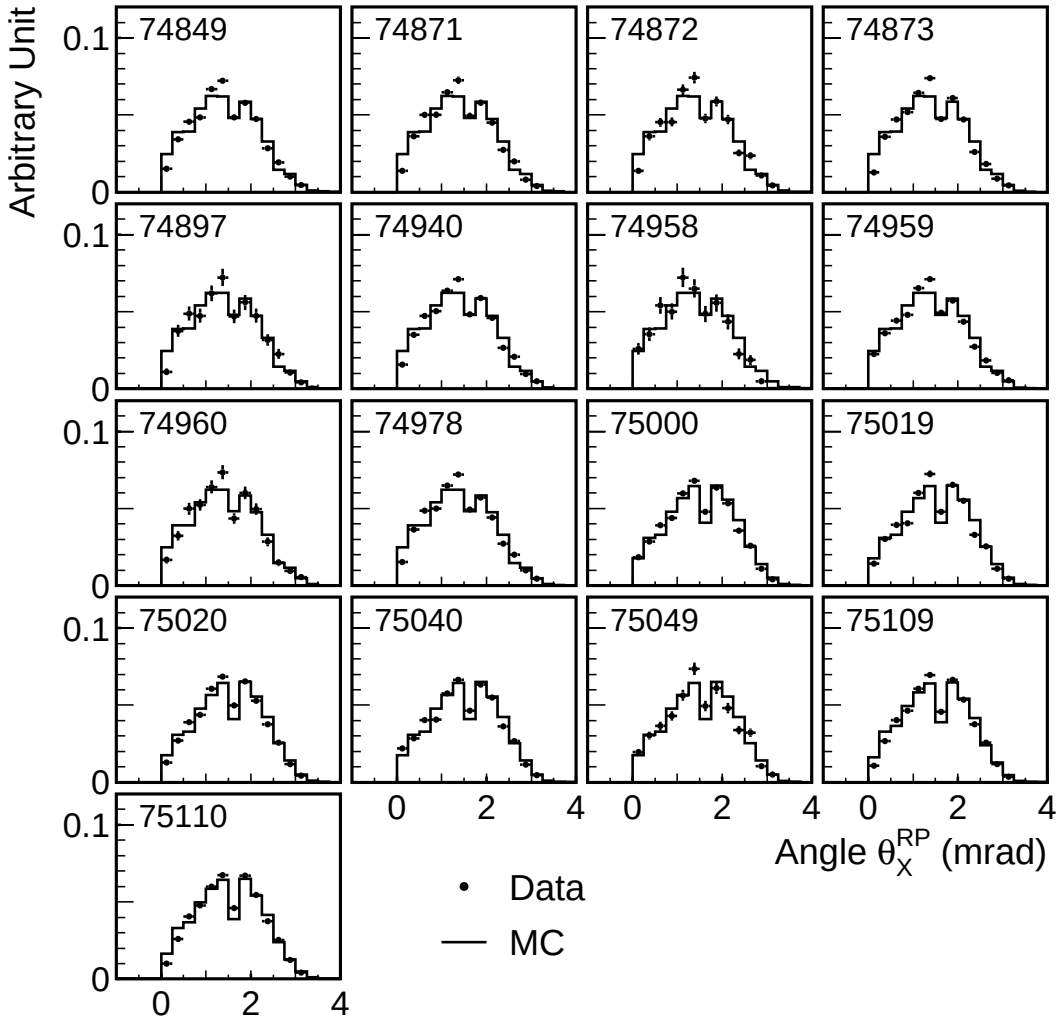

Figure B.4: Distributions of the angle θ_X^{RP} of reconstructed Roman Pot tracks in the horizontal direction with respect to the beam line for the data (points) and the MC simulation (histogram) for each run. When a Roman Pot track is running toward the inside of the Tevatron ring, θ_X^{RP} is positive.

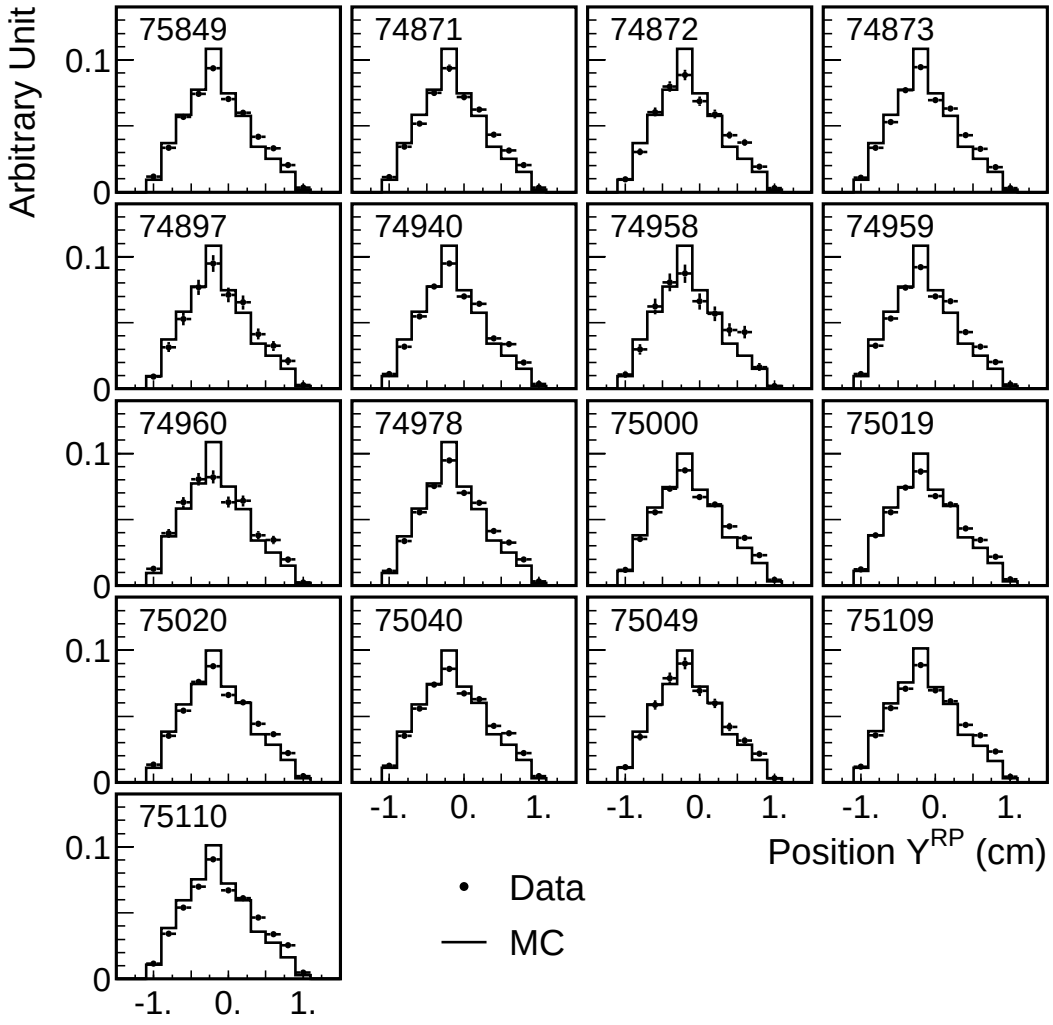

Figure B.5: Distributions of the position Y^{RP} of reconstructed Roman Pot tracks in the vertical direction relative to the center of the beam pipe for the data (points) and the MC simulation (histogram) for each run. When a Roman Pot track is above the center of the beam pipe, Y^{RP} is positive.

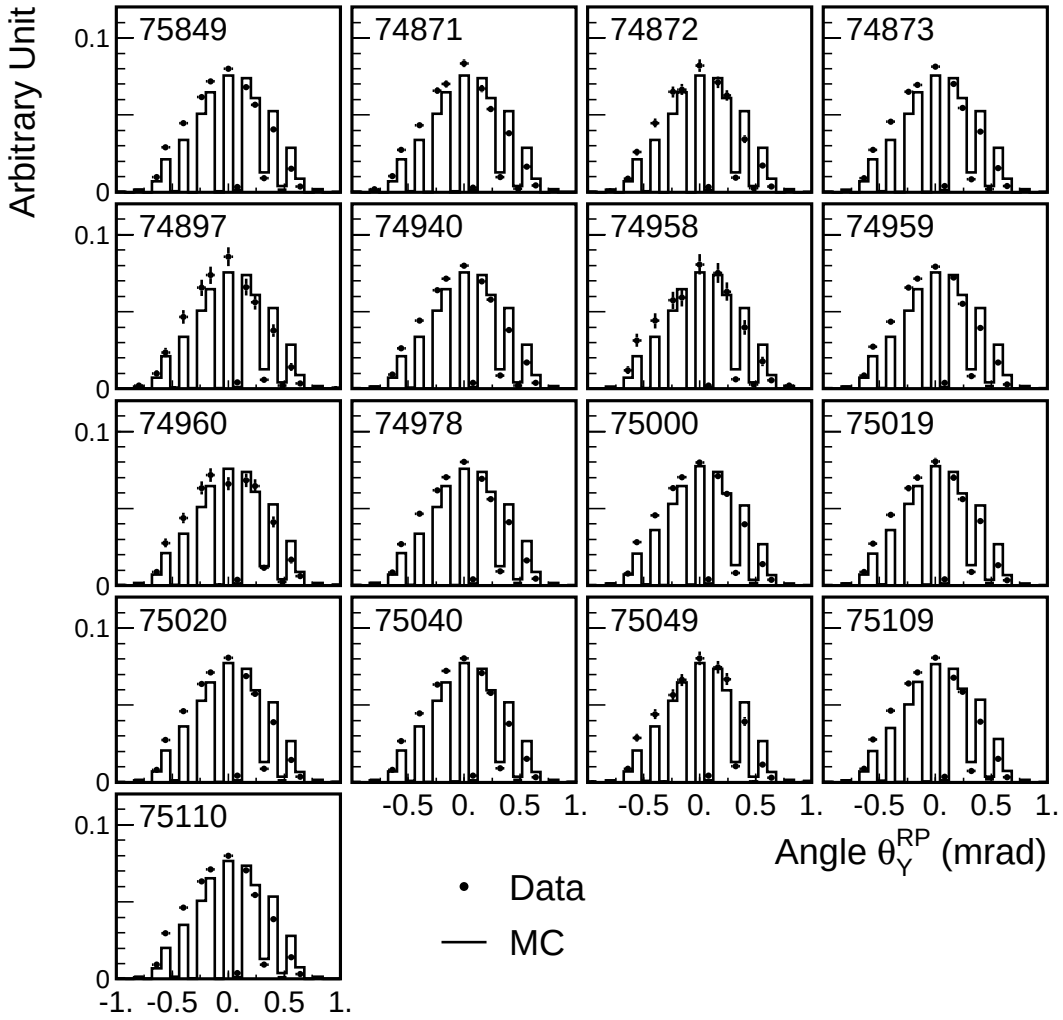

Figure B.6: Distributions of the angle θ_Y^{RP} of reconstructed Roman Pot tracks in the vertical direction with respect to the beam line for the data (points) and the MC simulation (histogram) for each run. When a Roman Pot track is running downward, θ_Y^{RP} is positive.

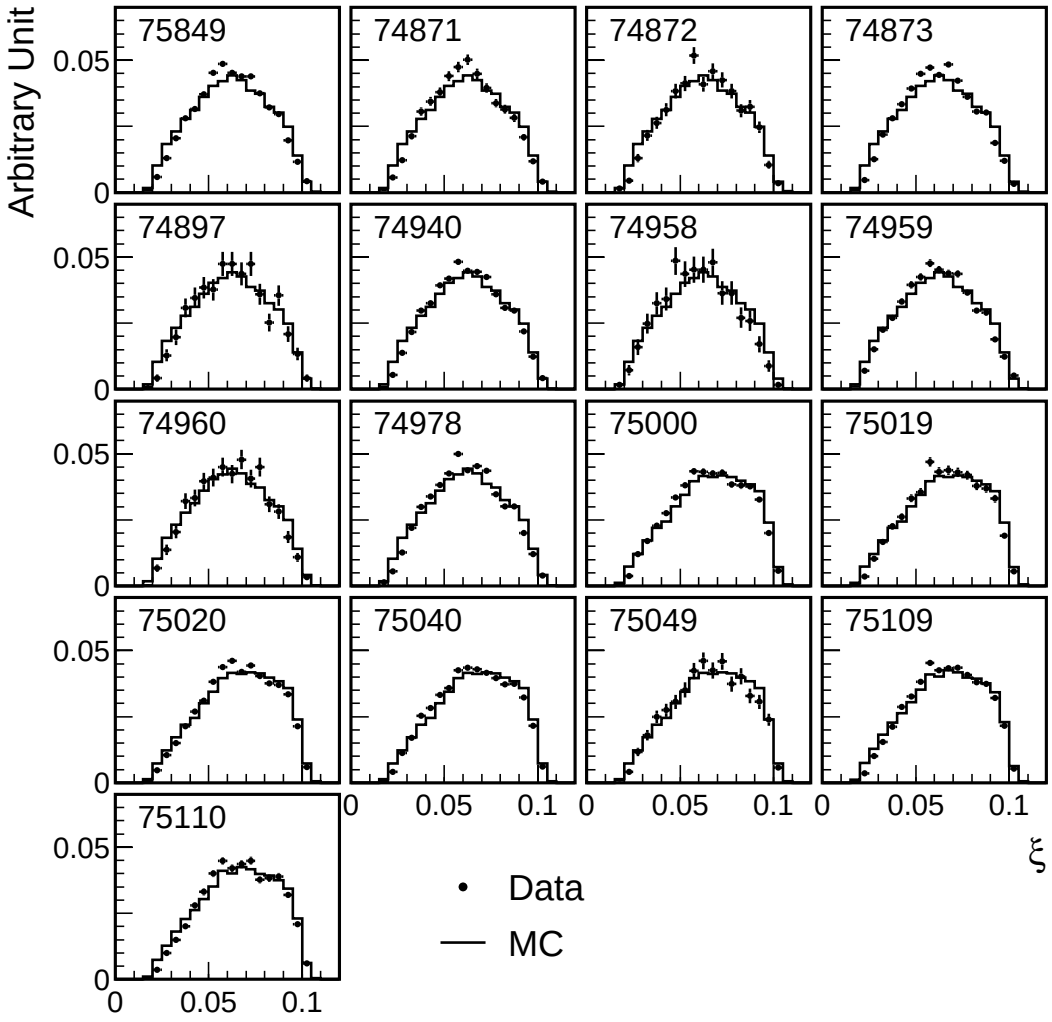

Figure B.7: Reconstructed ξ distributions for the data (points) and the MC simulation (histogram) for each run.

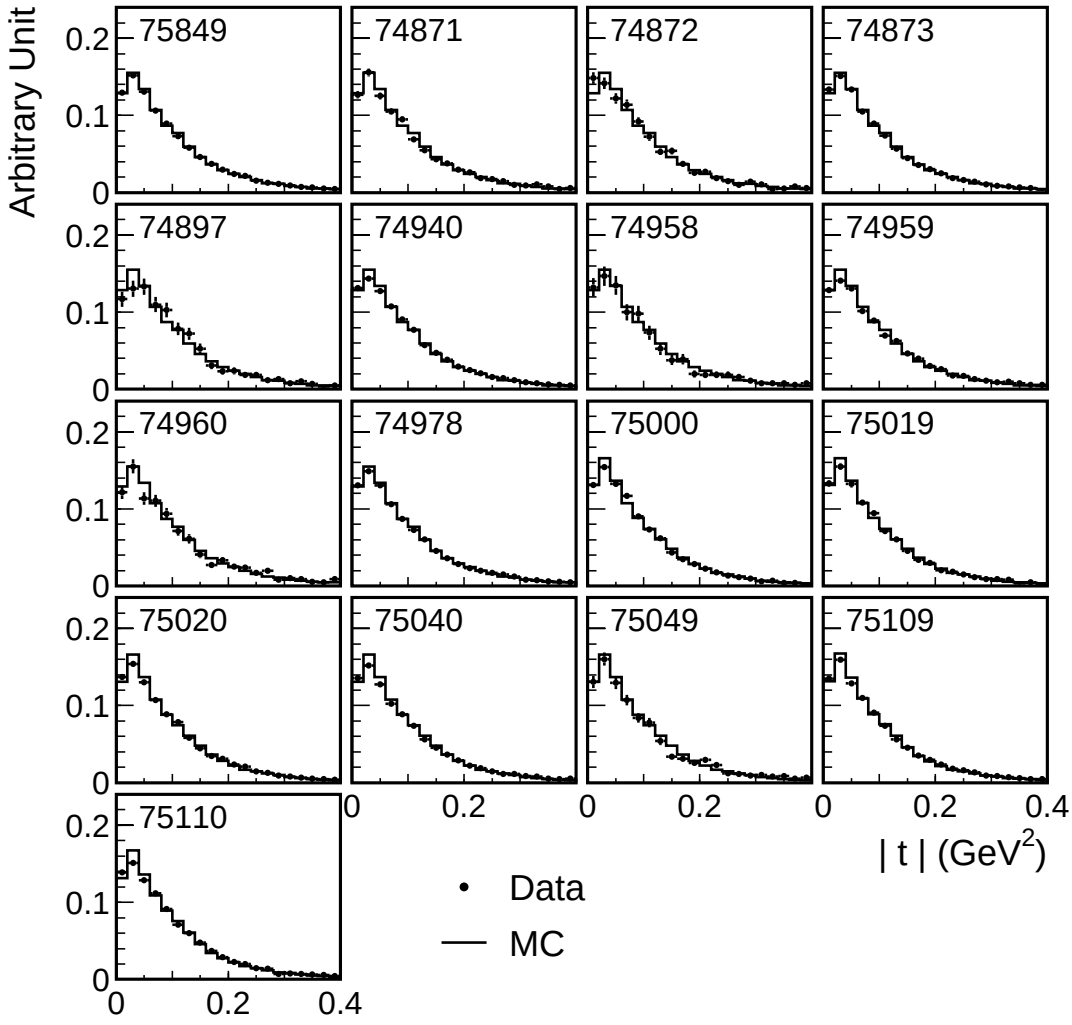

Figure B.8: Reconstructed $|t|$ distributions for the data (points) and the MC simulation (histogram) for each run.

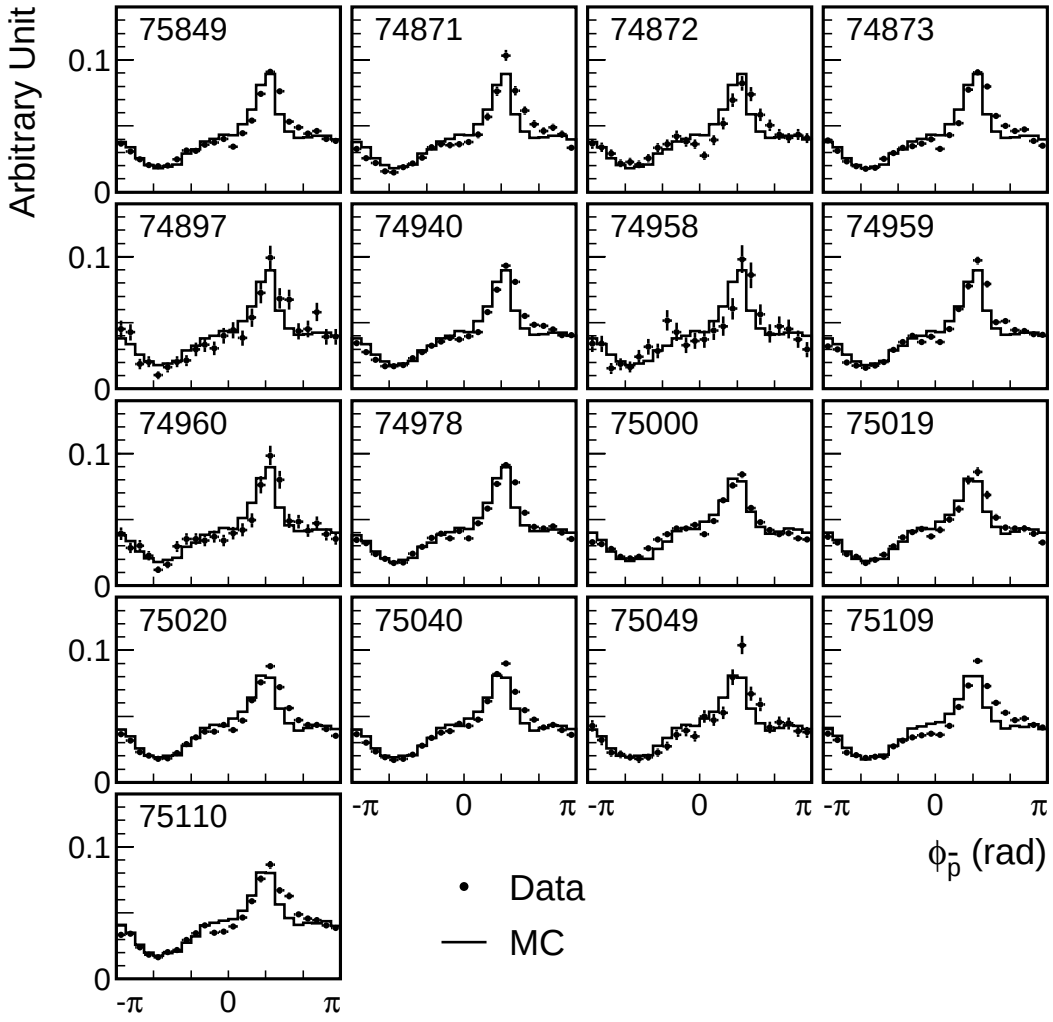

Figure B.9: Distributions of the azimuthal angle $\phi_{\bar{p}}$ of quasielastically-scattered recoil antiprotons for the data (points) and the MC simulation (histogram) for each run. When an antiproton is scattered toward the inside of the Tevatron ring, $\phi_{\bar{p}} = 0$ (rad), and when an antiproton is scattered downward, $\phi_{\bar{p}} = \pi/2$ (rad).

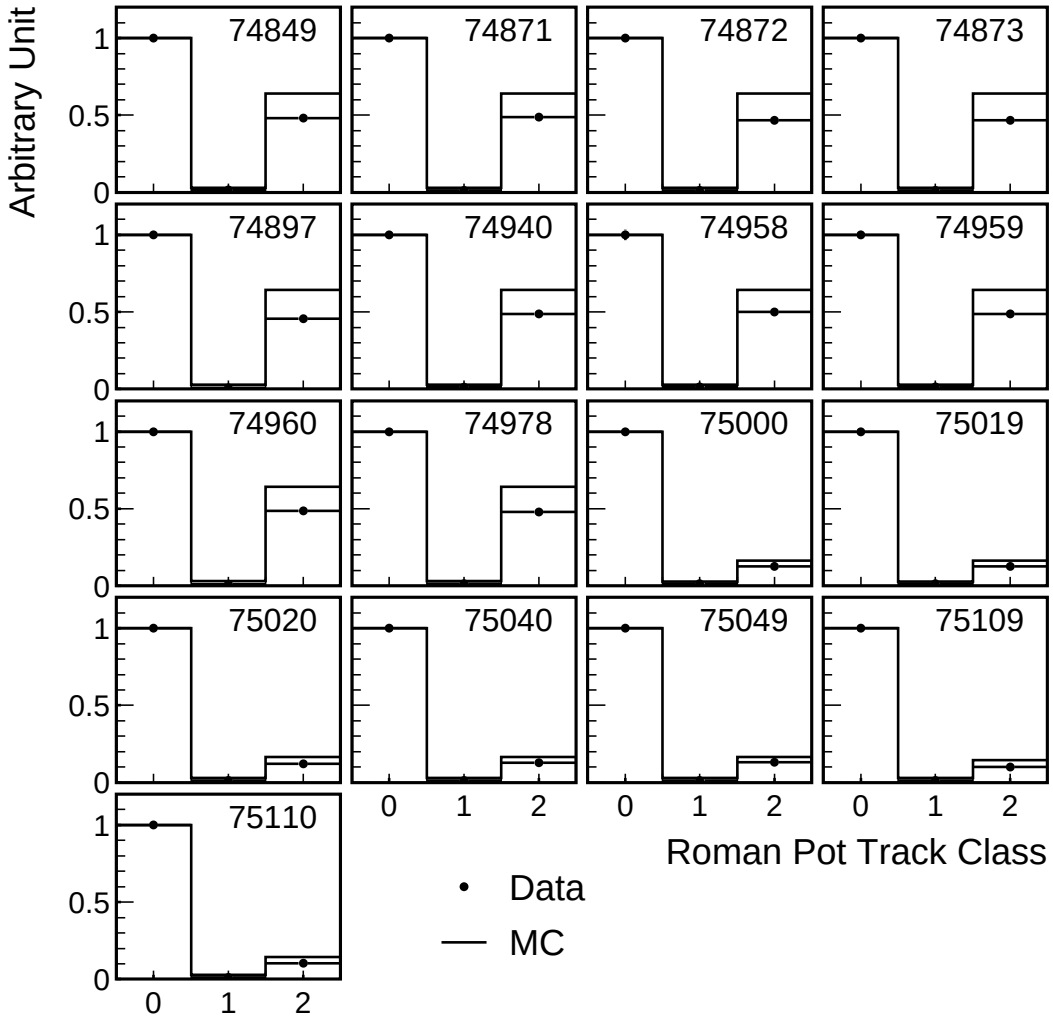

Figure B.10: Distributions of the Roman Pot track hit pattern for the data (points) and the MC simulation (histogram) for each run. The MC distributions are normalized to the data distributions at the zero bin.

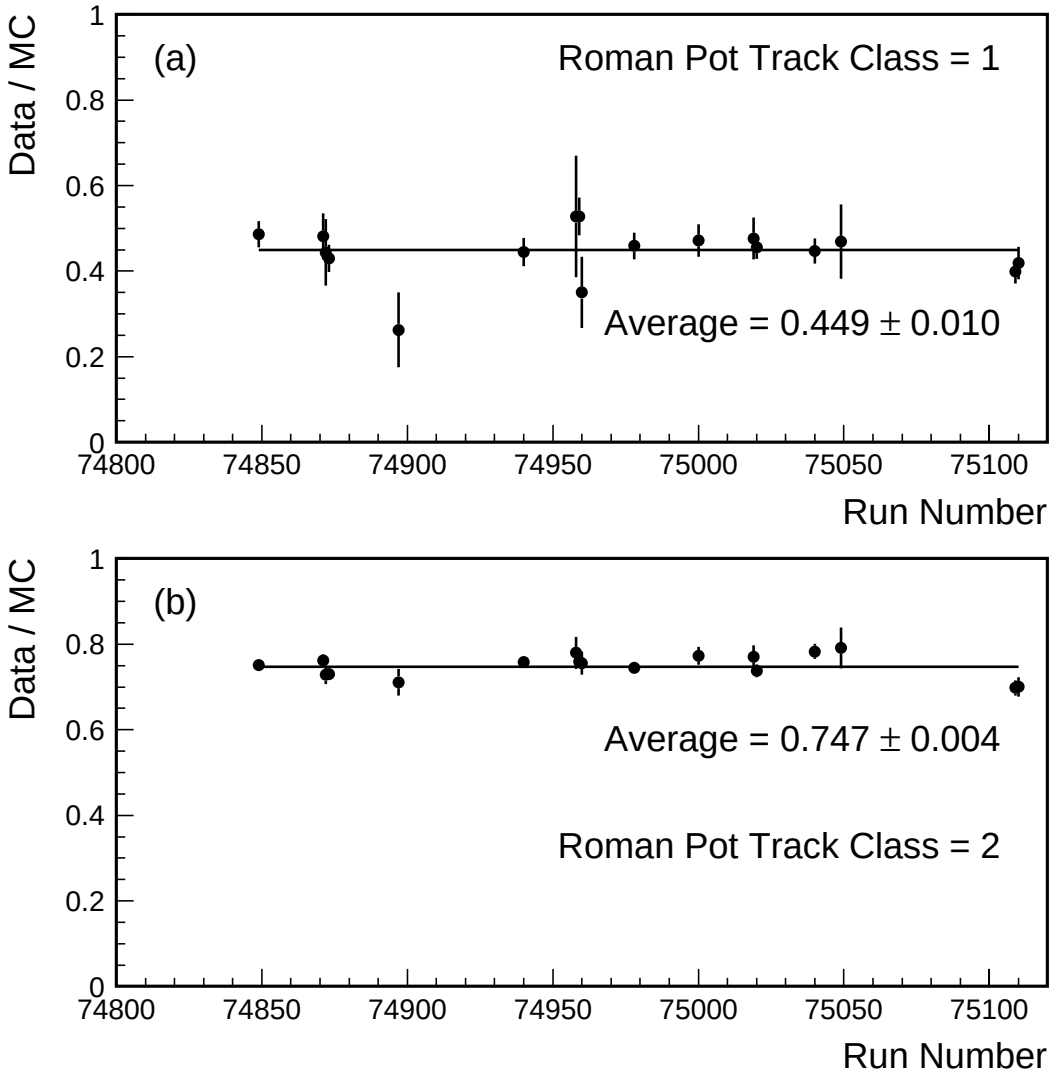

Figure B.11: Ratios of the data to the MC simulation in the class=1 and 2 bins in Figure B.10 as a function of run number.

class=1 and 2 tracks, respectively. The higher efficiency for the class=2 Roman Pot tracks than that for the class=1 Roman Pot tracks can be explained by the fact that the Roman Pot tracking detectors have more noise in the Y detector than in the X detector. This is probably because the Y detector, which was closer to the interaction point than the X detector, absorbs junk particles before they reach the X detector.

When the Roman Pot acceptance and resolutions in ξ and t are evaluated using this MC simulation, these efficiencies are taken into account.

B.3 Roman Pot Acceptance Evaluation

The acceptance of the Roman Pot spectrometer is evaluated from the ratio of events with a quasielastically-scattered recoil antiproton which does not collide with the beam pipe and electrostatic beam separators and passes through the Roman Pot fiducial region, to all the Monte Carlo generated events as a function of ξ and t. The results are shown for the three sets of Monte Carlo events separately in Figure B.12. The Roman Pot acceptance for the 630 GeV data shown in Figure 3.16(b) is the average of the three sets of results shown in Figure B.12. The Roman Pot acceptance is on average 59 % in the region $0.035 \leq \xi \leq 0.095$ and $|t| \leq 0.2$ GeV^2 at $\sqrt{s} = 630$ GeV; this ξ-t region is used in this analysis.

B.4 Resolutions in ξ and t

Using the Monte Carlo simulation, resolutions in ξ and t can be estimated by taking the differences between the ξ and t values initially generated by the Monte Carlo simulation and the ξ and t values determined from a Roman Pot track reconstructed

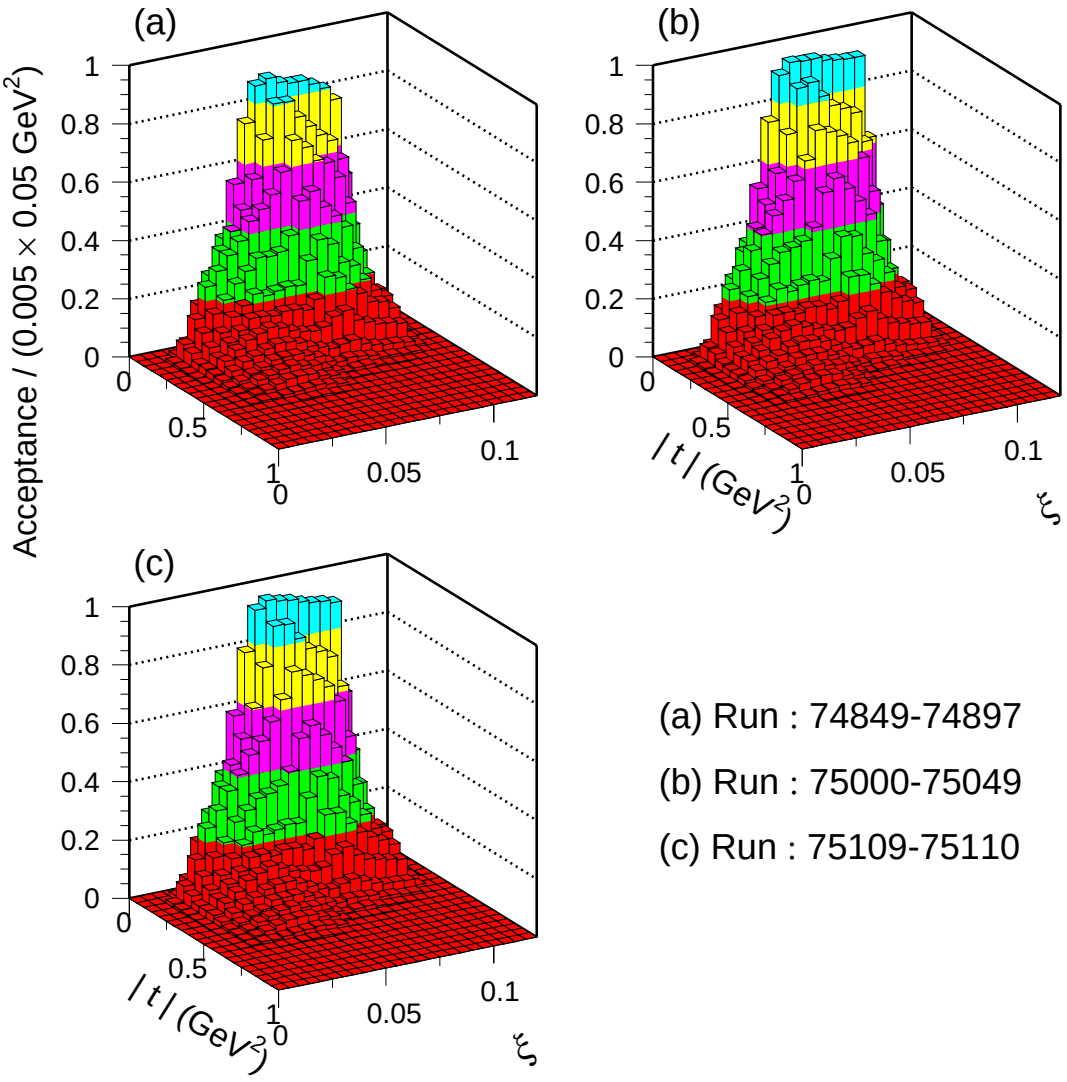

Figure B.12: The Roman Pot acceptance as a function of ξ and $|t|$ for the three sets of Monte Carlo event samples; (a) for runs 74849−74978, (b) for runs 75000−75049, and (c) for runs 75109−75110.

in the Monte Carlo simulation, which takes into account the spread of the antiproton beam and the fiber structure of the Roman Pot tracking detectors. The results are shown in Figures B.13 and B.14 for events with $0.035 \leq \xi \leq 0.095$ and $|t| \leq 0.2$ GeV^2. From these results, the resolutions in ξ and t are estimated to be $\sigma(\xi) = 0.0015$ and $\sigma(t) = 0.02$ GeV^2 for the region $0.035 \leq \xi \leq 0.095$ and $|t| \leq 0.2$ GeV^2 at $\sqrt{s} = 630$ GeV.

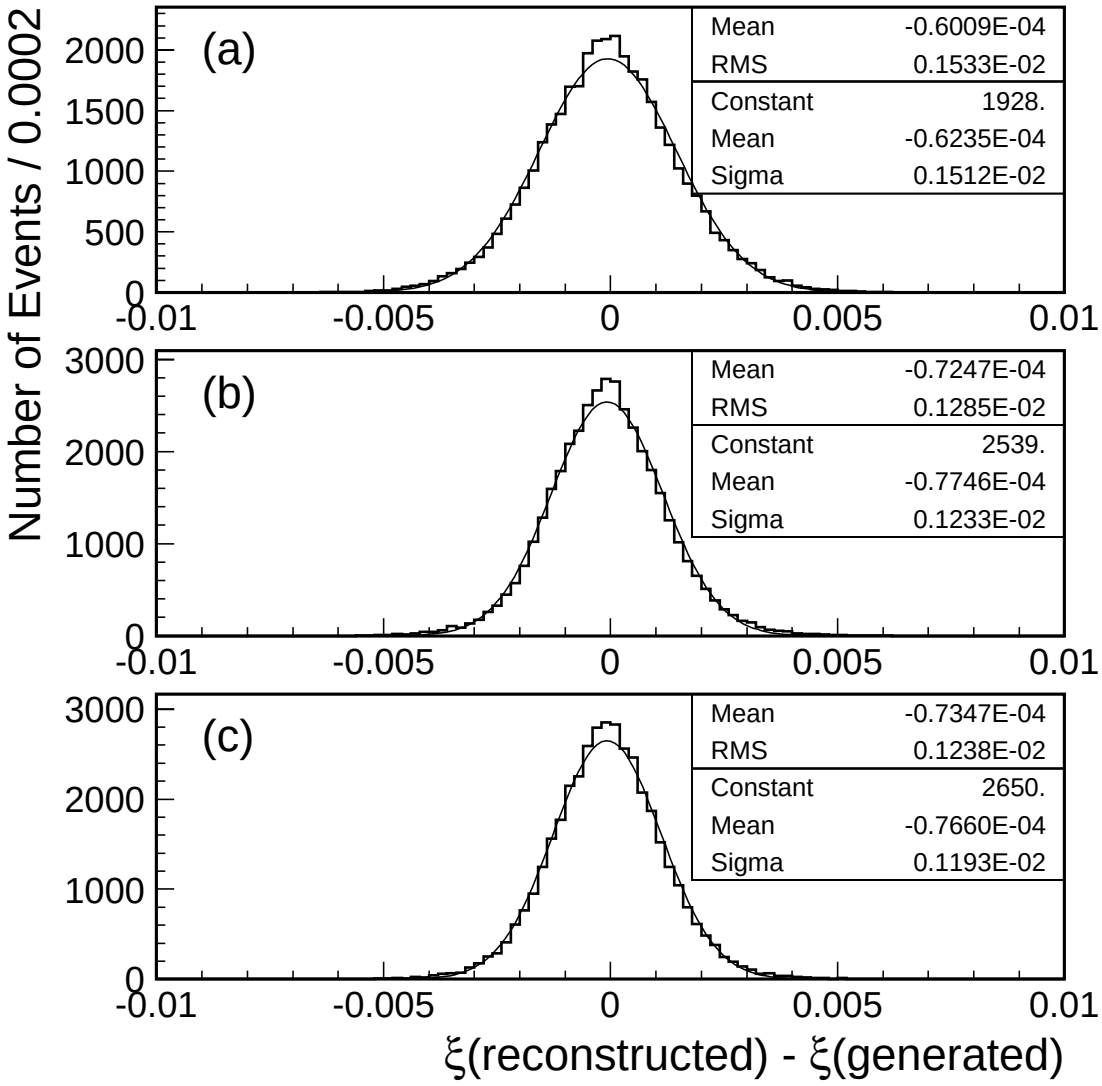

Figure B.13: Distributions of the difference between the reconstructed ξ and the generated ξ for the three sets of Monte Carlo event samples; (a) for runs 74849−74978, (b) for runs 75000−75049, and (c) for runs 75109−75110.

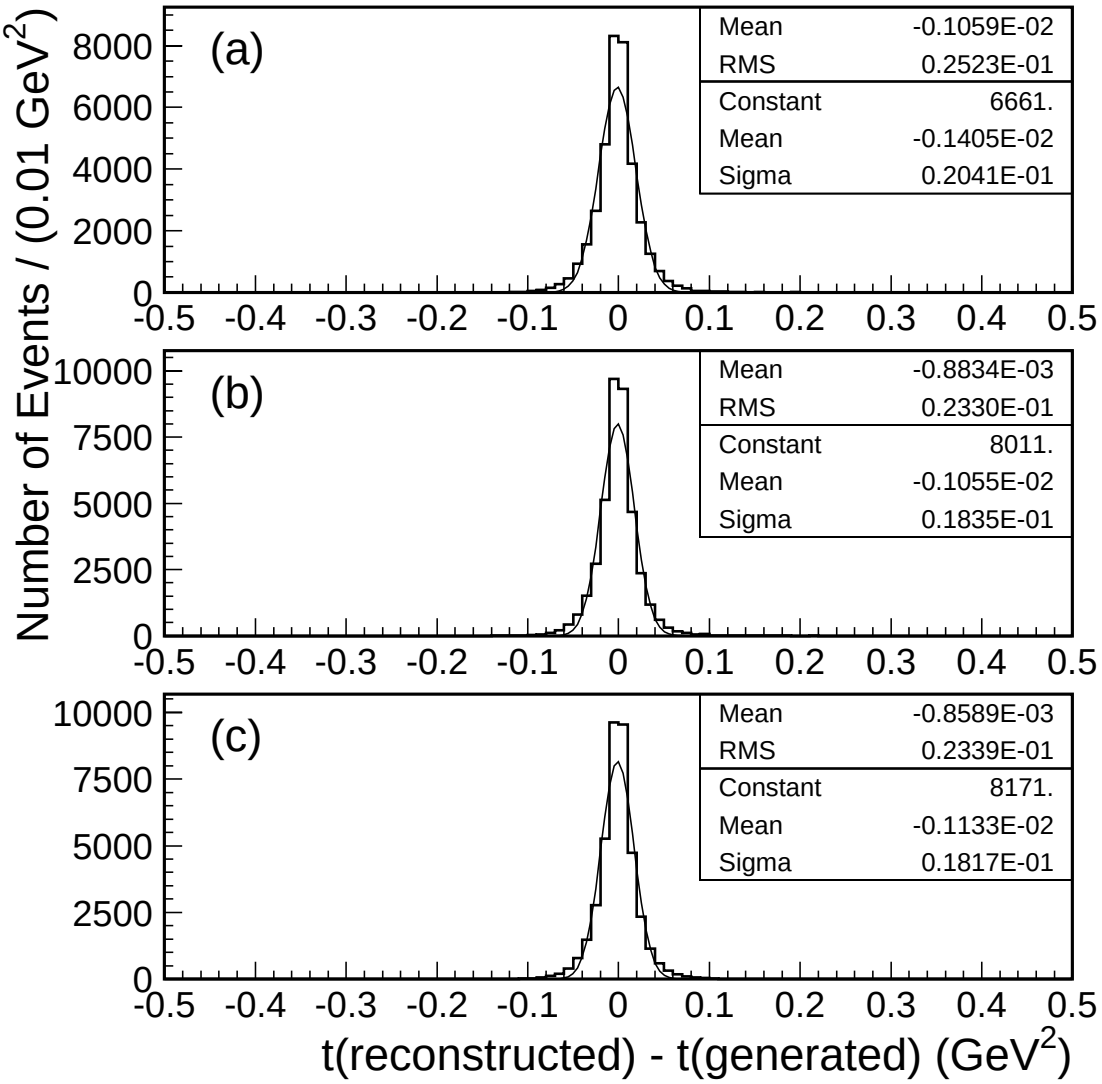

Figure B.14: Distributions of the difference between the reconstructed t and the generated t for the three sets of Monte Carlo event samples; (a) for runs 74849−74978, (b) for runs 75000−75049, and (c) for runs 75109−75110.

Appendix C

Events with Two Roman Pot Tracks

An event with two reconstructed Roman Pot tracks has one track in X (Y) and two tracks in Y (X). If two particles pass through the Roman Pot detectors in an event, the event should have two reconstructed tracks in both X and Y, and four Roman Pot tracks in total. Therefore, in events with two Roman Pot tracks, one of the two reconstructed tracks is probably a fake track. In approximately 90 % of events with two Roman Pot tracks, two tracks in X or Y are reconstructed from the same hits in two Roman Pot fiber detectors and have different hits only in one Roman Pot fiber detector. Figure C.1 shows the difference in the Roman Pot hit channel between two tracks for the 630 GeV diffractive data. The hit channel difference is concentrated at 2, 4 and 5. The hit channel difference becomes 2, 4 and 5, when the Roman Pot fiber detector has hit patterns shown in Figure C.2, which are most likely due to optical cross talk between fiber ribbons. For events with two Roman Pot tracks in the 630 GeV diffractive data, only the events in which two tracks are reconstructed from the same hits on two Roman Pot detectors and the hit channel difference is 2, 4 or 5 on the other Roman Pot detector are accepted; the best χ^2

track is used for further analysis.

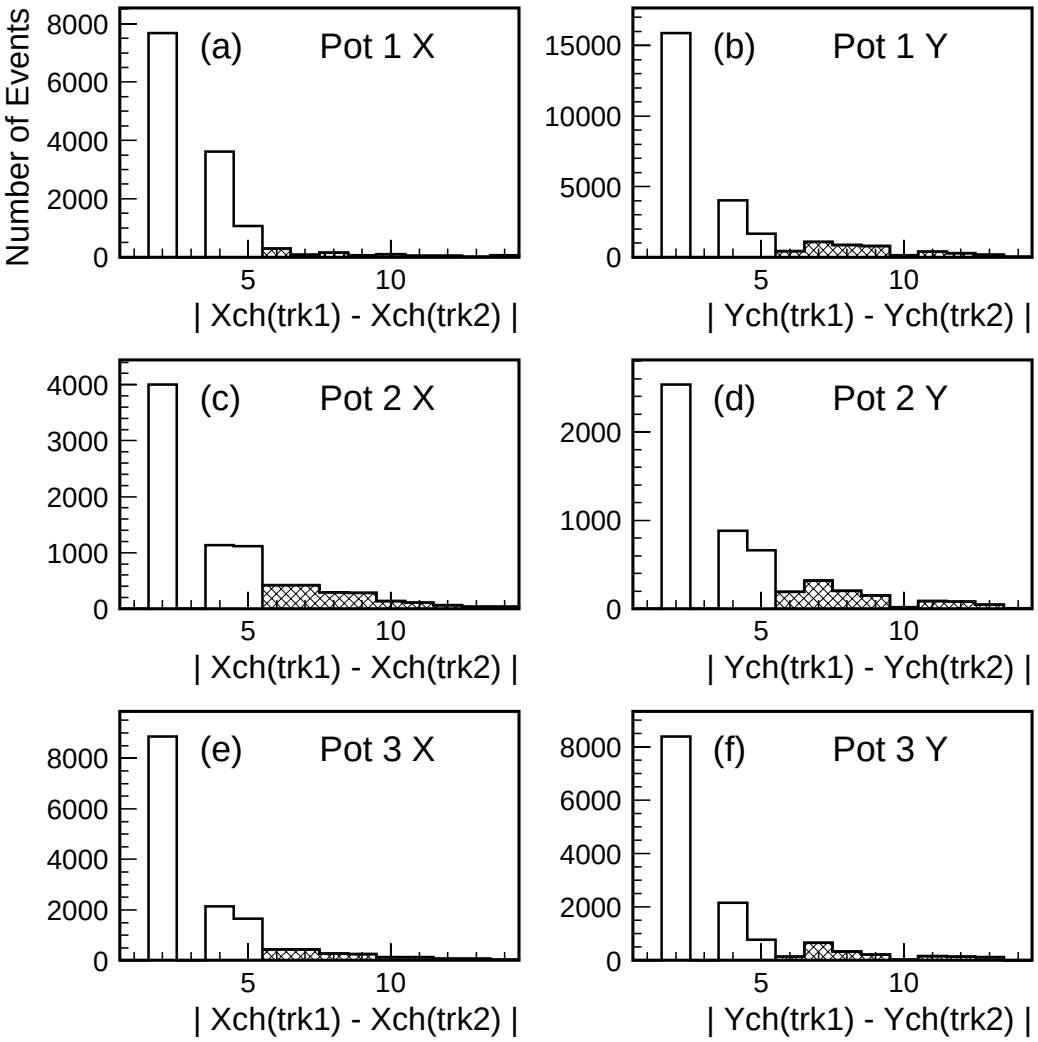

Figure C.1: The hit channel differences between two reconstructed Roman Pot tracks on the (a,b) Roman Pot 1 X and Y detectors, (c,d) Roman Pot 2 X and Y detectors, and (e,f) Roman Pot 3 X and Y detectors for the 630 GeV diffractive data. The events in the cross-hatched region are removed from our 630 GeV diffractive data samples.

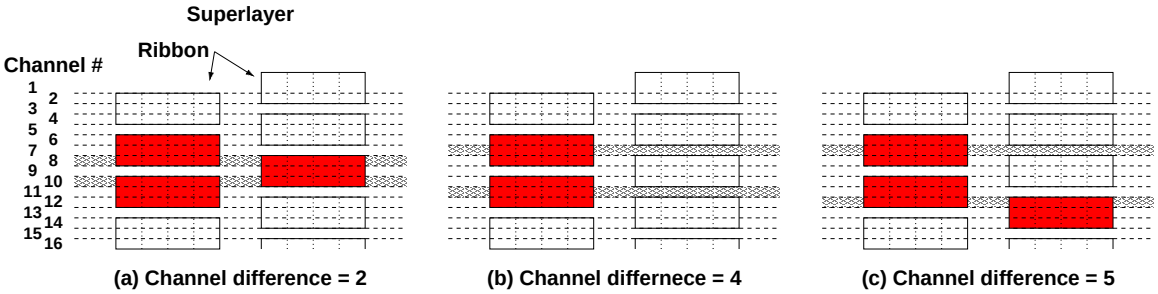

Figure C.2: The Roman Pot hit patterns when the hit channel difference is 2, 4 and 5. The filled regions are ribbons which have a hit. The hit channels are indicated by the cross-hatched regions.

Appendix D

Calorimeter Hot Towers

This appendix presents a study of fake jets due to calorimeter noise. In both the 1800 GeV and 630 GeV data samples used in this analysis, jets emerging with an anomalously high rate from some specific η-ϕ spots in certain runs were found in both the diffractive dijet and non-diffractive dijet samples. Such jets were found to have an unusual and unique distribution of EM fraction, defined as the ratio of the electromagnetic to total (electromagnetic and hadronic) energy of a jet. Therefore, they were identified as fake jets and were removed from the data samples by a *hot tower filter* (HTFLT), which imposes cuts on the position and EM fraction of a jet. Details are described below.

D.1 The 1800 GeV Data

Figures D.1 and D.2 show distributions of jets in detector-η (η_{det}) versus ϕ for diffractive dijet and non-diffractive dijet events with at least two jets with $E_T \geq 7$ GeV. In runs 75644−75713, several "hot spots" appeared in the plug and forward calorimeter regions. In runs 75714−75738, most of the hot spots disappeared, but

still some noisy spots remained. Figure D.3 shows distributions of EM fraction for jets found within the hot spots and outside the hot spots. The distributions of EM fraction for jets found within the hot spots are very different from the distribution for jets outside the hot spots. The characteristics of the five categories of hot spots are summarized in Table D.1.

In the 1800 GeV data analysis, jets in the hot spots with EM fraction in the ranges written in Table D.1 are removed by the HTFLT, regardless of run number, to simplify the analysis, as was done in Refs. [74, 85]. Figure D.4 shows distributions of jets on the η-ϕ plane after the HTFLT cut is applied.

The HTFLT used in this analysis is the same as that used in the study of di-jet production by double pomeron exchange [25, 74, 85]. The efficiency $\epsilon_{SD\,jj}^{HTFLT}$ of the HTFLT, defined as the fraction of real dijet events retained by the HTFLT, is estimated to be $\epsilon_{SD\,jj}^{HTFLT} = 97.1 \pm 0.5$ % [85].

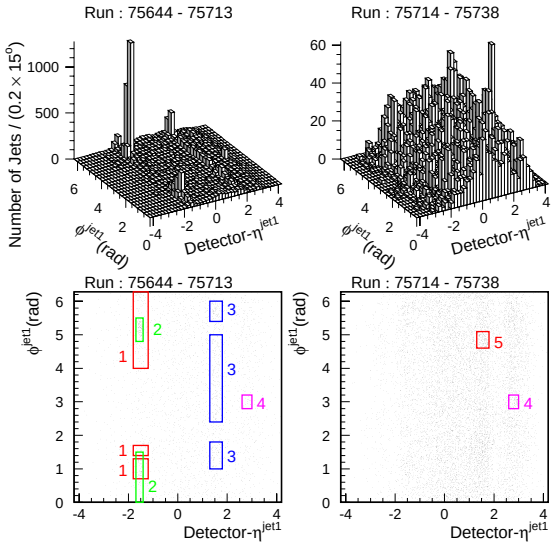

Figure D.1: Distributions of leading jets on the plane of detector-η versus ϕ for 1800 GeV diffractive dijet events with at least two jets with $E_T \geq 7$ GeV in runs 75644−75713 (left) and 75714−75738 (right). The five categories of hot spots listed in Table D.1 are indicated by boxes in the bottom two plots.

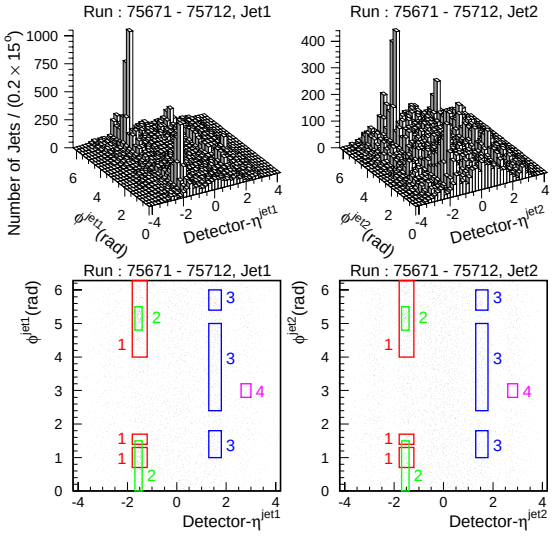

Figure D.2: Distributions of leading (left) and next-to-leading (right) jets on the plane of detector-η versus ϕ for 1800 GeV non-diffractive dijet events with at least two jets with $E_T \geq 7$ GeV. The five categories of hot spots listed in Table D.1 are indicated by boxes in the bottom two plots.

D.2 The 630 GeV Data

Figures D.5 and D.6 show distributions of jets on the η-ϕ plane for diffractive dijet and non-diffractive dijet events with at least two jets with $E_T \geq 7$ GeV. In runs $74919-74959$, jets are concentrated around the area of detector-$\eta \approx 2.6$ and $\phi \approx 255°$. The EM fraction distribution for jets which appeared around this hot spot is shown in Figure D.7(a), which is seen to be different from the normal distribution shown in Figure D.7(b). Since the jets which appeared around the hot spot with EM fraction of about 0.7 are presumably due to calorimeter noise, jets which satisfy the following conditions are rejected from the 630 GeV data by the HTFLT:

- $74919 \leq$ run ≤ 74959.
- $2.4 \leq$ detector-$\eta^{jet} \leq 2.8$.

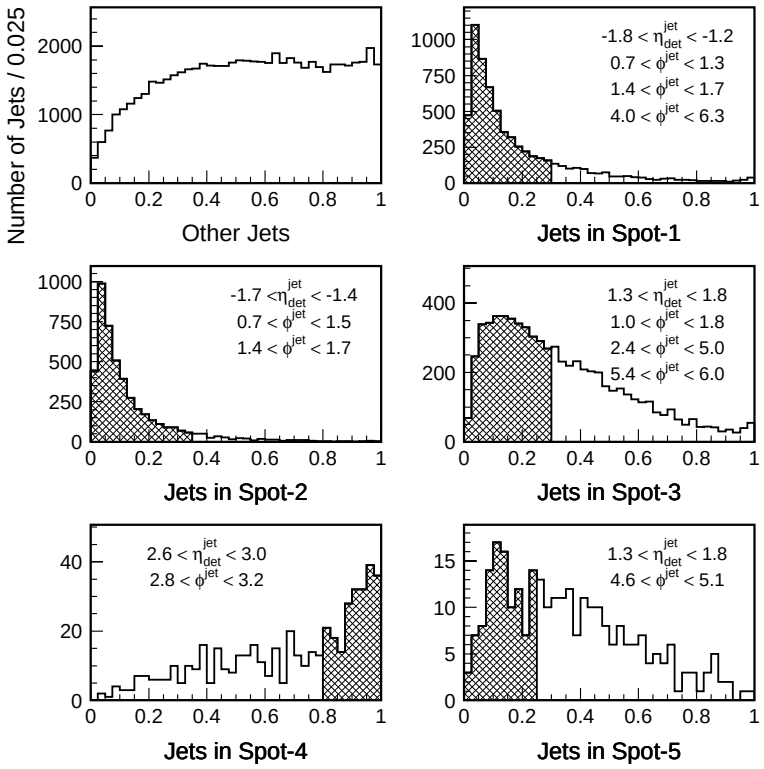

Figure D.3: Distributions of EM fraction of jets in the five categories of hot spots and outside the hot spots for the 1800 GeV diffractive dijet sample. Jets in the cross-hatched regions are rejected by the hot tower filter.

Table D.1: Summary of hot towers in the 1800 GeV data samples.

Hot tower spot (Run #)	Detector-η^{jet}	ϕ^{jet} (rad)	EM fraction
Spot 1 (75644−75713)	$-1.8 < \eta^{jet} < -1.2$	$0.7 < \phi^{jet} < 1.3$ $1.4 < \phi^{jet} < 1.7$ $4.0 < \phi^{jet} < 6.3$	< 0.3
Spot 2 (75644−75713)	$-1.7 < \eta^{jet} < -1.4$	$\phi^{jet} < 1.5$ $4.8 < \phi^{jet} < 5.5$	< 0.35
Spot 3 (75644−75713)	$1.3 < \eta^{jet} < 1.8$	$1.0 < \phi^{jet} < 1.8$ $2.4 < \phi^{jet} < 5.0$ $5.4 < \phi^{jet} < 6.0$	< 0.3
Spot 4 (75644−75738)	$2.6 < \eta^{jet} < 3.0$	$2.8 < \phi^{jet} < 3.2$	> 0.8
Spot 5 (75714−75738)	$1.3 < \eta^{jet} < 1.8$	$4.6 < \phi^{jet} < 5.1$	< 0.25

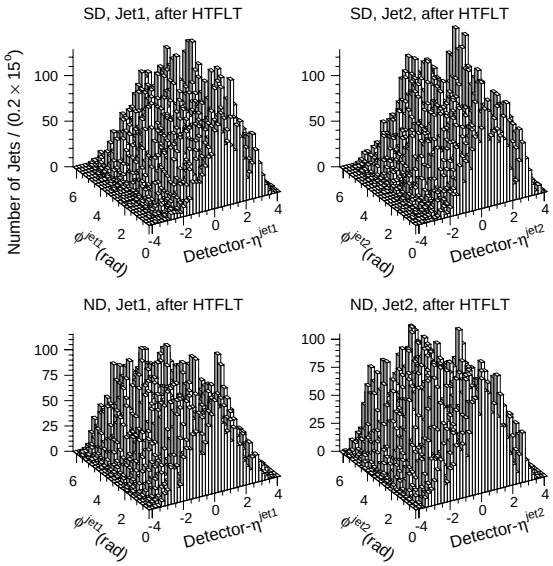

Figure D.4: Distributions of leading (left) and next-to-leading (right) jets on the plane of detector-η versus ϕ for 1800 GeV diffractive dijet (top) and non-diffractive dijet (bottom) events with at least two jets with $E_T \geq 7$ GeV which survive the hot tower filter requirements.

- $240^\circ \leq \phi^{jet} \leq 270^\circ$.
- $0.55 \leq$ EM fraction ≤ 0.80.

The HTFLT is applied only to events in runs 74919$-$74959, which are only 19 (16) % of the total 630 GeV diffractive (non-diffractive) data sample. After applying the HTFLT consisting of the above conditions, reasonable jet distributions are obtained, as shown in Figures D.5(c) and D.6(c).

The efficiency $\epsilon_{SD\,jj}^{HTFLT}$ of the HTFLT was estimated by applying the HTFLT to both the diffractive dijet and non-diffractive dijet samples collected in runs < 74919 or > 74959, in which there is no distinct noisy spot, and evaluating the fraction of the surviving events. The fraction was found to be larger than 99 % for both the diffractive and non-diffractive data samples. Since the fraction is very close to 100 % and also the HTFLT is applied only to less than 20 % of the total data samples, the

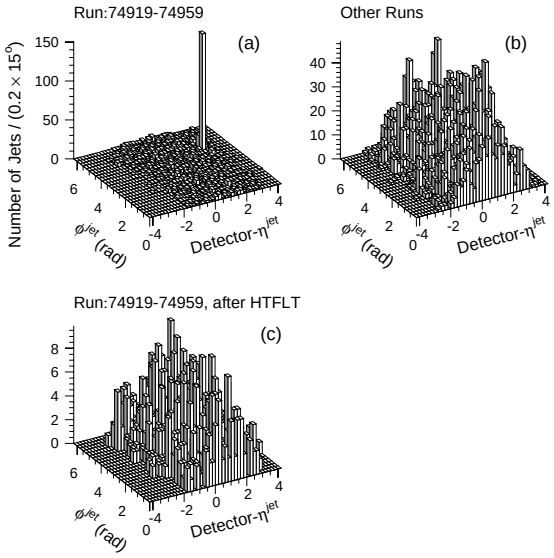

Figure D.5: Distributions of the leading two jets on the plane of detector-η versus ϕ for 630 GeV diffractive dijet events with at least two jets with $E_T \geq 7$ GeV (a) in runs 74919−74959 and (b) in the other runs before the hot tower filter is applied, and (c) in runs 74919−74959 after the hot tower filter is applied.

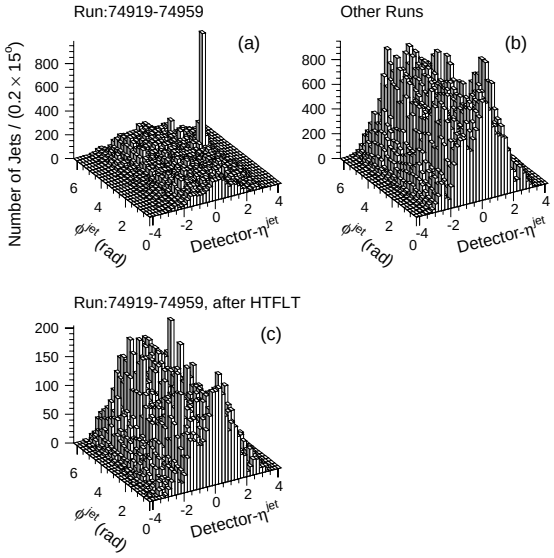

Figure D.6: Distributions of the leading two jets on the plane of detector-η versus ϕ for 630 GeV non-diffractive dijet events with at least two jets with $E_T \geq 7$ GeV (a) in runs 74919−74959 and (b) in the other runs before the hot tower filter is applied, and (c) in runs 74919−74959 after the hot tower filter is applied.

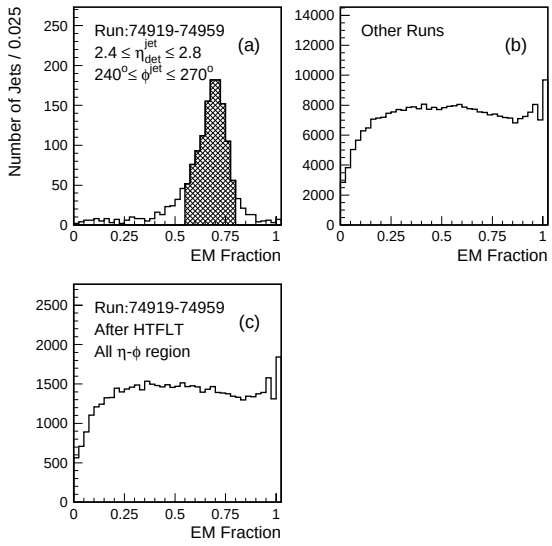

Figure D.7: Distributions of EM fraction of the leading two jets in 630 GeV non-diffractive dijet events with at least two jets with $E_T \geq 7$ GeV (a) in runs 74919−74959 in the hot spot and (b) in the other runs for the entire η-ϕ plane, and (c) in runs 74919−74959 for the entire η-ϕ plane after the hot tower filter is applied.

HTFLT efficiency is set to 100 % in the analysis.

Bibliography

[1] M. L. Good and W. D. Walker, *Diffractive dissociation of beam particles,* Phys. Rev. **120**, 1854 (1960).

[2] G. Ingelman and P. E. Schlein, *Jet structure in high mass diffractive scattering,* Phys. Lett. **152B**, 256 (1985).

[3] UA8 Collaboration, R. Bonino *et al.*, *Evidence for transverse jets in high-mass diffraction,* Phys. Lett. B **211**, 239 (1988).

[4] UA8 Collaboration, A. Brandt *et al.*, *Evidence for a super-hard pomeron structure,* Phys. Lett. B **297**, 417 (1992).

[5] ZEUS Collaboration, M. Derrick *et al.*, *Observation of events with a large rapidity gap in deep inelastic scattering at HERA,* Phys. Lett. B **315**, 481 (1993);
ZEUS Collaboration, M. Derrick *et al.*, *Measurement of the diffractive structure function in deep elastic scattering at HERA,* Z. Phys. C **68**, 569 (1995);
ZEUS Collaboration, M. Derrick *et al.*, *Measurement of the diffractive cross section in deep inelastic scattering,* Z. Phys. C **70**, 391 (1996).

[6] H1 Collaboration, T. Ahmed *et al.*, *Deep inelastic scattering events with a large rapidity gap at HERA*, Nucl. Phys. **B429**, 477 (1994);

H1 Collaboration, T. Ahmed *et al.*, *First measurement of the deep-inelastic structure of proton diffraction*, Phys. Lett. B **348**, 681 (1995).

[7] H1 Collaboration, T. Ahmed *et al.*, *Observation of hard processes in rapidity gap events in γp interactions at HERA*, Nucl. Phys. **B435**, 3 (1995).

[8] ZEUS Collaboration, M. Derrick *et al.*, *Observation of hard scattering in photoproduction events with a large rapidity gap at HERA*, Phys. Lett. B **346**, 399 (1995).

[9] H1 Collaboration, C. Adloff *et al.*, *Inclusive measurement of diffractive deep-inelastic ep scattering*, Z. Phys. C **76**, 613 (1997).

[10] ZEUS Collaboration, J. Breitweg *et al.*, *Measurement of the diffractive structure function $F_2^{D(4)}$ at HERA,* Eur. Phys. J. C **1**, 81 (1998).

[11] ZEUS Collaboration, J. Breitweg *et al.*, *Measurement of the diffractive cross section in deep inelastic scattering using ZEUS 1994 data*, Eur. Phys. J. C **6**, 43 (1999).

[12] H1 Collaboration, *Measurement and NLO DGLAP QCD interpretation of diffractive deep-inelastic scattering at HERA*, Paper submitted to 31st International Conference on High Energy Physics, ICHEP02, Amsterdam, The Netherlands, Jul. 24−31, 2001 (abstract 980).

[13] ZEUS Collaboration, M. Derrick *et al.*, *Observation of jet production in deep inelastic scattering with a large rapidity gap at HERA*, Phys. Lett. B **332**, 228 (1994);

ZEUS Collaboration, M. Derrick *et al.*, *Comparison of energy flows in deep inelastic scattering events with and without a large rapidity gap*, Phys. Lett. B **338**,

483 (1994);

ZEUS Collaboration, J. Breitweg *et al.*, *Event shape analysis of deep inelastic scattering events with a large rapidity gap at HERA*, Phys. Lett. B **421**, 368 (1998);

ZEUS Collaboration, S. Chekanov *et al.*, *Three-jet production in diffractive deep inelastic scattering at HERA*, Phys. Lett. B **516**, 273 (2001);

ZEUS Collaboration, S. Chekanov *et al.*, *Properties of hadronic final states in diffractive deep inelastic ep scattering at DESY HERA*, Phys. Rev. D **65**, 052001 (2002).

[14] H1 Collaboration, C. Adloff *et al.*, *Thrust jet analysis of deep-inelastic large-rapidity-gap events*, Eur. Phys. J. C **1**, 495 (1998);

H1 Collaboration, C. Adloff *et al.*, *Multiplicity structure of the hadronic final state in diffractive deep-inelastic scattering at HERA*, Eur. Phys. J. C **5**, 439 (1998);

H1 Collaboration, C. Adloff *et al.*, *Hadron production in diffractive deep-inelastic scattering*, Phys. Lett. B **428**, 206 (1998);

H1 Collaboration, C. Adloff *et al.*, *Diffractive jet production in deep-inelastic e^+p collisions at HERA*, Eur. Phys. J. C **20**, 29 (2001);

H1 Collaboration, C. Adloff *et al.*, *$D^{*\pm}$ meson production in deep-inelastic diffractive interactions at HERA*, Phys. Lett. B **520**, 191 (2001).

[15] ZEUS Collaboration, M. Derrick *et al.*, *Diffractive hard photoproduction at HERA and evidence for the gluon content of the pomeron*, Phys. Lett. B **356**, 129 (1995).

[16] ZEUS Collaboration, J. Breitweg *et al.*, *Diffractive dijet cross sections in photo-*

production at HERA, Eur. Phys. J. C **5**, 41 (1998).

[17] H1 Collaboration, C. Adloff *et al.*, *Diffractive dijet production at HERA*, Eur. Phys. J. C **6**, 421 (1999).

[18] CDF Collaboration, F. Abe *et al.*, *Observation of diffractive W-boson production at the Fermilab Tevatron*, Phys. Rev. Lett. **78**, 2698 (1997).

[19] CDF Collaboration, F. Abe *et al.*, *Measurement of diffractive dijet production at the Fermilab Tevatron*, Phys. Rev. Lett. **79**, 2636 (1997).

[20] DØ Collaboration, V. M. Abazov *et al.*, *Hard single diffraction in $\bar{p}p$ collisions at $\sqrt{s} = 630$ and 1800 GeV*, Phys. Lett. B **531**, 52 (2002).

[21] CDF Collaboration, T. Affolder *et al.*, *Observation of diffractive b-quark production at the Fermilab Tevatron*, Phys. Rev. Lett. **84**, 232 (2000).

[22] CDF Collaboration, T. Affolder *et al.*, *Observation of diffractive J/ψ production at the Fermilab Tevatron*, Phys. Rev. Lett. **87**, 241802 (2001).

[23] L. Alvero, J. C. Collins, J. Terron, and J. J. Whitmore, *Diffractive production of jets and weak bosons and tests of hard-scattering factorization*, Phys. Rev. D **59**, 074022 (1999).

[24] R. J. M. Covolan and M. S. Soares, *Analysis of the diffractive production of W's and dijets at the DESY HERA and Fermilab Tevatron colliders*, Phys. Rev. D **60**, 054005 (1999); **61**, 019901(E) (2000).

[25] CDF Collaboration, T. Affolder *et al.*, *Dijet production by double pomeron exchange at the Fermilab Tevatron*, Phys. Rev. Lett. **85**, 4215 (2000).

[26] V. Barone and E. Predazzi, *High-energy particle diffraction*, Springer Press (2001).

[27] R. J. M. Covolan, J. Montanha, and K. Goulianos, *A new determination of the soft pomeron intercept*, Phys. Lett. B **389**, 176 (1996).

[28] K. Goulianos, *Diffractive interactions of hadrons at high energies*, Phys. Rep. 101, 169 (1983).

[29] A. Donnachie and P. V. Landshoff, *Hard diffraction: production of high p_T jets, W or Z, and Drell-Yan pairs*, Nucl. Phys. **B303**, 634 (1988).

[30] CDF Collaboration, F. Abe *et al.*, *Measurement of $\bar{p}p$ single diffraction dissociation at $\sqrt{s} = 546$ and 1800 GeV*, Phys. Rev. D **50**, 5535 (1994).

[31] K. Goulianos, *Renormalization of hadronic diffraction and the structure of the pomeron*, Phys. Lett. B **358**, 379 (1995); B **363**, 268(E) (1995).

[32] S. Erhan and P. E. Schlein, *Evidence for ξ- and t-dependent damping of the pomeron flux in the proton*, Phys. Lett. B **427**, 389 (1998).

[33] S. Erhan and P. Schlein, *Inelastic diffraction data and the effective pomeron trajectory*, Phys. Lett. B **481**, 177 (2000).

[34] C.-I Tan, *Diffractive production at collider energies and factorization*, Phys. Rep. **315**, 175 (1999).

[35] R. P. Feynman, *Very high-energy collisions of hadrons*, Phys. Rev. Lett. **23**, 1415 (1969).

[36] J. C. Collins, J. Huston, J. Pumplin, H. Weerts, and J. J. Whitmore, *Measuring parton densities in the pomeron*, Phys. Rev. D **51**, 3182 (1995).

[37] V. N. Gribov and L. N. Lipatov, *Deep inelastic ep scattering in perturbation theory*, Sov. J. Nucl. Phys. **15**, 438 (1972);

V. N. Gribov and L. N. Lipatov, e^+e^- pair annihilation and deep inelastic *ep* scattering in perturbation theory, Sov. J. Nucl. Phys. **15**, 675 (1972);

Y. L. Dokshitzer, *Calculation of the structure functions for deep inelastic scattering and e^+e^- annihilation by perturbation theory in Quantum Chromodynamics*, Sov. Phys. JETP **46**, 641 (1977);

G. Altarelli and G. Parisi, *Asymptotic freedom in parton language*, Nucl. Phys. **B126**, 298 (1977).

[38] B. L. Combridge and C. J. Maxwell, *Untangling large-p_T hadronic reactions*, Nucl. Phys. **B239**, 429 (1984).

[39] B. L. Combridge and C. J. Maxwell, *Large-p_T three-jet events at the $\bar{p}p$ collider*, Phys. Lett. **151B**, 299 (1985).

[40] M. Gluck, E. Reya, and A. Vogt, *Dynamical parton distributions revisited*, Eur. Phys. J. C **5**, 461 (1998).

[41] CTEQ Collaboration, H. L. Lai *et al.*, *Global QCD analysis of parton structure of the nucleon: CTEQ5 parton distributions*, Eur. Phys. J. C **12**, 375 (2000).

[42] A. D. Martin, R. G. Roberts, W. J. Stirling, and R. S. Thorne, *Parton distributions: a new global analysis*, Eur. Phys. J. C **4**, 463 (1998).

[43] E. Gotsman, E. Levin, and U. Maor, *Survival probability of large rapidity gaps in a three channel model*, Phys. Rev. D **60**, 094011 (1999).

[44] A. B. Kaidalov, V. A. Khoze, A. D. Martin, and M. G. Ryskin, *Probabilities of rapidity gaps in high energy interactions*, Eur. Phys. J. C **21**, 521 (2001).

[45] J. D. Bjorken, *Rapidity gaps and jets as a new-physics signature in very-high-energy hadron-hadron collisions*, Phys. Rev. D **47**, 101 (1993).

[46] Private communication with the author of Ref. [31].

[47] A. Bialas, *Hard diffraction in lepton-hadron and hadron-hadron collisions*, Acta Phys. Polon. B **33**, 2635 (2002).

[48] R. Enberg, G. Ingelman, and N. Timneanu, *Soft color interactions and diffractive hard scattering at the Fermilab Tevatron*, Phys. Rev. D **64**, 114015 (2001).

[49] D. Mohl, G. Petrucci, L. Thorndahl, and S. V. D. Meer, *Physics and technique of stochastic cooling*, Phys. Rep. **58**, 73 (1980).

[50] F. Abe *et al.*, *The CDF detector: an overview*, Nucl. Instrum. Methods Phys. Res. A **271**, 387 (1988).

[51] L. Balka *et al.*, *The CDF central electromagnetic calorimeter*, Nucl. Instrum. Methods Phys. Res. A **267**, 272 (1988).

[52] S. Bertolucci *et al.*, *The CDF central and endwall hadron calorimeter*, Nucl. Instrum. Methods Phys. Res. A **267**, 301 (1988).

[53] K. Yasuoka *et al.*, *Response maps of the CDF central electromagnetic calorimeter with electrons*, Nucl. Instrum. Methods Phys. Res. A **267**, 315 (1988).

[54] R. G. Wagner *et al.*, *Cosmic ray test of the CDF central calorimeters*, Nucl. Instrum. Methods Phys. Res. A **267**, 330 (1988).

[55] S. R. Hahn *et al.*, *Calibration systems for the CDF central electromagnetic calorimeter*, Nucl. Instrum. Methods Phys. Res. A **267**, 351 (1988).

[56] Y. Fukui *et al.*, *CDF end plug electromagnetic calorimeter using conductive plastic proportional tubes*, Nucl. Instrum. Methods Phys. Res. A **267**, 280 (1988).

[57] G. Brandenburg *et al.*, *An electromagnetic calorimeter for the small angle regions of the Collider Detector at Fermilab*, Nucl. Instrum. Methods Phys. Res. A **267**, 257 (1988).

[58] S. Cihangir *et al.*, *The CDF forward/backward hadron calorimeter*, Nucl. Instrum. Methods Phys. Res. A **267**, 249 (1988).

[59] CDF Collaboration, F. Abe *et al.*, *Measurement of* $\sigma B(W \to e\nu)$ *and* $\sigma B(Z^0 \to e^+e^-)$ *in* $p\bar{p}$ *collisions at* $\sqrt{s} = 1.8$ *TeV*, Phys. Rev. Lett **76**, 3070 (1996).

[60] A. Beretvas, B. Flaugher, and J. Lamoureux, *BBC cross section at* $\sqrt{s} = 630$ *GeV*, CDF Note 4771 (1998).

[61] D. Amidei *et al.*, *A two level FASTBUS based trigger system for CDF*, Nucl. Instrum. Methods Phys. Res. A **269**, 51 (1988).

[62] G. Drake *et al.*, *CDF front end electronics: the RABBIT system*, Nucl. Instrum. Methods Phys. Res. A **269**, 68 (1988).

[63] E. Barsotti *et al.*, *FASTBUS data aquisition for CDF*, Nucl. Instrum. Methods Phys. Res. A **269**, 82 (1988).

[64] CDF Collaboration, F. Abe *et al.*, *Topology of three-jet events in* $\bar{p}p$ *collisions at* $\sqrt{s} = 1.8$ *TeV*, Phys. Rev. D **45**, 1448 (1992).

[65] N. Eddy, *New relative jet corrections for Run 1A and 1B data*, CDF Note 3534 (1996).

[66] F. E. Paige and S. D. Protopopescu, *ISAJET 5.30: a Monte Carlo event generator for pp and $\bar{p}p$ interactions*, Report No. BNL-38034, 1986.

[67] R. D. Field and R. P. Feynmann, *A parametrization of the properties of quark jets*, Nucl. Phys. **B136**, 1 (1978).

[68] S. Bagdasarov, *Observation of diffractive W-boson production at the Tevatron*, Ph.D. thesis, Rockefeller University, 1997.

[69] CDF Collaboration, K. Goulianos, *Double-gap soft diffraction results from CDF*, Acta Phys. Polon. B **33**, 3467 (2002).

[70] G. P. Lepage, *A new algorithm for adaptive multidimensional integration*, J. Comput. Phys. **27**, 192 (1978);
G. P. Lepage, *VEGAS - An adaptive multi-dimensional integration program,* CLNS-80/447 (1980).

[71] K. Goulianos and J. Montanha, *Factorization and scaling in hadronic diffraction*, Phys. Rev. D **59**, 114017 (1999).

[72] A. Beretvas *et al.*, *Event z vertex cut efficiency as a luminosity correction for Run 1B*, CDF Note 5066 (1999).

[73] B. Flaugher, *Efficiency of the* 60 *cm z-vertex cut*, CDF Note 5094 (1998).

[74] K. Terashi, *Observation of dijet production by double pomeron exchange in* 1.8-*TeV proton-antiproton collisions*, Ph.D. thesis, University of Tsukuba, 2000.

[75] H. Nakada, *Measurement of the diffractive structure function of the antiproton in* 1.8-*TeV proton-antiproton collisions*, Ph.D. thesis, University of Tsukuba, 2001.

[76] H1 Collaboration, P. R. Newman, *Inclusive measurements of diffraction in deep-inelastic scattering and photoproduction at HERA*, Presented at Topical Conference on Hard Diffraction, Eilat, Israel, Feb. 2−5, 1996, and at International Workshop on Deep-Inelastic Scattering and Related Phenomena, Rome, Italy, Apr. 15−19, 1996.

[77] J. Phillips, `http://www-h1.desy.de/h1/www/h1work/dif/h1f2d1994.html`.

[78] J. F. Owens, *Q^2-dependent parametrizations of pion parton distribution functions*, Phys. Rev. D **30**, 943 (1984).

[79] Private communication with the authors of Ref. [9].

[80] Private communication with the authors of Ref. [44].

[81] J. C. Collins, *Light cone variables, rapidity and all that*, hep-ph/9705393.

[82] R. Blair *et al.*, *The CDF II detector technical design report*, FERMILAB-PUB-96/390-E (1996).

[83] K. Goulianos *et al.*, *The CDF MiniPlug calorimeters*, Nucl. Instrum. Methods Phys. Res. A **496**, 333 (2003).

[84] D. C. Carey, K. L. Brown, and F. Rothacker, *Third-order transport, A computer program for designing charged particle beam transport systems*, SLAC-R-95-462, Fermilab-Pub-95/069, UC-414 (1995).

[85] K. Terashi *et al.*, *Observation of dijet production in double pomeron exchange in $\bar{p}p$ collisions at $\sqrt{s} = 1800$ GeV*, CDF Note 4711, Version 3.0 (1999).